Coupling of a FPGA digital filter with a QCM resonator for mass detection using modelocalization

Claude Humbert

To cite this version:

> Claude Humbert. Coupling of a FPGA digital filter with a QCM resonator for mass detection using modelocalization. Micro and nanotechnologies/Microelectronics. Université Bourgogne Franche-Comté, 2020. English. NNT : 2020UBFCD051 . tel-03220660

HAL Id: tel-03220660
https://theses.hal.science/tel-03220660v1

Submitted on 7 May 2021

THESE DE DOCTORAT DE L'ETABLISSEMENT UNIVERSITE BOURGOGNE FRANCHE-COMTE

Ecole doctorale n°37

Sciences physiques pour l'ingénieur et microtechniques

Doctorat de spécialité sciences de l'ingénieur

Financé par le programme EIPHI

Et préparé à l'université de Franche-Comté

Par Monsieur HUMBERT, Claude

COUPLAGE D'UN FILTRE NUMERIQUE SUR FPGA AVEC UNE MICROBALANCE A QUARTZ POUR LA DETECTION DE MASSE PAR LOCALISATION DE MODES

Thèse présentée et soutenue à FEMTO-ST, le 19 mars 2020

Composition du Jury :

Monsieur	CHOLLET, Franck	Professeur, UBFC	Président
Monsieur	KRAFT, Michael	Professeur, ESAT/MICAS	Rapporteur
Monsieur	JUILLARD, Jérôme	Professeur, CentraleSupélec	Rapporteur
Monsieur	BASROUR, Skandar	Professeur, TIMA	Examinateur
Monsieur	NICOLAY, Pascal	Professeur, CUAS	Examinateur
Madame	LEBLOIS, Thérèse	Professeur, UBFC	Directrice de thèse
Monsieur	WALTER, Vincent	Maître de conférences, UBFC	Co-directeur de thèse
Monsieur	KACEM, Najib	Maître de conférences, UBFC	Co-directeur de thèse

Acknowledgements

Ces quelques lignes mettent un terme à trois ans de travail et signent aussi l'aboutissement de mes études. Ce long parcours n'aurait certainement pas le même visage sans la présence de mes parents qui ont toujours fait leur possible pour soutenir nos choix, ce qui n'est pas offert à tous. Ces trois années m'ont donné l'opportunité d'apprendre, découvrir, voyager et rencontrer, tant sur le plan professionnel que personnel.

Je souhaite ici chaleureusement remercier ma directrice de thèse Thérèse Leblois de m'avoir accueilli dans son équipe pour ce projet ambitieux et très intéressant. Au delà de ses compétences scientifiques, Thérèse possède des qualités humaines qui rendent les discussions à la fois agréables et productives. Malgré un temps libre particulièrement restreint à cause de ses nombreuses casquettes, elle prend toujours le temps d'écouter et proposer des solutions rapidement, sans demander à repasser plus tard. Elle sait encourager ses doctorants et les incite vivement à partir en conférence à l'international pour valoriser leur recherche, ce qui entretient la motivation à long terme. Thérèse, toutefois, n'est pas la seule à m'avoir épaulé car ce doctorat était une collaboration entre le département Micro Nano Sciences and Systems et le Département de Mécanique Appliquée. Ainsi, mes remerciements vont aussi à mon premier encadrant Vincent Walter, maître de conférences et artiste toujours de bonne humeur. Je souhaite particulièrement le remercier d'avoir partagé ses heures d'enseignement avec moi, je pense qu'elles m'ont apporté au moins autant qu'à ses étudiants. Il est également une partie de sa contribution au projet que j'ai beaucoup appréciée mais qui reste un peu dans l'ombre : ses corrections remarquablement méticuleuses du présent manuscrit ! En outre, j'adresse mes remerciements à mon second encadrant, Najib Kacem, pour son accompagnement tout au long de la thèse et en particulier pour son idée de normaliser l'ensemble des paramètres du système. Enfin, je les remercie tous les trois de m'avoir donné la liberté de mettre sur pied l'idée de système hybride avec laquelle je suis un jour arrivé au bureau, alors que cette solution sortait partiellement de leurs domaines d'expertise.

Il est maintenant tant pour moi de remercier Gonzalo Cabodevila qui a beaucoup contribué à la réussite du projet par son apport conséquent sur le plan théorique. Bien entendu, rien n'aurait été possible sans le département Temps-Fréquence qui m'a fourni une aide précieuse sur les aspects techniques. Ainsi, je suis redevable à Gwenhael Goavec-Merou pour ses outils numériques sur FPGA et son temps. Gwen répond toujours présent et fournit des informations précises en jargon mais avec une patience exemplaire. Je tiens également à adresser mes remerciements à Baptiste Marchal pour son aide significative sur l'interface graphique et l'utilisation de la RedPitaya ainsi qu'à Thomas Bertin, ingénieur avant l'heure qui a su développer un premier prototype du système et me transmettre son travail avec pédagogie. Du côté Temps-Fréquence, je suis également redevable à Pierre-Yves Bourgeois et Jean-Michel Friedt pour leur implication dans le projet.

Les résultats présentés ici et dans nos publications sont donc issus d'un travail collectif. C'est pourquoi je souhaite encore remercier Franck Chollet et Franck Lardet pour leur aide sur le dis-

positif analogique, Sébastien Euphrasie pour ses explications sur le fonctionnement du FPGA et son histoire, Aleksandr Oseev pour ses indications concernant les microbalances à quartz, Julia Peisker pour la correction du glossaire, Julien Dufourmantelle et Daniel Guneysu pour leur participation sur la partie expérimentale. Enfin, merci à Vincent Tissot pour la fabrication du support pour le prototype board, mais aussi pour les bons moments partagés lors de nos nombreux covoiturages ! Je souhaite aussi remercier mon ancien professeur Gaël Chevalier ainsi qu'Emeline Sadoulet-Reboul d'avoir partagé avec moi leurs heures d'enseignement. Je suis également reconnaissant envers nos administratifs Sandrine Pyon, Ayoko Afanou et Sandrine Chatrenet pour leur sourire et efficacité indispensables au bon déroulement de la recherche. Je tiens par ailleurs à remercier mon maître de stage de fin d'études Pascal Nicolay de m'avoir encouragé à poursuivre en doctorat et aiguillé dans cette démarche avec bienveillance. Enfin, j'adresse une reconnaissance particulière aux membres de mon jury qui ont tous accepté d'avancer la soutenance au surlendemain afin d'éviter un report lié au début de la crise sanitaire.

Mon doctorat n'aurait pas eu la même saveur s'il ne régnait pas une ambiance agréable au sein du département Micro Nano Sciences and Systems et de l'institut en général. Ainsi, pour tous les bons moments, merci à mes voisines de bureau Magali Barthes et Sophie Marguier qui ont toujours un soleil dans les yeux, merci à Nicolas Pasilly et Quentin Tanguy pour ces échanges toujours plus passionnants et plaisants. Enfin merci aux doctorants, stagiaires ou autres membres de l'institut pour tous ces partages : Toky, Maya, Raya, Asma, Juiliana, Svenia, Alpha, Fernando, Jean, Jean-Loup, Daniel, Sylvain, Mark, Ophélie, Aymen, Venancio, Louïs, Muamer et l'ensemble de l'équipe BMD. D'une manière plus générale, je remercie l'ensemble du personnel de l'institut ainsi que la région Bourgogne Franche-Comté pour le financement de ce projet à travers le programme EIPHI.

Enfin, la vie ne s'arrête pas aux portes du labo ! Bien que la fin du doctorat ne laisse plus beaucoup de temps libre, j'ai tout de même pu satisfaire mon désir de découverte et d'apprentissage à travers diverses activités durant ces trois années. Ainsi, merci à Josette de m'avoir régulièrement laissé essuyer la vaisselle à la Boutique Jeanne Antide, merci à James, mon professeur de piano, mais aussi à Valérie, Greg, Anne et Philippe, mes professeurs de Tango ainsi que Laure, Virginie et Claudine qui ont supporté que je leur marche sur les pieds durant les premiers mois... J'ai aussi eu la chance de voyager à l'international dans le cadre de la thèse (en Bulgarie avec Vincent et Najib, au Japon avec Thérèse, aux Etats-Unis avec Fernando et en Suisse avec Sophie), mais aussi en dehors : Italie, Autriche, Slovénie, Suisse, Tunisie, Islande, Hongrie, Portugal et Belgique. Merci Maman et Jérémy pour ces voyages, et pour tout le reste merci à toi, Souha.

Contents

Summary in french

Le présent mémoire étant rédigé en anglais pour une plus large diffusion, son contenu est résumé ici en quelques pages en français. Le lecteur y trouvera les motivations et objectifs de ce travail, une version concise de chaque chapitre ainsi que les conclusions sur les résultats obtenus et les perspectives du projet. Enfin à titre d'information, l'ensemble des acronymes utilisés ici sont définis à la page 155.

Titre de la thèse en français : Couplage d'un filtre numérique sur FPGA avec une microbalance à quartz pour la détection de masse par localisation de modes.

Introduction

Contexte et problématique

Depuis les premiers développements des capteurs MEMS dans les années 1960, de nombreuses applications comprenant de tels dispositifs ont fleuri dans différents domaines tels les télécommunications ou le transport. Parmi toutes les catégories de capteurs MEMS, les biocapteurs suscitent depuis nombre d'années un intérêt croissant, en particulier dans les secteurs de l'agroalimentaire, l'environnement et la santé.

Parmi les différents capteurs de masse existants se trouvent les résonateurs, dont les principaux avantages sont le faible coût, la portabilité et une limite de détection basse. Cependant, la mesure classique du décalage en fréquence de résonance lié au dépot de masse ne donne qu'une sensibilité normalisée fixe de $\frac{1}{2}$, indépendamment des caractéristiques du dispositif tel que le facteur de qualité. La nécessité de disposer de capteurs à haute résolution pour la détection précoce d'agents pathogènes par exemple demande la conception de nouvelles architectures de résonateurs ayant une plus grande sensibilité.

Les deux dernières décennies ont ainsi vu l'émergence de capteurs de masse résonants basés sur la localisation de modes. Ce phénomène se produit dans un réseau de résonateurs identiques et faiblement couplés soumis à une perturbation de masse. La littérature montre qu'une telle structure possède des sensibilités quelques ordres de grandeur plus élevées par rapport au décalage en fréquence. De nombreuses recherches sont toujours en cours, notamment pour estimer le gain en résolution, c'est à dire si le gain en sensibilité permet de compenser la perte de ratio signal sur bruit qui est généralement plus faible pour les mesures en amplitude que pour celles en fréquence.

Ce phénomène s'avère particulièrement sensible aux variations des différents paramètres intrinsèques tels que la raideur de couplage ou le facteur de qualité, mais des études supplémentaires sont nécessaires pour cartographier les valeurs de sensibilité par rapport à ces paramètres. Par ailleurs, la localisation de modes n'a jamais été mise en œuvre, à notre connaissance, sur l'un des biocapteurs très largement répandu : la microbalance à quartz (QCM). En effet, ce résonateur spécifique possède des facteurs de qualité particulièrement élevés et sa grande surface facilite tout dépôt de masse. Toutefois, les QCM couplés mécaniquement entre eux sont difficiles à fabriquer car leurs modes de vibration impliquent des ondes de cisaillement. En outre, ces dispositifs sont difficiles à accorder une fois fabriqués, et les conditions requises pour la localisation de modes ne seraient dans ce cas pas remplies. Afin de travailler sur de tels dispositifs, il est donc nécessaire d'imaginer une autre manière d'implémenter la localisation de modes, ce qui est le but du présent projet.

Objectifs

Les objectifs de cette thèse, établis d'après le contexte détaillé ci-dessus, sont les suivants.

- Etude bibliographique : Rappeler les différents transducteurs existants pour la détection de masse et donner le positionnement des capteurs à localisation de modes.
- Modèles analytiques et simulations : Trouver des règles génériques pour concevoir de tels capteurs (permettant d'atteindre la configuration optimale) et identifier les limites actuelles de la localisation des modes.
- Conception : Imaginer une solution polyvalente qui permette d'implémenter la localisation de modes sur des résonateurs à facteur de qualité élevés tels que le QCM, à l'aide d'une approche numérique.
- Validation expérimentale : Mettre en œuvre, caractériser et tester le système hybride en tant que prototype de capteur de masse.

Organisation du manuscrit

Le présent document est composé de quatre chapitres, dont les objectifs sont brièvement présentés ici.

- Le chapitre I introduit l'histoire des capteurs MEMS et le développement des transducteurs pour les applications de détection de masse. Le lecteur trouvera ici un aperçu scientifique général sur le vaste sujet des MEMS et de la détection de masse.
- Le chapitre II donne quelques éléments théoriques sur les résonateurs simples et couplés et renvoie à la littérature sur la localisation de modes. Des études approfondies sont également exposées dans ce chapitre afin d'examiner le gain et les limites de la localisation de modes par rapport aux capteurs classiques à mesure de fréquence de résonance.
- Le chapitre III comprend une description détaillée de la solution proposée dans cette thèse, à savoir la conception d'un filtre résonant numérique, son implémentation dans un FPGA et sa caractérisation.

- Le chapitre IV présente la conception et la fabrication d'un filtre résonant comprenant un QCM et la réalisation du système hybride. Enfin, la mise en œuvre expérimentale de la localisation de modes est présentée et discutée.

Chapitre I : Histoire des capteurs MEMS et état de l'art sur les transducteurs pour la détection de masse

I. A - Les capteurs MEMS : des origines à aujourd'hui

Des premiers thermoscopes datant du 17ème siècle aux micro-thermomètres à transistor actuels, des capteurs de tous types se sont développés au fil des dernières décennies pour répondre à nos besoins industriels. Ce développement soudain des capteurs MEMS est majoritairement dû à l'invention du transistor par William Shockley en 1947 et la découverte de propriétés piézorésistives exceptionnelles du silicium par Charles S. Smith en 1954. La dernière a permis la conception de capteurs (tout d'abord de pression) particulièrement sensibles et dont la fabrication a indirectement été rendue possible par la première. En effet le transistor, d'abord en germanium puis en silicium, a rapidement trouvé sa place en traitement du signal et a donné naissance aux premiers microprocesseurs ainsi qu'aux procédés de micro-fabrication nécessaires à leur production. Ces procédés, très axés sur le silicium, ont dans le même temps profité aux autres micro-dispotitifs tels que les capteurs MEMS.

Ceux-ci peuvent être classés en différentes catégories selon les grandeurs qu'ils mesurent. Bien que l'essor de certains d'entre eux provienne principalement de celui du secteur automobile, comme c'est le cas des capteurs de pression (contrôle moteur) ou des accéléromètres (airbags), presque tous les domaines sont aujourd'hui concernés par les capteurs MEMS tels que la navigation ou la santé. Le développement des télécommunications et donc des MEMS radio-fréquences et celui du contrôle des fluides à petite échelle ont aussi donné naissance à de nouvelles architectures de capteurs plus complexes pouvant répondre à des besoins d'analyses biologiques : les μTAS, de micro laboratoires capables de mener à bien une série de tâches sur des échantillons et en communiquer les résultats à distance, comme c'est le cas de certains capteurs de glycémie pour le traitement du diabète. En résumé, l'évolution des capteurs MEMS permet la démocratisation d'une mesure plus précise, moins encombrante et souvent peu onéreuse.

I. B - Présentation de différentes techniques de micro détection de masse

La détection et la quantification des substances chimiques ou biologiques sont essentielles dans les domaines de l'environnement, de la santé ou de l'agroalimentaire. Depuis que le premier capteur de gaz, la lampe de sûreté, a été présenté en 1816 pour détecter et éviter les coups de grisou dans les mines de charbon, de nombreuses techniques ont été développées pour la détection de masse en milieu gazeux ou liquide et les technologies MEMS ont considérablement amélioré leurs performances.

Un capteur de masse se compose en trois partie : reconnaissance, transduction et mesure. L'étape de reconnaissance, souvent délicate pour les bio-capteurs, consiste en la génération d'un signal à partir de l'espèce chimique à quantifier (analyte). La transduction correspond à la traduction de ce signal en une réponse de nature électrique pouvant être lue par la dernière partie, l'électronique de mesure. La limite de détection (LOD) qui est la plus petite quantité d'analyte détectable par le capteur, correspond, à un facteur de confiance près, au niveau de bruit de mesure généralement dominant divisé par la sensibilité du capteur. C'est pourquoi nous chercherons ici à atteindre des sensibilités à la variation de masse les plus hautes possibles.

Une fois encore, une classification des différents transducteurs peut être faite : electrochimique, optique et mécanique. La transduction électrochimique, dans laquelle se trouvent la potentiométrie, l'ampérométrie, la conductimétrie, certaines méthodes basées sur des semi-conducteurs ou encore des nanotubes de carbone, est probablement la famille de méthodes la plus courante permettant de détecter et quantifier des substances chimiques ou biologiques, en raison de la génération directe d'une information de nature électrique à partir de la reconnaissance de l'analyte. Il s'agit souvent des moyens de détection les moins chers et les plus faciles à implémenter. Cependant, les principaux inconvénients des capteurs utilisant ces techniques restent leur LOD élevée et leur faible sélectivité. La deuxième famille de transducteurs est de nature optique. Il s'agit de systèmes plus complexes et plus onéreux, comprenant photo-diodes, lasers ou fibres optiques, mais aussi très rapides, permettant la mesure en temps réel. On y trouve cette fois les techniques de réflectométrie telles que la bien connue résonance à plasmon de surface, celles d'interférométrie, d'absorbance et enfin la plus répandue, de fluorescence. Pour finir, il existe une population de transducteurs mécaniques qui nécessitent pour la plupart des procédés de micro-fabrication car plus la taille de la structure est réduite, plus la LOD a le potentiel de diminuer. En conséquence, ces transducteurs sont généralement moins chers que les techniques optiques mais plus coûteuses que les techniques électrochimiques. La plupart de ces structures sont résonantes comme les cantilevers ou les dispositifs à ondes élastiques de surface ou de volume et sont souvent appréciées car elles constituent un bon compromis sur différents plans : durée d'analyse, coût, portabilité et précision.

Chapitre II : Positionnement des capteurs à localisation de modes parmi les capteurs résonants

II. A - Résonateurs mécaniques à un degré de liberté pour la détection de masse

D'un point de vue spectral, un résonateur est un filtre dont le gain est supérieur à l'unité pour certaines fréquences spécifiques. D'un point de vue physique, un résonateur mécanique est un système dynamique échangeant alternativement de l'énergie entre les formes potentielles et cinétiques s'accumulant pour certaines fréquences d'excitation, appelées fréquences de résonance. En considérant le modèle masse-ressort classique, ces fréquences particulières sont inversement proportionnelles à la racine carrée de la masse du résonateur. L'ajout d'une substance à la surface de celui-ci diminue alors ces fréquences dont la mesure fournit une information quantitative sur la masse ajoutée par le biais de la sensibilité normée du capteur, égale à un demi pour cette méthode de décalage en fréquence de résonance. La bande passante de chacune de ces résonances est déterminée par les pertes énergétiques internes au système dynamique, représentées quantitativement par le facteur de qualité qui se doit donc d'être élevé pour former des capteurs performants. Les résonateurs sont excités en boucle ouverte (configuration choisie ici pour plus de simplicité) ou fermée (configuration oscillateur). La première est plus facile à implémenter que la dernière mais demande un balayage en fréquence pour atteindre la fréquence de résonance, ce qui est chronophage. Enfin, comme annoncé dans l'introduction générale, une des limites actuelles des capteurs de masse résonants est la sensibilité à la variation de fréquence de résonance fixée à un demi. C'est pourquoi une méthode de mesure d'amplitude de vibration dans un réseau de résonateurs couplés est explorée depuis quelques années : la localisation de modes.

II. B - Etat de l'art sur les capteurs à localisation de modes

La localisation de modes est un phénomène de répartition énergétique des ondes aussi appelé localisation d'Anderson en référence au physicien américain Philip Warren Anderson. En effet, il décrit en 1958 l'absence de diffusion des ondes dans un milieu désordonné, entraînant ainsi leur localisation géométrique. Initialement présentée pour décrire la localisation des électrons dans un semi-conducteur contenant des impuretés, ce travail théorique met aussi en évidence un phénomène pouvant être étendu à d'autres domaines de la physique tels que la mécanique ou l'acoustique. Il est d'ailleurs possible de l'observer dans un réseau d'au moins deux résonateurs identiques faiblement couplés dans lequel est introduit une perturbation en raideur ou en masse. Ainsi dans un système masse-ressort à deux degrés de libertés possédant deux modes de vibration, en phase et en opposition de phase, l'introduction d'une masselotte sur l'un des résonateurs conduit à la localisation (augmentation ou diminution de l'amplitude de vibration) du premier mode sur ce résonateur et du second sur son voisin. Ce phénomène est connu pour être particulièrement sensible à ces perturbations de masse ou de raideur à condition que la raideur de couplage soit faible. Toutefois, si cette raideur est trop faible, les deux modes de vibrations fusionnent (mode aliasing) et la mesure d'amplitude de chaque mode n'est plus possible.

Depuis la première implémentation de la localisation de mode pour la détection de masse en 2006 par Matthew Spletzer et al, de nombreux travaux décrivent la conception, la fabrication et la caractérisation de tels capteurs à deux degrés de liberté ou plus. Ils se divisent en deux catégories : les dispositifs à couplage mécanique ou électrostatique. Il s'agit de résonateurs soit hors plan tels que des cantilevers ou dans le plan comme les tuning forks. Bien que les dispositifs sans électrostatique sont plus simples à implémenter, leurs caractéristiques mécaniques restent fixées par la micro-fabrication et sujettes aux défauts de cette dernière. Les dispositifs à actuation et couplage électrostatique peuvent quant à eux compenser ces défauts et régler la raideur de couplage à la limite du mode aliasing, permettant alors d'obtenir des sensibilités plus hautes. Cependant, cette catégorie de dispositifs ne peut fonctionner en milieu liquide en raison de l'apparition de courants parasites. Enfin, les capteurs à localisation de modes peuvent mesurer un ajout de masse mais aussi une variation de raideur, ce qui permet la conception d'accéléromètres, de capteurs de force ou encore d'électromètres via des effets raidissants ou assouplissants.

II. C - Les potentiels de la localisation de modes

Les sensibilités à la variation de masse théoriquement atteignables par un système à deux degrés de liberté sont évaluées en fonction des différents paramètres intrinsèques tels que le facteur de qualité Q, la raideur de couplage mais aussi la perturbation introduite, à l'aide de développements analytiques et de simulations. Il est ainsi montré que les sensibilités normées maximales se situent entre $\frac{Q}{4}$ et Q en fonction de la grandeur de mesure : amplitude d'un seul résonateur à la résonance, à fréquence fixe ou ratio d'amplitudes. Il s'avère que ces valeurs n'excèdent pas celles trouvées pour un résonateur seul excité à fréquence fixe, bien que la plage de perturbation dans laquelle la sensibilité reste haute est largement plus grande dans le cas du ratio d'amplitude. Toutefois ce dernier résultat est à mettre en rapport avec la perte de ratio signal sur bruit qui apparaît lorsque la localisation est forte puisqu'un mode voit son amplitude fortement diminuée. Le résultat concernant la sensibilité maximale a aussi été démontré analytiquement pour un système à trois degrés de liberté, et peut probablement s'étendre à N degrés de liberté puisque la contribution d'un mode donné à la localisation d'un autre diminue avec l'écart de fréquence entre ces deux modes.

Enfin, nous pensons que la seule façon d'éventuellement améliorer la sensibilité normée est de travailler sur un système à plus de deux degrés de liberté avec une rangée de résonateurs centraux plus raides comme cela est déjà proposé dans la littérature. Les conditions de mode aliasing devraient alors être redéfinies pour s'assurer que ce gain est réel. Il est important de souligner que dans l'état actuel de l'étude, il n'est pas prouvé que ces dispositifs améliorent la LOD par rapport à la mesure de fréquence de résonance d'un résonateur simple parce que la résolution de mesure d'une fréquence est bien meilleure que celle d'une mesure en déplacement. Des études complémentaires devraient être menées sur ce sujet en ce qui concerne des systèmes couplés à plus de deux degrés de liberté, notamment avec des résonateurs en extrémités de réseau plus souples.

Chapitre III : Conception et implémentation d'un résonateur numérique à haut facteur de qualité

III. A - Vers un système hybride pour la localisation de modes

Les différentes mises en œuvre de la localisation de modes présentées dans le chapitre précédent ne sont pas optimales pour différentes raisons. L'une de ces limitations est la difficulté de créer un couplage à la fois faible et connu ainsi qu'une série de résonateurs identiques pour assurer une grande sensibilité. La solution qui semble la plus modulable à ce jour est de nature électrostatique, mais cette technologie limite considérablement les géométries sur lesquelles la localisation de modes peut être générée. Par exemple à notre connaissance, aucun couplage mécanique ni électrostatique n'a jamais été mis en œuvre sur des QCM qui possèdent pourtant des facteurs de qualité très élevés et qui sont surtout largement utilisés dans le domaine de la détection de masse.

L'idée derrière un système hybride repose sur le remplacement d'éléments mécaniques non accordables par d'autres non mécaniques mais accordables dans un réseau MEMS classique. En modélisant le système couplé par une série de fonctions de transfert, les résonateurs et le couplage peuvent être séparés. Par conséquent, si un résonateur piézoélectrique tel qu'un QCM se voit intégré dans un circuit électrique à une entrée et une sortie, le couplage peut être simplement remplacé par un traitement du signal en boucle fermée entre les résonateurs. Les additions, soustractions et multiplications peuvent donc être effectuées soit avec des composants analogiques (amplificateurs opérationnels, condensateurs et résistances) ou sur hardware. Ainsi, le couplage peut être facilement ajusté et implémenté sur n'importe quel résonateur piézoélectrique, indépendamment de sa géométrie. Plus intéressant encore, certains des résonateurs du réseau sont remplaçables par leurs équivalents électriques ou numériques, ce qui permet un équilibrage du réseau avant mesure.

La solution numérique a ici été sélectionnée pour sa faible dépendance aux paramètres environnementaux et sa plus grande souplesse : l'implémentation de n'importe quelle fonction polynomiale est possible, y compris celle représentant des systèmes à faibles pertes internes difficiles à mettre en place avec une solution analogique. Une condition doit toutefois être respectée sur la vitesse de calcul puisque la fréquence de résonance d'un QCM est au moins égale à 1 MHz. Etant donnée le nombre de calculs à effectuer dans le même temps, une architecture qui parallélise les opérations est préférable. C'est pourquoi a été choisi le FPGA, un circuit intégré constitué de portes logiques programmables qui convient à la modélisation d'un système dynamique fixe. La carte choisie est la Redpitaya, qui comprend un FPGA, mais aussi un CPU pour gérer les acquisitions et des convertisseurs numérique/analogique.

III. B - Conception du filtre numérique

Le présent travail vise l'implémentation de la localisation de modes dans un système à deux degrés de liberté à partir d'un modèle masse-ressort. Sachant qu'à partir d'un tel modèle, la force de couplage est proportionnelle à la différence des déplacements mécaniques des deux résonateurs, la sortie de leur fonction de transfert doit être en phase avec ce même déplacement. Or le comportement dynamique d'un QCM peut être représenté par le modèle électrique de Butterworth Van Dyke. Le recours aux équivalences électro-mécaniques (charge électrique - déplacement mécanique) mène donc au choix d'ajouter une capacité en impédance de sortie du QCM.

Un tel filtre possède une fonction de transfert dans le domaine de Laplace. La transformée en Z bilinéaire précompensée à la fréquence de résonance du QCM permet de basculer vers les signaux échantillonnés tout en minimisant la distorsion fréquentielle à la fréquence de fonctionnement. Il en résulte une relation de récurrence dans laquelle la valeur de sortie à un échantillon temporel donné est une combinaison linéaire des précédentes entrées et sorties. Il s'agit de l'équation à implémenter dans le FPGA pour émuler en temps réel le comportement du résonateur [QCM + condensateur].

III. C - Implémentation sur FPGA

L'outil de conception des circuits logiques pour FPGA utilisé ici est Vivado design suite. Certains blocs déjà développés par le département Temps-Fréquence de l'institut FEMTO-ST sont employés ici comme par exemple le générateur de signal numérique. De plus, une interface graphique en langage Python a été développée pour ce projet afin de contrôler les paramètres du système et procéder à des acquisitions manuelles ou automatiques.

Le filtre résonant est donc un FIR suivit d'un IIR dont les coefficients sont calculés par le programme générant l'interface, puis envoyés au FPGA à partir des paramètres d'entrée tels que le facteur de qualité ou la fréquence de résonance. Ces coefficients sont écrits en virgule flottante en base deux puisque tous les nombres codés dans le FPGA sont des entiers binaires. L'exposant doit prendre une valeur au delà d'un certain seuil, faute de quoi la réponse du filtre peut diverger car les coefficients injectés sont trop éloignés des valeurs demandées. Les temps de calculs sont régulés par un facteur décimation et enfin, la méthode de la virgule flottante est aussi implémentée sur les données transitant par la boucle de retour de l'IIR afin d'en augmenter le nombre de bits et ainsi diminuer le bruit de calcul résultant de ces approximations.

Les amplitudes sont calculées comme la moyenne des valeurs maximales moins minimales du signal sur plusieurs périodes, ce qui permet d'obtenir un écart relatif de moins de 0,5% entre données expérimentales et théoriques, ce qui est suffisant pour une première implémentation.

Chapitre IV : Implémentation et caractérisation de la localisation de modes sur le système hybride pour la détection de masse

IV. A - Conception et caractérisation du système hybride couplé

Le filtre résonnant numérique étant désormais fonctionnel, il reste à fabriquer le résonateur électro-mécanique comprenant le QCM et à implémenter le système numériquement couplé. Ce résonateur analogique se compose, comme indiqué dans le chapitre précédent, d'un QCM en série avec un condensateur. Des résistances et amplificateurs opérationnels y sont ajoutés pour remplir des rôles d'adaptation d'impédance en entrée et sortie du filtre. Celui-ci a alors été assemblé à la main et le comportement du filtre est expérimentalement celui attendu.

Le système couplé se compose du résonateur analogique externe au FPGA, du filtre et couplage numériques ainsi que de deux générateurs de signaux eux aussi numériques, représentés au sein du FPGA. Chaque résonateur a en signal d'entrée l'excitation sinusoïdale d'un générateur, additionnée au terme de couplage étant lui calculé comme la différence des deux sorties des filtres multipliée par un coefficient de couplage. Le système, une fois couplé, est bien capable de générer deux modes de vibration : l'un en phase, l'autre en opposition de phase.

Chaque opération effectuée au sein du FPGA ainsi que la conversion des signaux entre formes numérique et analogique génèrent un déphasage qui s'accumule lorsque ces opérations sont en série. Des registres sont alors ajoutés à la sortie du filtre numérique afin qu'elle soit expérimentalement en phase avec celle de son homologue. Toutefois, il n'est pas possible de compenser le retard dans la boucle de retour (couplage) qui donne pourtant lieu à des amplitudes de vibration du second mode plus importantes que prévues par les modèles lorsque le système est couplé, ce qui génère souvent une saturation des convertisseurs. Ce retard est alors accentué dans le but de remettre le signal en phase avec la période suivante, ce qui s'avère être une solution efficace expérimentalement.

IV. B - Implémentation de la localisation de modes dans le système hybride

Avant de mettre en évidence la localisation de modes, il est nécessaire d'équilibrer les deux résonateurs en modifiant leur facteur de qualité et fréquence de résonance mais aussi en réglant les retards artificiellement rajoutés mentionnés plus haut. Un protocole a donc été mis en place dans ce but : les deux résonateurs restent d'abord découplés et excités en phase pour ajuster l'ensemble de ces paramètres intrinsèques manuellement, puis un couplage non nul est appliqué et les générateurs de signaux sont placés en quadrature de phase afin d'observer les deux modes de vibration.

Une manière simple de générer la localisation de modes dans ce système est d'appliquer une perturbation sur le filtre numérique équivalente à une légère variation de masse sur le QCM. En effet, par l'intermédiaire de l'interface graphique, il est aisé de procéder à un balayage de ce paramètre mais aussi de comparer les mesures d'amplitudes avec celles issues de simulations puisque la masse ajoutée est connue. Il est alors observé que ces résultats sont particulièrement proches, tant pour les diagrammes de Bode que les valeurs de sensibilités normées calculées en fonction du couplage et de la perturbation. Ces sensibilités sont au-delà de toutes celles trouvées ou calculées à partir de la littérature, ce qui est un résultat qui confirme que cette architecture a le potentiel d'améliorer les performances de capteurs de masse basés sur la localisation de modes.

Enfin, des particules sont déposées à la surface du QCM afin d'observer la localisation de modes et de quantifier cette masse ajoutée. Pour confirmer la justesse des résultats, une mesure de fréquence de résonance du QCM seul est aussi réalisée en parallèle à chaque dépôt, à l'aide d'un interrupteur permettant de déconnecter le QCM du reste du filtre et de le connecter à un analyseur d'impédance. Les particules utilisées sont des micro-billes de moins d'un micron en résine fluorescente, afin d'observer les dépôts à l'aide d'un microscope adéquat. Pour ces expériences préliminaires, la variation de fréquence de résonance du QCM seul permet de déterminer une première valeur de la masse ajoutée. Cette valeur permet de calculer la sensibilité normée pour la localisation de modes correspondant à cette perturbation, ce qui permet d'effectuer une calibration. Il apparaît alors que les résultats des deux méthodes sont cohérents et permettent même de calculer une première valeur de LOD à partir de l'écart type des mesures : 50 ng.

Conclusion

Résultats théoriques

Comme annoncé dans l'introduction, le chapitre II met en évidence les configurations pour lesquelles la sensibilité normée est maximale avec une paire de résonateurs faiblement couplés. En effet, ces valeurs maximales sont proportionnelles au facteur de qualité et inversement proportionnel à la valeur de couplage jusqu'à ce que le mode aliasing ait lieu. En outre, la plage sensible (arbitrairement fixée lorsque la sensibilité normée baisse de moitié) est également inversement proportionnelle à la perturbation en masse.

Le chapitre II présente également divers résultats sur les réseaux de résonateurs identiques par le biais de développements analytiques et de simulations, notamment en ce qui concerne l'impact de la grandeur de mesure sur les sensibilités normalisées, la LOD et la plage de sensibilité :

lorsqu'il s'agit d'une mesure d'amplitude (soit sa variation ou son ratio à la résonance, ou encore sa variation à fréquence fixe), la sensibilité normée et la LOD sont dans le même ordre de grandeur pour les petites perturbations ($ns_{max} \in \left[\frac{Q}{4}..Q\right]$). Toutes ces mesures donnent une plage sensible relativement faible sauf pour le rapport d'amplitude, mais au prix d'une diminution drastique de la LOD lorsque la perturbation augmente, en raison d'une chute de ratio signal sur bruit. Il est également montré analytiquement que ces résultats semblent être applicables aux systèmes couplés à plus de deux degrés de liberté, bien qu'aucune étude approfondie n'ait été menée sur le sujet.

Enfin, le chapitre III donne les bases théoriques et une méthode pour concevoir un filtre numérique constitué d'un FIR en série avec un IIR du troisième ordre permettant de modéliser des résonateurs à facteur Q élevé. Il a été démontré par simulation et expérimentalement que la méthode de la virgule flottante permet d'éliminer le bruit corrélé et de réduire l'erreur sur les coefficients du filtre.

Résultats expérimentaux

Plusieurs résultats des chapitres III et IV peuvent être soulignés concernant la mise en œuvre de localisation de modes sur des résonateurs hybrides. Ils sont détaillés comme suit.

- Filtre résonant numérique : Implémentation sur FPGA d'un résonateur numérique au facteur de qualité égalant ceux des QCM. Comme annoncé dans l'introduction, il est entièrement ajustable et fournit une réponse proche de celle donnée par les modèles analytiques (moins de 0,5% d'erreur sur l'amplitude). Par ailleurs, les paramètres injectés dans le FPGA sont contrôlés par une interface graphique personnalisée qui permet aussi l'enregistrement et le traitement des données.
- Filtre analogique : Conception et fabrication d'un filtre résonant comprenant un QCM et dont la sortie est proportionnelle à la charge électrique et donc au déplacement mécanique.
- Système couplé : Conception et implémentation du système hybride avec couplage et excitation accordables permettant de générer deux modes de vibration. Le système comprend les compensations des délais de propagation du signal et est fourni avec un protocole de réglage.
- Localisation de modes sur des résonateurs hybrides : Génération de la localisation de modes accordable dans le système hybride avec une perturbation successivement numérique et en masse. Il est observé une très bonne corrélation avec les modèles, notamment en ce qui concerne les amplitudes de vibration et les valeurs de sensibilité. La limite de détection atteinte est estimée à ce jour à 50 ng.

En outre, les principales performances propres à notre système peuvent être énumérées ci-dessous. En effet, notre système permet de :

- Générer un second mode de vibration et exploiter la localisation de modes sur un résonateur à ondes de cisaillement largement utilisé dans la biodétection (QCM) avec un facteur Q élevé jusqu'à au moins 200 000 et une fréquence de résonance jusqu'à au moins 2 MHz.

- Effectuer un réglage complet des paramètres du filtre numérique et de la valeur de couplage avant chaque expérience. Cela permet d'atteindre des valeurs de sensibilité normée élevées par rapport à la littérature, jusqu'à 35 000.
- Remplacer facilement le QCM et s'adapter à la géométrie du résonateur piézoélectrique le cas échéant.

Enfin, le principal inconvénient de notre système est la perte de la réjection de mode commun qui permet de s'affranchir des variations lentes des conditions ambiantes.

Perspectives

La littérature montre qu'un réseau de résonateurs couplés dont ceux aux extrémités sont plus souples possèdent des sensibilités à la variation de masse plus élevées que dans le cas de résonateurs identiques. La résolution du problème aux valeurs propres dans le cas d'un système à trois degrés de liberté montre en effet que les deux premiers modes sont plus proches en fréquence pour une valeur donnée de couplage par rapport à un système à deux degrés de liberté, ce qui augmente la sensibilité normée. Néanmoins, il faut aussi garder à l'esprit que le mode aliasing se produit alors pour des valeurs plus élevées de couplage, ce qui peut donc empêcher le système d'atteindre des sensibilités aussi hautes. Comme première perspective de cette thèse, des études approfondies pourraient être menées pour connaître le gain réel en sensibilité et la diminution de la LOD de ces systèmes.

De nombreuses améliorations sont aussi possibles sur le système hybride présenté. Si la diminution de la LOD peut être prouvée sur un système à trois degrés de liberté avec un résonateur central plus rigide, un second filtre numérique pourrait être ajouté dans le FPGA, permettant alors de reproduire et d'exploiter cette configuration.

Un autre développement possible concerne la manière de calculer les amplitudes de vibration. A la place de faire la moyenne des valeurs maximales moins minimales sur plusieurs périodes, il est envisageable de faire la moyenne des amplitudes des transformées de Fourier à la fréquence d'excitation qui devrait être plus précise puisque le bruit des autres fréquences n'est pas pris en compte dans ce calcul. En outre, l'application de fenêtres spécifiques sur les signaux enregistrés tels que la fenêtre de Hanning limiterait la fuite spectrale aux alentours de la fréquence de résonance. Plus généralement, les différentes sources de bruit qui corrompent les signaux doivent être identifiées et analysées afin de trouver un moyen de diminuer la LOD aujourd'hui assez haute (bruit de quantification, gigue de l'horloge, etc.).

En outre, l'étalonnage du capteur pourrait être amélioré. En effet jusqu'à présent, il est réalisé en utilisant l'écart de masse calculé à partir du décalage en fréquence du QCM seul, ce qui nécessite la présence d'un analyseur d'impédance. La bonne corrélation entre les expériences et les modèles montre que cet étalonnage peut être effectué en utilisant des données générées à l'avance par simulation.

Afin de gagner du temps, le protocole de réglage pourrait être automatisé. Il est jusqu'à présent exécuté à la main mais l'aspect numérique du système peut accueillir un programme supplémentaire permettant d'automatiser cette partie délicate du processus à chaque fois que l'opérateur souhaite l'appliquer. De plus, le suivi de l'amplitude de résonance pourrait également faire l'objet d'une automatisation avec une PLL directement intégrée au circuit sur FPGA. Une telle modification évite de longs balayages de fréquence et diminue donc les temps d'analyse.

Une dernière perspective, plus générale à la localisation des modes, consiste à coupler un ensemble de résonateurs de manière à ce que le mode aliasing se produise pour tous les modes sauf au moins un qui devrait être à la limite de cette condition. Dans une telle configuration hypothétique, ce mode pourrait fortement se localiser avec l'introduction d'une perturbation puisqu'il capterait l'énergie vibratoire de tous les autres modes qui sont très proches en fréquence à cause du mode aliasing.

Conférences internationales et publications

Présentation orale : International Conference on Engineering Vibration, Septembre 2017, Sofia, Bulgarie.

Poster et proceeding : IEEE Ultrasonic Symposium, Octobre 2018, Kobe, Japon / [1].

Article dans un journal (letter) : Smart Materials and Structures, Janvier 2020 / [2].

General introduction

Context and motivations

Since the early developments of Micro electro mechanical systems (MEMS) in the 1960s, many applications including such devices flourished in different domains such as telecommunication, transportation or healthcare. Indeed, the invention of the silicon transistor, in parallel with the discovery of the silicon piezoresistive properties, enabled both the development of micro fabrication processes and micro sensors [3]. Since then, micro sensors bloomed in all the scientific fields for different sensing purposes (pressure, temperature, mass...). The most challenging category for the last 20 years are the biosensors, because of the interaction between the sensor and biological entities. However, the interest in such devices is ever growing especially in the agri-food, environment and health domains.

Among the various existing mass sensors are resonators, the main advantages of which are their low cost, portability and low limit of detection. However, the shift of resonant frequency yields a fixed normalized sensitivity to mass perturbations of $\frac{1}{2}$, independently from the device characteristics such as the Q-factor. The need of high resolution sensors (for early pathogen detection for instance) fosters the design of new architectures of resonators having higher sensitivities.

The last two decades have thus seen the emergence of resonant mass sensors based on mode localization as an alternative to frequency shift based sensors [4]. This phenomenon occurs in an array of weakly coupled and identical resonators subjected to a mass mismatch. The literature shows such structure yields sensitivities of a few orders of magnitude higher, and many researches are still ongoing, especially to find out whether this gain in sensitivity overcomes the loss of signal to noise ratio which is lower for amplitude than frequency measurements [5]. This phenomenon is known to be extremely sensitive for small coupling stiffness, identical resonators and high Q-factors, but additional studies should be carried out to map the sensitivity values with respect to these different parameters.

Besides, mode localization has never been implemented, to our knowledge, on one of the most widely used biosensor : the quartz cristal microbalance (QCM). Indeed, this specific resonator yields very high Q-factors and its large surface makes easier any mass deposition. However, an array of QCMs mechanically coupled to one another is hard to implement because their vibration modes involve shear waves. Furthermore, such devices are difficult to tune once fabricated, and the required conditions for sensitive mode localization might not be fulfilled. Therefore, there is a need to think of another way to implement mode localization, which is the purpose of the present work.

Main objectives

The objectives of the present thesis are as follow.

- Literature review : Remind the different transducers existing for mass sensing applications and give the position of mode localized based sensors.
- Analytical models and simulations : Find generic rules to design such sensors (allowing to reach the optimal configuration) and identify the current limits of mode localization.
- Design : Create a versatile solution that can be implemented on high Q-factor resonators widely used in bio sensing (QCMs), based on a digital approach.
- Experiments : Implement, characterize and test the hybrid system as a mass sensor prototype.

Novelties overview

In this context, we are proposing an original alternative to classic arrays of coupled resonators based on a hybrid system. Indeed, this hybrid system digitally couples a QCM and a digital resonator in real time, which makes it possible to get rid of any geometric constraint and to tune the whole system in such a way that optimal conditions are reached. All digital elements of the system are implemented in a field programmable gate array (FPGA). Below are listed the main advantages of our system over mechanically or electrostatically coupled mechanical resonators.

- No restrictions on geometry due to the coupling design, since this function is digital, as long as the resonator is piezoelectric (which is the case with the QCM), allowing the implementation of mode localization on high Q-factor resonators.
- Full tunability on the coupling value.
- Full tunability on the digital resonator physical parameters.

This new way of implementing mode localization results in normalized sensitivities never achieved before.

Conferences, posters and publications

We hereby list the opportunities we had to present the results given in this thesis :

Oral presentation : International Conference on Engineering Vibration, September 2017, Sofia, Bulgaria.

Poster and proceeding : IEEE Ultrasonic Symposium, October 2018, Kobe, Japan / [1].

Journal article (letter) : Smart Materials and Structures, January 2020 / [2].

Manuscript organization

The present manuscript is composed of four chapters, which purposes are briefly presented here.

- Chapter I is an introduction on the history of MEMS sensors and the development of transducers for mass sensing applications. The reader will here find a general scientific overview on the vast topic of MEMS and mass sensing.
- Chapter II presents a theoretical background on single and coupled resonators, along with a literature review on mode localization. Extended studies are also exposed in this chapter to examine the gain and the limits of mode localization over classic sensors based on their resonant frequency shift.
- Chapter III includes a detailed description of the solution proposed in this thesis, the design of the digital filter, its implementation in the FPGA and its characterization.
- Chapter IV presents the design and fabrication of a resonant filter including a QCM and the final design and test of the hybrid system. Finally, the experimental implementation of mode localization is presented and discussed.

Comment : The terms defined in the glossary and the acronyms are indicated between stars (*) and between brackets, respectively, when used for the first time.

On se lasse de tout, sauf de connaître.

Jean Rostand

Chapter I

Short history of MEMS sensors and state of the art of mass micro-sensing transducers

In this chapter are traced the origins and evolution of the first micro *sensors* and their applications. The current main mass sensing techniques are then presented and discussed in a second section.

I. A From the origins to nowadays MEMS sensors

From the first *thermoscopes* dated of the 17th to nowadays microscale *transistor* thermometers, sensors of all types have grown to fulfill our needs in terms of transportation or healthcare for instance. Nowadays, low cost, reliable, accurate and small size sensors are available in many industrial fields, allowing better control of human industrial environment.

In the following section is explained how the discovery of certain silicon properties and the invention of the transistor led to the development of MEMS technologies, and are shown the different existing application fields of MEMS sensors.

I. A. 1 The beginning of semiconductor sensors

I. A. 1. a Discovery of piezoresistivity

The first seminal work leading to the development of micro sensors as we know them today took place in the 19th century, when the development of the telegraph prompted researchers to study the harmful effects of the propagation of a signal by wire [6]. In this context, the British physicist William Thomson (later Lord Kelvin) demonstrated in 1856 the influence of strain on the resistance of iron and copper [7]. The resistance R of a wire follows Eq.1.

$$R = \rho \cdot \frac{l}{a} \tag{1}$$

where ρ is the resistivity, l the length of the wire and a its cross-sectional area.

Since l and a variations are linked by Poisson's ratio ν, the elongation of a wire indeed generates a variation of its resistance R. But William Thomson went further in his investigations and set up an experiment where two parallel wires (one made of copper and the other of iron) of identical length were equally stretched by a weight. As the measured resistances did not vary in equal proportions, William Thomson thus demonstrated this resistance variation could not only come from the geometry change of the wires, but also from a change in the resistivity of the materials. However, the low reliability of the instrumentations at that time prevented from efficiently quantify the phenomenon. The first measurements of resistivity change under stress were only carried out in 1883 by Tomlinson, and later by Bridgman [8]. Finally, *piezoresistivity* could be efficiently described with the adaptation of the tensor notation previously proposed by Voigt in 1910 for *piezoelectricity* and Hook's laws.

I. A. 1. b First silicon sensors

It happens that the geometric effects are greater than the relative change in resistivity in the case of metals, which is limiting the *sensitivity* of any strain gauge based on piezoresistivity. However, in april 1954, Charles S. Smith published a paper describing exceptionally large shear stress effects on resistivity in silicon and germanium [9]. This precursor work carried out at Bell Laboratories will appear to be a milestone [3,10] in the next decades for the development of sensors two order of magnitude more sensitive. Indeed, the dependency of silicon resistivity on pressure was pointed out one year later [11] and the first silicon gauge for displacement, force and torque sensing are reported in 1957 [12], 1961 [13], 1962 [14] and later.

I. A. 2 Towards micro and nano scales throughout the invention of the transistor

I. A. 2. a Apparition of integrated circuits

In 1947, William Shockley and his team from Bell Laboratories invented the point contact transistor [15], the first device able to amplify a signal using a semiconductive material (germanium) [16]. However, it was a few centimeters high and had to be wired to other electronics. The will to shrink it led to the first *integrated circuits* (IC), that include different components on the same piece of *semiconductor* [17]. Indeed in 1959, Jack Kilby and Robert Noyce designed the first IC that consisted of a transistor, three resistances and a capacitor on a germanium *substrate* [18]. This innovation is now considered as a seminal work in the development of *Micro Electro Mechanical Systems* (MEMS).

I. A. 2. b Birth of microprocessors with the silicon transistor

In 1951, William Shockley proposed an improved version of the transistor : the *bipolar transistor*, easier to manufacture, and in 1954, Morris Tanenbaum, also from Bell Labs, built the first bipolar transistor made of silicon. Since transistors can also be used as switches and not only amplifiers [19], these new inventions, combined with IC technology, opened the door to electronic communication at a smaller scale. As a consequence, ICs became more numerous and complex in the next years and many of them included silicon transistors such as the Intel 4004, the first microprocessor invented in 1971 that paved the way for personal computer and electronic engine control.

I. A. 2. c Evolution of microfabrication processes

Since smaller devices mean higher production volumes, cost drops and lower detection limits for sensors, the emergence of both planar ICs and silicon transistors led to microfabrication processes development during the 1960s and 1970s. Amongt them we can cite : *photolithography*, *bulk silicon etching*, *surface micromachining* and *batch processes*. In 1967, the resonant gate transistor is invented [20]. This electrostatically actuated *cantilever* was acting like a narrow bandwidth bandpass *filter* and was the first batch fabricated MEMS device and the first demonstration of surface micromachining techniques as well. Since then, components and devices have not stopped shrinking, from microscale (MEMS) to nanoscale (*NEMS*).

I. A. 2. d Gordon Moore and Richard Feynman predictions

A graphic example of this microscale rush is the evolution of memory : the number of bits per *chip* has dropped by order of magnitudes, as well as the cost per bit in the last decades. This observation was already made in 1965 by the co-founder of Intel, Gordon Moore, who stated that the number of transistors per square inch on ICs doubles every year [21]. Both an observation and a prediction that happened to be true.

The ever scaling down property of MEMS evolution over years in general had previously been predicted by Richard Feynman in 1959 in his famous talk ”There’s Plenty of Room at the Bottom” [22], where he explained we could always fabricate smaller. He suggested for instance to ”write the entire 24 volumes of the Encyclopedia Britannica on the head of a pin”, and challenged his audience to write the information of a book’s page at a scale of 1/25000, which a student from Stanford university succeeded in 1985.

Figure 2: Richard Feynman / *source : Wikipedia*

I. A. 3 Diversification of microsensors and their applications

I. A. 3. a Silicon, a material of choice for high-performance MEMS

Silicon had proved its value in electronic applications as a semiconductor material, with the silicon bipolar transistor. However, the development of silicon microfabrication techniques since the 1960s, initially motivated by the development of transistors, also benefited to the development of MEMS sensors that could evolve from simple piezoresistive silicon pressure sensors (previously presented) to more complex devices. Indeed, this material has many advantages : it is abundant in the earth crust, its oxide is stable, pure silicon cristal can be obtained, it has high piezoresistive coefficients especially when doped, it can be etched almost as desired and in general, its mechanical and thermal behaviors are known because broadly studied. One of the most cited article listing interesting silicon characteristics, thus encouraging scientists to use it for MEMS designs, is a review published in 1982 by Kurt Petersen [23].

In addition to silicon, other materials with different properties appeared in the design of MEMS with years (*ceramics*, materials with piezoelectric or optic properties...), allowing to improve sensor performances and contributing to the diversification of their applications.

I. A. 3. b Classical MEMS sensors

I. A. 3. b. i Pressure sensors

In 1971, Samaun et al. set up the very first IC pressure sensor based on the high piezoresistivity of silicon [24]. Two years later was designed the first capacitive pressure sensor [25]. Unlike the piezoresistive *transducer*, the capacitive one does not turn a shift in pressure into a variation of electric signal directly from the deformation of the diaphragm, but by its displacement, since the diaphragm is one of the two plates of a capacitor. The main advantage of this type of transducer compared with piezoresistive one is its lower sensitivity to temperature change. Nonetheless, the capacitance of such sensors is too small to neglect the parasitic capacitances of bonded wires, thus requiring to set the readout circuitry on the chip. Pressure sensors then started to be integrated and ready for commercialization around 1983 [26, 27]. In 1990, a first ultra precise resonant sensor for pressure appeared [28]. It was made of a diaphragm which resonant frequency depends on the strain triggered by the pressure. Another type of pressure sensor based on piezoelectricity also appeared in the late 1960s [29] and spread in the next decades [30].

Pressure sensors have met a great success since their invention, and there are nowadays numerous and widespread applications in the automotive industry (engine monitoring and fuel delivery) and more recently aerospace [31] and health care [32–34].

I. A. 3. b. ii Accelerometers and gyroscopes

In 1979, Roylance and Angell designed a first accelerometer using batch process, opening the door to its potential industrialization in the years to come [35]. The blooming of automotive industry since the beginning of the 20th century led to an ever increasing number of fatalities on the roads during more than 70 years. Unappropriated legislation and education probably led to many of these accidents, but the vehicles were not adapted to crashes as well : the lack of safety belt and the non compressibility of the car bodywork during a violent impact are in cause, to name a few. Within this context, the accelerometer appeared very attractive to the automotive industry in the 1980s and 1990s with the development of airbags [36]. The car market was indeed the main one that allowed to reduce the cost of accelerometers and improve their reliability. In 1993, such an accelerometer to be integrated in a vehicle was proposed [37].

With the invention of micro *gyroscopes* [38, 39] and accelerometers, many applications have grown, from video game controller to navigation control in drones [40]. Like the pressure sensors, they are based either on piezoresistive [41], piezoelectric [42] or capacitive [43] transducers.

I. A. 3. b. iii RF-MEMS sensors

The apparition of resonant structures led to the development of *Radio Frequency* (RF) MEMS in the 1990s [44]. Microfabrication evolution quickly permitted to scale down *resonators* (thus increasing their resonant frequencies), and Q-factors drastically increased as well [45]. High frequency bandpass filters (until several dozen of GHz) started to be developed, opening the door to telecommunication [46]. Among them we can cite *surface acoustic waves* (SAW) [47] and *bulk acoustic waves* (BAW) filters [48]. They are piezoelectric substrates either sandwiched between two electrodes in the case of BAWs, or on which are laid *inter digital transducers* (IDT) generating SAWs.

These devices are passive filters and their incredible rapid development for telecommunication applications also gave birth to a new generation of sensors. Indeed, SAW and BAW resonators can be used to design gas, pressure or even temperature sensors [49–51], because their resonant frequencies and amplitudes vary with a shift of one of these physical parameters.

I. A. 3. b. iv Temperature MEMS sensors

Semiconductor devices generally show a dependence on the temperature such as resistors, *diodes* or transistors. This is a problem in many applications, but this dependence can be used to design temperature sensors. This is how the first temperature micro sensors appeared in 1962 [52]. Today, temperature sensors can be classified in different categories : *thermoresistive*, thermo-mechanical (or *thermal bimorph*), thermo-electrical (the most common ones being *thermocouples*) sensors [53] and SAW sensors for high temperature applications [54].

I. A. 3. b. v Magnetic field MEMS sensors

Most of magnetic field sensors relies on the *Hall effect*. The first Hall plates were made of germanium [55], a semiconductor quickly replaced by silicon with the bipolar transistor revolution. Hall plates thus benefited of classical IC processes and the first MEMS magnetic sensor was proposed in 1968 [56]. They could be manufactured by millions, especially for the automotive industry attracted by contact-less sensors for measuring the velocity of metallic components.

I. A. 3. c MOEMS sensors

The invention of the transistor in 1947 at Bell labs quickly led to the one of the first phototransistor (a *photodetector*) in 1950 by John Northrup Shive from the same laboratory [57, 58]. The first laser was invented by Theodore Maiman in 1960 [59] and since then, lasers and photodetectors have been improved, microfabrication processes have enabled the invention of optical waveguides and micro mirrors, lenses and photodetectors. Working in tandem with the diversification of *actuators*, these new technologies permitted the emergence in the 1990s of *micro optic electro mechanical systems* (MOEMS) that combines the strengths of micro scale and optics [60]. Initially presented as a mean to answer the growing need of high data traffic caused by the telecommunication rise, MOEMS also offers a few new sensing approaches since the 2000s with micro interferometers for acceleration and pressure sensing [61, 62], gas sensing [63] or fluid velocity sensing [64] with laser *Doppler velocimetry*.

I. A. 3. d Bio-MEMS sensors

I. A. 3. d. i Origin and today's applications

The first known bio sensor is recognized to be the glucose sensor designed by Clark an Lyons in 1962 [65], and a first generation of glucose sensors could be commercialized in 1975 based on this work [66]. Since then, many devices has been developed, especially for the last 30 years, when microfabrication processes and MEMS technologies started to be well established. To follow on the glucose sensor, many of them exist today and are broadly commercialized for diabetes treatment, or are still in development. Some are designed to be cheap, some for hospital environment and others for painless or home diagnostics [67]. Research on *bio-MEMS* sensors in general bloomed by the end of the 1990s to answer pathogen screening needs in environmental [68], agri-food [69] and healthcare [70, 71] areas, as depicted on Fig. 3.

The clinical applications of bio sensors are from far the most challenging ones, because of the interaction between the sensor and a complex biological environment such as blood. This is especially true for in vivo applications, where the materials must be bio-compatible not to harm the patient, such as in the case of continuous glucose monitoring [73]. Among them are some metallic alloys, ceramics, glass and natural or synthetic *polymers* (collagen, silicones, etc) [74].

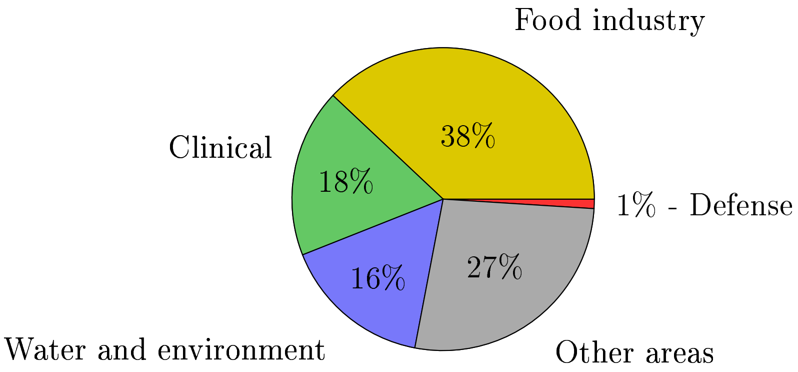

Figure 3: Areas of interest for pathogen detection (classification by number of works appearing in the literature - all types of sensors) / *adapted from [72]*

I. A. 3. d. ii Microfluidic devices

Even though the medium in which bio-MEMS sensors operate may be gas, many applications involve liquids. As a consequence, bio-sensors development relies on the existing techniques to manipulate fluids. Many actuators allow to control fluid flow such as pumps, valves and fluid sampling systems. Sensors using microfluidic technologies thus range from simple *chromatographs* to more complex sensors [75], and are called *lab-on-chip*.

Furthermore, RF-MEMS pushed the development of wireless MEMS sensors in the 2000s that enable a device to communicate with a remote one for control or data analysis. Wireless MEMS and microfluidics together with classic MEMS technologies gave birth to *Micro Total Analysis Systems* (μTAS), especially for medical applications, such as neural probes or glucose sensors for painless home diagnostic of diabetes. μTAS are, since the 2000s, genuine micro-scale laboratories involving several fields of physics and combining the strength of different materials. Their high performances make them very attractive : they are rapid and cheap pathogen sensors with low fluid volumes needed for analysis, but also portable diagnostic tools with high sensitivities enabling in-situ monitoring.

I. A. 4 Conclusion

Since the birth of the first pressure micro sensors and the silicon bipolar transistor, microfabrication technologies have developed, enabling the rise of different types of sensors for many application fields : accelerometers for the automotive industry, RF-MEMS for telecommunication, and lately, bio-MEMS that must answer detection needs for health, agri-food or environment. Mass sensors are thus the center of many current research, especially to lower the minimum detectable mass in a given time of analysis.

I. B Presentation of different microsensing techniques for mass quantification

As pointed out in the last section, the detection and quantification of chemical or biological entities are essential in environment, healthcare or agri-food fields, in order to prevent or heal. Since the first gas sensor, the flame safety lamp, was presented in 1816 to avoid explosion in coal mines [76], many different techniques have been developed for mass sensing in gas or in liquid and MEMS technologies drastically enhanced their performances.

This way, the main mass sensing techniques existing today are presented and discussed in this section for *analytes* present either in gas or in liquid phases. The purpose is to give a general overview of the different transduction principles existing for mass sensing purposes.

I. B. 1 Mass sensors principle

Micro mass sensors are meant to measure biological or chemical entities and in both cases, the operating principle is the same. Indeed, the analyte, present in a gas or liquid medium, is first captured by specific receptors chosen for their chemical affinity with the analyte. The signal triggered by this capture is then changed into a measurable quantity (generally an electrical signal) by the transducer with a specific sensitivity before being treated by electronics yielding the measurement itself. To take the example of bio-sensors, they are composed of *bioreceptors*, a transducer and an electronics as depicted on Fig. 4.

The typical response of a mass sensor can be scattered in four parts as depicted on Fig. 5. If the concentration of analyte c is too small, the sensor signal is lost in the noise (electrical, thermal...). However, if the sensor is designed to have a high sensitivity, the *limit of detection* (LOD) may decrease if the main source of noise comes from the electronics after the transducer output. For values of c above the limit of detection, the sensor has a linear response in a certain range that depends on the physics involved (the *linear range* may even not exist). For high values of c, saturation occurs either when all the remaining sites are no longer accessible by the analyte or when the physics of the transducer limits the maximum output signal value.

Comment : Improving the sensitivity of the transducer does not always result in a LOD drop. Indeed, the bio-recognition can also corrupt the signal because of non-specific binding for instance, called bio noise [77]. These errors are multiplied by the sensitivity and therefore, the corresponding output noise.

Finally, the main characteristics of a mass sensor for bio entities are : **the sensitivity, LOD, linear range, *dynamic range*, *selectivity*, regeneration of the bio-interface, *time response* and *repeatability***. Additional practical parameters should be considered like the price, the difficulty to implement the sensing technique, its portability or its energy consumption.

In what follows, a focus is done on the techniques based on different transduction principles (non exhaustive), to identify a mass shift of a specific entity present in a medium.

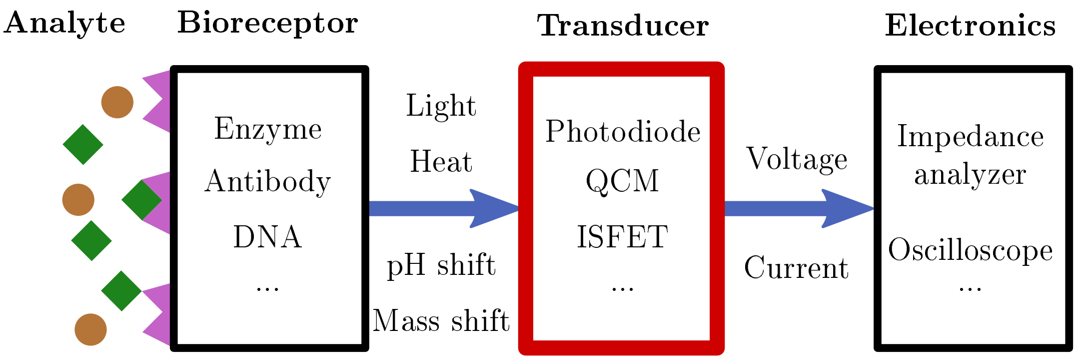

Figure 4: Operating principle of a biosensor / *adapted from [78]*

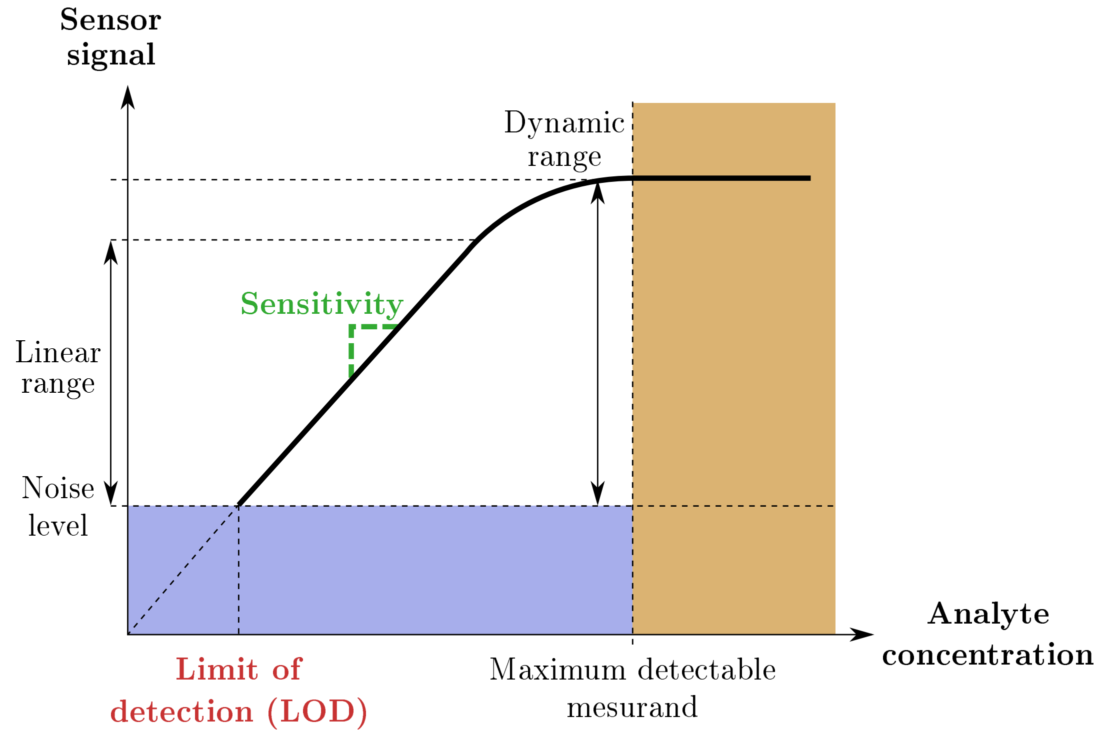

Figure 5: Example of biosensor characteristics

I. B. 2 Electrochemical transducers

I. B. 2. a Generalities

Electrochemical detection is one of the most common ways to detect and quantify chemical or biological species in a given medium because of the direct transformation of the analyte chemical behavior into electrical signal. It is also usually the cheapest and easiest way of detection. However, the main drawbacks of these techniques remain the high LOD and low selectivity for most of sensors based on these techniques.

I. B. 2. b Sensors based on oxidation/reduction reactions

I. B. 2. b. i Potentiometry

Potentiometry is a method based on the measure, at a fixed electrical current, of a potential difference caused by *oxidation/reduction* reactions in the solution between a working electrode and a reference electrode which potential is constant as depicted on Fig. 6. From this difference can be calculated the analyte concentration, using the Nernst Equation [79]

$$E = E_0 + \frac{R \cdot T}{n \cdot F} \cdot ln(C_{ox/red}) \tag{2}$$

where E_0 is the standard potential, R is the perfect gas constant, T the temperature, F the Faraday constant, n the number of exchanged electrons and $C_{ox/red}$ the activity ratio of the ion to measure (oxidized state over reduced state).

Potentiometric electrodes may be divided in two main categories : *ion selective electrodes* (ISE) such as pH sensors [80], CO_2 or NH_3 [81] gas sensors, and ion sensitive *field effect transistors* (ISFET) that appeared in 1968 [82, 83]. The first method is easy to implement, but is also quite expensive and the electrodes are relatively fragile. The second one requires microfabrication technologies but is less expensive and can process analyte quantification in a few minutes only. The selectivity of both methods depends on the presence of other species that may trigger additional oxido-reduction reactions.

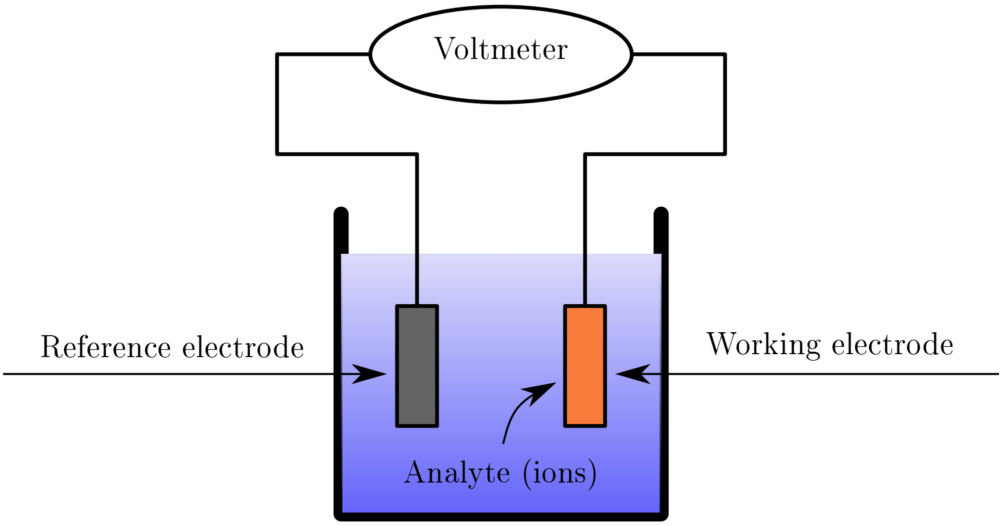

Figure 6: Potentiometric sensor principle

I. B. 2. b. ii Amperometry

Amperometry is a technique that consists of the measure of the electrical current coming from the oxido-reduction of specific entities between two electrodes at a fixed potential (electrolysis). For example, the glucose sensor of Clark is based on this principle, so as the detection of peroxide [79] according to the reaction

$$H_2O_2 \rightarrow O_2 + 2H^+ + 2e^- \tag{3}$$

The migration of electrons generates an electrical current which measurement enables the quantification of peroxide. This method is known to be fast, easy to implement, more sensitive than potentiometry with a lower LOD, and cheap. However, its selectivity is weak due to additional interactions that may happen with other species that can be oxidized or reduced.

I. B. 2. c Impedance sensors

I. B. 2. c. i Conductometry in liquid

Conductometry is a method that enables to quantify electrically charged species in a solution [84] as depicted on Fig. 7. The application of an alternative potential V between two electrodes plunged in the solution, combined with the measure of the electrical current I and the use of Ohm's law allows to determine the conductivity σ

$$\sigma = \frac{I}{V} \tag{4}$$

This method is also easy to implement, cheap and quick. However, the selectivity is very low due to the sensitivity to other charged species present in the solution.

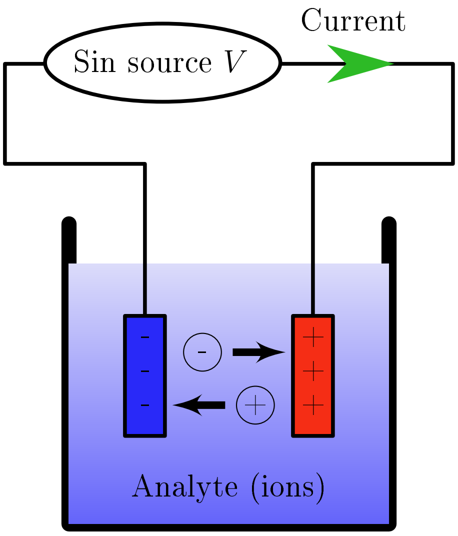

Figure 7: Conductometric sensor principle

I. B. 2. c. ii Polymer-absorption resistors and metal-oxide semiconductors

Polymers, sometimes doped with conductive particles to reduce their impedance, can also be used as sensor since their electrical resistance varies in presence of certain gases [85, 86]. Cheap and sensitive, these sensors provide repeatable measure and low LOD but also a high dependence on temperature and a low selectivity. However, the latter can be improved when crossing data from an array of different polymer gas sensors [87], and efforts are currently done to improve the performances of such sensors regarding their dependence to temperature [88].

One of the most common gas sensor is based on metal-oxide semiconductors. Indeed, the electrical resistance of certain metal oxides such as S_nO_2, CuO or Fe_2O_3 changes in presence of certain gases like O_2, H_2, CO or CO_2 [89, 90]. These sensors are known to be low cost and able to rapidly detect many different gases.

I. B. 2. c. iii Carbon nano-materials sensors

Carbon nano-material based gas sensors are chemical nano-resistors and have been attracting great interest in the last years [91, 92]. They are based on four distinct nano-structures : *carbon black*, *carbon fibers*, *carbon nanotubes* and *graphene*. When the analyte binds to one of these structures, the resistance of the carbon nano-material varies and provides electrical information. Although these structures seem to be good candidates for low LOD because of their small size, many limitations are still up to date. Indeed, the functionalization of such sensors is challenging, their selectivity is low and sensitivity to impurities quite high. Furthermore, their commercialization is not for a while because no cost effective fabrication technique exists yet.

I. B. 2. d Thermal sensors

I. B. 2. d. i Thermodynamic sensors

Thermodynamic sensors are meant to determine an analyte concentration in endothermic or exothermic chemical reactions (generally enzymatic reactions). Knowing the variation of enthalpy ΔH generated with one mole of a reagent i, the number of moles n of this reagent i can be calculated from the measure of the temperature shift ΔT as follow [93]

$$n = \frac{\Delta T \cdot C_p}{\Delta H} \tag{5}$$

where C_p is the thermal capacitance of the reactor in which the chemical reaction occurs. Knowing the balanced chemical equation of the reaction, the quantity of analyte can be obtained from n (in case the reagent i is not already the analyte).

This kind of sensors is quite cheap, easy to implement and selective as long as it is made sure only one chemical reaction triggers a temperature variation. However, the LOD is drastically limited by the thermal noise and the difficulty to localize the heat change near the probe.

I. B. 2. d. ii Heat-conduction sensors

The thermal conductivity of a gas mixture changes according to the nature and concentration of each of its components. This property can be used to design gas sensors by heating a chamber containing the gas sample [94, 95]. The measure of both ambient and heater temperature in addition to the power consumption give access to the conductivity through the Fourier's law.

Such sensors are cheap, easy to implement and have a fast response, but the LOD is again limited by thermal noise and the gap between the mixture and the analyte thermal conductivities. Furthermore, the selectivity is low since a change in the thermal conductivity can occur with any gas.

I. B. 3 Optical transducers

I. B. 3. a Generalities

With the emergence of the *optical fiber*, optics has nowadays a major role to play among mass sensors. The main advantage of the techniques based on optics is their low time of analysis, allowing real time sensing. However, they are usually more expensive than classic electro-chemical methods because a light emitter and photodetectors are needed.

I. B. 3. b Reflectometry

I. B. 3. b. i Surface plasmon resonance

A surface plasmon is an electromagnetic wave that propagates at the surface of a conductive material. Such a wave can be generated on a metal lightened with a polarized laser, and for a certain angle between the laser and the surface, this electromagnetic wave resonates : it is the surface plasmon resonance (SPR). In the resonance conditions, a part of the incoming light energy is transformed into the plasmon, thus diminishing the reflected beam energy. Since the surface plasmon is located at the interface of two media, these oscillations are very sensitive to any change at this boundary. In brief, the *adsorbtion* of biological or chemical entities changes the angle of resonance as depicted on Fig. 8. Therefore, the measure of the resonance angle or the light intensity at fixed angle provides information on the mass quantity fixed on the metallic surface [96]. The use of SPR also allows to scan the surface of a sensor, so called SPR imaging [97].

The SPR finds applications in gas sensing [98], but above all in bio-sensing [99, 100] because microfluidics can be implemented on one side of the metal in addition to bioreceptors to its surface, and the laser reflects on the other side of the metal. SPR sensing technique is not selective as such, except if specific bioreceptors are used. It has also low time response, but this technique is still expensive compared with MEMS or electro-chemical sensors.

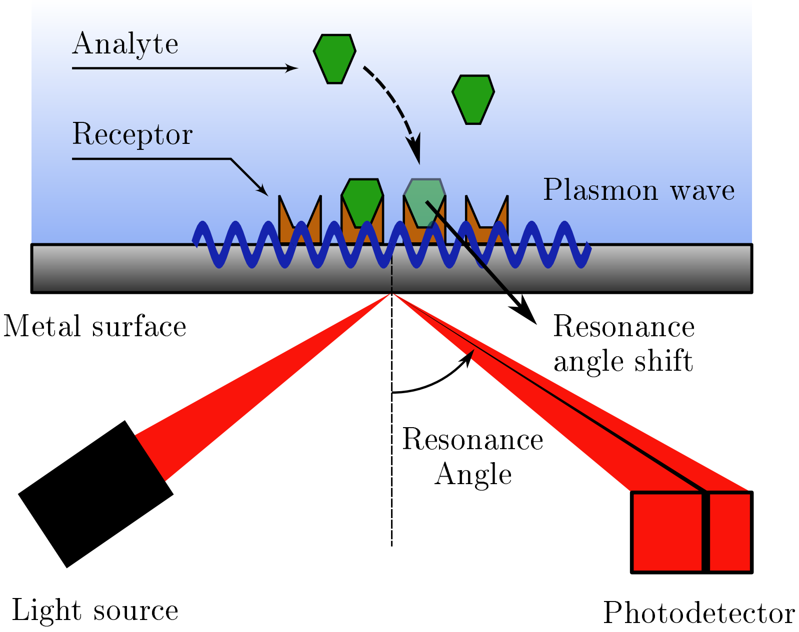

Figure 8: SPR principle

I. B. 3. b. ii Optical fibers

The reflective index at the tip of an optical fiber depends on the chemical nature of its interface with the external world. Therefore, a photodetector measuring the reflected light provides information on the composition and the quantity of analyte fixed at the tip of the fiber [101] as depicted on Fig. 9a.

Another way to sense the analyte in a liquid or a gas is to use the side of the fiber. Indeed, the analyte binding at the external border of an optical fiber interacts with the light reflecting inside the fiber : it generates an evanescent wave outside the fiber near its surface. Consequently, the transmitted light intensity is weaker, which can be quantified with a photodetector [102] as depicted on Fig. 9b.

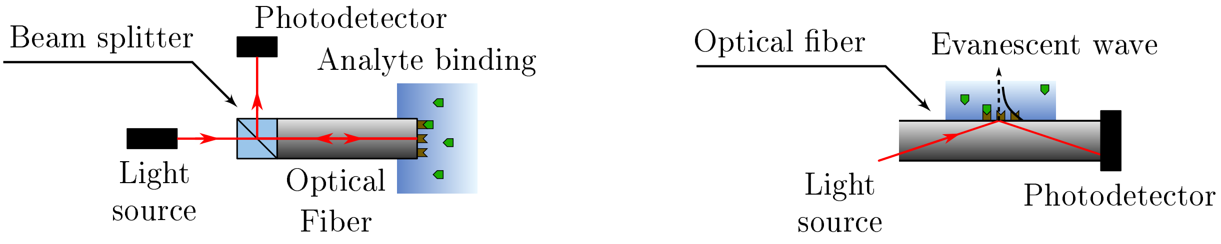

(a) Reflection at the tip of the fiber

(b) Reflection on the side of the fiber

Figure 9: Analyte detection with optical fibers using reflection

The selectivity of these techniques depends on the nature of the analyte and the ability of the sensor to capture it. Although these setups require optical components, they remain quite simple to implement since no beam alignment is needed.

I. B. 3. b. iii Ellipsometry

Ellipsometry is an analysis technique that consists of measuring the polarization change of light after reflection on a surface. This technique allows to characterize the optical properties of the surface, as well as the thickness of thin films with high precision [103]. This way, the quantity of analyte that is bond at the surface can be indirectly determined. This simple technique provides fast analysis but low selectivity (unless if specific bioreceptors are used), and requires expensive polarized optical components.

I. B. 3. c Interferometry

Interferometry allows to generate optical *interference* between a laser split in two beams having different paths. The two beams are then recombined and the difference of *optical path length* between them leads to constructive or destructive interference. This phenomenon allows to sense either a distance or a refractive index difference.

This phenomenon can be exploited for bio-sensing [104]. In this case, the analyte binding at the external surface of an optical fiber leads to small localized variations of refractive index, thus triggering a variation of optical path length and interference intensity on the photodetector.

Interferometry also benefits to gas sensing [105], when one of the beams crosses a chamber that contains the gas to sense (also called *hollow core waveguide*) as depicted on Fig. 10. The change in refractive index in the sample due to the presence of the analyte changes the optical path length and thus the generated interference intensity.

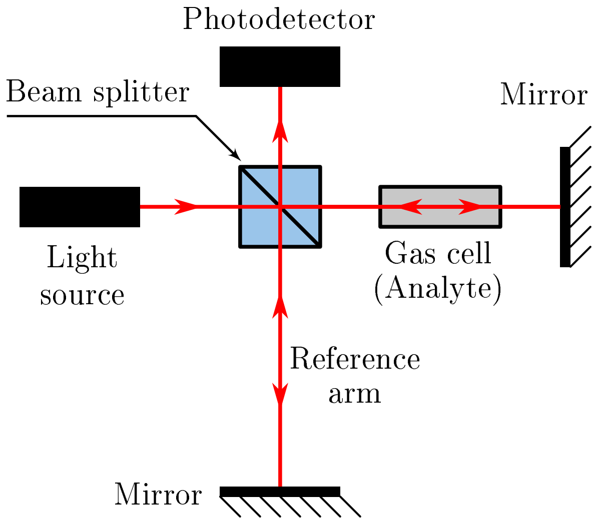

Figure 10: Example of a gas sensing interferometer

Because of the small wavelength of infra-red or visible light commonly used in interferometric sensors, the latter are known to yield lower LOD than the ones based on reflectometry, but they also require fine alignment of the beams.

I. B. 3. d Sensors based on absorbance

Sensors measuring absorbance aim at the determination of the concentration of a gas using its absorbance spectrum and Beer-Lambert-Bouguer law [106]

$$A = \epsilon \cdot c \cdot l \tag{6}$$

where A, ϵ, c and l are the absorbance of the sample, a constant that depends on the absorbtivity of the species at a particular wavelength, the analyte concentration and the length of the cell, respectively.

Such devices are thus equipped with a source emitting light through a hollow core waveguide containing the analyte, and a photodetector. Since the absorbance spectrum of a gas is often unique, these sensors also allows to identify different gases in the same sample. This method is selective, cheap, easy to implement and provide fast analysis. However, like methods based on reflectometry, the main limitation is the high LOD. This kind of transduction can also be used for an analyte being in liquid.

I. B. 3. e Fluorescence

Fluorescence is one of the most common bio-detection technique. It consists of the fixation of a fluorescent molecule on the analyte [107] (*label based technology*), which allows to detect and quantify it. The introduction of different fluorescent molecules emitting at different wavelength also permits multiple analytes identification at the same time [108]. Fluorescence provides quite low LOD and its selectivity depends on the chemical affinity between the fluorescent molecule and the analyte. However the major drawbacks comes from the labels : the introduction of a marker indeed requires long preparations and may be relatively expensive.

I. B. 4 Mechanical transducers

I. B. 4. a Generalities

Mechanical mass sensors usually require microfabrication processes since the smaller the structure is, the lower the LOD can be. As a consequence, these transducers are mostly cheaper than optical techniques but more expensive than electro-chemical ones. Their selectivity depends only on the analyte-binding properties.

I. B. 4. b Cantilevers with static deflection

The deposition of a bio-entity at the surface of a cantilever modifies its surface stress, thus leading to its deflection [109, 110]. The latter can be measured using optics (measure of the deflection with a laser and a photodetector) [111] or piezoresistivity (measure of the stress with a Wheatstone bridge) [112]. Capacitive measurement is also possible for cantilevers (the cantilever is one of the two plates of a capacitor). This last method is quite sensitive, but does not suit neither large displacement measures (non linearities) nor measures in liquid due to *faradaic currents* [113].

The deflection of the cantilever Δh can be expressed as a function of the stress difference $\Delta\sigma$ between both sides of the cantilever, following the Stoney's formula defined as

$$\Delta h = \frac{3\Delta\sigma \cdot (1-\nu)}{E} \cdot \left(\frac{L}{d}\right)^2 \tag{7}$$

where ν, E, L and d are the Poisson's ratio, the Young modulus, the length and thickness of the cantilever, respectively. Knowing the size of both bioreceptors and analyte, as well as their densities, it is possible to calculate the variation of mass Δm from Δh.

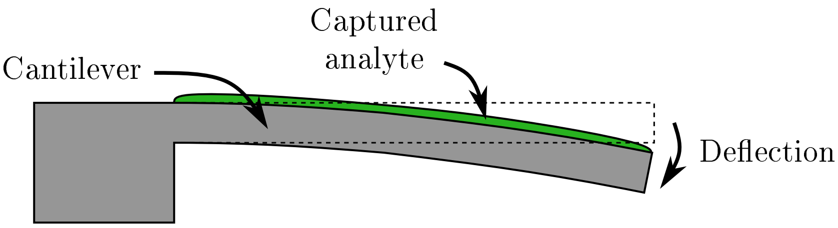

Figure 11: Static deflection of a cantilever

Although these sensors yield low LOD, they are very sensitive to local parasitic factors such as humidity, temperature or refractive index changes in the detection is optical. Differential measurements with a passive cantilever (without analyte) can be done in order to get rid of these spurious deflections.

I. B. 4. c Resonant sensors

I. B. 4. c. i Cantilevers

Cantilevers may also be used as resonant structures, with their resonant frequencies as a readout. The resonant frequency f_0 of a resonator is expressed as

$$f_0 = \frac{1}{2\pi} \cdot \sqrt{\frac{k}{m}} \tag{8}$$

where k and m are the stiffness and mass of the equivalent mass-spring system of the structure. As a consequence, the mass shift Δm can be expressed as follow

$$\Delta m = \frac{k}{4\pi^2} \cdot \left(\frac{1}{f_1^2} - \frac{1}{f_0^2} \right) \tag{9}$$

where f_0 and f_1 are the resonant frequency before and after the analyte capture, respectively.

Since the resonant frequency of the cantilever is proportional to $\sqrt{\frac{k}{m}}$, the fixation of the analyte at the surface of the cantilever modifies either its overall stiffness k, and/or its effective mass m. In particular, when the analyte is equally distributed on a cantilever, the change in stiffness overcomes the one in mass (due the stress induced by the binding of the analyte at the surface of the cantilever) [114, 115]. In contrast, when the mass is added at a specific location on the cantilever (specifically at the tip), the stiffening of the surface becomes negligible, and the additional inertia is the dominant effect on resonant frequency [116].

Damping is the main limitation of resonant cantilevers when they are operated in liquid. In order to solve this issue, a suspended microchannel resonator, depicted on Fig. 12, has been developed. This structure includes the liquid containing the analyte, instead of soaking into it, which allows to work with higher Q-factors and thus generally lower LOD [117–119].

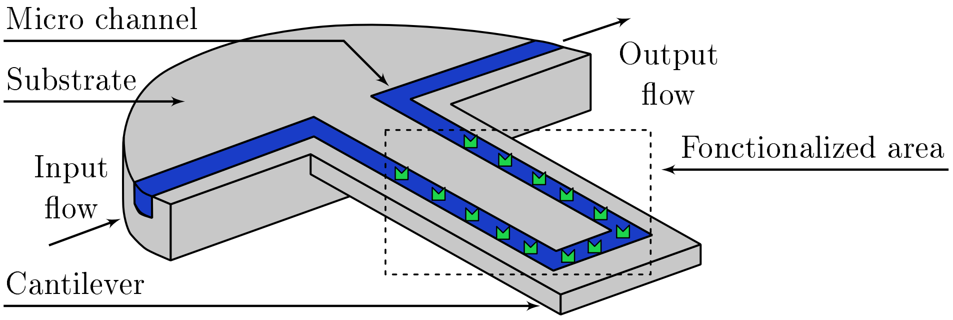

Figure 12: Suspended microchannel resonator

These examples are bio-sensors working in liquid, but resonant cantilevers can also operate in gas [120–122].

Comment : Other resonant structures that do not involve BAW or SAW exist such as double clamped beams or membranes excited on one of their first acoustic modes. Such structures are not detailed here because their operating principle is very similar to the one of cantilevers.

I. B. 4. c. ii Bulk acoustic wave resonators

Piezoelectricity is also widely used to design mass sensors, and BAW resonators are among them. BAWs are generated with the application of alternated potential between two electrodes, either placed next to each other or face to face on both sides of the crystal. The first configuration is called *lateral field excitation* (LFE) and the second one *thickness field excitation* (TFE). TFE is often preferable because the electrical field is more homogeneous in the crystal, yielding better piezoelectric coupling, but LFE is sometimes compulsory for sensing in liquid for instance, to separate the electronics from the liquid.

The most common BAW resonator is the quartz crystal resonator, usually named quartz crystal microbalance (QCM) when used for mass sensing purposes. This type of resonator works with thickness *shear waves* and not *longitudinal waves* in order to limit damping with the external medium (air or liquid). Similarly to resonant cantilevers, the resonant frequency is often chosen as the output metric but unlike cantilevers, the analyte deposition only modifies the effective mass and not the stiffness of the resonator since a QCM operates with *thickness shear waves*. Thus, its resonant frequency always decreases with the analyte fixation. This mass variation can be calculated using the Sauerbrey equation [123]

$$\Delta m = -\frac{A \cdot \sqrt{\rho_q \cdot \mu_q}}{2 f_r^2} \cdot \Delta f \tag{10}$$

where Δm, Δf, f_r, A, ρ_q and μ_q are the mass variation, resonant frequency variation, resonant frequency, piezoelectric active area, density and shear modulus of quartz, respectively.

In comparison with cantilevers, QCMs are appreciated for their larger surface for the analyte deposition and higher Q-factors in fluid. QCMs are thus widely used for sensing [124] in gas [125], liquid [126], and above all for bio-sensing [127–130].

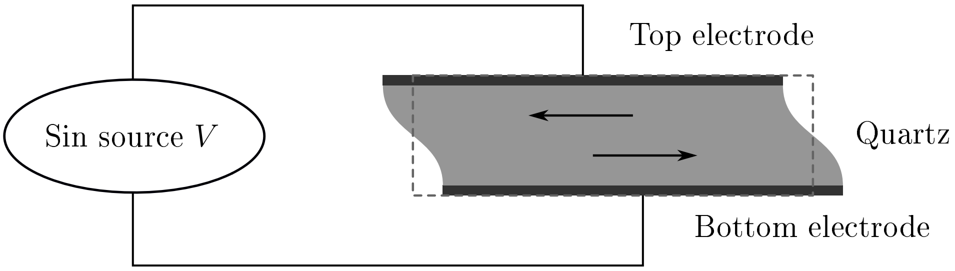

Figure 13: Quartz cristal resonator principle

Despite the different advantages of QCMs, their resonant frequency are limited to around 100 MHz [131] due to the minimum quartz thickness achievable. Therefore, other BAW resonators appeared such as thin film bulk acoustic resonators (FBAR) made of different piezoelectric materials such as zinc oxide (ZnO), aluminium nitride (AlN), or lead zirconium titanate (PZT). The small thickness of FBARs makes their resonant frequencies being higher than that of conventional QCMs (a few GHz) and their effective mass is lower. As a consequence, a variation of mass generates higher effects on the resonant frequency : the sensitivity is again higher. FBARs are then used for sensing [132] bio-entities [133, 134] and gas [132].

In order to increase even more the Q-factor of FBARs, they can be mounted on a *Bragg reflector* to confine the acoustic energy in the resonator at the resonance, the so-called solid-mounted resonators (SMR) [135, 136] depicted on Fig. 14a. This structure can be excited using either LFE or TFE to generate thickness shear waves or longitudinal bulk waves. SMRs also allow to design mass sensors [137].

Another way to get a high frequency and high Q-factor resonator is to fix the FBAR on a low loss substrate like sapphire, much thicker than the FBAR [138]. Such a structure is called a high tone bulk acoustic resonator (HBAR), because the excited mode has a wavelength much smaller than the substrate's thickness as shown on Fig. 14b. The Q-factor of this kind of resonator is determined by the mechanical losses in the substrate, where most of the acoustic energy is confined [139]. That is why HBARs are also used in mass sensing [140].

Although FBARs, SMRs and HBARs have higher Q-factors and so higher sensitivities than QCMs, QCMs remain a reference in term of BAW resonator because they are more robust (they can operate under different conditions), reproducible, less fragile, cheaper and easier to characterize.

(a) Surface mounted resonator (b) High-tone bulk acoustic resonator

Figure 14: Resonators based on FBARs

I. B. 4. c. iii Surface acoustic wave devices

The application of an alternative potential difference across an IDT triggers a variable strain at the surface of the substrate, thus generating a SAW which amplitude depends on the frequency (the IDT acts like a filter). Indeed, the IDT resonates when the excitation frequency f follows

$$f = \frac{v}{\lambda} \tag{11}$$

where v the phase velocity of the SAW (which depends on the density and the Young and/or shear modulus of the substrate) and λ the geometric period of the IDT.

Different SAWs can be generated, depending on the relative orientation between IDTs and the piezoelectric crystal cut : *Rayleigh waves*, *Love waves*, *SH-SAWs* and *Lamb waves* are the main ones. The design of mass sensors based on SAWs is one way to increase their sensitivity, since the acoustic energy is focused at the surface of the substrate (close to the analyte binding) [141]. When sensing in liquid for biological applications, Love waves or SH-SAWs are generally selected [142] because the particle displacement is in the plane of the surface, so there are less energy lost in the liquid [143–145].

A first configuration of SAW sensors is the delay lines, in which a first IDT emits the SAW and a second one, located a few wavelengths further on the substrate, receives the SAW as depicted on Fig. 15. The gas or bio sensing area is in between the two IDTs and the presence of a chemical entity delays the SAW (it modifies the SAW group phase) [146, 147]. A delay line can also be design with only one IDT being both emitter and receiver, with a reflector on the other side of the sensing area [148] such as on Fig. 16.

A second configuration is the SAW resonator, again either with one or two IDTs. Reflectors are usually placed around them in order to confine the acoustic energy in the area of interest and minimize energy loss [149, 150]. The fixation of the analyte modifies the resonant frequency and amplitude, that can be the sensor readout.

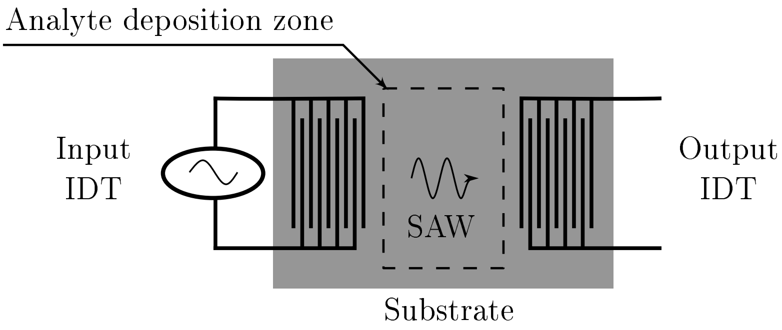

Figure 15: Delay line with two IDTs

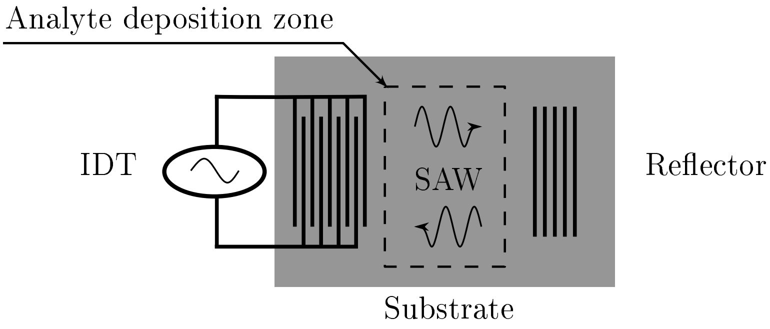

Figure 16: Delay line with an IDT and a reflector

The major advantage of SAWs over BAWs mass sensors is their sensitivity to the analyte concentration because the acoustic energy is focused at the surface, close to the analyte. However, SAW's resonant frequency, group phase and amplitude also depends on pressure, humidity and temperature, which require careful design and control over these parameters [151].

I. B. 5 Short discussion

The performances of mass sensors are usually given by the relation between their LOD and analysis time : the lower the LOD, the longer the analysis. The minimum LOD for a given analysis time thus gives the current state of the art as explained in [77, 152].

Among all the presented transducer, it appears that mechanical sensors are promising because of their portability (in comparison with SPR for instance), low cost and power consumption, low LOD and because they are label free technologies. Therefore in this thesis, efforts are done to lower the LOD of mechanical resonant structures for sensing analytes present either in gas or in liquid.

Chapter I in a nutshell

The first chapter provides a quick history of the development of MEMS sensors. Their diversification was mainly made possible by the invention of the transistor, the discovery of the high piezoresistive coefficients of silicon and the evolution of microfabrication processes. MEMS sensors include mass sensors, mainly used in biological applications (environment, health and food), which are composed of specific receptors, a transducer and signal processing electronics. The nature of the transducer can be electrochemical, optical or mechanical. Each of them has different performances in terms of detection limit, portability, low cost, short analysis time or the use of unlabelled technologies. The state of the art of these sensors generally highlights the analysis time in relation to the detection limit. Mechanical resonators are among the systems capable of achieving a low detection limit while being portable. It is on this type of system that the thesis will focus.

Mieux vaut éclairer que briller.

Saint Thomas d'Aquin

Chapter II

Positioning of mode localized based sensors among resonant sensors

In this chapter are firstly described the operating principles of mechanical sensors working either in resonator or *oscillator* mode. One challenge of mass sensors is to lower their LOD, and the last decade saw the emergence of a new approach for resonant sensors that may take over classical sensors based on frequency shift readout : mode localization (ML). Therefore in a second section, this phenomenon is described throughout its current state of the art and finally discussed in a last section, where its potential is evaluated considering different resonator configurations.

II. A One degree-of-freedom mechanical resonators for mass sensing

The following section reminds the basics of mechanical resonators and the different configurations in which they can be used (open-loop or closed loop), especially for mass sensing purposes.

II. A. 1 Mechanical resonators

II. A. 1. a Generalities

From a spectral point of view, a resonator is a filter which gain is above one for specific frequencies. From a physical point of view, a mechanical resonator is a dynamic system internally and alternatively exchanging energy between potential and kinetic forms, and that accumulates this energy for certain excitation frequencies. Such systems thus have a resonant frequency (RtF), also called eigenfrequency when the system is conservative (no energy losses). Basic examples are the simple pendulum or the linear mass-spring system which naturally oscillate at their eigenfrequencies when there is a non zero initial condition on their position or velocity.

Let's apply the second Newton's law to the mass of the undamped resonator depicted on

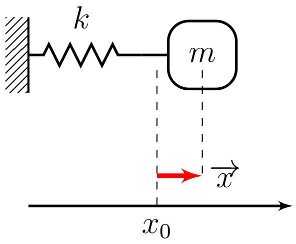

Figure 17: Schematics of a mass spring system

Fig. 17

$$m \cdot \frac{d^2}{dt^2}x(t) + k \cdot x(t) = 0 \tag{12}$$

The solution of this differential equation is

$$\begin{cases} x(t) = A \cdot cos(\omega_0 \cdot t + \phi) \\ \omega_0 = \sqrt{\dfrac{k}{m}} \end{cases} \tag{13}$$

where A and ϕ are constants determined with initial conditions and ω_0 the angular eigenfrequency.

However in reality, any dynamic system is subjected to friction. Therefore, any resonator movement will stop after a certain number of oscillations. These losses are commonly quantified using the dimensionless parameter Q-factor, defined as follow [153]

$$Q = \frac{2\pi \cdot W}{\Delta W} \tag{14}$$

With W the initial total energy stored in the resonator and ΔW the energy loss after one oscillation.

In order to keep a resonator oscillating, energy must be provided from the outside. One way to do it is to apply in open loop a periodic excitation at the RtF of the system like the swaying movement of someone legs on a swing.

The linear model of these losses is the damper. The basic damped resonator is then the linear mass-spring-damper system depicted on Fig. 18.

Let's again apply Newton's second law to the mass

$$m \cdot \frac{d^2}{dt^2}x(t) + \eta \cdot \frac{d}{dt}x(t) + k \cdot x(t) = F(t) \tag{15}$$

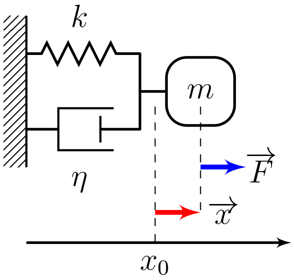

Figure 18: Schematics of a mass spring damped system

which yields

$$\begin{cases} \dfrac{d^2}{dt^2}x(t) + \dfrac{\omega_0}{Q} \cdot \dfrac{d}{dt}x(t) + \omega_0^2 \cdot x(t) = \dfrac{1}{m} \cdot F(t) \\ \omega_0 = \sqrt{\dfrac{k}{m}} \\ Q = \dfrac{\sqrt{k \cdot m}}{\eta} \end{cases} \tag{16}$$

When the friction is weak enough ($Q > \frac{1}{2}$), the solution of the corresponding homogeneous equation (Eq. 16 with $F = 0$) is

$$\begin{cases} x(t) = A \cdot e^{\left(-\frac{\omega_0}{2Q} \cdot t\right)} \cdot cos(w_r \cdot t + \phi) \\ \omega_r = \omega_0 \cdot \sqrt{1 - \dfrac{1}{4Q^2}} \end{cases} \tag{17}$$

where A and ϕ are constants determined with initial conditions and ω_r the resonant angular frequency.

The quality factor Q in Eq. 17 has the same meaning than its definition given in Eq. 14. It describes the decreasing exponential envelope due to friction containing the sinusoidal behavior of a free damped resonator. From this property can be experimentally determined Q using the logarithmic decay method.

Let's F now be a sinusoidal angular excitation frequency ω, we can then introduce complex notations (underlined), with $j^2 = -1$

$$\left(-\omega^2 + j \cdot \omega \cdot \frac{\omega_0}{Q} + \omega_0^2\right) \cdot \underline{x}(t) = \frac{1}{m} \cdot \underline{F}(t) \tag{18}$$

Let's be $s = j \cdot \frac{\omega}{\omega_0}$ and divide by ω_0^2

$$\left(s^2 + \frac{1}{Q} \cdot s + 1\right) \cdot \underline{x}(t) = \frac{1}{m \cdot \omega_0^2} \cdot \underline{F}(t) \tag{19}$$

Since $\frac{1}{m\cdot\omega_0^2}\cdot\underline{F}(t)=\frac{\underline{F}(t)}{k}$ is the *static displacement* x_{st}, the last equation yields the transfer function of the damped resonator

$$\frac{\underline{x}}{x_{st}}=\frac{1}{s^2+\frac{1}{Q}\cdot s+1} \tag{20}$$

The typical amplitude and phase of such a resonant filter are depicted on Fig. 19.

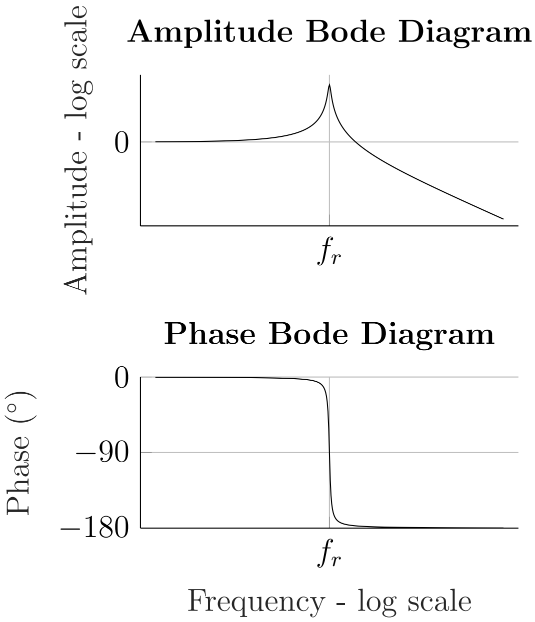

Figure 19: Amplitude and phase Bode diagrams of a damped resonator

The presence of friction widens the resonance spectrum around the resonant frequency $f_r=\frac{1}{2\pi}\cdot\omega_r$, which also allows to calculated Q. Indeed in practice, Q is usually determined using the filter bandwidth at $-3\,\mathrm{dB}$, Δf_{-3dB}, as follow [154]

$$Q=\frac{f_r}{\Delta f_{-3dB}} \tag{21}$$

Δf_{-3dB} also corresponds to the frequency bandwidth for which the amplitude is that of the resonance divided by $\sqrt{2}$.

II. A. 1. b Electrical equivalence

The exact same differential equations can be obtained for resonators of different physical nature. The most common one is the series RLC-resonator, depicted on Fig. 20.

The application of the mesh equation to the previous circuit leads to the following differential equation (with q the electric charge at the capacitor terminal)

$$L_m\cdot\frac{d^2}{dt^2}q(t)+R_m\cdot\frac{d}{dt}q(t)+\frac{1}{C_m}\cdot q(t)=V_{input}(t) \tag{22}$$

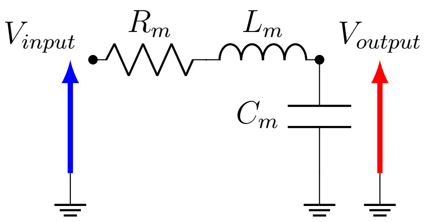

Figure 20: Series RLC-resonator

In relation with Eq. 15, we can thus write the following table

Table 1: Electro-mechanical equivalence for resonant systems

Mechanics	**Electrics**
Displacement $x(t)$	Capacitance charge $q(t)$
Damping η	Resistance R_m
Mass m	Inductance L_m
Stiffness k	Inverse of capacitance $\frac{1}{C_m}$
Angular eigenfrequency $\omega_0 = \sqrt{\frac{k}{m}}$	Angular eigenfrequency $\omega_0 = \frac{1}{\sqrt{L_m \cdot C_m}}$
Q-factor $Q = \frac{\sqrt{k \cdot m}}{\eta}$	Q-factor $Q = \frac{1}{R_m} \cdot \sqrt{\frac{L_m}{C_m}}$

And the transfer function is identical to Eq. 20

$$\frac{\underline{V_{output}}}{\underline{V_{input}}} = \frac{1}{\left(s^2 + \frac{1}{Q} \cdot s + 1\right)} \tag{23}$$

This equivalence is widely used to design the input and output electronics associated with a device.

II. A. 1. c The Butterworth-Van Dyke model

Most of the mechanical resonators are actuated throughout a potential difference between two terminals (electrostatic actuation, piezoelectric crystals...). Since a *dielectric* sandwiched between two electrodes applying an electric field is, by definition, a capacitor, this effect must be taken into account in a mechanical resonator model [155]. The addition of a capacitor C_0 at the terminals of the RLC series model, such as depicted on Fig. 21, enables to model this parasitic phenomenon. It is named the Butterworth-Van Dyke model (BVD), which is the most widely used one.

The application of a sinusoidal excitation $\underline{U}(j \cdot \omega)$ at the terminals of this electrical circuit yields a periodic mechanical motion and an alternative electrical current $\underline{I}(j \cdot \omega)$.

The RLC series (the motional branch) represents the dynamic mechanical behavior as described in the previous section (with the same resonator *figures of merit*).

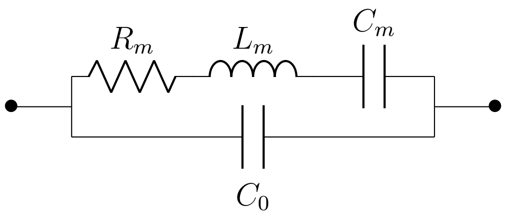

Figure 21: Schematics of the Butterworth-Van Dyke model

The admittance $\underline{Y}(j \cdot \omega) = \frac{I}{\underline{U}}(j \cdot \omega)$ of this resonant filter is

$$\begin{cases} \underline{Y}(j \cdot \omega) = \omega_0 \cdot C_0 \cdot s \cdot \dfrac{s^2 + \frac{1}{Q} \cdot s + (1 + g_1)}{s^2 + \frac{1}{Q} \cdot s + 1} \\ s = \dfrac{j \cdot \omega}{\omega_0} \\ Q = \dfrac{1}{R_m} \cdot \sqrt{\dfrac{L_m}{C_m}} \\ \omega_0 = \dfrac{1}{\sqrt{L_m \cdot C_m}} \\ g_1 = \dfrac{C_m}{C_0} \end{cases} \tag{24}$$

The impedance is more commonly considered, but we here base our reasoning on the admittance that allows to see the resonances more easily.

Let's now consider a high Q-factor resonator ($Q \gg 1$), Y becomes

$$\underline{Y}(j \cdot \omega) \simeq \omega_0 \cdot C_0 \cdot s \cdot \frac{s^2 + (1 + g_1)}{s^2 + 1} \tag{25}$$

Since a frequency is positive, this admittance is equal to zero when

$$\begin{cases} \omega = 0 \\ \omega = \omega_0 \cdot \sqrt{1 + g_1} = \omega_p \end{cases} \tag{26}$$

It means the electrical current is equal to zero for low frequencies. This is due to the infinite impedance of the capacitors. The second solution is called the parallel resonance. At this particular frequency happens alternative energy exchanges between the two capacitors C_m and C_0, but no current goes out of the BVD.

Furthermore, the admittance tends to infinity when

$$\omega \to \omega_0 = \omega_s \tag{27}$$

The maximum of current (resonance) is obtained when the frequency equals the series resonance ω_s. In that case, there are energy exchanges between the motional inductance and capacitor, making the current flow through the motional branch and out of the BVD.

In reality, R_m never equals zero, and the typical admittance is plot on Fig. 22, where ω_s and ω_p are the angular frequencies of series and parallel resonances, respectively.

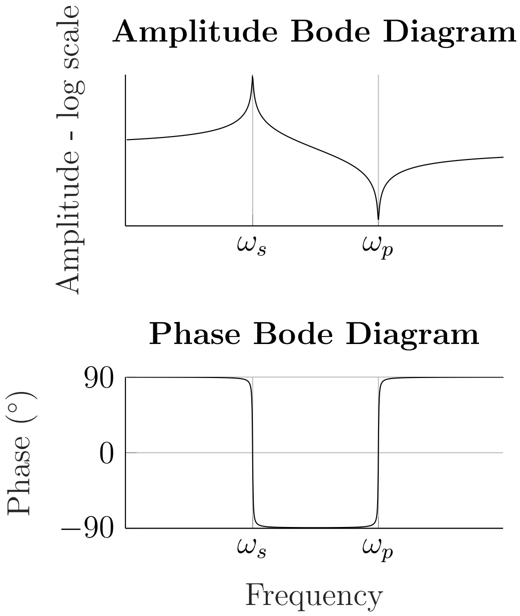

Figure 22: Amplitude and phase Bode diagrams of the BVD admittance

With this model, the quality of the resonance (characterized by its phase jump for instance) no longer depends only on the Q-factor, but also on the frequency difference between the series and parallel resonances. Indeed, if both resonances are too close in frequency, they may merge, the phase never reach −90°and the maximum amplitude is lower. Assuming $g_1 \ll 1$, this frequency gap can be expressed as

$$\omega_p - \omega_s \simeq \frac{g_1}{2} \cdot \omega_s \tag{28}$$

When the resonator is working in gas or liquid, other passive electric components may be added to the model in order to take these loads into account [155].

Comment : The observed physical quantity of the admittance on Fig. 22 is the electrical current (in mechanics, the velocity) and not a charge (in mechanics, the displacement), so both input and output are in phase at the resonance.

II. A. 2 Electronic environment of resonant sensors

II. A. 2. a Feedthrough transmission

The open-loop transfer function of a resonant MEMS device is a combination of the transfer functions of the resonator H_r, the surrounding actuation H_{act} and detection H_{det} electronics and the feedthrough transmission H_{ft} such as depicted on Fig. 23. The latter represents the parasitic electronic elements due to the wires for instances (additional unwanted capacitance). H_{ft} may have different expressions depending on the device. Somehow, the parallel capacitance C_0 of the BVD can be considered as an unwanted feedthrough capacitance [154].

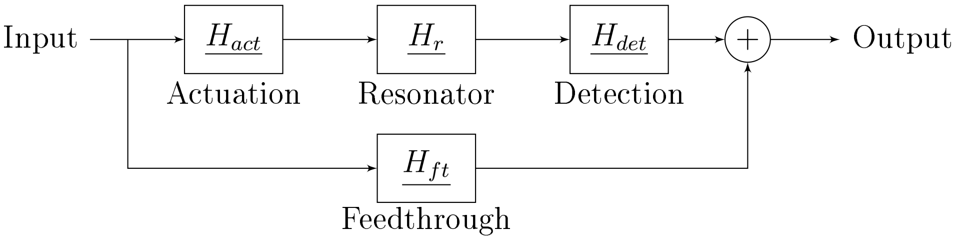

Figure 23: Transfer function of a resonant MEMS

II. A. 2. b Resonators in open loop

One way to measure the shift of RtF is to scan around the RtF, which has the drawback to be quite time consuming, such as with an impedance analyzer for piezoelectric resonators. However, other systems with *feedback* (closed loop systems) exist to either automatically follow their resonance or improve some of their characteristics such as the Q-factor.

II. A. 2. c Resonators in closed-loop

II. A. 2. c. i Mechanical oscillators

A closed-loop oscillator, also called self oscillating loop, is the association of a filter (usually a resonator) and an amplifier with tunable gain and phase interacting in closed loop. The amplifier aims at creating and maintaining oscillations in the filter in order to get a device oscillating, ideally, forever. In the most common way to represent a self oscillating loop, the resonator has the role of the direct chain (open loop transfer function $\underline{H_1}$) and the amplifier and phase shifter the one of the reaction chain (open loop transfer function $\underline{H_2}$), such as depicted on Fig. 24.

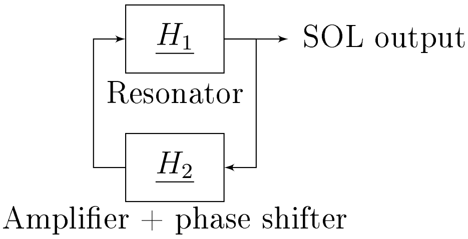

Figure 24: Self oscillating loop schematics

Let's denote $\underline{H} = \underline{H_1} \cdot \underline{H_2}$ the transfer function in closed loop. The system can oscillate at a frequency ω_a if it respects the Barkhausen stability criterion

$$\underline{H}(j \cdot \omega_a) = 1 \tag{29}$$

which is equivalent to

$$\begin{cases} |\underline{H_1}(j \cdot \omega_a)| \cdot |\underline{H_2}(j \cdot \omega_a)| = 1 \\ arg(\underline{H_1}(j \cdot \omega_a)) + arg(\underline{H_2}(j \cdot \omega_a)) \equiv 0 \pmod{2\pi} \end{cases} \tag{30}$$

The operating principle is as follow : the system is slightly put in unstable conditions (gain above 1) to generate the oscillations out of the noise, and is then stabilized either at the limit between stability and unstability (gain equal to 1 by the mean of a variable gain amplifier) or is working at the saturation regime of the system.

Self oscillating loops are used for mass sensing purposes such as in [156]. This configuration allows to easily track the resonant frequency, which is usually the chosen output metric for resonant mass sensors.

II. A. 2. c. ii Phase-locked loop

A phase-locked loop (PLL) usually consists of three functional blocks : phase detector, controller, and voltage-controlled oscillator (VCO). The phase difference between the reference and the output is compared by the phase detector. The phase difference creates an error signal, sent to the controller. From this error signal, the controller calculates the control voltage of the VCO, and the oscillating frequency of the VCO is an affine function of this control voltage in the operating range. Thus, it is possible to track the reference signal in both frequency and phase, thanks to the output of the PLL, such as in [157].

II. A. 3 Resonant mass sensors

II. A. 3. a Operating principle

The previously presented models enable the understanding and design of resonant mass sensors. Indeed a mass addition down-shifts the resonant frequency, which measurement allows to calculate this change in mass. Thus in 1986, a first ultra precise resonant sensor appeared for vapor detection [158]. Since frequency *resolution* is usually very good, this technique allows to reach reasonably low LOD. Therefore until today, most of the mechanical resonant mass sensors use this RtF down shift as a readout [159, 160]. The typical frequency responses of a resonant mass sensor are depicted on Fig. 25.

The sensitivity of resonant mass sensors measuring the shift of RtF generated by the additional inertia of the analyte deposition is [161]

$$\frac{\delta f_r}{\delta m} = \frac{1}{2} \cdot \frac{f_r}{m} \tag{31}$$

Scaling down the mechanical structures diminishes their mass and increases their RtF, which increases their sensitivities. Thus, the two last decades saw the emergence of NEMS resonant mass sensors [162–165].

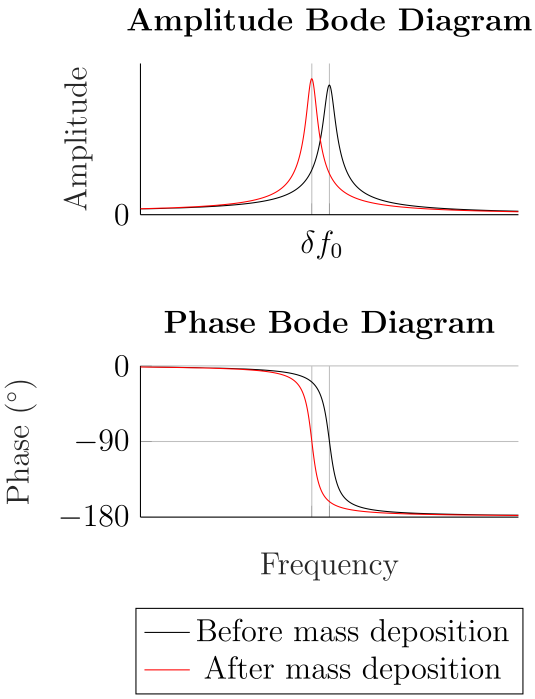

Figure 25: Frequency shift of a mechanical resonator due to a mass load

II. A. 3. b Limitations of single resonators

Even though mass sensors based on RtF shift are known to yield low LOD, they have a fixed *normalized sensitivity* (NS) of one half (Eq. 31). Thus the only way to lower the LOD even more is to reduce frequency fluctuations (jitter), which is a real challenge. Another way to lower the LOD could lay in the choice of the output metric. Rather than frequency based measurements, the last decade saw the emergence of a new mass sensing principle based on resonance amplitude shift in an array of weakly coupled resonators. The phenomenon used in that kind of sensors is called *mode localization*, and is known to yield very high sensitivities (a few order of magnitude higher), depending on a set of parameters. Of course, the gain in sensitivity is not enough to evaluate the gain of this method over RtF shift, since the noise levels are different, but it is worth to be investigated.

II. B State of the art on mode localized based sensors

The present section is firstly introducing the Anderson ML in an array of weakly coupled resonators (WCR). This phenomenon indeed yields much higher sensitivity to mass perturbation than the classic frequency shift based method for small amount of analyte. The different developments and devices based on ML found in the literature are then exposed and classified by the nature of their coupling.

II. B. 1 Introduction to mode localization

II. B. 1. a From Anderson localization to mode localization in coupled resonators

The American physicist Philip Warren Anderson was the first one to describe in 1958 the absence of wave diffusion in a disordered medium, leading to their geometric localization [166]. Initially presented to describe electron localization (in a semiconductor containing impurities that trap the waves for instance), this theoretical work points out a phenomenon that can actually be extended to many fields of physics, such as acoustic waves [167–170].

As an illustration, let's consider the case described in Annex 1 : two coupled mechanical resonators. The system has two modes of different frequencies, and each of them is characterized by specific relative displacements of the resonators described by the eigenvectors. In such a coupled system, a mode corresponds to natural vibrations of the system. They are standing waves that are the sum of waves propagating back an forth between the resonators. In the case of a balanced two degrees of freedom (DOF) undamped resonators system, the energy of each mode is equally distributed on each resonator. Anderson localization (here called ML), happens when a perturbation occurs in the undamped resonators system, such as a stiffness or mass variation on one of the resonators. Such a disorder hinders the waves propagation, leading to their geometric localization : the energy of each mode gets trapped by one of the resonators. This phenomenon is known to be stronger when the eigenfrequencies are close (i.e. when the coupling spring k_c is weak).

ML is illustrated on Fig. 26, depicting the two first modes of two coupled cantilevers, where the first cantilever (on the left) is 0.5 % longer than the second one and the coupling is achieved through the overhang. Figures 26c and 26d show a configuration with a relative weak coupling compared with Fig. 26a and Fig. 26b (the cantilevers are separated by a larger distance). We can notice that the in-phase mode gets localized on the first cantilever, and the out-of-phase mode on the second one. Moreover, the modes are more localized when the coupling is weaker (the term ”localized” refers to the relative difference between the displacement of the resonators, represented by the eigenvectors on Fig. 26. The higher this difference is, the more localized the modes are).

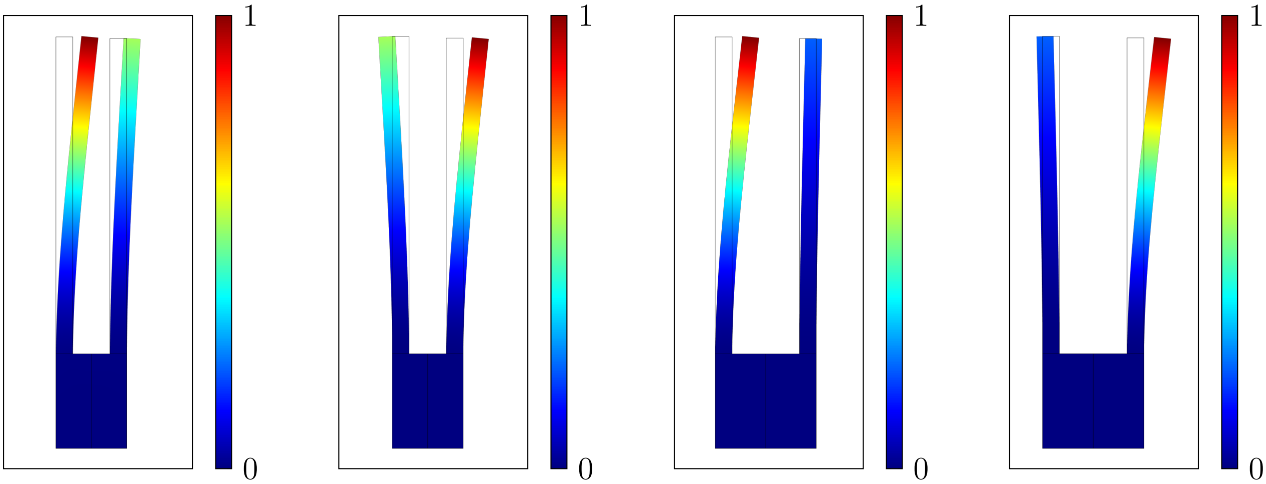

(a) "Strong" coupling, first mode (b) "Strong" coupling, second mode (c) "Weak" coupling, first mode (d) "Weak" coupling, second mode

Figure 26: Eigenstates of two models of 2 DOF coupled cantilevers in two dimensions (Comsol®), where the bottom segment is fixed. The first cantilever (on the left) is 0.5 % longer than the second one. For each simulation, the maximum displacement (normalized to 1) is represented by the red color and the minimum displacement (0) is given by the blue color.

II. B. 1. b Analytical development on a undamped resonators system

Since ML in a weakly coupled undamped resonators system yields high sensitivity to mass perturbation, the exploitation of this phenomenon may be interesting for the design of mass sensors. Therefore in Annex 2 we derived the analytical expressions of the eigenstate variations under slight mass addition in the system, which results are reminded below.

Expressions of the shifts of eigenfrequencies and eigenvectors due to a small mass variation in a N DOF coupled undamped resonators system

$$\begin{cases} \delta\omega_n \simeq -\dfrac{\delta\mu_{n,n}}{2}\cdot\omega_{0n} \\ \delta u_n \simeq -\dfrac{\delta\mu_{n,n}}{2}\cdot u_{0n} + \displaystyle\sum_{p=1,\ p\neq n}^{N} \dfrac{\delta\mu_{p,n}}{\left(\frac{\omega_{0p}}{\omega_{0n}}\right)^2 - 1}\cdot u_{0p} \\ \delta\mu_{i,n} = u_{0i}^T\cdot\delta M\cdot u_{0n} \end{cases} \tag{32}$$

With N the number of DOF and for $n \in \{1..N\}$, ω_{0n}, u_{0n}, $\delta\omega_n$ and δu_n are the n^{th} angular eigenfrequency and eigenvector before the addition of mass, small variation of angular eigenfrequency and eigenvector after the introduction of a mass perturbation in the system, respectively. δM is the diagonal N by N matrix containing the normalized small mass shifts $\frac{\delta m}{m}$.

We can see that the NS of eigenfrequency over mass mismatch $\frac{\delta\omega_n}{\omega_{0n}}\cdot\frac{m}{\delta m}$ is indeed equal to $-\frac{1}{2}$ when $N = 1$, since $u_{01} = 1$ and $\delta\mu_{1,1} = \frac{\delta m}{m}$ in that case. However, when $N > 1$, each modes p also contribute to the n^{th} eigenvector shift for $p \neq n$, and this contribution is indeed stronger when the eigenfrequencies of the p^{th} and n^{th} modes are close to each other.

Let's take the example of a 2 DOF undamped resonators system, which eigenvectors are given in Annex 1. Supposing a mass mismatch $\epsilon = \frac{\delta m}{m}$ on resonator number 1, we get for mode number 1 $(n = 1)$

$$\begin{cases} \delta\mu_{1,1} = \frac{1}{2} \cdot \begin{pmatrix} 1 & 1 \end{pmatrix} \cdot \begin{bmatrix} \epsilon & 0 \\ 0 & 0 \end{bmatrix} \cdot \begin{pmatrix} 1 \\ 1 \end{pmatrix} \\ \delta\mu_{2,1} = \frac{1}{2} \cdot \begin{pmatrix} 1 & -1 \end{pmatrix} \cdot \begin{bmatrix} \epsilon & 0 \\ 0 & 0 \end{bmatrix} \cdot \begin{pmatrix} 1 \\ 1 \end{pmatrix} \end{cases} \tag{33}$$

That is

$$\begin{cases} \delta\mu_{1,1} = \frac{\epsilon}{2} \\ \delta\mu_{2,1} = \frac{\epsilon}{2} \end{cases} \tag{34}$$

The shift of eigenvector number 1 is then

$$\delta u_1 \simeq -\frac{\epsilon}{4} \cdot u_{01} + \frac{1}{2} \cdot \frac{\epsilon}{\left(\frac{\omega_{02}}{\omega_{01}}\right)^2 - 1} \cdot u_{02} \tag{35}$$

According to Annex 1, the previous equation can be expressed as

$$\begin{aligned} \delta u_1 &\simeq -\frac{\epsilon}{4} \cdot u_{01} + \frac{1}{2} \cdot \frac{\epsilon}{\frac{1+2\kappa}{1} - 1} \cdot u_{02} \\ \delta u_1 &\simeq -\frac{\epsilon}{4} \cdot u_{01} + \frac{\epsilon}{4\kappa} \cdot u_{02} \end{aligned} \tag{36}$$

Where $\kappa = \frac{k_c}{k}$ (like in annex 1 and the rest of the present manuscript). Since we consider weak coupling, $\kappa \ll 1$, the previous equation yields

$$\delta u_1 \simeq \frac{\epsilon}{4\kappa} \cdot u_{02} \tag{37}$$

The first eigenvector after mass deposition is then expressed as

$$u_1 \simeq \begin{pmatrix} 1 + \frac{\epsilon}{4\kappa} \\ 1 - \frac{\epsilon}{4\kappa} \end{pmatrix} \tag{38}$$

In a 2 DOF undamped resonators system, the first mode localized on the resonator being perturbed with an additional small mass. The same reasoning can be done for the second mode

$$\begin{aligned} \delta u_2 &\simeq -\frac{\epsilon}{4} \cdot u_{02} + \frac{1}{2} \cdot \frac{\epsilon}{\left(\frac{\omega_{01}}{\omega_{02}}\right)^2 - 1} \cdot u_{01} \\ \delta u_2 &\simeq -\frac{\epsilon}{4\kappa} \cdot u_{01} \end{aligned} \tag{39}$$

The second eigenvector after mass deposition is then expressed as

$$u_2 \simeq \begin{pmatrix} 1 - \frac{\epsilon}{4\kappa} \\ -1 - \frac{\epsilon}{4\kappa} \end{pmatrix} \tag{40}$$

Mode number 2 gets localized on the resonator 2, where there is no mass addition. Obviously the same results are obtained when the mass is added to the second resonator.

Finally, the NS can be written for any mode i as follow for small perturbations $\epsilon \ll 1$

$$\begin{aligned} ns &= \left| \frac{\delta u_i}{u_{0i} \cdot \epsilon} \right| \\ ns &\simeq \frac{1}{4\kappa} \end{aligned} \tag{41}$$

According to this estimation, the lower the coupling is, the higher the NS becomes.

II. B. 1. c Visualization of ML and mode aliasing in a two DOF damped resonators system

Although Eq. 41 yields promising results, it is well known the NS is actually limited because of *mode aliasing*, which occurs when two modes have their eigenfrequencies too close to each other. Indeed, the resonance bandwidth prevents two resonances to occur in a certain range of frequency. In order to avoid two modes to merge, the coupling ratio κ should be high enough compared with the Q-factor Q.

Figure 27 illustrates both ML and mode aliasing. In a 2 DOF damped resonators system, a mass perturbation is added on resonator 1. It can be observed mode i localizes on resonator i, $i \in \{1, 2\}$, and this phenomenon is stronger when the coupling is weaker (the resonance peaks are very close). However, when the coupling is too weak, both resonances merge and ML is not visible anymore.

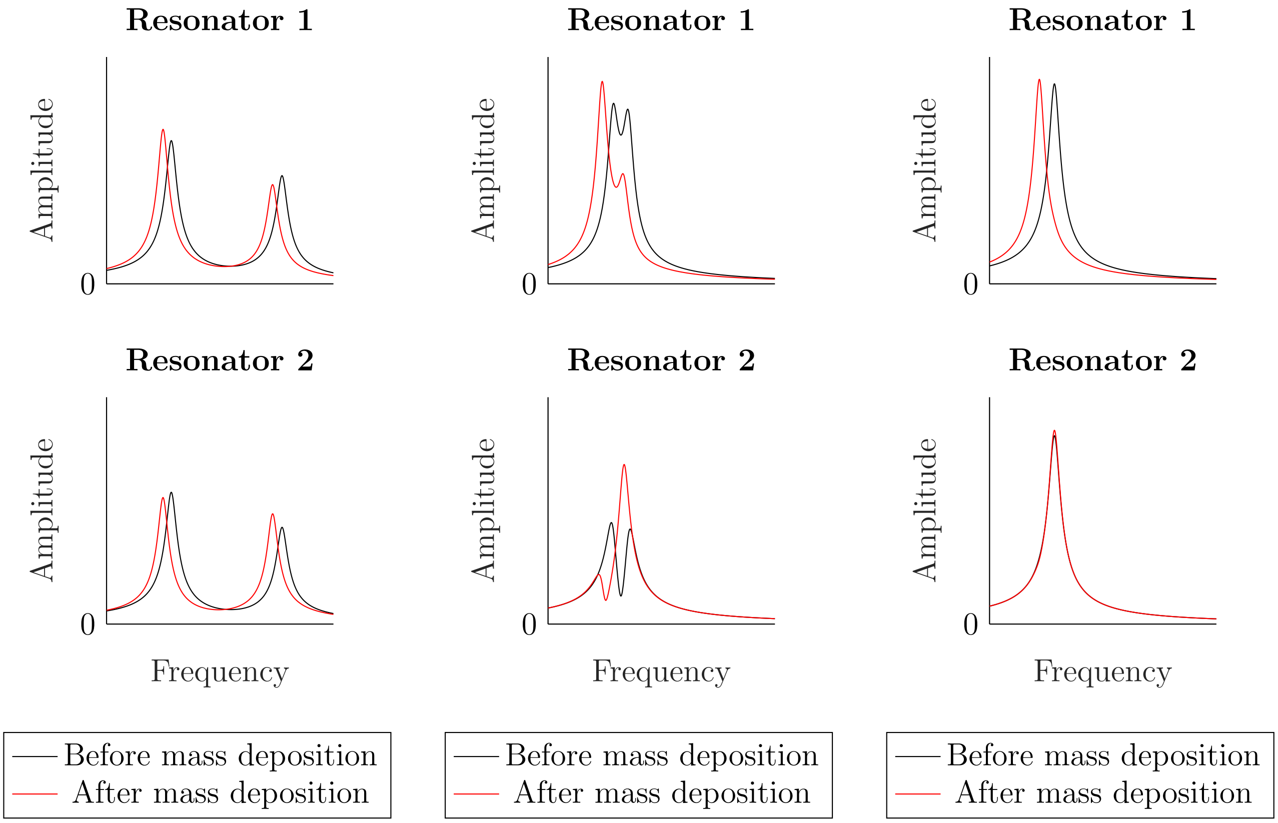

(a) Strong coupling : weak ML (b) Weak coupling : Strong ML (c) Very weak coupling : mode aliasing

Figure 27: Visualization of ML and mode aliasing in a 2 DOF damped resonators system. A mass perturbation is added to resonator 1 for different coupling stiffness, and a phase of −90 degrees is applied on the excitation force of resonator 2, in order to see both modes. The axis are identical for each graphic, but no value is given here since these phenomena may be observed for all order of magnitudes. This figure is only meant to illustrate ML and mode aliasing.

II. B. 1. d Feedback control

As detailed in the next sections, the literature shows that ML has been studied and implemented for sensing applications. Most of such sensors are open loop devices requiring frequency sweep to obtain the resonances amplitude, which is time consuming. Recently however, mode localized sensors started to integrate PLL and oscillator configurations allowing to automatically track the resonant frequency, resulting in a gain of time [171–176].

II. B. 2 Different coupling methods

II. B. 2. a Mechanical coupling

Many research groups have exploited ML to design mechanical resonant sensors, which may be classified according to the coupling nature. The most intuitive way to couple mechanical resonators is to perform a mechanical coupling as well. This method has been implemented for cantilevers and suspended resonators for two or more DOF.

The first work aiming at the design and fabrication of WCR based on Anderson localization for mass sensing purposes is dated of 2006 [177]. The system, depicted on Fig. 28a was made of two gold cantilevers with a coupling overhang fixed on a silicon substrate. The addition of a microsphere at the tip of cantilever 2 leads to mode localization.

The main disadvantage of mechanical resonators is the microfabrication defects that prevent the cantilevers from having the same dimensions and thus identical frequency response. One way to overcome this problem was recently proposed by [178,179], where the cantilevers are resonating with electrostatic actuation. The idea is to fabricate two cantilevers with different lengths and lower the stiffness of the shortest with electrostatic softening effect, as depicted on Fig. 28b. This way, balanced resonators are obtained, a condition favorable to ML.

ML has also been investigated for mass sensing purposes on coupled cantilevers with a higher number of DOF, such as [180–184].

An array of weakly coupled cantilevers using ML can also be used for multiple analyte detection and identification, since the shape of each mode strongly depends on the DOF that is perturbed by the deposition of a mass [185–188]. For instance, Fig. 29 depicts the shape of the 6^{th} mode before and after a microsphere deposition. This technique allows to design single-input single-output sensors : proceeding a frequency sweep in open loop while recording the vibration amplitude of a single cantilever enables to get each mode amplitude on this particular resonator, which is enough to detect on which resonator a mass has been added.

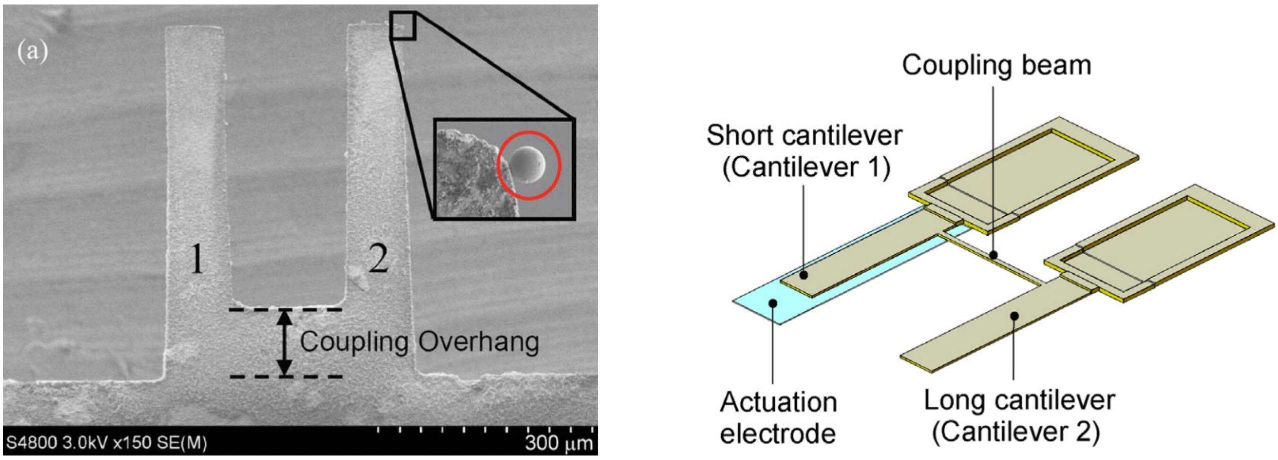

(a) Scanning electromicroscopy image of the coupled gold foil cantilevers / *source : [177]*

(b) Schematics of coupled cantilevers with electrostatic defects compensation / *source : [179]*

Figure 28: Weakly and mechanically coupled pair of cantilevers using ML for mass sensing purposes

Apart from cantilevers, in-plane resonators are also commonly used to implement ML for

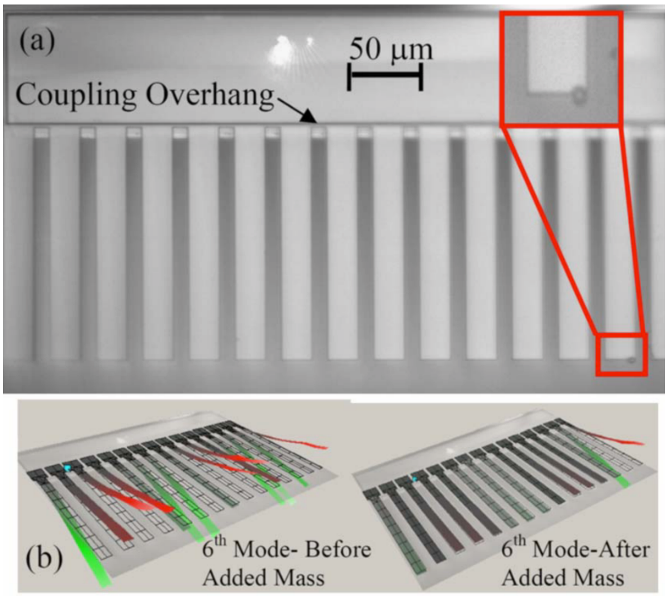

Figure 29: Photograph and schematics of an array of coupled cantilevers for multiple analyte detection / *source : [186]*

sensing applications and are meant to measure either a mass (such as piezoelectric bulk acoustic MEMS resonators [189]) or a stiffness change. Many of them actually measure a stiffness perturbation, because this physical parameter may vary with stress, namely allowing the measure of force [190] or acceleration [191–194]. Since an electric potential difference between an electrode and a resonator generates an electrostatic force and the softening or the hardening of the resonator, a stiffness sensor also allows to measure electric charges, making ML based sensors good candidates for electrometers [195–198]. In [191] for instance, an external acceleration triggers the motion of a *proof mass* which modifies the gaps between itself and the suspended resonators of a 3 DOF WCR system (Fig. 30), which generates a stiffness mismatch between the resonators leading to ML.

The change in stiffness caused by an external phenomenon can also be used to design hair flow sensors [199]. In the latter, an artificial hair perpendicular to a frame bends according to the surrounding fluid flow. This bending generates strain of the support beams of the in-plane resonators located in the frame, which results again in a stiffness shift (Fig. 31).

Such in-plane resonators may be tuning forks such as in [200–202] which measure a shift in the stiffness of one resonator by the mean of ML. This stiffness perturbation can be introduced using additional strain by electrostatic actuation either from the side [201, 202] or in the axis of the tuning fork [200], as depicted on Fig. 32.

A summary of mechanically coupled WCR for ML implementation is available on Table 2.

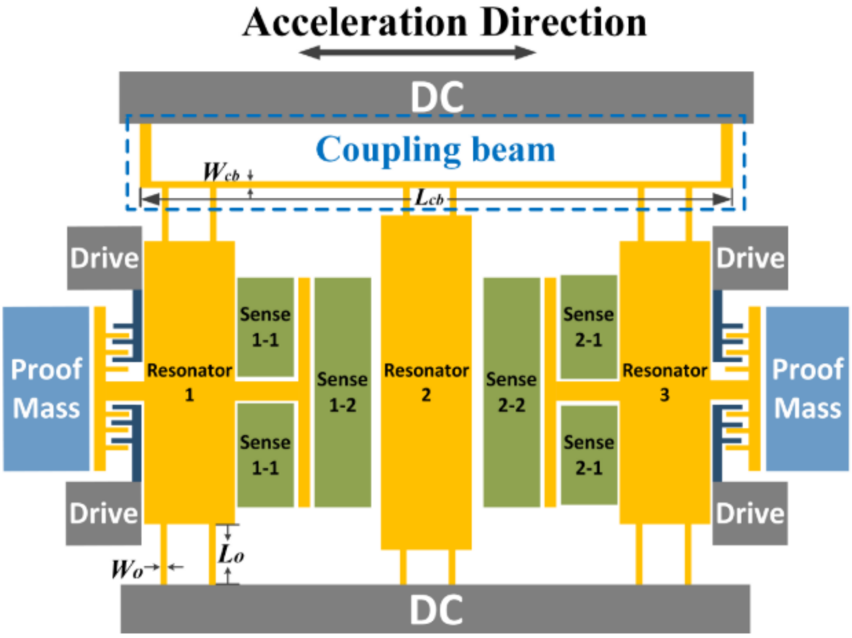

Figure 30: Schematics a 3 DOF accelerometer using ML / *source : [191]*

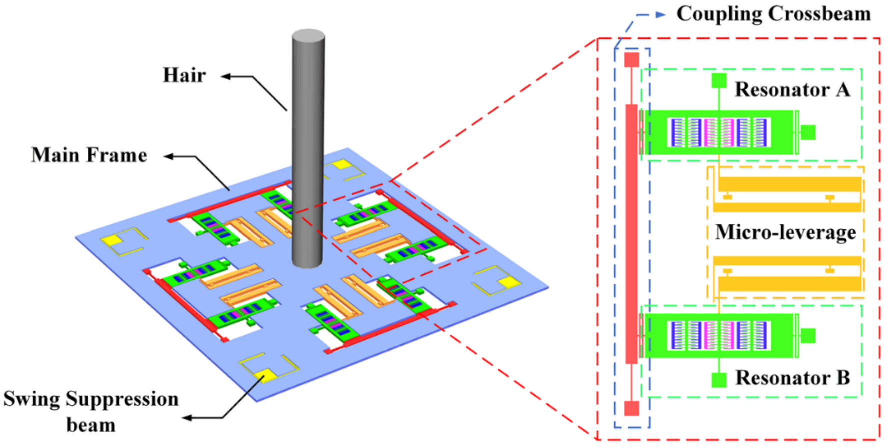

Figure 31: Schematics of a hair flow sensor using ML / *source : [199]*

II. B. 2. b Electrostatic coupling

The main disadvantage of mechanical coupling is the fact its value is fixed. Because of microfabrication defects and the fragility of such structures, the designed coupling is often too stiff, thus limiting the sensor sensitivity.

One way to overcome this limitation is to design a tunable coupling of a different physical nature, such as the electrostatic coupling. Initially presented for coupled MEMS bandpass filters [204], this method has been adapted to in-plane resonators for ML based devices. The application of a potential difference ΔV on two consecutive resonators generates a coupling stiffness k_c between

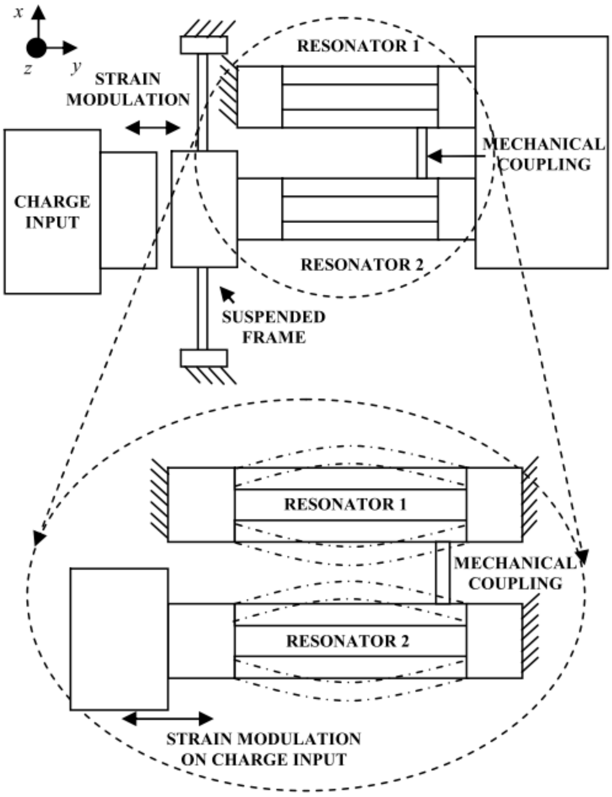

Figure 32: Schematics of two mechanically coupled tuning forks with a tunable stiffness (electrometer) / *source : [200]*

Table 2: Classification of mechanically coupled resonators using ML found in the literature

Application	**2 DOF**	**3 DOF**	**4 DOF**	**> 10 DOF**
Mass identification		[187]	[185]	[186, 188]
Mass sensor	[177–179]	[181–184]	[180]	
Electrometer (stiffness)	[197, 198, 200]	[195, 196]		
Force sensor (stiffness)		[190]		
Accelerometer (stiffness)	[192–194]	[191]	[203]	
Flow sensor (stiffness)	[199]			
Stiffness sensor	[201, 202]			

them that can be expressed as follow [205]

$$k_c = -\Delta V^2 \cdot \frac{\epsilon_0 \cdot A}{g^3} \tag{42}$$

where ϵ_0, A and g are the permittivity of free space, the area of the cross section of the parallel plates in-between the two resonators and the coupling gap, respectively.

Different prototypes of stiffness sensors have been presented in the literature. A few of them are mass sensors [206, 207], but most of them are meant to detect another physical quantity by the mean of stiffness variation (like for mechanically coupled WCR sensors). For instance, the stiffness of a resonator can be modulated with a variable gap such as the distance between the resonator and a proof mass. The measure of the generated stiffness mismatch by the mean of ML thus allows to calculate the displacement of the proof mass such as in the case of a displacement sensor [208] (Fig. 33a). Following the same principle, many WCR sensors have been designed with tunable coupling, such as force sensors [209,210], a pressure sensor [211] and an electrometer [212]. In addition, many stiffness sensors have been set up [213–218]. A first 4 DOF accelerometer using both mechanical and electrostatic coupling have also been presented [219].

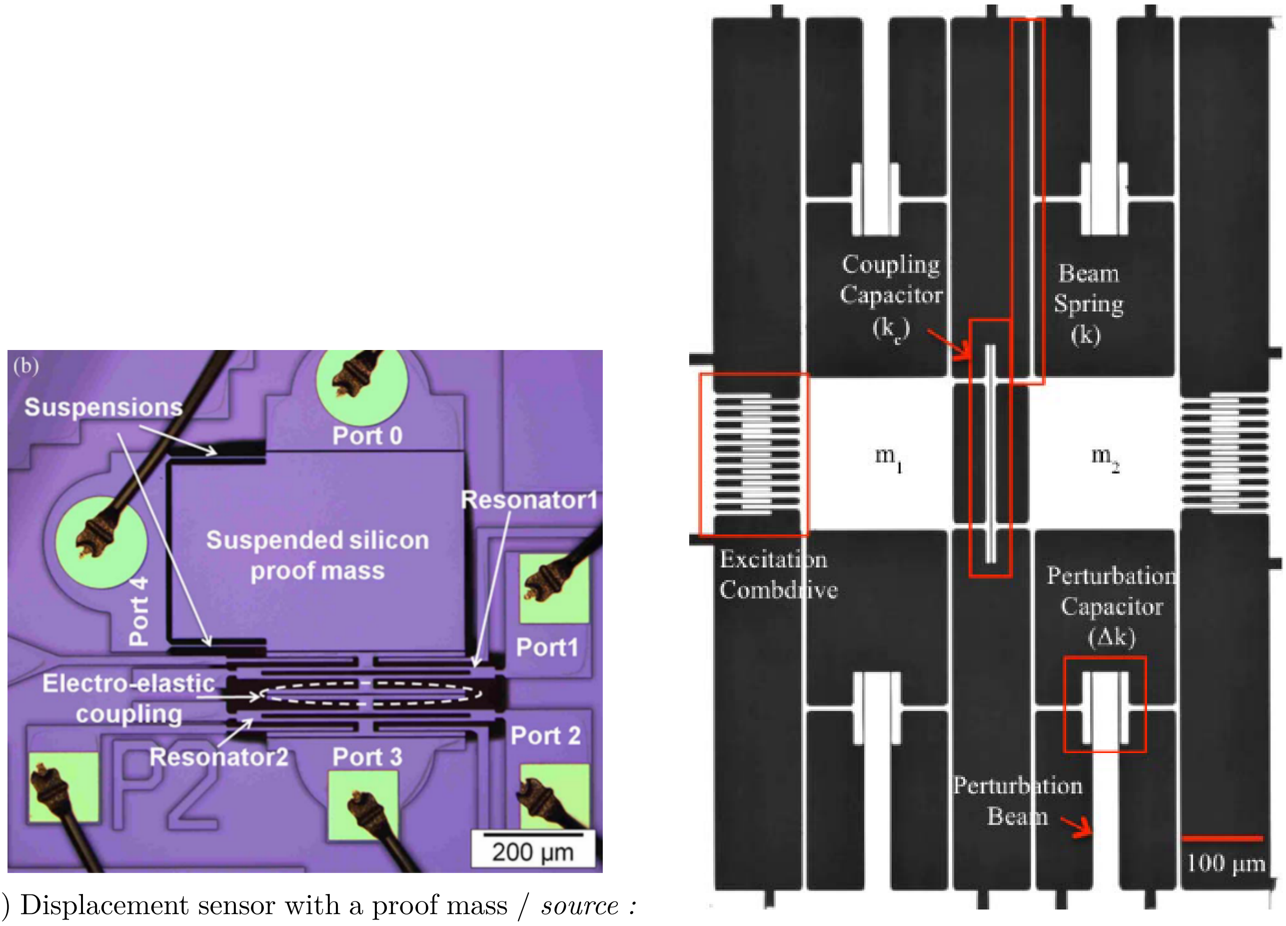

(a) Displacement sensor with a proof mass / *source : [208]*

(b) Stiffness sensor / *source : [217]*

Figure 33: Optical micrographs of two 2-DOF WCR with electrostatic coupling

The major disadvantage of electrostatic coupling over mechanical coupling is the difficulty to work in liquid environment due to Faradaic currents. One solution, proposed in [220], would be to use the output signal of a QCM on which is fixed the analyte present in a liquid to generate a variable electrostatic force being the stiffness perturbation for an external WCR working in vacuum.

A summary of WCR with electrostatic coupling based on ML is given in Table 3.

Table 3: Classification of resonators using ML coupled with electrostatic force found in the literature

Application	2 DOF	3 DOF	4 DOF
Mass sensor	[206]	[207, 220]	
Electrometer (stiffness)		[212]	
Force sensor (stiffness)		[209, 210]	
Pressure sensor (stiffness)		[211]	
Accelerometer (stiffness)			[203, 219]
Displacement sensor (stiffness)	[208]		
Stiffness sensor	[205, 215–217]	[213, 214, 218]	

II. C Mode localization capabilities

The purpose of this section is to estimate the gain of ML over classic methods. In this section, an undamped resonator corresponds to a mass/spring system, or an inductance/capacitance system. In contrast, a damped resonator describes a mass/spring/viscous damper system, or its electrical equivalent the inductance/capacitance/resistance series (RLC) system.

II. C. 1 Optimal configuration of a 2 DOF damped resonators system

II. C. 1. a Amplitude shift at the resonance

II. C. 1. a. i Analytic resolution

Equation 41 gives the NS of a 2 DOF undamped resonators system. This expression shows the NS is in inverse proportion with κ. However, the two modes become indistinguishable when the coupling is too weak (mode aliasing). Therefore, an anti aliasing condition must be satisfied to avoid this limitation. Such a condition can be set using the modes bandwidth such as [218]

$$\begin{aligned} \omega_{02} - \omega_{01} &\geqslant \gamma \cdot \Delta\omega_{-3dB} \\ \frac{\omega_{02}}{\omega_{01}} &\geqslant 1 + \gamma \cdot \frac{\Delta\omega_{-3dB}}{\omega_{01}} \end{aligned} \tag{43}$$

where ω_{01} and ω_{02} are the angular eigenfrequencies of the in-phase and out-of-phase modes, respectively, γ an anti aliasing coefficient which value could be set around 1 or 2 (mode aliasing slightly depending on the phases of the excitation forces, as shown in section II. C) and $\Delta\omega_{-3dB}$ the bandwidth at $-3\,\mathrm{dB}$.

Using the expression of Q, the previous equation becomes

$$\left(\frac{\omega_{02}}{\omega_{01}}\right)^2 \geqslant \left(1 + \frac{\gamma}{Q}\right)^2 \tag{44}$$

Considering only high Q-factors, we only keep the first order. The minimum anti aliasing condition is then defined as follow

$$\left(\frac{\omega_{02}}{\omega_{01}}\right)^2 - 1 \simeq \frac{2\gamma}{Q} \tag{45}$$

Replacing Eq. 45 in Eq. 35 yields

$$\delta u_1 \simeq -\frac{\epsilon}{4} \cdot u_{01} + \frac{\epsilon \cdot Q}{4\gamma} \cdot u_{02} \tag{46}$$

Following the previous steps, the maximum NS achievable is thus defined as

$$ns_{max} \simeq \frac{Q}{4\gamma} \tag{47}$$

II. C. 1. a. ii Simulations

The calculated NS in Eq. 41 and Eq. 47 have been established for a undamped resonators system in the former, and a undamped resonators system with an anti aliasing condition for the latter. We here compute the NS for a 2 DOF, taking losses into account. Therefore, the equations presented in Annex 3 have been computed in Matlab®for two coupled damped resonators, with the following transfer functions

$$\begin{cases} H_1 = \dfrac{1}{(1+\epsilon)\cdot s^2 + \frac{1}{Q}\cdot s + 1} \\ H_2 = \dfrac{1}{s^2 + \frac{1}{Q}\cdot s + 1} \end{cases} \tag{48}$$

Figure 34 depicts the typical amplitude Bode diagrams of a 2 DOF coupled damped resonators with high Q-factors and a set of mass perturbations, with two different excitation phases. It can be seen a phase of 90 degrees allows to observe both modes and a phase of 180 degrees only the out-of-phase mode (in the same way, only the in-phase mode gets excited for a phase equal to zero). Moreover on Fig. 34a, the first mode gets localized on the first resonator, where the mass perturbation occurs and this mode appears also on resonator 1 on Fig. 34b when the mismatch increases. The amplitude shifts are very similar in both cases and it is assumed that the maximum NS should not depend on the excitation phase for small perturbations and weak coupling.

We now plot the NS for a range of coupling κ and mass perturbation ϵ, for each mode i and resonator j. Each mode of each resonator is tracked to calculate this NS, following its definition

$$ns(i,j,Q,\kappa,\epsilon) = \frac{1}{x_{r,\epsilon=0,\kappa=0}(Q)} \cdot \frac{\partial x_r}{\partial \epsilon}(i,j,Q,\kappa,\epsilon) \tag{49}$$

where $x_{r,\epsilon=0,\kappa=0}$ and x_r are the resonance amplitudes before mass perturbation and without coupling, and after mass perturbation, respectively.

Figure 36 depicts the NS of a 2 DOF damped resonators system where both resonators are excited, with a phase of -90 degrees on the second resonator. The first observation is that these sensitivities, perturbations and couplings are linked by the Q-factor. Indeed, the same graphs are obtained for different scales, as long as $Q \gg 1$. The second observation is the presence of mode aliasing that indeed prevents the sensitivity to skyrocket. This phenomenon does not appear exactly at the same coupling value (because the phase of 90 degrees make the modes of resonator 1 slightly closer to each other than for resonator 2). The value of γ is then between 0.5 and 1, depending on the resonator. In order to get an order of magnitude of the sensitivity, γ is set to one, and the maximum sensitivity is then $|ns_{max}| = \frac{Q}{4}$ (Eq. 47). This value is reached in the simulation but rather for $\gamma = 0.5$. Indeed, the calculated eigenvector shift in Annex 2 is actually

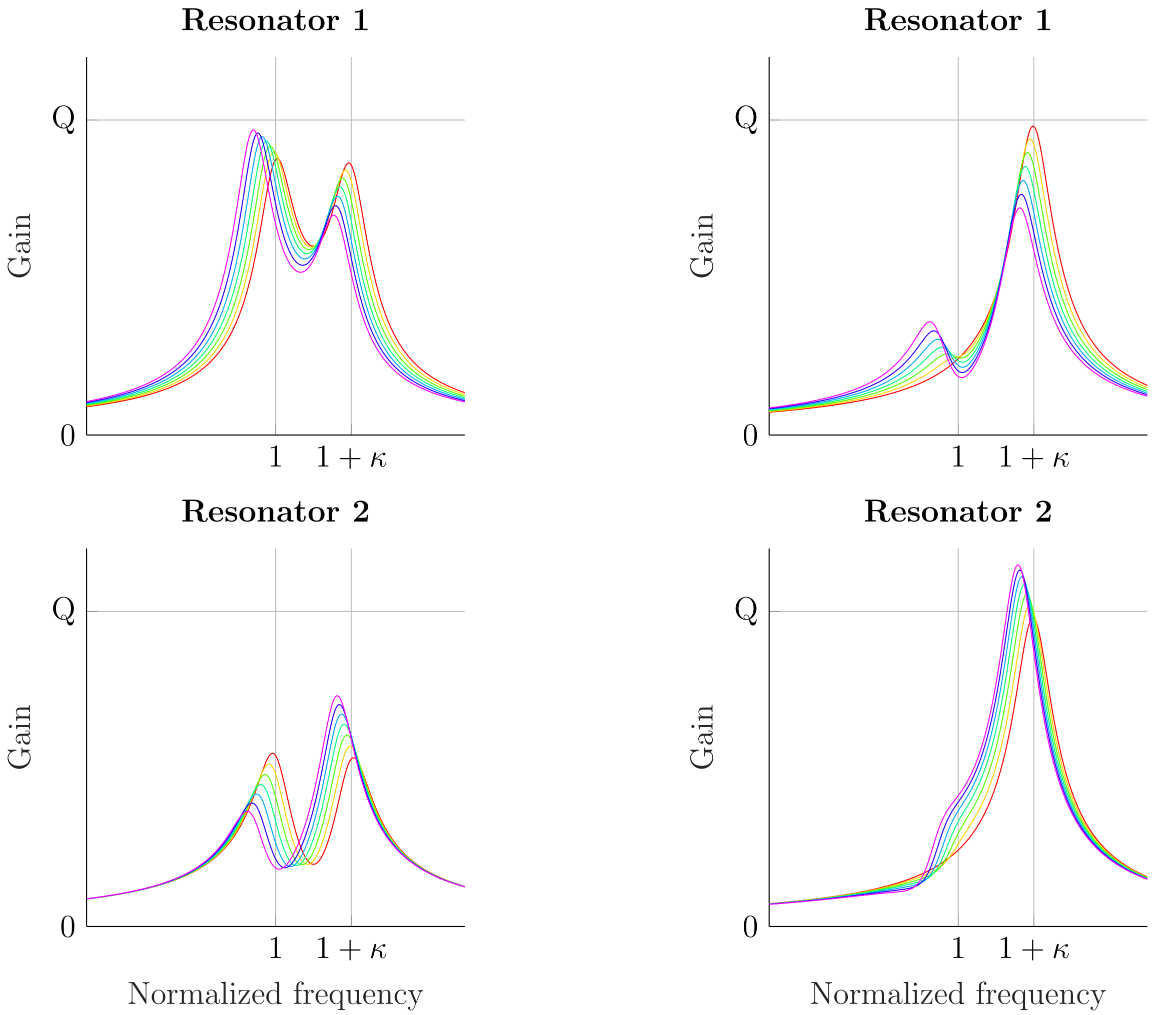

(a) Excitation phase of $\frac{\pi}{2}$ on resonator 2

(b) Excitation phase of π on resonator 2

Figure 34: Dimensionless amplitude Bode diagrams of a 2 DOF coupled damped resonators. The red curves correspond to the case $\epsilon = 0$. ϵ increases for each other curve following the rainbow colors, until a maximum perturbation of $\epsilon = \frac{2}{Q}$. In this example, $\kappa = \frac{2}{Q}$.

a little too optimist because it concerns the undamped resonators system : the NS involved are smaller in reality. Finally, it can be observed the NS decreases rapidly when either κ or ϵ increase.

Comment : The cases with an excitation phase of 0 or 180 degrees yield similar results in terms of maximum NS, mode aliasing and *sensitive range*. In the rest of the thesis, a phase of 90 degrees will always be applied in order to observe both modes and carry out data processing on each mode.

II. C. 1. b Resonant frequency shift

The result given in Annex 2 gives the expression of the eigenfrequency shift of a N DOF undamped resonators system. From this equation can be directly deduced the NS for the eigenfrequency shift following its definition

$$ns = \frac{\partial \omega_r}{\omega_r \cdot \partial \epsilon} \tag{50}$$

The NS is equal to one half for a single undamped resonator ($\delta\mu_{1,1} = \epsilon$), and one fourth for a 2 DOF one ($\delta\mu_{1,1} = \delta\mu_{2,2} = \frac{\epsilon}{2}$). According to this estimation, ML does not come up with a higher NS on the RtF shift. This result has been confirmed with Matlab®simulations as well for the damped resonators system. Figure 37 depicts the NS of the RtF shift for both modes and both resonators. In particular, the first mode of the first resonator yields the results mentioned above for $\kappa = 0$ and $\epsilon > 0$ on the one hand, and $\epsilon = 0$ and $\kappa > \frac{1}{Q}$ on the other hand.

II. C. 1. c Amplitude shift at fixed frequency

In this section is evaluated the amplitude shift NS firstly at the frequency of the unperturbed resonances ($\epsilon = 0$) of each mode, and secondly at a frequency slightly lower.

II. C. 1. c. i Analytic resolution

The transfer function of a damped resonator with a slight mass perturbation $\epsilon = \frac{\delta m}{m} \ll 1$ is

$$H(s) = \frac{1}{(1+\epsilon) \cdot s^2 + \frac{1}{Q} \cdot s + 1} \tag{51}$$

Let's set $\omega = \omega_0$ ($s = j$)

$$\begin{aligned} X &= |H(s=j)| \\ X &= \frac{1}{\sqrt{\left(-(1+\epsilon)+1\right)^2 + \frac{1}{Q^2}}} \\ X &= \frac{Q}{\sqrt{1+\epsilon^2 \cdot Q^2}} \end{aligned} \tag{52}$$

Now we derive with respect to ϵ

$$\frac{\partial X}{\partial \epsilon} = \frac{-Q^3 \cdot \epsilon}{(1+\epsilon^2 \cdot Q^2)^{\frac{3}{2}}} \tag{53}$$

The NS is then

$$\begin{aligned} ns &= \frac{\partial X}{\partial \epsilon \cdot X_{\epsilon=0}} \\ ns &= \frac{-Q^2 \cdot \epsilon}{(1+\epsilon^2 \cdot Q^2)^{\frac{3}{2}}} \end{aligned} \tag{54}$$

In order to simplify the calculations, the NS will rather have the following definition

$$\begin{aligned} ns &= \frac{\partial X}{\partial \epsilon \cdot X} \\ ns &= \frac{-Q^2 \cdot \epsilon}{1+\epsilon^2 \cdot Q^2} \end{aligned} \tag{55}$$

which is a little overestimation since the amplitude reference becomes smaller when the RtF is different from the excitation frequency. However, this drift is negligible for $\epsilon \ll 1$.

ns is then a negative function of ϵ which tends towards 0 when ϵ tends to 0, and also tends to 0 when ϵ tends to infinity. Therefore, ns has a maximum absolute value we wish to find. To this purpose, let's now derive ns in respect to ϵ

$$\frac{\partial ns}{\partial \epsilon} = \frac{-Q^2 \cdot (1+\epsilon^2 \cdot Q^2) + 2\epsilon^2 \cdot Q^4}{(1+\epsilon^2 \cdot Q^2)^2} \tag{56}$$

We now solve the equation

$$\begin{aligned} &\frac{\partial ns}{\partial \epsilon} = 0 \Leftrightarrow -Q^2 \cdot (1+\epsilon^2 \cdot Q^2) + 2\epsilon^2 \cdot Q^4 = 0 \\ &\frac{\partial ns}{\partial \epsilon} = 0 \Leftrightarrow \epsilon^2 \cdot Q^2 = 1 \\ &\frac{\partial ns}{\partial \epsilon} = 0 \Leftrightarrow \epsilon = \frac{1}{Q} \end{aligned} \tag{57}$$

We then obtain the maximum absolute value of the NS, using Eq. 54

$$ns_{max} \simeq |-0.35 \times Q| \tag{58}$$

This calculated NS is actually slightly higher than the maximum NS calculated previously for a 2 DOF damped resonators system using ML (Eq. 47), meaning there is apparently no NS gain in a 2 DOF WCR system.

For small perturbations, the amplitude shift is negligible with respect to the resonance amplitude for a single resonator. However, the RtF shift is not negligible with respect to the filter bandwidth for high Q-factors. Therefore, this signal decrease corresponds almost only to the resonance shift towards lower frequencies as depicted on Fig. 42a.

We can calculate the corresponding frequency shift using the NS of one half as follow

$$\frac{f_{01} - f_{00}}{f_{00}} \cdot \frac{1}{\epsilon} = -\frac{1}{2} \tag{59}$$

Where f_{00} and f_{01} are the RtF before and after mass deposition, respectively.

We then have

$$f_{01} = f_{00} \cdot \left(1 - \frac{1}{2Q}\right) \tag{60}$$

It could be considered to exploit both phenomena at the same time. If the mass perturbation occurs on the first resonator of a 2 DOF damped resonators system, exciting the structure at f_{01} indeed enable to see an increase of signal due to the localization of the first mode on the first resonator and the amplitude increase due to a frequency downshift.

II. C. 1. c. ii Simulations

The NS of amplitude shift at the fixed frequencies f_{00} (Fig. 38) and f_{01} (Fig. 39) have been computed with Matlab®for the damped resonators system where is applied a phase of -90 degrees on the excitation of resonator 2. These simulations yield the expected results from the analytic resolution. In particular, one can observe the first mode of the first resonator without coupling (the case of a single resonator). On Fig. 38, the NS is close to zero for $\epsilon = 0$, and is close to $-0.35 \times Q$ for $\epsilon = \frac{1}{Q}$ (as an illustration, Fig. 42a depicts the Bode diagrams of a single resonator subjected to a mass perturbation, along with the two frequencies f_{00} ($r = 1$) and f_{01} ($r = 1 - \frac{1}{2Q}$)). On Fig. 39, the amplitude firstly increases until $\epsilon = \frac{1}{Q}$ before decreasing, and reaches the same maximum NS absolute value, as expected.

Both figures show that mode aliasing occurs on both resonators for $\kappa < \frac{0.3}{Q}$. For a coupling value above $\frac{0.3}{Q}$, the perturbation ϵ to which the NS sign changes (so when the resonance is reached) doubles on Fig. 39 and reach $\epsilon = \frac{2}{Q}$ since the RtF decreases with a NS twice lower because of the coupling ($\frac{1}{4}$ instead of $\frac{1}{2}$). As a consequence, the amplitude gain due to the RtF downshift decreases by half as well when there is no mode aliasing, which is balanced by the effect of ML.

As a conclusion, it can be stated the maximum amplitude shift NS at a fixed frequency of a single resonator is almost the same than that from a 2 DOF WCR system, which is a significant result as for the high sensitivity of ML. However, the sensitive range of such a system at one DOF is lower than the one from mode localized based systems (around $\frac{1}{Q}$ and $\frac{2}{Q}$, respectively).

II. C. 1. d Phase shift at fixed frequency

II. C. 1. d. i Analytic resolution

The transfer function of a damped resonator with a slight mass perturbation (Eq. 51) allows to calculate the phase between the resonator displacement and its excitation force.

Denoting $s = j \cdot r$, its phase ϕ is then expressed as

$$\begin{aligned} \phi &= -\arctan\left(\frac{r}{Q \cdot (1 - r^2 \cdot (1+\epsilon))}\right) \\ \phi(r=1) &= \arctan\left(\frac{1}{Q \cdot \epsilon}\right) \end{aligned} \tag{61}$$

We now define the phase shift NS to be

$$ns = \frac{\partial \phi(r=1)}{\pi \cdot \partial \epsilon} \tag{62}$$

π being the reference phase. We now obtain

$$\begin{aligned} ns &= -\frac{Q}{\pi \cdot \epsilon^2 \cdot Q^2} \cdot \frac{1}{1 + \frac{1}{\epsilon^2 \cdot Q^2}} \\ ns &= -\frac{Q}{\pi \cdot (\epsilon^2 \cdot Q^2 + 1)} \end{aligned} \tag{63}$$

For $\epsilon = 0$, we thus obtain $ns = -\frac{Q}{\pi}$.

Knowing the NS of the RtF shift decreases with the coupling for $\epsilon = 0$, the phase shift at fixed frequency should also do so.

II. C. 1. d. ii Simulations

Once more, simulations have been done using Matlab®on the damped resonators system in order to evaluate the NS for the phase shift at $r = 1$, following its definition in Eq. 62. A phase of -90 degrees is still applied on resonator 2. Firstly, it can be observed on Fig. 40 that the NS is indeed equal to $-\frac{Q}{\pi}$ for $\kappa = 0$ and $\epsilon = 0$ (mode 1, resonator 1), as predicted by the analytic resolution. This NS value is indeed the highest for $\epsilon = 0$. More interestingly, we can observe a much higher sensitivity on the first mode of the second resonator for $\kappa = \frac{1}{Q}$ and $\epsilon = \frac{3}{2Q}$. This particular case is depicted on Fig. 42b. This strong phase shift corresponds to a minimum of amplitude between the two modes, which is thus not really exploitable since the signal to noise ratio (SNR) is extremely low in this region. Such an anti resonance appears on each excited resonator, and may be have its frequency located either between the resonances or outside them, depending on the sign of the perturbation. This phenomenon has already been described in [202] in WCR using ML.

As a conclusion, WCRs do not yield higher phase shift NS in comparison with a single resonator.

II. C. 1. e Amplitude ratio

II. C. 1. e. i Analytic resolution

It is stated in the literature [5, 175, 198, 213, 214, 218, 221–223] that the shift of resonance amplitude ratio between two resonators for a specific mode is more sensitive than the relative resonance amplitude shift for a single resonator.

We here show this result through the example of the 2 DOF undamped resonators system. However one man should keep in mind that a gain in sensitivity should always be considered in pair with the gain or loss in resolution.

Let's consider a 2 DOF damped resonators system which is excited at the frequency of the first mode. We first denote x_0, x_1, and x_2 the amplitudes of both resonators before the mass deposition, the ones of resonator 1 and 2 after the mass deposition, respectively.

If the perturbation occurs on resonator 1, the following equations can be written

$$\begin{cases} x_1 = x_0 \cdot (1 + ns_1 \cdot \epsilon) \\ x_2 = x_0 \cdot (1 - ns_1 \cdot \epsilon) \end{cases} \tag{64}$$

Where ns_1 is the NS of the resonance amplitude shift (equal to $\frac{Q}{4}$ in the optimal case of a 2 DOF damped resonators system). Let's now denote ns_2 the NS of the amplitude ratio $\frac{x_1}{x_2}$, thus written as

$$ns_2 = \frac{\partial \frac{x_1}{x_2}}{\partial \epsilon} \tag{65}$$

Replacing by the expressions of x_1 and x_2, the previous equation yields

$$ns_2 = \frac{ns_1 \cdot (1 - ns_1 \cdot \epsilon) + ns_1 \cdot (1 + ns_1 \cdot \epsilon)}{1 - 2\epsilon \cdot ns_1 + \epsilon^2 \cdot ns_1^2} \tag{66}$$

And for $\epsilon = 0$ we have

$$ns_2 = 2ns_1 \tag{67}$$

This result is consistent with those presented in the literature ($ns_2 = \frac{1}{2\kappa}$ [222], $ns_1 = \frac{1}{4\kappa}$ [4]).

We now consider the measure uncertainty Δx identical for both resonators.

The absolute uncertainty of $x_1 - x_0$ is then equal to $2\Delta x$. Considering $x_1 \simeq x_0$, the relative uncertainty of the relative amplitude shift equals $\frac{2\Delta x}{x_0}$. Concerning the amplitude ratio shift, the relative uncertainties may be directly added, yielding also $\frac{2\Delta x}{x_0}$, as confirmed in [198]. The resolution is thus identical for both methods for small perturbations. This reasoning also gives an estimation on the maximum NS reachable with amplitude ratio : $ns_{max} = \frac{Q}{2\gamma}$. The amplitude ratio based measures should thus enable to measure perturbations twice smaller than the relative amplitude shift close to $\epsilon = 0$ (a NS twice higher with the same resolution). However we here supposed that both resonators have initially the same amplitude and that the NS of resonance amplitude shift is identical for both resonators, which may not be true since both of these hypothesis depend on the excitation phase (and, for the second one, on the aliasing condition).

Comment : Another method to determine the NS of amplitude ratio was proposed by [5] directly based on the equations of movement. In this case, the perturbation is on the stiffness and on resonator 2, but this yields the same ML behavior. The expression of this NS is, for $\epsilon = 0$

$$ns = \frac{Q}{\sqrt{1 + Q^2 \cdot \kappa^2}} \tag{68}$$

which, for the anti aliasing condition $\kappa = \frac{1}{Q}$ ($\gamma = 1$), rather yields $ns = \frac{Q}{\sqrt{2}}$.

II. C. 1. e. ii Simulations

Different amplitude ratio NS has been computed on Matlab®and plot on Fig. 41, where a phase of −90 degrees is still applied on resonator 2. The NS can be calculated either using the ratio of the amplitude of resonator 1 over that of resonator 2, or the other way round. It can be seen the maximum NS is indeed higher (Q), and the sensitive range is much larger than in the case of simple amplitude shift. The NS is still non linear with ϵ, as described in the literature [209, 214, 221].

II. C. 1. e. iii Other developments based on amplitude ratio

Figure 35 depicts a method presented in [209] allowing to get rid of mode aliasing while guaranteeing high sensitivity. The idea it to initially unbalance the resonators by setting a fixed stiffness shift ΔK around which a small stiffness perturbation can be measured with high and linear sensitivity. This method was also implemented in [172].

Comment : One should also minds the fact that when ϵ increases, the signal at the denominator is getting quite low, so as its SNR (this ratio being close to ϵ/κ [5]). Therefore, even though the resolution of amplitude ratio is the same than resonance amplitude shift close to $\epsilon = 0$ (as shown previously), it is not the case anymore for higher ϵ values (as pointed out in [5]). The LOD of may then be higher, despite the high sensitivity.

Besides, a way to improve the linear range was proposed in [224], using the sum of amplitude ratios of both modes. This method is nonetheless quite time consuming since it requires frequency searching over a certain range in order to measure the amplitude of both modes.

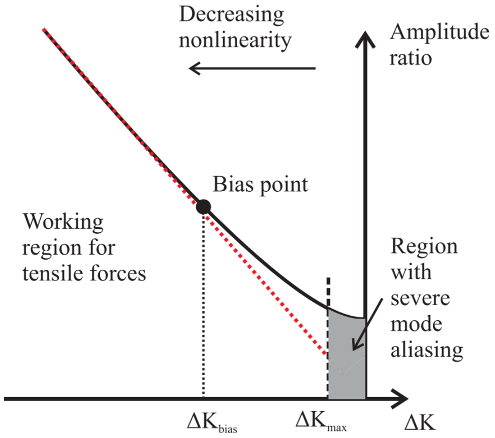

Figure 35: Stiffness sensor with a perturbation offset allowing to get out of mode aliasing *source : [209]*

II. C. 2 Reflections on the mass sensitivity of a 3 DOF damped resonators system

II. C. 2. a Array of identical resonators

Based on the results given in Annex 2, we can estimate the maximum NS gain achievable with more than 2 DOF.

Such a condition is reached when the frequencies of the different modes are close while respecting the anti aliasing condition

$$\omega_{0p} - \omega_{0n} \geqslant \gamma \cdot \Delta\omega_{-3dB} \tag{69}$$

where ω_{0n} and ω_{0p} are the angular eigenfrequencies of two consecutive modes.

Assuming now the existence of a N DOF WCR system where two consecutive modes have their frequencies separated by $\gamma \cdot \Delta\omega_{-3dB}$, the following expression can be written for any coupled of modes p and n

$$\begin{aligned} \frac{\omega_{0p}}{\omega_{0n}} &= 1 + \gamma \cdot (p-n) \cdot \frac{\Delta\omega_{-3dB}}{\omega_{0n}} \\ \left(\frac{\omega_{0p}}{\omega_{0n}}\right)^2 - 1 &\simeq \frac{2\gamma \cdot (p-n)}{Q} \end{aligned} \tag{70}$$

The eigenvectors of a 3 DOF undamped resonators system have been computed using Matlab®. They can also be found in [187] and are expressed as follow

$$u_{01} = \frac{1}{\sqrt{3}} \cdot \begin{pmatrix} 1 \\ 1 \\ 1 \end{pmatrix}, \; u_{02} = \frac{1}{\sqrt{2}} \cdot \begin{pmatrix} 1 \\ 0 \\ -1 \end{pmatrix}, \; u_{03} = \frac{1}{\sqrt{6}} \cdot \begin{pmatrix} 1 \\ 2 \\ 1 \end{pmatrix} \tag{71}$$

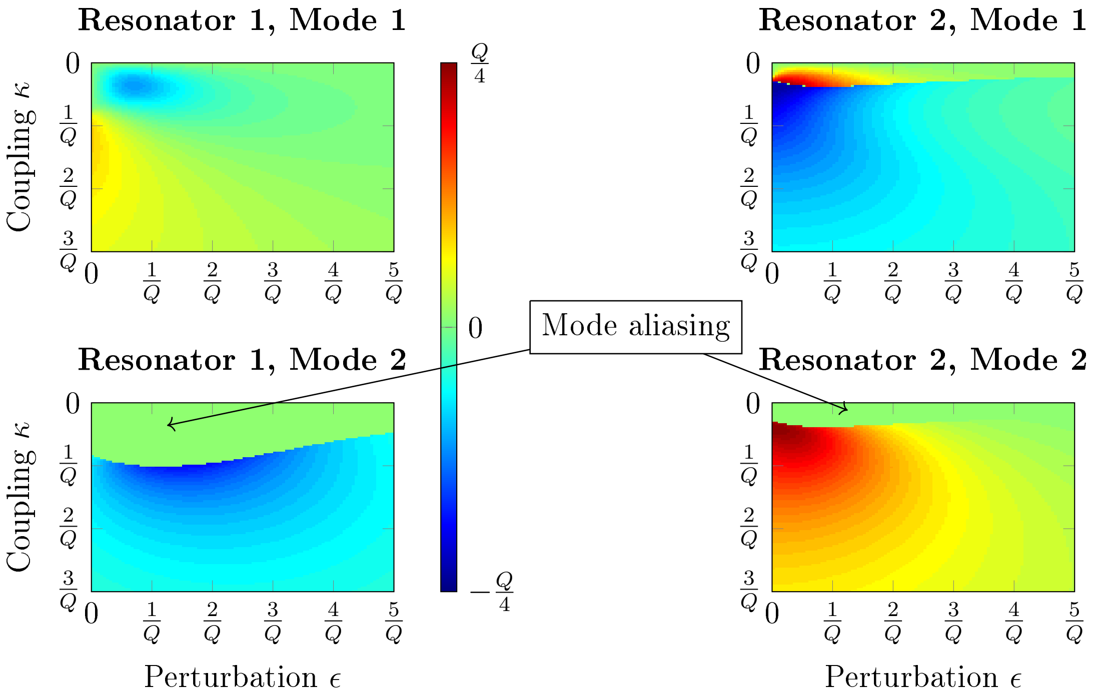

Figure 36: Normalized sensitivity graphics of a 2 DOF damped resonators system / Output metrics : Resonance amplitude shift.

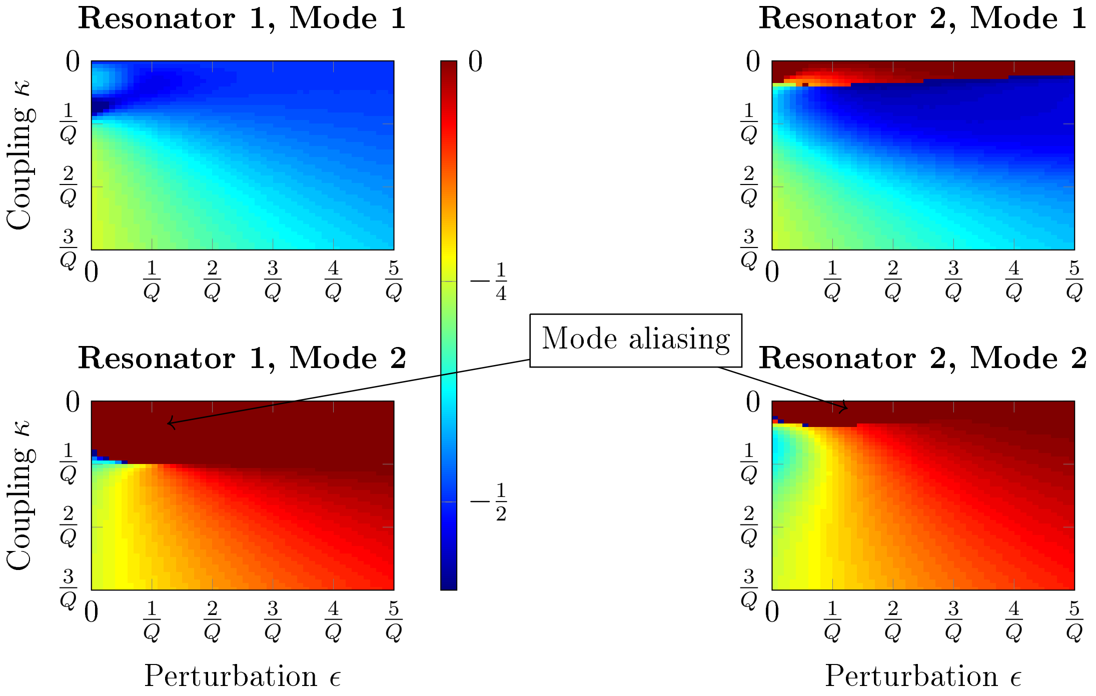

Figure 37: Normalized sensitivity graphics of a 2 DOF damped resonators system / Output metrics : Resonance frequency shift.

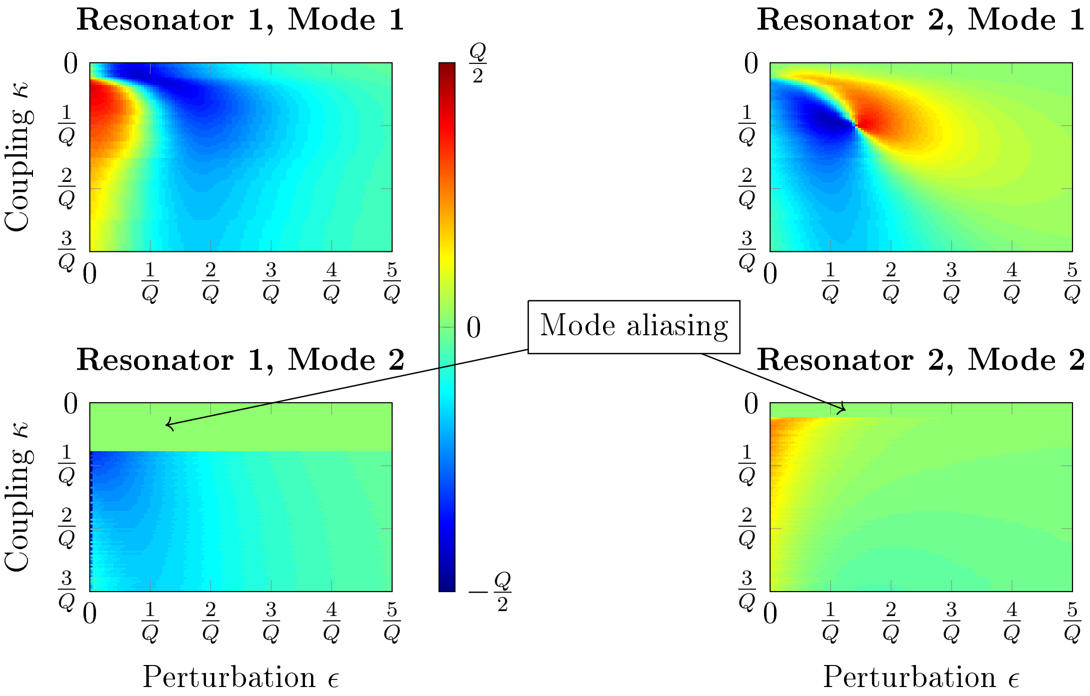

Figure 38: Normalized sensitivity graphics of a 2 DOF damped resonators system / Output metrics : Amplitude shift at $\omega = \omega_r$.

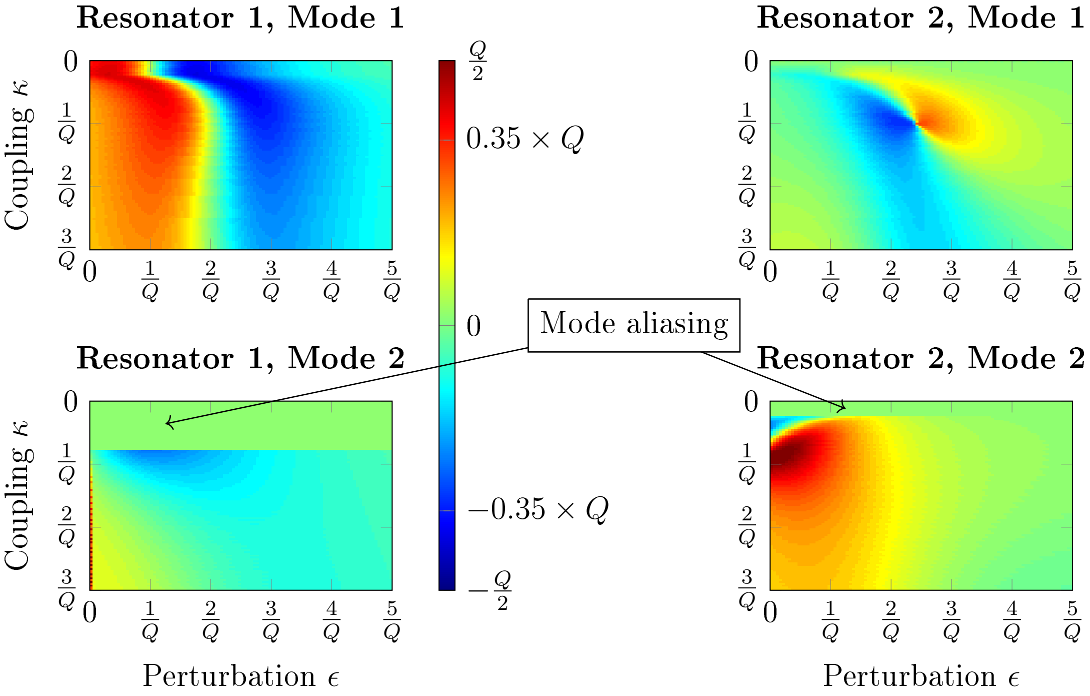

Figure 39: Normalized sensitivity graphics of a 2 DOF damped resonators system / Output metrics : Amplitude shift at $\omega = \omega_r \cdot \left(1 - \frac{1}{2Q}\right)$ for both resonances.

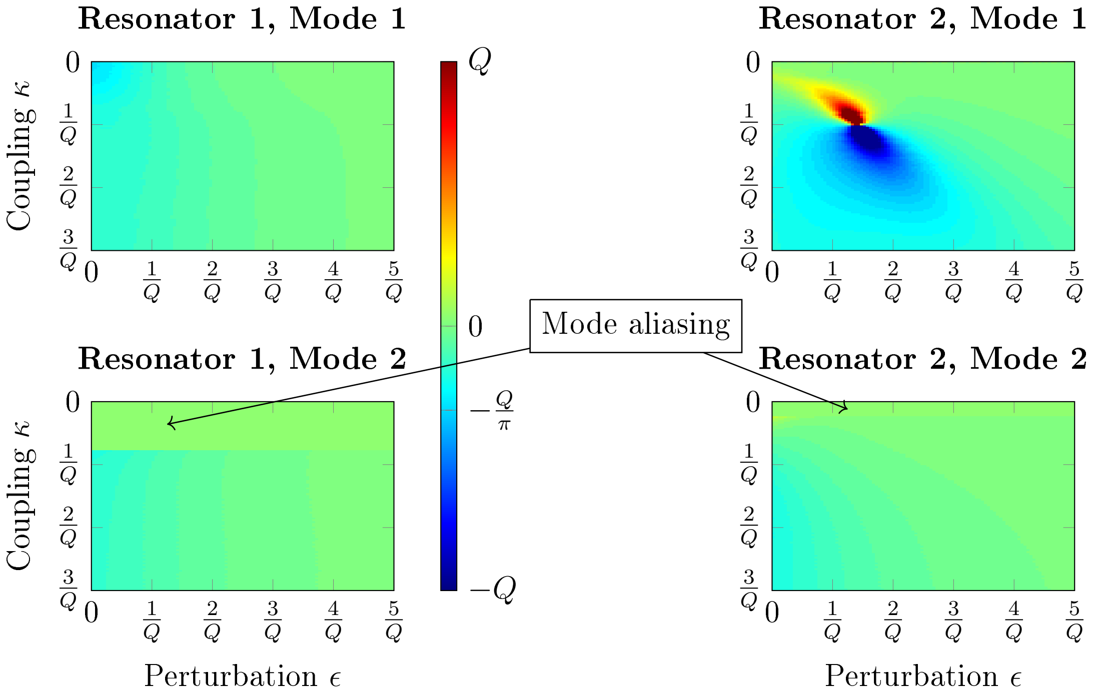

Figure 40: Normalized sensitivity graphics of a 2 DOF damped resonators system / Output metrics : Phase shift at $\omega = \omega_r$.

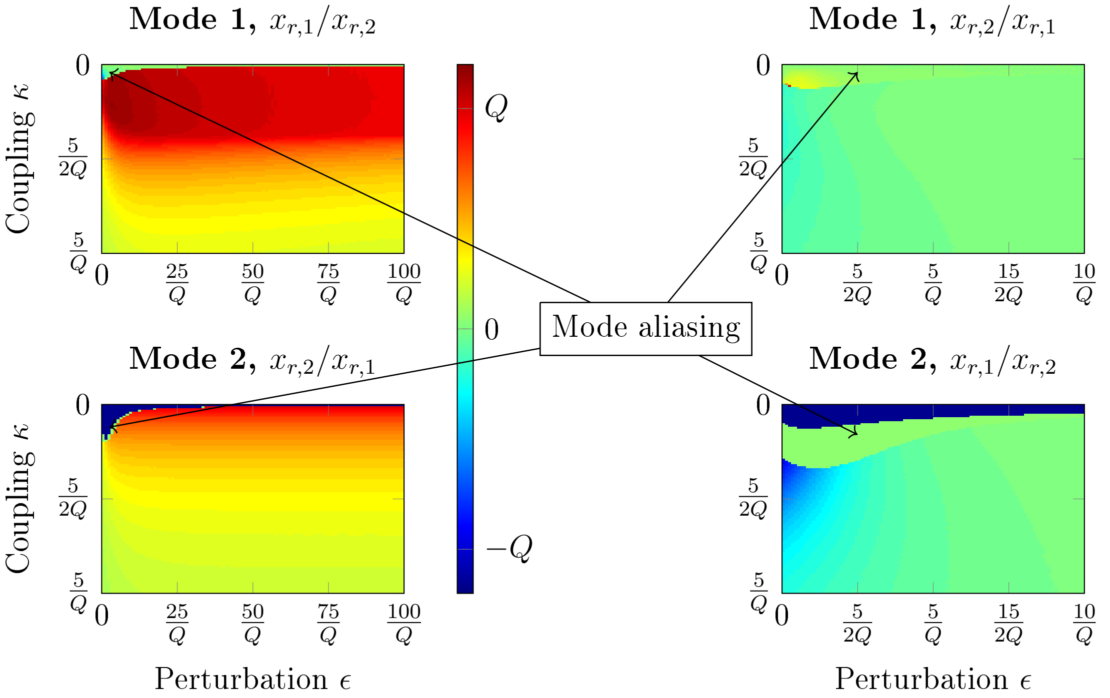

Figure 41: Normalized sensitivity graphics of a 2 DOF damped resonators system / Output metrics : resonance amplitude ratios.

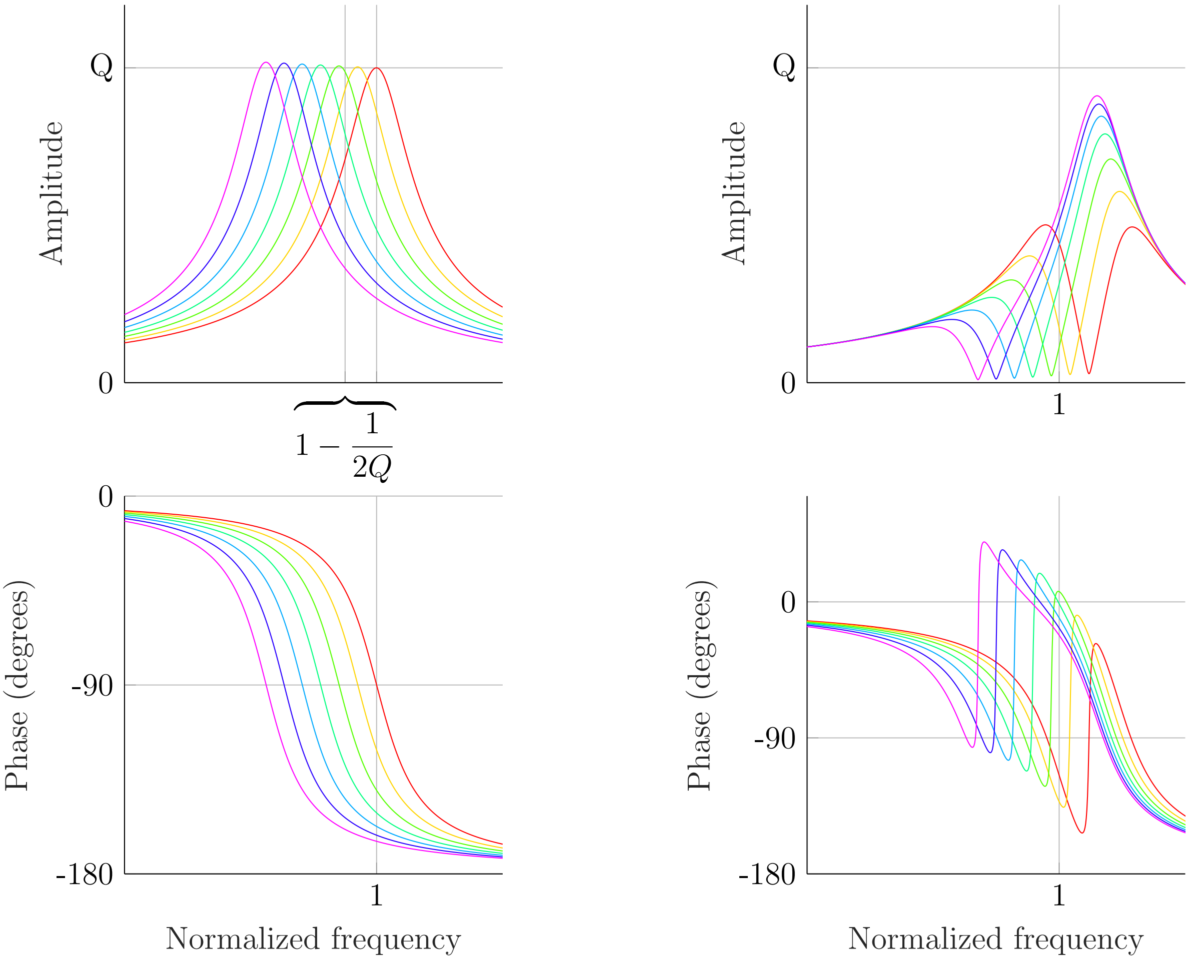

(a) Single resonator frequency response

(b) Second resonator of a 2 DOF coupled damped resonators system, excited with a phase of -90 degrees. In this example, $\kappa = \frac{0.95}{Q}$.

Figure 42: Dimensionless amplitude and phase Bode diagrams. The red curves correspond to the case $\epsilon = 0$. ϵ increases for each other curve following the rainbow colors, until a maximum perturbation of $\epsilon = \frac{3}{Q}$.

The mass mismatch can be deposed on any of the three resonators. If this perturbation occurs on the second one, any contribution to ML of the second mode would equals zero through the expression of $\delta\mu$ (because of the vibration node of u_{02}). Energy exchanges would then only happen between the first and the third modes.

Highly sensitive ML can occur when the mismatch is located on one of the external resonators, such as the first one. We then have

$$\delta M = \begin{bmatrix} \epsilon & 0 & 0 \\ 0 & 0 & 0 \\ 0 & 0 & 0 \end{bmatrix} \tag{72}$$

We can now calculate the optimal NS ns_{u_n} for each mode n at the anti-aliasing limit, knowing the initial eigenvectors u_{0n} are normalized, as follow

$$\begin{cases} ns_{u_n} = \dfrac{\delta u_n}{\epsilon} \\ \quad n \in \{1..3\} \end{cases} \tag{73}$$

Using Eq. 70 and the result presented in Annex 2, the previous equation yields

$$\begin{cases} ns_{u_n} \simeq \dfrac{Q}{2\gamma} \cdot \displaystyle\sum_{p=1,\ p\neq n}^{3} \frac{1}{p-n} \cdot \frac{\delta \mu_{p,n}}{\epsilon} \cdot u_{0p} \\ \quad n \in \{1..3\} \end{cases} \tag{74}$$

So

$$\begin{cases} ns_{u_1} \simeq \dfrac{Q}{2\gamma} \cdot \left(\dfrac{1}{\sqrt{6}} \cdot \begin{pmatrix} 1 \\ 0 \\ -1 \end{pmatrix} + \dfrac{1}{2} \cdot \dfrac{1}{\sqrt{3}\sqrt{6}} \cdot \begin{pmatrix} 1 \\ 2 \\ 1 \end{pmatrix} \right) \\ ns_{u_2} \simeq \dfrac{Q}{2\gamma} \cdot \left(-\dfrac{1}{\sqrt{6}} \cdot \begin{pmatrix} 1 \\ 1 \\ 1 \end{pmatrix} + \dfrac{1}{2\sqrt{3}} \cdot \begin{pmatrix} 1 \\ 2 \\ 1 \end{pmatrix} \right) \\ ns_{u_3} \simeq \dfrac{Q}{2\gamma} \cdot \left(-\dfrac{1}{2} \cdot \dfrac{1}{\sqrt{3}\sqrt{6}} \cdot \begin{pmatrix} 1 \\ 1 \\ 1 \end{pmatrix} - \dfrac{1}{2\sqrt{3}} \cdot \begin{pmatrix} 1 \\ 0 \\ -1 \end{pmatrix} \right) \end{cases} \tag{75}$$

Which finally yields

$$ns_{u_1} \simeq \frac{Q}{2\gamma} \cdot \begin{pmatrix} 0.53 \\ 0.24 \\ -0.29 \end{pmatrix},\ ns_{u_2} \simeq \frac{Q}{2\gamma} \cdot \begin{pmatrix} -0.12 \\ 0.17 \\ -0.12 \end{pmatrix},\ ns_{u_3} \simeq \frac{Q}{2\gamma} \cdot \begin{pmatrix} -0.41 \\ -0.12 \\ 0.17 \end{pmatrix} \tag{76}$$

One can notice the maximum NS barely gets over $\frac{Q}{4\gamma}$.

This result shows that the resonance amplitude shift NS is not improved with a 3 DOF WRC system. According to the result presented in Annex 2, it is most likely the same for a larger number of DOF, since ML for mode n is mainly due to the contribution of the other modes p_i that depend on the frequency gap between the modes n and p_i. However, this gap increases for further modes, thus diminishing their contribution to ML. This comes in addition to the sign of this contribution that is not always the same due to that of $p-n$, such as in the case of the second mode of a 3 DOF undamped resonators system (Eq. 75).

As a conclusion, there seem to be no gain in the implementation of ML in an array of resonators having more than 2 DOF, at least not in an array of identical resonators that respect an anti aliasing condition for all its modes.

II. C. 2. b Array of different resonators

Recently, another type of resonant array for ML purposes appeared [213, 214, 218, 221, 223], based on at least 3 DOF WCR, where the middle resonator-s- is -are- much stiffer than the two terminal ones. It has been demonstrated that the amplitude ratio of the two terminal resonators is proportional to $\frac{1}{\kappa^{N-1}}$, with N the number of DOF [223] and proportional to the stiffness difference between the middle and outer resonators in the case of a 3 DOF system [221]. However in the latter for instance, simulations on the analytical model show the higher this stiffness difference is, the closer the two first modes are (in terms of frequency). Thus for such designs, careful studies like the ones done in this section should be carried out in order to take mode aliasing into account, since it may not occur following the same rules. Nonetheless, this technique has been able to experimentally reach an amplitude ratio NS quite over the Q-factor [213, 218].

II. C. 3 Other properties of mode localization

II. C. 3. a Common mode rejection

The effect of external unwanted perturbations such as pressure or temperature drifts may be a problem for long term measures. These effects can be suppressed if the resonant sensor is based on an array of WCR using differential measurement such as amplitude ratio or eigenstate shift, since these effects occur to the entire array at the same time. This way, some WCR operating in close loop with the resonance amplitude ratio as an output metric have been found to be more stable than frequency based shift resonators over a certain time [173]. Temperature drift has been suppressed with amplitude ratio [225] and eigenstate shift [226] output metrics, so as the effect of pressure [221].

II. C. 3. b Noise and limits

Despite the high NS that the amplitude ratio can yield, a quite recent work [5, 227] demonstrated, throughout a reasoning based on random amplitude fluctuations in a 2 DOF damped resonators system for both open and close loop configurations, that the actual LOD of amplitude ratio does not depend on the coupling κ, and is actually worse than the one of a single resonator based on the measure of its RtF shift. However, this result is only valid for $\kappa \cdot Q \gg 1$ (strong anti aliasing condition) and two identical coupled resonators. No such work have been carried out neither on an array of more than 2 DOF, nor with stiffer middle resonators, which should be the next case to consider in the study of mode localized based sensors. Another paper studied the theoretical limit of measurable mismatch [222], but was criticized by [5] on one step in the reasoning. Another recent work using amplitude ratio as well, however, shown the LOD is dependent on κ [175]. The difference between these two results is explained in [175] to be due to different assumptions on the noise behavior (*correlated noise* or uncorrelated one). This makes the question of the LOD being still a current issue to be addressed in the future.

Comment : The higher resolution of frequency over amplitude measurements has been illustrated in [228] with inverse eigenvalue sensing method, where the amplitudes of the modes are calculated from the RtF of each resonators. The results were more accurate than the direct measures of the amplitudes, which points out that the high resolution of frequency measurement can compensate the low sensitivity of frequency shift.

II. C. 4 Conclusion

It can be concluded from the previous studies that the maximum sensitivity in amplitude shift of a 2 DOF damped resonators system using ML ($\frac{Q}{4}$) is actually lower than the one of a 1 DOF at fixed frequency ($0.35 \times Q$). However, the sensitive range is different, around $\frac{1}{Q}$ for a single DOF and $\frac{2}{Q}$ for 2 DOF. Since both cases are considering amplitude shift, any noise consideration is not an absolute necessity to lead to this conclusion (unlike the comparison with RtF shift often done in the literature). The same result over the NS has also been demonstrated analytically for a 3 DOF system, and this result is most likely to be extended to a N DOF array of identical WCR because the contribution of a given mode to the localization of another mode decreases with the frequency gap between these two modes. Still concerning amplitude measurements, the amplitude ratio NS is slightly for 2 DOF, and the linear range is drastically improved. However, a strongly localized WCR ($\epsilon >> 0$) also means one signal is low and thus the SNR as well, which is not a configuration to be in. It is also being observed there is no NS improvement on the RtF shift nor the phase shift at fixed frequency when it comes to couple two resonators. Table 4 gives the maximum NS reached, the sensitive range and the LOD for different output metrics and number of DOF.

Comment : It is here assumed that the main noise source comes from the readout (no bionoise for instance). Therefore, the LOD here corresponds the output resolution divided by the sensitivity.

Finally, we believe the only way to improve the NS is to have more than 2 DOF with stiffer resonators in the middle as proved in the literature [214]. Additional work on the sensitivity gain and noise should be also carried out in that direction to know the gain of ML over the RtF shift method in terms of LOD. The present manuscript however does not make any further study on more than 2 DOF WCR because it aims at the development of a new way to implement ML for ultra sensitive mass sensing purposes. Indeed, another limit to ML is the implementation of the coupling between the resonators. Even though one original work recently presented some simulations on weakly coupled SAWs for ML purposes [229], no experimental work has been done so far to get an array of coupled resonators working with a different kind of acoustic waves that those propagating either in cantilevers or in-plane resonators. For instance, it could be interesting to design a ML based sensor on QCMs working with thickness shear waves, since they are widely used in mass sensing for their high Q-factors and large binding surface. The challenge of our work is now to make a proof of concept on a 2 DOF with the design and implementation of a device able to sense a mass perturbation deposed at the surface of a QCM throughout mode localization. The present work is meant to be carried on with a higher number of DOF for ultra sensitive sensing if the gain in LOD can indeed be proved.

Comment : The Matlab®script that generates amplitude Bode diagrams and sensitivity maps is available in Annex 4.

Table 4: Performances summary for different configurations of single or coupled resonators.

Number of DOF (array of identical resonators)	**Output metric**	**Maximum NS**	**Sensitive range**	**LOD**
1	Resonant frequency shift	$\frac{1}{2}$	$\gg \frac{1}{Q}$	ψ_{ref}
2	Amplitude shift at the resonance	$\simeq \frac{Q}{4}$	$\simeq \frac{2}{Q}$	ψ_1 when $\epsilon \simeq 0$ [1]
1	Amplitude shift at fixed frequency	$\simeq 0.35 \times Q$	$\simeq \frac{1}{Q}$	$\simeq \psi_1$ when $\epsilon \simeq 0$
2	Amplitude ratio of the two resonators for a given mode	$\simeq Q$	$\gg \frac{1}{Q}$	$\psi_2 \simeq \frac{\psi_1}{2}$ when $\epsilon \simeq 0$ but drastically increases as ϵ increases.
3	Amplitude shift at the resonance	$\simeq \frac{Q}{4}$	Not studied here	Not studied here
$\geqslant 3$, stiffer middle resonators	Amplitude shift or ratio at the resonance	Not studied here	Not studied here	Not studied here

Chapter II in a nutshell

The second chapter first gives the theoretical background on mechanical resonators and their electrical equivalents. Mode localization is then introduced and the different developments and ML implementations found in the literature are presented and discussed : many structures are used to design sensors based on ML such as cantilevers or tuning forks that are coupled either mechanically or electrostatically. The capabilities of ML is then being evaluated through both analytical models and simulations, for different output metrics and configurations. The *figure of merit* used here is the normalized sensitivity like in the literature, and it was shown that the maximum NS reachable are between $\frac{Q}{4}$ and Q for a 2 DOF or 3 DOF array of identical resonators, depending on the output metric. It was however also pointed out that such devices may not break the LOD of the sensing methods based on the RtF shift of single resonators because of the resolution of these output metrics. Further extended studies should be conducted on that topic for more than 2 DOF systems.

---

[1] $\psi_1 \geqslant \psi_{ref}$ [5]

Le hasard, c'est Dieu qui se promène incognito.

Albert Einstein, dans Comment je vois le monde

Chapter III

Design and implementation of a high Q-factor digital resonator

This chapter is firstly describing an original way to overcome some limitations of sensors using ML, based on a digital approach. The design of this digital resonant filter is then presented and simulated before being implemented and tested in a specific hardware.

III. A Towards a hybrid system for ML purposes

The present section reminds some of the limitations of ML based sensors before describing the concept of the above mentioned solution. The way to implement it is then discussed and some theoretical basics are given in pair with some technical details about the chosen hardware, the field programmable gate array (FPGA). A couple of its application fields found in the literature are finally presented at the end of the section.

III. A. 1 Working principle

III. A. 1. a Remind of the current ML limits

The different implementations of ML on resonant structures, presented in the previous chapter, still have limited performances for different reasons. One of these limitations is the difficulty to create a coupling that is both weak and precisely known to ensure high sensitivity. The only solution presented so far to tune this value is the electrostatic coupling, but this technology drastically limits the geometries on which ML can be implemented (mainly in-plane resonators). For instance neither mechanical nor electrostatic coupling has ever been implemented on QCMs which yield much higher Q-factors (from 50 000 in air or vacuum), to our knowledge. Another limit is the tunability of each resonator in the array. It has been demonstrated ML is much stronger when the resonances are closer in frequency. Therefore, not only is necessary a weak coupling but also identical resonators before the addition of the mismatch (otherwise the modes are already partially localized, thus reducing the sensitivity of ML phenomenon).

In short, it would be interesting to find a way to tune both the coupling value and the filters physical parameters on the one hand, and to implement it on a higher Q-factor resonators such as QCMs on the other hand (since the NS depends on the Q-factor as shown in the previous chapter), in order to make the most of ML for sensing applications.

III. A. 1. b Concept of a hybrid system for mass sensing

Tunable ML has already been demonstrated on electrical resonators (RLC) [230], which are systems without a mechanical structure to realize an interface with an analyte. The use of a mechanical component being compulsory in a mass sensor, the association of mechanical and non mechanical resonators (here called hybrid system) can be interesting for the improvement of mode localized based mass sensors.

The idea behind a hybrid WCR system indeed lays on the replacement of mechanical and non tunable components by non mechanical but tunable elements in a classic MEMS array (the electrostatic coupling being a first step toward such an adjustable system). The will to implement ML on piezoelectric resonators can provide an interesting approach since the electro mechanical transduction is naturally done with such materials in both ways : the application of a voltage at the terminals of a piezoelectric transducer triggers its deformation, and its deformation generates a variation in the electric potentials at these terminals. The introduction of components directly interacting with electrical signals could thus be realized.

Considering the transfer function approach presented in Annex 3, both resonators and the coupling contribution are separated. Therefore, if a piezoelectric resonator such as a QCM could be integrated in an electrical circuitry with two terminals, an input and an output, the coupling contribution could be simply replaced by a signal processing in closed loop such as depicted on Fig. 43. The additions, subtractions and multiplications could thus either be done with active and passive analog components (operational amplifiers, capacitors and resistors) or with a digital implementation in a hardware. In this way, the coupling value could be easily tuned and also implemented to any kind of piezoelectric resonator, independently from its geometry.

More interestingly, some of the resonators in the array of WCR could be replaced by either their electrical or digital equivalents, thus providing perfect initial tuning of the array before the mismatch introduction. This method (electrical resonator electrically coupled to an array of MEMS) has already been introduced for resonant MEMS characterization, with Q-factors of a few hundred [231].

In this thesis, we present a fully tunable 2 DOF WCR using ML, based on the digital coupling of a QCM and a digital resonator. This chapter is specifically dedicated to the description of the hardware used and the design and implementation of the digital filter (resonator 1 on Fig. 43).

In summary, the main advantages of the system to be created here are its ability to adjust the parameters of the digital resonators according to those of the mechanical resonator, the tunable coupling, the possibility to implement this solution on any kind of piezoelectric resonator regardless to their geometry, and the easy access to the resonator mechanical quantities, since all signals are directly either electrical or digital.

Comment : Even though this thesis focuses on the QCM, the concept of hybrid resonators could actually be generalized to any kind of mechanical resonator, as long as a it can be both excited and observed through electrical signals.

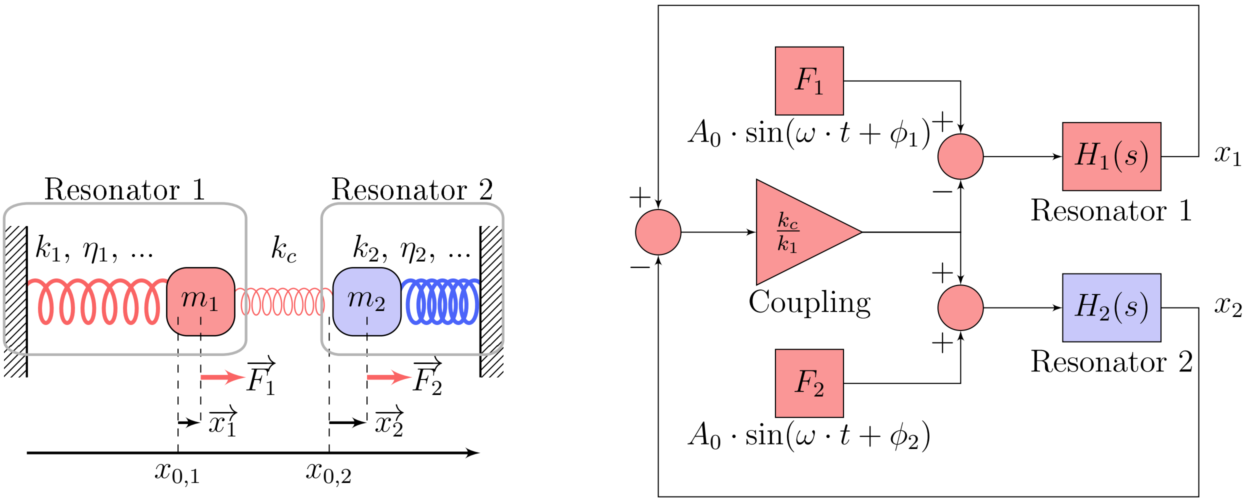

(a) Mass-spring like coupled resonators

(b) Equivalent block diagram of Fig. 43a

Figure 43: Two coupled resonators : the blue part represents the mechanical resonator on which the mass perturbation is introduced (for instance a QCM based filter), and the red part either an electrical circuit or a function implemented in a hardware.

III. A. 2 Electrical versus digital solutions

III. A. 2. a Electrical resonators

III. A. 2. a. i Passive filters

The easiest way to design an electrical resonator is to use passive components such as resistors, capacitors and inductors as described in the previous chapter, since classic mechanical resonators can be translated into their electrical passive equivalent (such as a RLC circuit or the BVD). However, this equivalence only allows such design on paper, because of the technical limits of those components. For example, a classic RLC circuit cannot reach high Q-factors (not more than a few hundred) and high RtF (not above a few kilo Hertz). The implementation of such filters thus requires active components.

III. A. 2. a. ii Active filters

Many different architectures of analog filters based on the combination of both active components (such as *operational amplifiers*) and passive ones (mainly resistors and capacitors) are broadly used in signal processing (low-pass, high-pass, band-pass filters applications) [232] : Rauch, Sallen-Key, Tow-Thomas, universal Fleisher-Tow and universal Kerwin Huelsman Newcombe (KHN) filters, to cite only a few of them.

Although active filters are known to be cheap solutions because these components are manufactured in high volumes and less limited than passive filters, several disadvantages can still be pointed out when faced with our application that requires very high Q-factors (around 200 000) and high RtF (around 2 MHz) :

- Only a few structures allow to build any polynomial transfer function and permit independent tuning of their coefficients (the universal Fleisher-Tow and KHN filters) [232].
- All of the active filters have both *passive and active sensitivities*, which may generate high output noise due to the desired high values of Q-factor and RtF [232].
- The required values of the different characteristics of the passive and active components may not be reachable technically (especially as parasitic resistance and capacitance can interfere).
- It remains difficult to know the exact value of each parameter (RtF, Q-factor...) and to proceed to their fine tuning.

In the end, analog resonant filter yield quite limited performances when it comes to deal with high Q-factor and RtF, custom transfer function, fine tuning and long term stability.

III. A. 2. b Digital resonators

III. A. 2. b. i Introduction to the Z-transform

Considering a sampled time signal x_k, $k \in \mathbf{Z}$, its Z-transform $\mathcal{Z}(x_k)$ is defined as

$$\mathcal{Z}(x_k) = \sum_{k=-\infty}^{+\infty} x_k \cdot z^{-k} \tag{77}$$

where z in a complex number for which the above series converges.

Let's now consider the term x_{k-n}, $(k,n) \in \mathbf{Z}^2$. Its Z-transform is then

$$\begin{aligned}
\mathcal{Z}(x_{k-n}) &= \sum_{k=-\infty}^{+\infty} x_{k-n} \cdot z^{-k} \\
\mathcal{Z}(x_{k-n}) &= \sum_{j=-\infty}^{+\infty} x_j \cdot z^{-j-n} \\
\mathcal{Z}(x_{k-n}) &= z^{-n} \cdot \sum_{j=-\infty}^{+\infty} x_j \cdot z^{-j} \\
\mathcal{Z}(x_{k-n}) &= z^{-n} \cdot \mathcal{Z}(x_k)
\end{aligned} \tag{78}$$

In short, the Z-transform of a signal delayed by n samples is equal to the Z-transform of the same signal at the considered sample multiplied by z^{-n}.

In general, it is supposed that $x_k = 0$ for $k < 0$, Eq. 77 then yields

$$\mathcal{Z}(x_k) = \sum_{k=0}^{+\infty} x_k \cdot z^{-k} \tag{79}$$

III. A. 2. b. ii Filtering applications

The Z-transform can be seen as the discrete equivalent of the Laplace transform, which is broadly used in the continuous system analysis. In the general case, the transfer function of a dynamic system after Z-transform $\mathcal{Z}(H)$ can be written as a ratio of polynomial (like a transfer function from the Laplace transform). After a division by z^n on both numerator and denominator, with n the highest degree of both polynomials, $\mathcal{Z}(H)$ is

$$\mathcal{Z}(H) = \frac{\sum_{k=0}^{n} \alpha_k \cdot z^{-k}}{\sum_{k=0}^{n} \beta_k \cdot z^{-k}} \tag{80}$$

where $\beta_0 \neq 0$.

Denoting S the output and E the input of the filter, the previous equation becomes

$$\begin{aligned} \beta_0 \cdot \mathcal{Z}(S_i) + \sum_{k=1}^{n} \beta_k \cdot z^{-k} \cdot \mathcal{Z}(S_i) &= \sum_{k=0}^{n} \alpha_k \cdot z^{-k} \cdot \mathcal{Z}(E_i) \\ \mathcal{Z}(S_i) &= \sum_{k=0}^{n} \frac{\alpha_k}{\beta_0} \cdot z^{-k} \cdot \mathcal{Z}(E_i) - \sum_{k=1}^{n} \frac{\beta_k}{\beta_0} \cdot z^{-k} \cdot \mathcal{Z}(S_i) \\ \mathcal{Z}(S_i) &= \sum_{k=0}^{n} a_k \cdot \mathcal{Z}(E_{i-k}) - \sum_{k=1}^{n} b_k \cdot \mathcal{Z}(S_{i-k}) \end{aligned} \tag{81}$$

where i denotes a given time sample. Applying the inverse Z-transform and using its linearity, Eq. 81 gives

$$S_i = \sum_{k=0}^{n} a_k \cdot E_{i-k} - \sum_{k=1}^{n} b_k \cdot S_{i-k} \tag{82}$$

The filter output, at a given time sample i, can be then written as a linear combination of the input, previous inputs and previous outputs.

When $b_k = 0$, $\forall k \in \{1..n\}$, the output only depends on the input. Such filters are called finite impulse response (FIR), because an impulse (an input being equal to zero at all time except for a few consecutive time samples) can only yield a response finite in time, before being again equal to zero. In contrast, if $\exists k \in \{1..n\}$, $b_k \neq 0$, the filter is called an infinite impulse response filter (IIR), because the output feedback generates a response infinite in time from a simple impulse.

Most of the dynamic systems are IIRs, which demands careful design since the feedback can lead to instability. However, Eq. 82 is a simple linear combination of signals at different time and such a *sequential logic* equation can be implemented in hardware that performs calculations at a high sample rate.

III. A. 2. b. iii Advantages of digital filters

Digital filters do not have the limits of the electrical ones : any polynomial transfer function can be implemented, all their coefficient can be chosen and finely tuned with no drift due to ambient conditions. In addition, a well chosen hardware can also host a routine for signal recording, data processing, graphical user interface (GUI), and so on. The implementation of a high Q-factor IIR has not been done so far in the literature to our knowledge, since IIR are usually used for high order filtering applications.

III. A. 3 Hardware

III. A. 3. a Requirements

The system to design is made of a first filter based on a QCM coupled with a second filter implemented in a hardware using Eq. 82. These constraints require mainly two conditions to fulfill.

Firstly, the sampling frequency f_s of the hardware must be high enough compared to the RtF f_r. The Nyquist condition demands $f_s > 2f_r$, and a minimum of 10 samples per period is fixed here to describe each sine wave in the digital system. The minimum sampling frequency then satisfies $f_s = 10f_r$. Given that the lowest RtF of commercial QCMs is between 1 MHz and 2 MHz, we can then set the highest RtF for which our design can work at 2 MHz, which thus requires a minimum sampling frequency of $f_s = 20\,\text{MHz}$.

Secondly, Eq. 82 requires each addition and multiplication to be done within only a few time samples (because of the feedback). The different operations thus have to be carried out in a few nanoseconds only. Massive parallel computation is then necessary.

III. A. 3. b Selection of the type of hardware

Comment : Each of the digital devices presented here has an internal *clock* allowing to sample time and process data step by step.

III. A. 3. b. i Central processing unit (CPU)

A CPU can execute a software (different queued up instructions). It is composed of one or more (n) *processor cores*, allowing to run n independent instructions at the same time : each of them is fetched from the memory, decoded and then executed by a processor core. A CPU can this way carry out logic operations at a very high frequency (up to a few gigahertz), which makes it efficient when it comes to deal with a large series of small tasks. However our application needs high throughput since the different operations must be done indeed in a short time but above all on several signals having a high number of digits. The selected hardware should then rather be able to carry out parallel computation, which is hence putting aside the CPU.

III. A. 3. b. ii Graphical processing unit (GPU)

Another widespread processing unit running software is the GPU. In such devices, each queued up instruction is first decomposed in sub-instructions before being sent to a large array of ICs handling similar logic operations but on different data, which results are then recombined. Therefore, they yield much higher throughput but also higher *latency* than the CPUs : they enable parallel computation but still on one instruction at a time per processor core (a single multiplication for instance), which does not fit our application, since we need all the operations (additions and multiplications) to be executed in parallel at the same time.

III. A. 3. b. iii Complex programmable logic device (CPLD)

In contrast with processors, programmable logic devices are not reading and executing instructions, but directly process the signals, and they first need to be configured by an external program before being able to do so. Each of them is a grid of configurable connections, allowing to create *combinational logic* (such as and, or, xor...) and thus to implement mathematical operations such as additions and products. The output of these cells may be connected to a *data flip-flop* and, consequently, to proceed with sequential logic. A CPLD is then an IC made of an array of such blocks, where the interconnections are configurable in order to implement any logical circuit. Since this architecture also allows parallel data processing, it also seems to suit our application.

The concept of programmable logic devices more generally fits our requirements since they can not only split one calculation in parallel sub-operations, but on many of them at the same time (unlike the GPU that carries out queued up tasks). Such devices can process only specific tasks once the design is determined on contrary to CPUs and GPUs, but they carry them out more efficiently : for instance, the latency of a CPLD is more deterministic than that of a GPU or CPU, because there is no instruction to execute.

III. A. 3. b. iv Field programmable gate array (FPGA)

In parallel to CPLDs, another type of programmable IC has been developed in the last decades : the FPGA. Similarly to the CPLD, the FPGA is a configurable IC allowing to carry out parallel calculations for combinational logic circuits and data storing for sequential logic circuits at a rate of several dozen of megahertz. The FPGA logical block is primarily made of *look-up tables* (LUT) which output may also be connected to a data flip-flop. However these logical blocks, embedded in a set of configurable interconnecting wires, are much more complex than those of the CPLD and the way the FPGA resources are used is usually automatically determined by synthesis routines.

Besides, the data stored in the FPGA is volatile memory and not flash memory like in the CPLD, meaning the data is lost when the device is powered off (except for *antifuse FPGAs*). However, flash memory requires more area on the chip and, consequently, the number of logical blocks on the chip is lower. This is the main reason why FPGAs are more popular than CPLDs when it comes to implement complex logical circuits that require massive parallel operations.

Finally, the FPGA is the hardware chosen for our design, because of its massive parallel computation capabilities and fixed delays.

III. A. 3. c Short history and nowadays applications of FPGAs

Xilinx, now the biggest FPGA manufacturer with Altera, introduced the first FPGA in 1984 [233]. At that time, *application-specific integrated circuits* (ASIC) were already quite well established. These devices yielded much better performances than this first FPGA made of only 64 logical block (themselves made of two three input LUTs and one *register*). However, Moore's law and the apparition of static random access memory (RAM) enabled FPGAs to be cheaper, gain in capacity (a factor of 10 000) and speed (a factor of 100) over 30 years. These improved performances, in pair with versatility, made FPGAs gain popularity by the 1990s. However, the complex architecture and extremely high number of logical blocks started to make their placement and routine done by hand quite challenging. Thus by the end of the 1990s, FPGAs companies had to provide automated synthesis tools in order to target the device and help in the design process.

Nowadays, FPGAs are involved in many different applications such as imaging [234–237], frequency control (PLLs) [238–240], feedback controls [241–244], characterizations [245], simulations [246], *hardware-in-the-loop * [247–253], neural networks [254,255], FIR filters [256–259], IIR filters [260–265] (and an IIR resonator emulator [266]) and *Kalman filters* [267–274]. FPGAs can also have the role of cheap instrumentation (oscilloscope, network analyzer, modulation/demodulation [275]...) and proceed, more generally, to customized digital signal processing. However, no high Q-factor IIR has been implemented on FPGAs so far to our knowledge since most of them are high-order filters for filtering applications, without a high gain over a small bandwidth (high Q-factor).

III. A. 3. d The Red Pitaya card

Nowadays, most of the FPGAs include a CPU (for external monitoring, data extraction...) and come along with additional RAM for data storage, PLLs for signal generation (when a clock of a different frequency or phase is needed) and digital signal processors that are meant to carry out different operations that would take too much space in the LUTs or the RAM such as products.

Red Pitaya is a company created in 2013 aiming at the development of a reconfigurable and open-source instrumentation. Their board, of the same name and depicted on Fig. 44, integrates all the components listed above (its datasheet is available in [276]). Amongst others, it includes two processor cores along with the FPGA (Zynq7000, datasheet available at [277] along with details on its logical blocks in [278]), two analog-to-digital converters (ADC) and two digital-to-analog converters (DAC) for communication with an analog system (which we here need), a SD card slot and an Ethernet connector. The clock signal of the DACs and ADCs (which will also be used to synchronize the registers in the FPGA) equals 125 MHz, which satisfies our requirements. The Red Pitaya has also the advantage to be a quite cheap hardware (less than 300€).

Since the Red Pitaya fulfills the requirements set up above and the department of Time-Frequency of FEMTO-ST has previously developed different tools for this card, we selected this hardware for the present work.

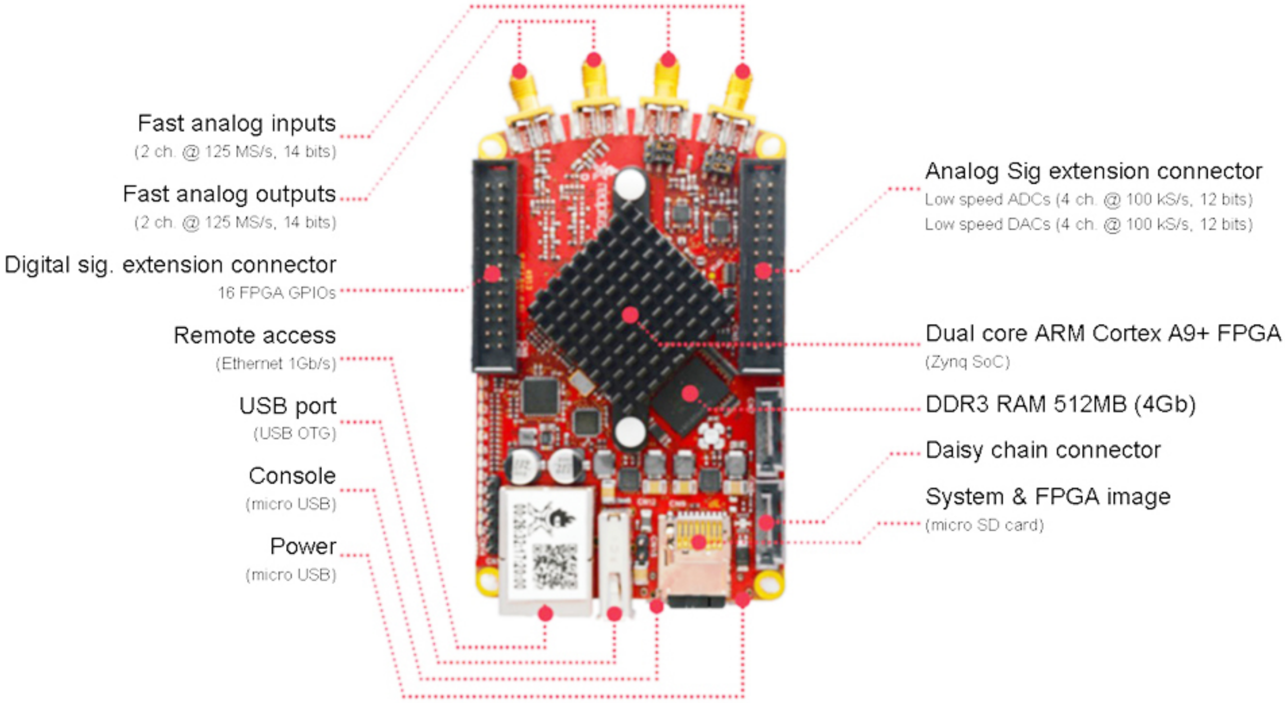

Figure 44: Commented photography of the Red Pitaya card / *source : [279]*

III. B Design of the digital filter

In this section, we describe the architecture of the analog filter along with the mathematical expression of its digital equivalent and the method to switch from analog to digital transfer functions.

III. B. 1 Link between the Laplace and Z transforms

III. B. 1. a The Laplace transform as a limit of the Z transform

Let's consider a time dependent signal $x(t)$ sampled at the times $t_k = k \cdot T_s$, with T_s the sampling period and $k \in \mathbf{Z}$. The Z transform of this signal can be written as

$$\mathcal{Z}(x) = \sum_{k=-\infty}^{+\infty} x(k \cdot T_s) \cdot z^{-k} \tag{83}$$

Let's now express z as $z = e^{p \cdot T_s}$, where p is also a complex number.

Equation Eq. 83 becomes

$$\mathcal{Z}(x) = \sum_{k=-\infty}^{+\infty} x(t_k) \cdot e^{-p \cdot t_k} \tag{84}$$

We can now calculate the following limit $\lim\limits_{T_s \to 0} \{\mathcal{Z}(x) \cdot T_s\}$ as follow

$$\begin{aligned} \lim_{T_s \to 0} \{\mathcal{Z}(x) \cdot T_s\} &= \int_{-\infty}^{+\infty} x(t) \cdot e^{-pt} \, \mathrm{d}t \\ \lim_{T_s \to 0} \{\mathcal{Z}(x) \cdot T_s\} &= \mathcal{L}(x) \end{aligned} \tag{85}$$

Where $\mathcal{L}$ is the Laplace transform.

Therefore, the Z transform times the sampling period of a discrete signal approaches the Laplace transform of the continuous signal as T_s decreases. The Z transform is then considered to be the discrete equivalent of the Laplace transform.

III. B. 1. b Derivation approximation

Since the Laplace transform of an electrical circuit can be found from the different impedances in sinusoidal regime, there is a great interest in finding a relation between the Laplace and the Z transforms. If replacing z by $e^{p \cdot T_s}$ enables to do so, it has the drawback to yield non polynomial transfer functions, which is limiting the interpretation in terms of sequential logic (Eq. 82).

On way to overcome this limitation is to proceed to an approximation of the z, knowing that $T_s \ll 1$.

The first one is expressed as follow

$$\begin{aligned} z &= e^{p \cdot T_s} \simeq 1 + p \cdot T_s \\ p &\simeq \frac{z-1}{T_s} \end{aligned} \tag{86}$$

A second approach is

$$\begin{aligned} z &= e^{p \cdot T_s} = \frac{1}{e^{-p \cdot T_s}} \simeq \frac{1}{1 - p \cdot T_s} \\ p &\simeq \frac{z-1}{z \cdot T_s} \end{aligned} \tag{87}$$

These two approaches can be illustrated by the different approximations done to calculate the derivatives with respect to time. Indeed, both forward and backward differences can be considered as follow

$$\begin{cases} \dfrac{dx}{dt}(t) \simeq \dfrac{x(t+T_s) - x(t)}{T_s} \\ \dfrac{dx}{dt}(t) \simeq \dfrac{x(t) - x(t-T_s)}{T_s} \end{cases} \tag{88}$$

Applying the Z transform the previous equation yields

$$\begin{cases} \mathcal{Z}\left\{\dfrac{dx}{dt}\right\} \simeq \dfrac{z-1}{T_s} \cdot \mathcal{Z}\{x\} \\ \mathcal{Z}\left\{\dfrac{dx}{dt}\right\} \simeq \dfrac{1-\frac{1}{z}}{T_s} \cdot \mathcal{Z}\{x\} = \dfrac{z-1}{z \cdot T_s} \cdot \mathcal{Z}\{x\} \end{cases} \tag{89}$$

Besides, one property of the Laplace transform concerning the derivative with respect to time is

$$\mathcal{L}\left\{\frac{dx}{dt}\right\} = p \cdot \mathcal{L}\{x\} \tag{90}$$

Therefore, the relations between z an p from Eq. 86 and Eq. 87 can also be deduced from Eq. 89 and Eq. 90.

One last approach, called the bilinear transform, is defined as follows

$$\begin{aligned} z &= e^{p \cdot T_s} = \frac{e^{\frac{p \cdot T_s}{2}}}{e^{\frac{-p \cdot T_s}{2}}} \simeq \frac{1 + \frac{p \cdot T_s}{2}}{1 - \frac{p \cdot T_s}{2}} \\ p &\simeq \frac{2}{T_s} \cdot \frac{z-1}{z+1} \end{aligned} \tag{91}$$

Comment : This approximations can be found from either the forward or backward difference divided by the corresponding normalized signal average $\frac{x(t+T_s)+x(t)}{2x(t)}$ (forward) or $\frac{x(t-T_s)+x(t)}{2x(t)}$ (backward).

The presented transforms have the drawback to distort frequencies (called warping) [280]. For instance the cut-off or resonant frequency of a filter can be different from what the analogic model yields. Therefore, a pre-warp bilinear transform allows to compensate this shift at a given frequency. The filter response then follows the one predicted by the continuous model around this particular frequency.

The expression of p for the pre-warp bilinear transform is given by [280] as

$$p = \frac{\omega_i}{\tan\left(\frac{\omega_i \cdot T_s}{2}\right)} \cdot \frac{z-1}{z+1} \tag{92}$$

where ω_i is the angular frequency at which the frequency warping is compensated.

III. B. 1. c Convergence domains

For a given time signal, it can be considered that its value is zero before $t = 0$ and its maximal absolute value is denoted M. This way, the Laplace transform can be maximized as follow

$$\mathcal{L}(x) < M \cdot \int_0^{+\infty} e^{-pt}\,\mathrm{d}t \tag{93}$$

Therefore

$$\begin{aligned} \left|\int_0^{+\infty} e^{-pt}\,\mathrm{d}t\right| &\leqslant \int_0^{+\infty} \left|e^{-\mathbf{Re}(p)\cdot t}\right| \cdot \left|e^{-j\cdot\mathbf{Im}(p)\cdot t}\right| \mathrm{d}t \\ \left|\int_0^{+\infty} e^{-pt}\,\mathrm{d}t\right| &\leqslant \int_0^{+\infty} e^{-\mathbf{Re}(p)\cdot t}\,\mathrm{d}t \end{aligned} \tag{94}$$

Since $\int_0^{+\infty} e^{-\alpha\cdot t}\mathrm{d}t$ converges when $\alpha > 0$, the Laplace transform converges for $\mathbf{Re}(p) > 0$ for signals equal to zero before $t = 0$ and to finite values after.

With $z = e^{p\cdot t_k}$, and applying the same reasoning on Eq. 84, the Z transform converges for the same signals when $\mathbf{Re}(p) > 0$, that is $|z| > e^0 = 1$.

There is thus an equivalence between the convergence regions of the Laplace and Z transforms. However, it is different when the relation between p an z is approximated. Indeed, the forward and backward difference map the stability domain of the p plane into one of the z plane that is different from the Z transform convergence region. It means some stable configurations in the Laplace domain can be changed into unstable ones in the z plane [280]. However, the convergence regions are conserved for the bilinear transform, which makes it the most common method to switch between the two complex domains and the one that is chosen in this thesis.

III. B. 2 Description of the filter

III. B. 2. a Architecture of the electrical resonator

In order to implement mode localization between two filters (following Fig. 43), the filter output must represent the resonator displacement (or its equivalent the electrical charge), like the RLC circuit example previously depicted on Fig. 20. From this consideration, a filter including a QCM based on the BVD can be designed, by simply connecting one of its terminals to a capacitor C_e in parallel of a resistor R_e (for further impedance tuning), as depicted on Fig. 45.

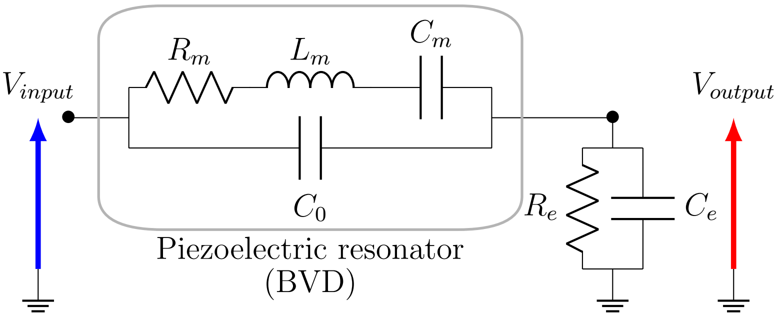

Figure 45: Low pass QCM-based resonant filter

The transfer function $H(s)$ of this electrical circuit is given by

$$\begin{cases} H = \dfrac{(1+\epsilon)\cdot s^3 + \frac{1}{Q}\cdot s^2 + (1+g_1)\cdot s}{(1+\epsilon)\cdot(1+g_2)\cdot s^3 + \left[\frac{1+g_2}{Q} + g_2\cdot g_3\cdot(1+\epsilon)\right]\cdot s^2 + \left[1+g_1+g_2+\frac{g_2\cdot g_3}{Q}\right]\cdot s + g_2\cdot g_3} \\ Q = \dfrac{1}{R_m}\cdot\sqrt{\dfrac{L_m}{C_m}} \\ \omega_0 = \dfrac{1}{\sqrt{L_m\cdot C_m}} \\ \epsilon = \dfrac{\delta L_m}{L_m} \\ g_1 = \dfrac{C_m}{C_0} \\ g_2 = \dfrac{C_e}{C_0} \\ g_3 = \dfrac{\omega_e}{\omega_0} \\ \omega_e = \dfrac{1}{R_e\cdot C_e} \\ s = j\cdot\dfrac{\omega}{\omega_0} \end{cases} \tag{95}$$

The parameter g_1 only depends on the QCM, and g_2, g_3 must be chosen. In particular, g_3 must satisfy $g_3 \ll 1$ in order to obtain a integrator behavior of the output impedance (then almost equivalent to a single capacitor).

The typical response of this resonant filter is depicted on Fig. 46 (parameters values given below). In this case, it can be observed that the series resonance is a little higher than ω_0, in contrast with the classic BVD response. This is due to the parameter g_2 : the presence of the output capacitor C_e slightly lower the overall motion capacitance (stiffening effect). Indeed, the lower the value of g_2 is, the higher the RtF is. The value of g_2 has to be relatively high in order to obtain the previously mentioned condition $g_3 \ll 1$. The parallel resonance, however, is only affected by g_1.

The chosen parameters for the simulations in the present chapter (chosen to be close to those selected for the experiments in the next chapter) are as follow

$$\begin{cases} Q = 100\,000 \\ f_0 = 1\,\mathrm{MHz} \\ g_1 = 2 \times 10^{-3} \\ g_2 = 25 \\ g_3 = 1.5 \times 10^{-2} \\ \epsilon = 0 \end{cases} \tag{96}$$

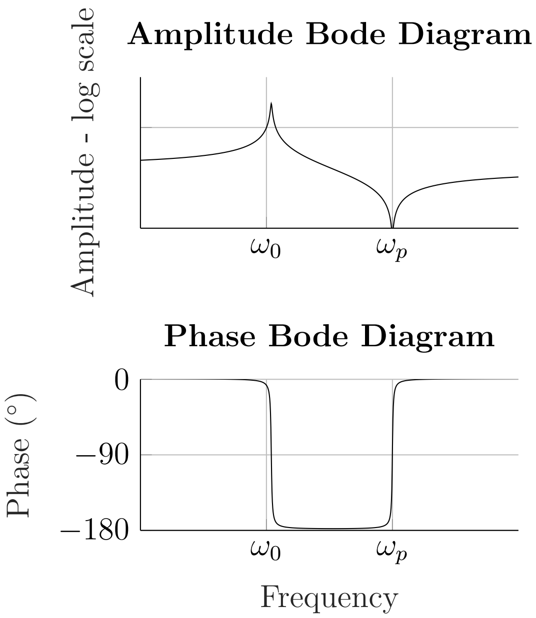

Figure 46: Simulated amplitude and phase Bode diagrams of the filter (parameters from Eq. 96)

Comment : The phase switches from 0 to −180°, which is the typical response of a resonator displacement.

III. B. 2. b Expression of the discrete transfer function of our QCM based filter

The transfer function in Eq. 95 now has to be switch from the p plane to z plane. The chosen approximation is the bilinear transform with prewarp at the RtF (given in Eq. 97), since the stability regions are maintained (the one from the p plane is entirely mapped into that of the z plane, and vice versa), and the filter input will be a sine wave which frequency is close to the RtF.

$$s = \frac{1}{\tan\left(\pi \cdot \frac{f_0}{f_s}\right)} \cdot \frac{z-1}{z+1} \tag{97}$$

The discrete recurrence equation resulting from this change of variable is

$$S_i = \sum_{k=0}^{3} a_k \cdot E_{i-k} - \sum_{k=1}^{3} b_k \cdot S_{i-k} \tag{98}$$

The coefficients a_k and b_k are calculated using Maple®and are given in Annex 5.

III. C Implementation in the FPGA

An overview of the different numerical tools is given in this section, but without all technical details. Indeed, a tutorial allowing to reproduce the present work would be far to long for the present manuscript, since it includes the Red Pitaya working environment, different functions implemented in the FPGA, graphical interfaces, data processing scripts, and so on. Some of them have been previously developed by the Time-Frequency department of FEMTO-ST and others have been specifically designed for this project. Finally, the implementation of the numerical filter described and studied earlier is exposed in details, along with its characteristics.

III. C. 1 Working environment

III. C. 1. a Design tools

III. C. 1. a. i Vivado Design Suite

Vivado Design Suite is a software developed by Xilinx (it can be downloaded from [281]). It enables to design the logical circuits to be implemented in their FPGAs (the file allowing to flash the design in the FPGA is called the bitstream and takes a few minutes to be generated by Vivado). Once the design is done and before the bitstream file generation, Vivado also runs a synthesis (bug detection in the design and generation of a representation close to the hardware, in terms of LUT and registers for instance) and proceeds to an automatic implementation (block placements on the chosen FPGA type) along with timing constraints reports of the implementation, helping the user in the design improvement.

Vivado is provided with a library containing many blocks such as additions, multiplications or *muliplexers*, to name a few, but also allows the user to write customized blocks, whether they need to communicate with the CPU (hence requiring external *drivers*) or not (called sources in this case). A source is written using *hardware description languages* (HDL) such as Verilog or VHDL, nowadays mostly used in the USA and Europe, respectively.

III. C. 1. a. ii Tools developed at FEMTO-ST

The Red Pitaya company provides a free online instrumentation platform called STEMlab [282], which includes ready-made applications such as oscilloscopes or signal generators. However, the use of the FPGA for research purposes demands tailored designs. Therefore, our teams from FEMTO-ST have developed some tools for any FPGA that include a CPU (such as that from the Red Pitaya) based on the Linux operating system core, including customised blocks and their drivers (they are indicated between quotation marks when used in the design). These tools are available online on the GitHub platform from [283].

III. C. 1. b Communication between the computer and the board CPU

III. C. 1. b. i Buildroot

In order to work with these tools, Linux has hence been installed both on the computer and the Red Pitaya. However, since the CPU of the Red Pitaya has a different architecture than that from the computer, the files allowing to boot the Red Pitaya on Linux have to be modified (a step called cross-compilation), which is the role of buildroot (to be downloaded from [284]). Once the cross compilation is done, the Linux system is loaded on the SD card of the Red Pitaya. The latter can then be connected to the computer via an ethernet cable allowing to boot the card using the secure shell protocol.

III. C. 1. b. ii Network file system (NFS)

Several files have to be moved from the computer to the board (such as the bitstream file). This could be done by writing on the SD card, but there is only little space available on it, and a SD card wears out quickly when its contents changes often. Sharing a folder located on the computer is a preferable option (called NFS). In such a system, both the computer and the board can read and write in this folder.

The NFS folder contains three sub-folders. The first one contains the bitstream file, the second one the drivers of the blocks and the third one contains the recorded data files along with the applications allowing to generate the graphic interfaces.

III. C. 1. c Communication between the board CPU and the FPGA

III. C. 1. c. i Parameters tuning and data acquisition

Compulsory blocks must be introduced in the Vivado design in order to allow data exchanges between the FPGA and the board CPU. From these blocks can be connected a first kind of block called ”add const” allowing to add two numbers, among which one may be tuned by the user, and a second kind of block called ”data to ram”, which enables data packing and transfer from the FPGA to an external memory.

III. C. 1. c. ii Graphic interfaces

The graphical user interfaces (GUI) are part of the environment used in this thesis that have been developed in FEMTO-ST and adapted to this specific project. Two different tools are used : a virtual oscilloscope for signal visualization, and a graphic platform for control and data recording, as depicted on Fig. 47.

The first one is GNU-Radio, which is a free and open-source software providing signal processing blocks [285]. A python script reads the different channels from the ”data to ram” and proceeds to a trigger (detection of the first rising edge of the vector), because the ”data to ram” does not send continuous signals (the data is sent by blocks when the ”data to ram” is opened by the python routine). The processed vector is then send to GNU-radio in order to be plot in live.

The second one, also coded with Python (which library must be added on the Linux of the board using the options of buildroot), is a webserver that must be open in the browser with the IP address of the board. It displays spin boxes and sliders allowing to modify many parameters (among which those of the filter such as the Q-factor of the eigenfrequency). The filter coefficients are then calculated from the selected values and sent in the ”add const” blocks. This GUI also enables to proceed to acquisitions by writing different text files. A first text file in which the configuration (parameter values) of the acquisition is saved, and a second one to record the data from the ”data to ram” block. For the acquisition, the user can proceed to a sweep over different parameters such as the frequency, by defining the start and step values along with the number of samples to record. This data is to be processed by another Python script on the computer when the acquisition is complete, is order to plot Bode diagrams and sensitivity maps for further comparison with the studies from the previous chapter.

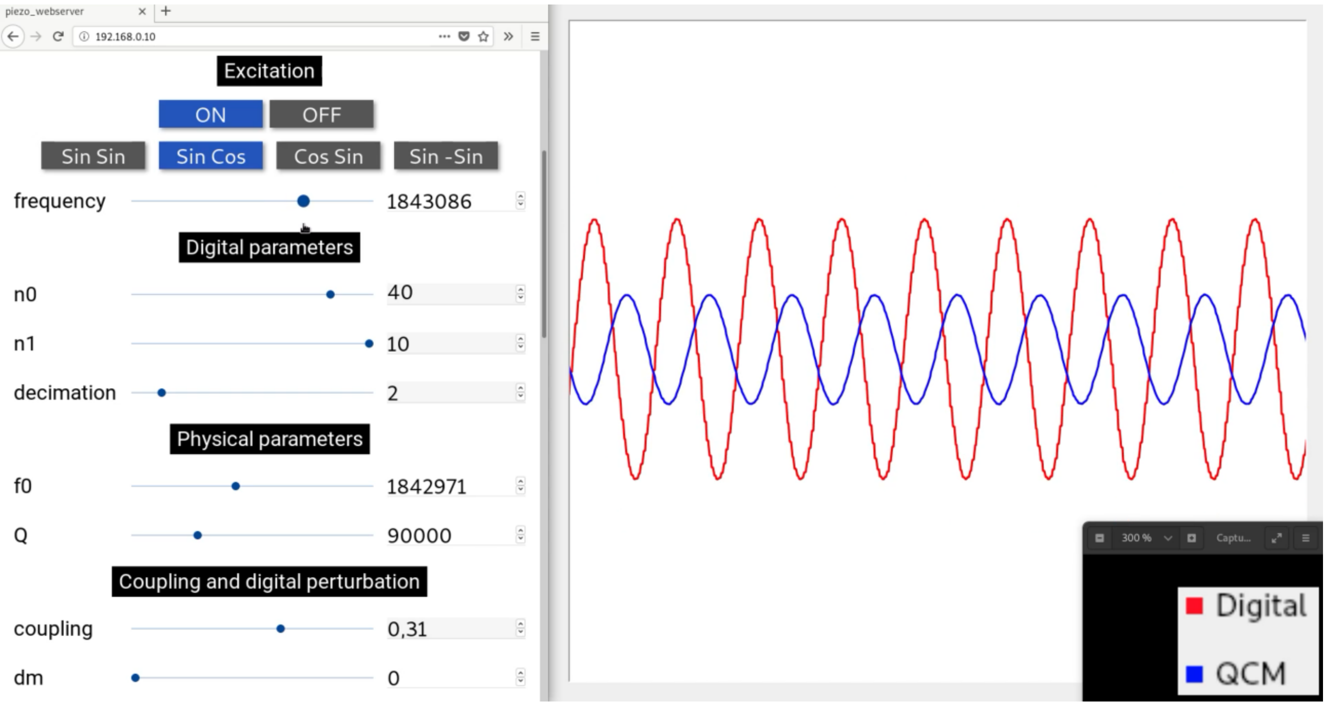

frequency 1843086

n0 40

n1 10

decimation 2

f0 1842971

Q 90000

coupling 0,31

dm 0

Figure 47: Screenshot of GUIs : Webserver on the left (buttons, sliders and spin boxes for parameters tuning) and GNU radio on the right (numerical oscilloscope). This figure is only meant to illustrate the interface of our system.

III. C. 1. d Generalities on binary numbers

All the numbers are integers coded in binary in the FPGA. The last digits are called the low-order bits, and the first ones the high-order bits. For instance, the number 1 coded on two bits is 01, so the lowest-order bit is 1, and the highest-order bit is 0.

There are mainly two ways to interpret a binary number, which are named signed and unsigned numbers. An unsigned number N_1 coded on n bits will be interpreted as a positive integer only, taking its values between 0 and $2^n - 1$. N_1 can be written as

$$N_1 = \sum_{k=0}^{n} D_k \cdot 2^k \tag{99}$$

Where D_k is the value of the bit number k. D_0 and D_n are the lowest and highest bits, respectively.

In contrast, a signed number N_2 can be read as a positive or negative number, since the highest-order bit contributes with a negative sign. The possible values taken by N_2 then belongs to $\{-2^{n-1}..2^{n-1} - 1\}$. N_2 is then written as

$$N_2 = \sum_{k=0}^{n-1} D_k \cdot 2^k - D_n \cdot 2^n \tag{100}$$

An example on three bits is given in Table 5.

Table 5: Signed and unsigned interpretations of binary numbers on three bits

Binary number	000	001	010	011	100	101	110	111
Unsigned	0	1	2	3	4	5	6	7
Signed	0	1	2	3	-4	-3	-2	-1

All the numbers are chosen to be signed in the FPGA for this project, because our system works in sinusoidal regime.

Comment : When a signed integer coded on a certain number digits has to be coded on more digits (or in the case of right *bit-shifting*), one should take care of propagating the highest order bit and not only fill the gaps with zeros.

III. C. 1. e Numerically controlled oscillator (NCO)

In order to observe its harmonic response, the IIR needs a sine wave in input. To do so, a digital signal generator must be first implemented in the FPGA. Such a block is called a NCO, which working principle is as follow.

A phase accumulator (counter) of size $n_{counter}$ counts the time samples multiplied by a phase increment p_{inc} (a positive integer). The first outputs of this counter are then $\{0, p_{inc}, 2 \times p_{inc}, 3 \times p_{inc}, ...\}$. The counter resets when its value is over $2^{n_{counter}} - 1$ (*overflow*). The highest-order bits of the phase accumulator constitute the input of a LUT in which are stored $2^{n_{lut}}$ amplitudes values of a sinus period themselves coded with a certain number of bits n_{size}. The frequency f at which the LUT is read (so the one of the generated signal since the LUT contains one period) is the same than that of the phase accumulator overflow, which is determined by p_{inc} and the sampling frequency f_s, as follow

$$f = \frac{p_{inc}}{2^{n_{counter}}} \cdot f_s \tag{101}$$

The ”NCO” used in this work has been created by the teams from the Time-Frequency department of FEMTO-ST, with the following characteristics : $n_{counter} = 32$, $n_{lut} = 12$ and $n_{size} = 14$ (because it is the Red Pitaya ADCs and DACs size). It is reminded the sampling frequency f_s of the Red Pitaya is 125 MHz. The smallest frequency increment, given by Eq. 101 for $p_{inc} = 1$, thus equals 29 mHz, and the highest frequency is given by the frequency of Nyquist here equaling 62.5 MHz.

III. C. 2 Implemented filter

III. C. 2. a Overall description of the digital filter

III. C. 2. a. i General structure

The filter implemented in the FPGA is depicted on Fig. 48. It is constituted of a FIR (block 1 to 20) in series with an IIR (blocks 21 to 37) that reproduces Eq. 98. Its architecture is being detailed in the next sections. As for the size of its input and output (20 bits), it will be explained in the next chapter.

Table 6: Expressions of the transfer functions from Fig. 48 (source code available in annex 6)

Source	H_1	H_2	H_3
Expression	$\beta = \alpha_1 \cdot 2^{\alpha_2}$	$\beta = \frac{\alpha_1}{2^{\alpha_2}}$	$\beta = \alpha_1$, for $\alpha_2 = 1$ $\beta = 0$ otherwise
Implementation	Left bit-shifting	Right bit-shifting	Conditional loop
Number of required registers	0	0	0
HDL	Verilog	Verilog	Verilog

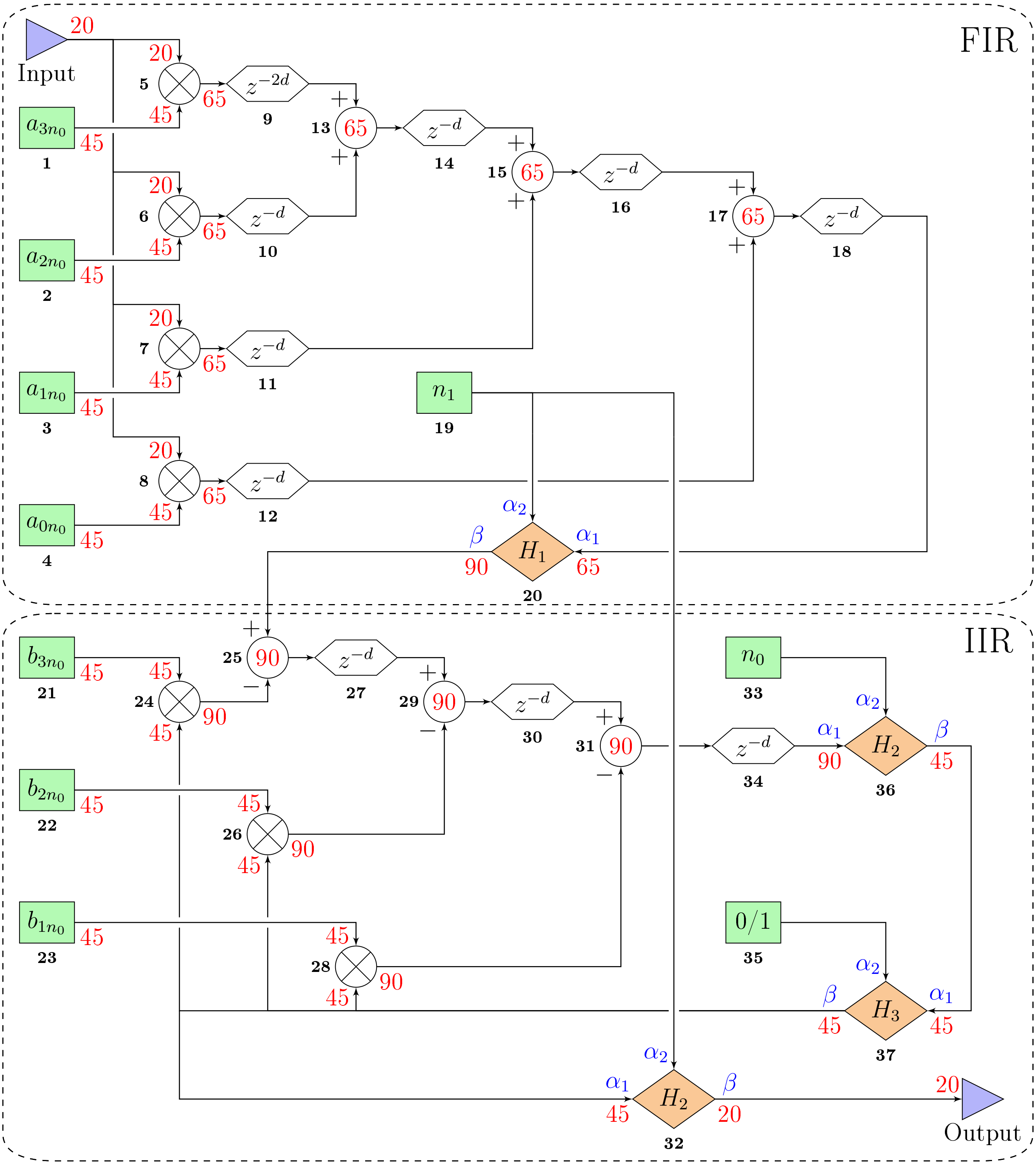

Figure 48: Simplified schematics of the implemented digital filter in the FPGA. The bold numbers in black are the blocks identifiers. The ones in red correspond to the number of bits on which the numbers are coded and d is the *decimation* factor. The hexagonal blocks are registers, the circular ones with a cross inside are multipliers, the green blocks are tunable values, and the orange ones are custom sources detailed in Table. 6.

III. C. 2. a. ii Timing constraints

Equation 98 demands strict timing constraints which may not be reachable by the hardware, especially in the IIR part, where there is an output feedback. It can be seen that a multiplication and an addition must be done in a single time sample (blocks 28-31, 26-29 and 24-25), what the FPGA cannot do experimentally. Therefore, an additional Verilog source (source code available in annex 6) has been set up in order to proceed to a down-sampling based on the decimation factor d (natural number). The new sampling frequency f_d then follows

$$f_d = \frac{f_s}{d} \tag{102}$$

This new clock is applied to each block of the filter, and as explained in the next chapter, to most of the blocks of the design. This decimation is implemented through a function called clock enable which has one argument allowing the targeted registers to open only when its value is equal to 1. Therefore, the decimation source is a time sample counter having two inputs (d and the clock signal) and one output being equal to one when the counter equals d.

Experimentally, the lowest value of d for which the timing constraint is respected is $d = 2$, whatever the number of digits on which the numbers are coded (because of parallel computation).

Comment : Since the FPGA is able to carry out an addition and a multiplication is two time samples, there could be one less register in the blocks 9 to 12 on Fig. 48. However, the FIR can afford additional delay and registers are added after each operation in order to avoid unnecessary timing constraints.

III. C. 2. a. iii Closed loop switch

The filter coefficients are introduced in the FPGA using the ”add const” block described earlier, where the added constant value is set to zero. When these coefficients are modified throughout the GUI (filter tuning), meaningless values can appear and propagate in the closed loop of the IIR, thus generating unpredictable output. This phenomenon only last a fraction of second before the correct steady state is reached (the meaningless values act like random initial conditions). However, the output value may reach high values, usually triggering overflow as well. Overflow, once introduced in the closed loop, has no chance to stabilize since the meaningless numbers do not only appear when the coefficients are modified, but propagates at each time sample and forever.

For this reason, an automatically controlled switch (block 37) has been added on the output feedback : when the coefficient values are modified, the switch opens (sending a zero feedback) and closes after one millisecond, a time large enough to allow a few thousand samples to pass through (it must be above $3 \times d$, which corresponds to the blocks 27, 30 and 34), and small enough not to be a nuisance to the experiment. In this way, parametric instability can be suppressed when the coefficients are changed.

III. C. 2. b Stability domains

III. C. 2. b. i Generality

Even though the Z transform of a signal defined in the Laplace domain exists with the bilinear transform, its expression can still lead to a divergent signal (if the Q-factor value is negative for instance).

The stability region of the dynamic system in the Laplace domain is defined by the denominator roots in the transfer function : their real part must be negative. This condition is satisfied in the Z domain by the root modulus being smaller than the unity. Indeed, the transfer function of a system, written with the Z transform and after a partial fraction decomposition, can be expressed as

$$\mathcal{Z}(H) = \sum_{i=1}^{n} \frac{c_i \cdot z}{z - z_i} \tag{103}$$

where n is a natural number, z_i the roots and c_i real coefficients.

Knowing that for a given complex number a

$$\mathcal{Z}^{-1}\left(\frac{z}{z-a}\right) = a^k \tag{104}$$

equation 103 becomes

$$H(k \cdot T_s) = \sum_{i=1}^{n} c_i \cdot z_i^k \tag{105}$$

Since the transfer function H is the system response to an impulse, the convergence is defined as

$$\lim_{k \to +\infty} H(k \cdot T_s) = 0 \tag{106}$$

which indeed yields the condition $|z_i| < 1$.

III. C. 2. b. ii Stability in the FPGA using floating point

In this work, we are interested in the roots of the following function

$$H(z) = z^3 + b_1 \cdot z^2 + b_2 \cdot z + b_3 \tag{107}$$

For a given set of parameters having a physical meaning (such as $Q > 0$), the roots of Eq. 107 always have their modulus being below one. However, one should keep in mind the numbers implemented in the FPGA are only integers. Therefore, there is a need to multiply the coefficients

b_1, b_2 and b_3 by a large integer in order to minimize the approximations done over these coefficients when injected in the hardware. Thus, these coefficients are multiplied by a power of two (which will facilitate the inverse operation within the FPGA this time, using right bit-shifting). This power of two is called n_0 in the thesis.

The roots of the following function have been computed using Matlab®

$$H(z) = 2^{n_0} \cdot z^3 + round(2^{n_0} \cdot b_1) \cdot z^2 + round(2^{n_0} \cdot b_2) \cdot z + round(2^{n_0} \cdot b_3) \tag{108}$$

where *round* is the function that rounds numbers to the closest integer. The roots modulus have been plot as a function of n_0 and the fraction $\frac{f_s}{f_r}$ (the only non-physical parameters having an influence on the coefficients a_i and b_i) on Fig. 49.

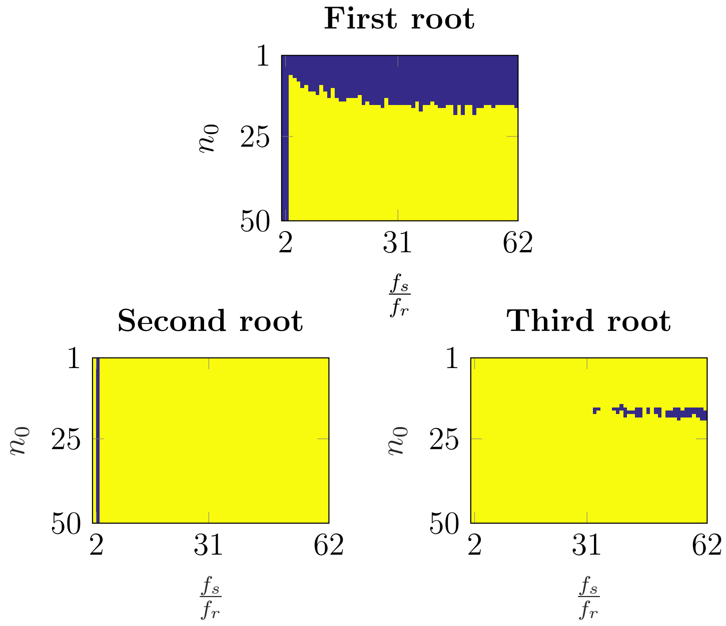

Figure 49: Roots modulus for the set of filter parameters given in Eq. 96. Modulus above and below unity are plot in dark blue and yellow, respectively. These results are essentially the same for a wide range of values of the different physical parameters (Q, g_1, g_2, g_3 and f_0), at least a factor of ten below and above. Knowing the lowest resonant frequency f_r used here is 1 MHz and the smallest decimation factor is $d = 2$, the maximum number of samples per period (ratio $\frac{f_s}{f_r}$) equals 62.5.

The stability condition is fulfilled when all the three roots have a modulus below unity, which roughly occurs when $\frac{f_s}{f_r} > 2$ (Shannon condition) and $n_0 > 22$. This result is confirmed experimentally with the digital filter in the FPGA.

The coefficients a_i and b_i introduced in the FPGA are then called a_{in_0} and b_{in_0}, with

$$\begin{cases} a_{0n_0} = round(2^{n_0} \cdot a_0) \\ a_{in_0} = round(2^{n_0} \cdot a_i) \\ b_{in_0} = round(2^{n_0} \cdot b_i) \\ \quad i \in \{1..3\} \end{cases} \tag{109}$$

The IIR part of the filter (Fig. 48) must include a division by 2^{n_0} before the feedback loop in order to get back to the real value of the output, which is the role of the block 36.

Comment : The representation of a real number in binary with a large integer (significand) divided by a power of two (exponent) is a method widely used in computing science and also in FPGAs [261,266]. It is called floating point because the point can be translated by the exponent, in contrast with the fixed point, where there is a fixed number of bits representing the integer and another set of bits being the digits after the point.

III. C. 2. c Filter correctness and correlated noise

III. C. 2. c. i Precision of the filter coefficients

Even though the digital filter is stable when $n_0 > 22$, its frequency response may not be the one desired because of the approximations done on the coefficients (integers and not floats). The only way to reduce this approximation is to increase the value of n_0.

This phenomenon has been simulated on Simulink®, following the sketch from Fig. 48, with the same parameters values including the sampling frequency. These simulations only provide the beginning of the transient regime because the high Q-factor (10^5) requires a quite large number of oscillations before the steady state is reached (as a consequence, the amplitude responses in their fast Fourier transforms (FFT) are lower). However, the purpose of this study is to compare different configurations, so the steady state is not required here.

The first simulation C_1, the reference, depicts the case with float numbers, both for the filter coefficients and the data flowing through the filter. A quantization is however applied on the input sinusoidal wave (coded on 14 bits like in the FPGA) in order to only study the effect of n_0 on the filter response.

The second simulation C_2 depicts the case with integers, both for the filter coefficients and the data flowing through the filter (exactly like in the FPGA). The time responses and their FFT are plot on Fig. 50 and Fig. 51, respectively (the parameter n_1 will be introduced in the next paragraph). It can be observed on Fig. 50 that the time response of C_2 is quite different from the one of C_1, which is confirmed on Fig. 51 : the gain at the RtF (1 MHz) is higher for C_2 than for C_1.

Increasing n_0 until $n_0 = 40$ (C_3 and C_4) yields responses much closer to C_1, which is visible both on the signal envelop of the time response and the module of the Fourier transform at 1 MHz. For this reason, the filter coefficients, which values before the multiplication by 2^{n_0} are close to the unity, are coded on 45 bits (Fig. 48). $n_0 = 40$ is chosen for the rest of the experiments in the thesis.

Comment : The coefficients a_{in_0} (FIR part) do not need a specific size for the stability condition (a FIR being stable by definition). The only necessity here is to introduce coefficients precise enough to implement a filter as close as possible to the desired one. For this reason, the same factor 2^{n_0} is applied both on b_i and a_i.

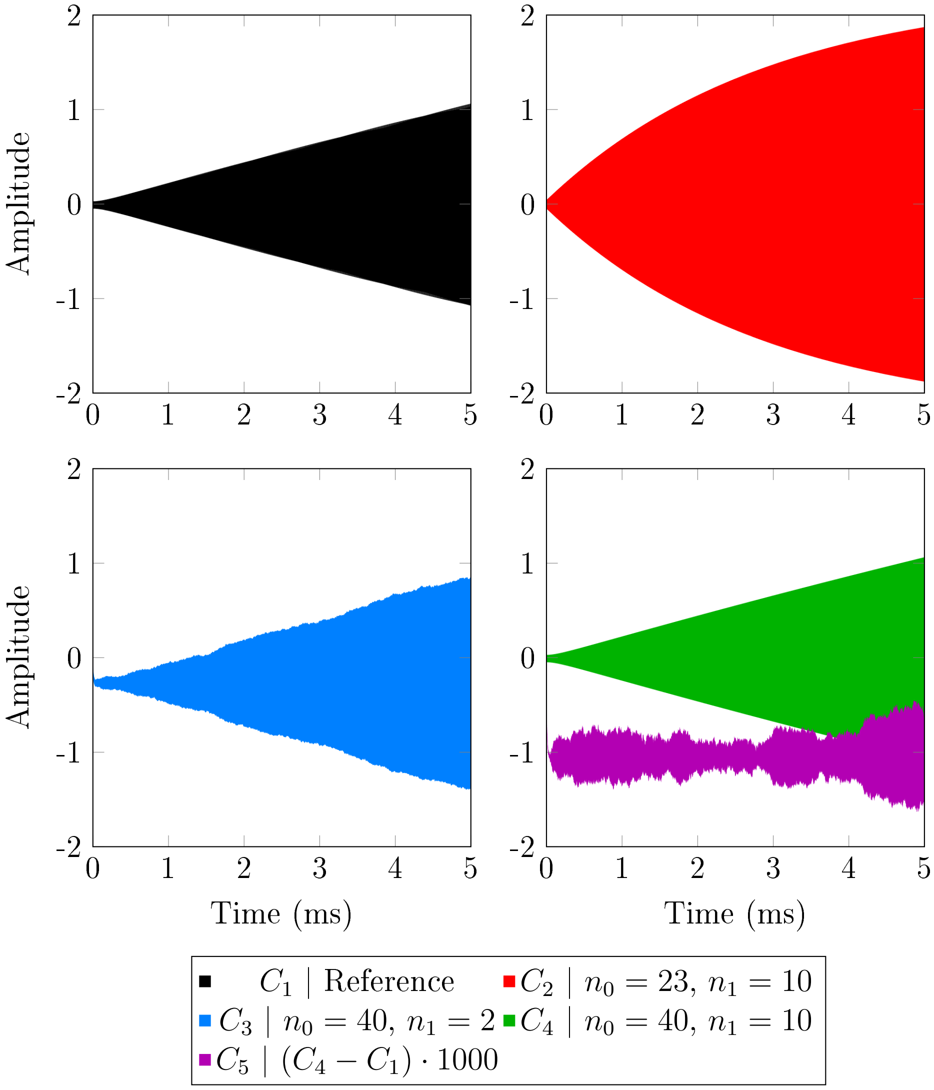

Figure 50: Simulated time responses (Simulink®) of the digital filter for different configurations (sinusoidal excitation of amplitude 1). Only a part of the transitory regime has been simulated. The reference C_1 corresponds to the case where the signals are sampled and all numbers are floats, whereas the other configurations only work with integers. A signal error is also plot on C_5.

III. C. 2. c. ii Correlated noise

Another phenomenon occurring within the digital filter is its unexpected variable output amplitude : it can be clearly seen on the oscilloscope (GNU radio scope) that the output amplitude is varying over a long period of time in comparison with the period of the signal (around 1 μs). It was found that these variations are due to the approximation done by the right bit-shifting of block 36 : the number of digits on which is coded the feedback signal in the IIR has an influence on the time response.

In order to reduce the influence of this function on the response, the signal is being multiplied by another factor 2^{n_1} at the output of the FIR, and is being divided by the same constant at the output of the IIR (blocks 20 and 32). This way, the feedback (between blocks 37, 24, 26 and 28) is coded on 45 bits and not 20 (n_1 can go up to 25).

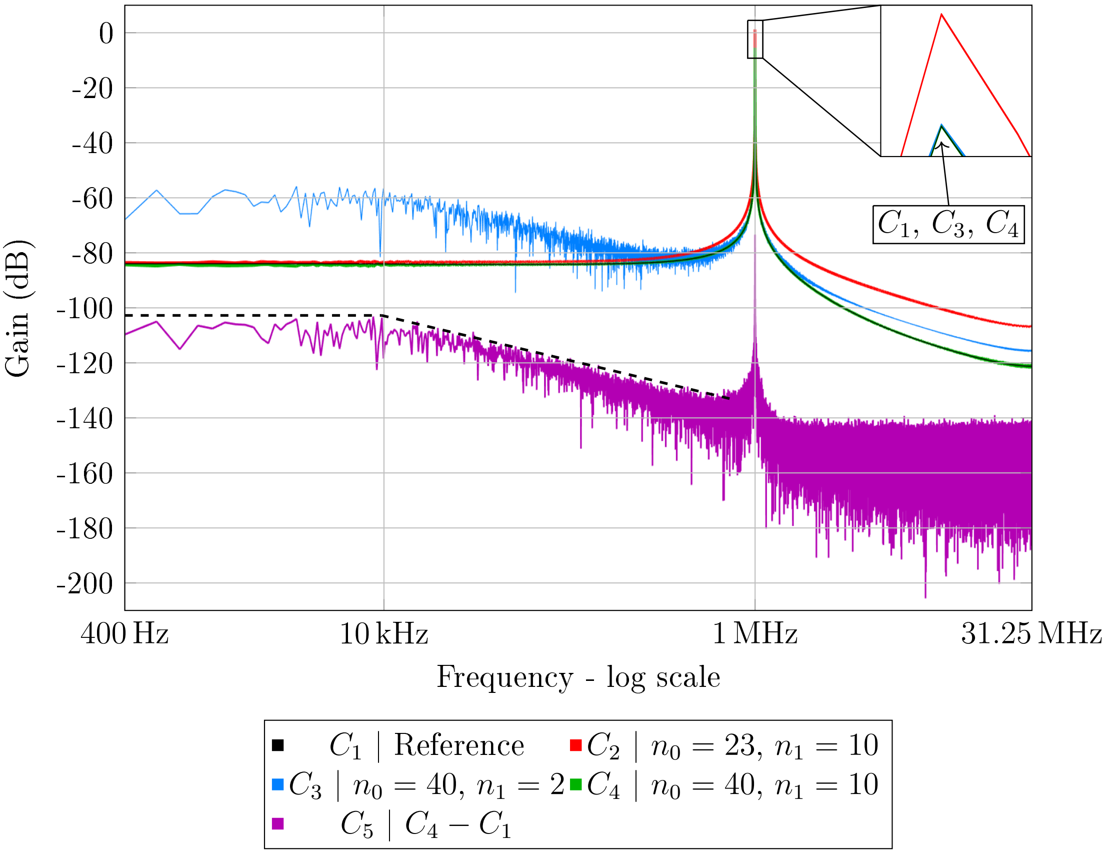

Figure 51: FFT modules of the signals from Fig. 50. The Nyquist frequency is 31.25 MHz because $d = 2$. The input signal amplitude being equal to 1, the gain in decibel is $20 \cdot log(C_i)$.

An example of signal corrupted with correlated noise is given in simulation C_3 ($n_1 = 2$). The time response given on Fig. 50 first shows the envelope of the signal is not as smooth as the one of the reference (it happens that this envelop does almost not exist for $n_1 = 0$), but it can be also observed the average signal is negative. This phenomenon is due to rounding of the numbers to the closest integer below (right bit-shifting of blocks 36). It has been simulated that this offset is positive when the numbers are rounded up, and equals zero when rounded to the closest integer (either up or down). However, this last possibility cannot be implemented in the FPGA because it demands either bit-shifting (round down) or bit-shifting plus an addition (+1 for round up), which requires registers that cannot be placed in this part or the IIR. Finally, the FFT of C_3 (Fig. 51) indeed shows higher noise level at low frequency.

Increasing n_1 to $n_1 = 10$ enables to obtain a signal much closer to C_1 (C_4). The drift C_5 is still noisy and yields a slight negative offset. However, its FFT shows that this noise is lower than that of the reference C_1, a factor of 10 (20 dB) in the low frequencies and close to the Nyquist frequency, which is here considered to be sufficient.

Comment : The correlated noise generated by the approximation of the right bit-shifting in the IIR feedback tends to increase when the frequency diminishes before reaching a fixed level from 10 kHz down to 400 Hz at least, but the computing time needed to get information at lower frequencies is too high. In our design, the "data to ram" block enables to register signals by blocks of 2048 samples, meaning no noise below $\frac{125\times10^6}{2048} = 61$ kHz can be registered in a single acquisition. Therefore, there is no need to know the behavior of the filter below 400 Hz.

III. C. 2. d Filter frequency response and data processing

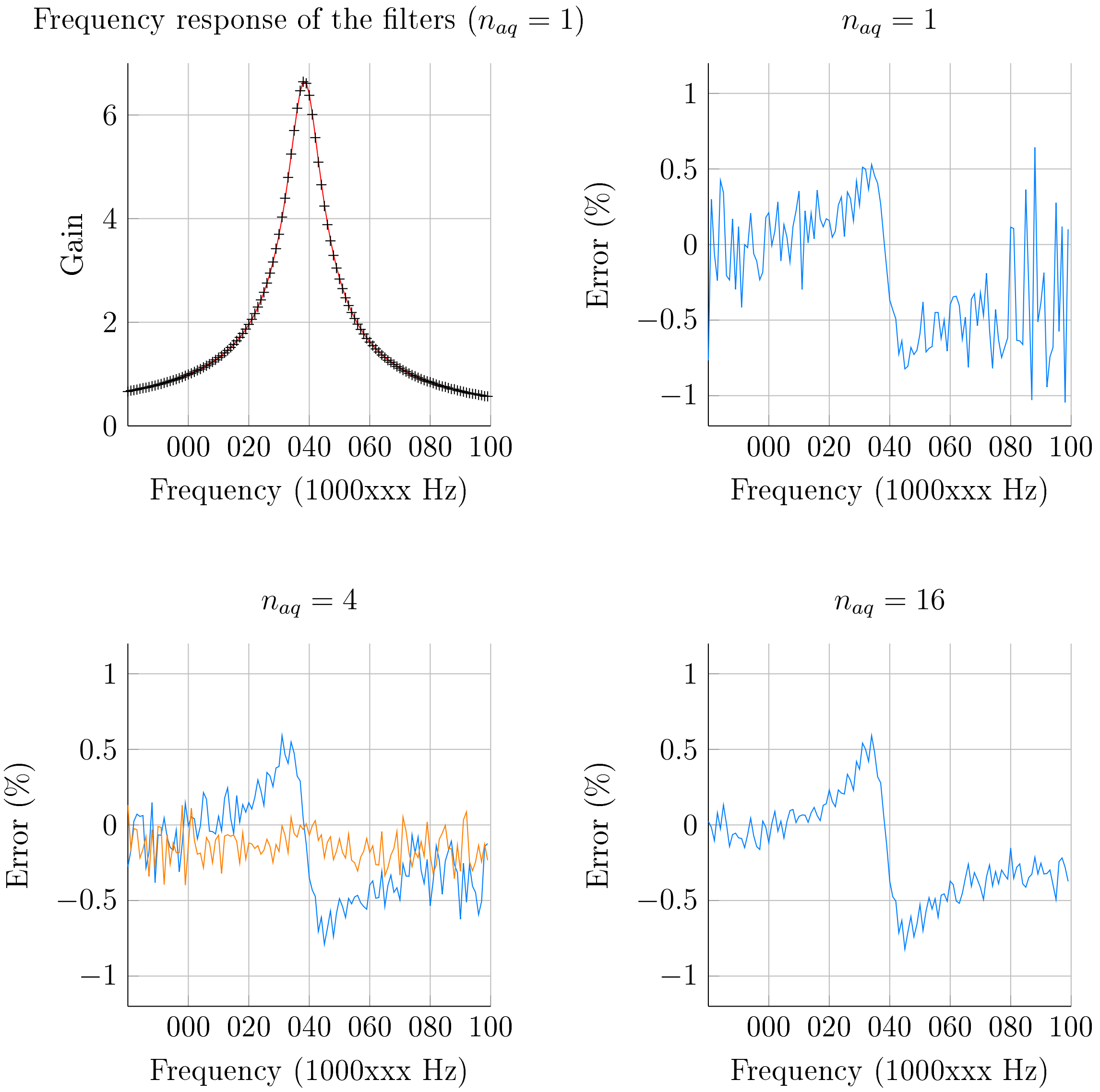

Figure 52: Experimental frequency response of the digital filter implemented in the FPGA, extracted from a single acquisition (black crosses), and computed frequency response of the analog filter using Matlab®(red curve). The relative differences between experimental and theoretical data is also plot in blue for different values of n_{aq} (averaging), along with a corrected version in orange, where the clock value used in the filter coefficient is slightly modified in order to fit the resonance from the model (124 999 992 Hz instead of 125 000 000 Hz).

We are interested in the amplitude bode diagrams of the digital filter since all the output metrics of ML sensing methods are related to the amplitude response of the resonators. The amplitudes are here calculated and averaged over several periods as follow.

The ”data to ram” block sends the data by slice of 2048 samples when asked by an external routine (webserver). There is thus a time lapse between two consecutive acquisitions, which creates discontinuities in the saved data, called v. Once all the acquisitions are done, the vector v is scattered in smaller arrays w_i. The peak to peak amplitude of the signal is then calculated for each w_i from the difference between the maximum and minimum amplitudes. The length of the w_i is $\frac{22}{10f_r}$ (which corresponds to a little more than two signal periods) in order to avoid fake measurement when the amplitude calculation is done over the discontinuity between two acquisitions as mentioned above. The amplitudes are then averaged over all the vectors w_i.

Comment : Another way to measure the amplitude of the signal at the RtF is to calculate its FFT. This option has not been explored, because the method described above yields satisfying results for both the digital filter response and a first demonstration of hybrid ML (see next chapter). However, the reader may keep in mind the data processing might be improved this way in a future work.

The frequency response of the digital filter implemented in the FPGA (still with the parameter values from Eq. 96) is plotted on Fig. 52, along with its analogical equivalent (Matlab®). It can be observed the two signal responses are very close to each other. The relative error is below 1%, but decreases when the number of acquisitions n_{aq} increases (averaging). It has been measured that these frequency sweep over 120 points, executed by the webserver, take 85 s, 200 s and 636 s for $n_{aq} = 1$, $n_{aq} = 4$, and $n_{aq} = 16$, respectively. Knowing that this kind of diagram yields only a single resonance amplitude, these times are those needed for a single measure of mass mismatch (except for measures at fixed frequency) when the sweep is done over 120 points.

Comment : There are between 8 and 9 vectors w_i in v for a frequency of 1 MHz. When there are n_{aq} acquisitions, the averaging is then done over a minimum of $8 \times n_{aq}$ amplitudes.

One can also notice that the average signal error is negative, which means the average amplitude of the digital filter is below the theoretical one. This is due to the sampling that prevents from reaching the actual minimum and maximum values. However, this should not be a problem for ML sensing applications, since these methods are based on differential measurements.

The last observation that can be done on the error signals is their abrupt shift close to the RtF, which is due to a slight RtF difference between both filters. This difference comes from the clock of the Red Pitaya, which frequency does not exactly equal 125 MHz. The clock value used to calculate the filter coefficients has then been slightly modified (a shift of 8 Hz) in order to remove this error shift (orange curve on Fig. 52). This value must of course be adapted when another Red Pitaya is used.

Comment : The experimental response plot on the first graphic of Fig. 52 is extracted from a filter which coefficients were not corrected with a modified clock. The frequency drifts mentioned are in fact quite negligible in relation to the bandwidth.

The pairs of problems/solutions treated in this chapter are reminded in Table 7.

Table 7: Summary of the difficulties met during the implementation of the third order IIR.

Problem	**Solution**
Timing constraints	Down-sampling (Decimation)
Fake values propagating in the FPGA due to a change in the filter coefficients	Automatic switch on the IIR output feedback
Stability and accuracy of the filter	Floating point method on the filter coefficients (n_0)
Correlated noise	Additional floating point implementation on the data flowing though the IIR (n_1)
Wrong experimental value of the resonant frequency	Modification of the clock value allowing to calculate the filter coefficients
Noise	Averaging over several periods

Chapter III in a nutshell

The third chapter exposes a new way to design and implement ML. The main limitations of ML implementation being the initial mistuning of the resonators, the coupling value and the geometry of the resonators, an original solution is being proposed based on a digital approach. A hybrid system coupling a mechanical and a digital resonator is proposed. To this purpose, a third order IIR filter was here successfully implemented in the FPGA of the Red Pitaya hardware. This filter is designed to be configured as a high Q-factor (100 000) resonator of RtF ranging from 1 MHz to at least 2 MHz for ML purposes (displacement-like filter output). After fine tuning of different parameters, correlated noise along with filter coefficients errors were minimized. The frequency response in amplitude of this filter yields a relative error smaller than 0.5% around the RtF. This result is very satisfying for our need to adapt this filter response to a QCM based resonator, which is presented in the next and last chapter.

En essayant continuellement on finit par réussir. Donc plus ça rate, plus on a de chance que ça marche.

Jaques Rouxel, dans Les Shadoks

Chapter IV

Implementation and characterization of mode localization on hybrid resonators for mass sensing purposes

In this last chapter, we detail the experimental implementation of ML in a hybrid system based on a QCM and a digital resonator. The architecture of the electromechanical resonator along with the one of the entire digital system are firstly given. The implementation of ML is then exposed, both by the mean of a virtual perturbation (digital-equivalent of a mass) and a real mass mismatch. The results are finally discussed and compared.

IV. A Design and characterization of the hybrid coupled system

This section firstly describes the design and fabrication of the QCM based resonator before giving the details of the general digital circuit implemented in the FPGA. Finally, a characterization of the entire system is carried out.

IV. A. 1 QCM based filter

IV. A. 1. a Architecture of the circuit

The fabricated electrical circuit including the QCM is depicted on Fig. 53 and its architecture is detailed in the following sections.

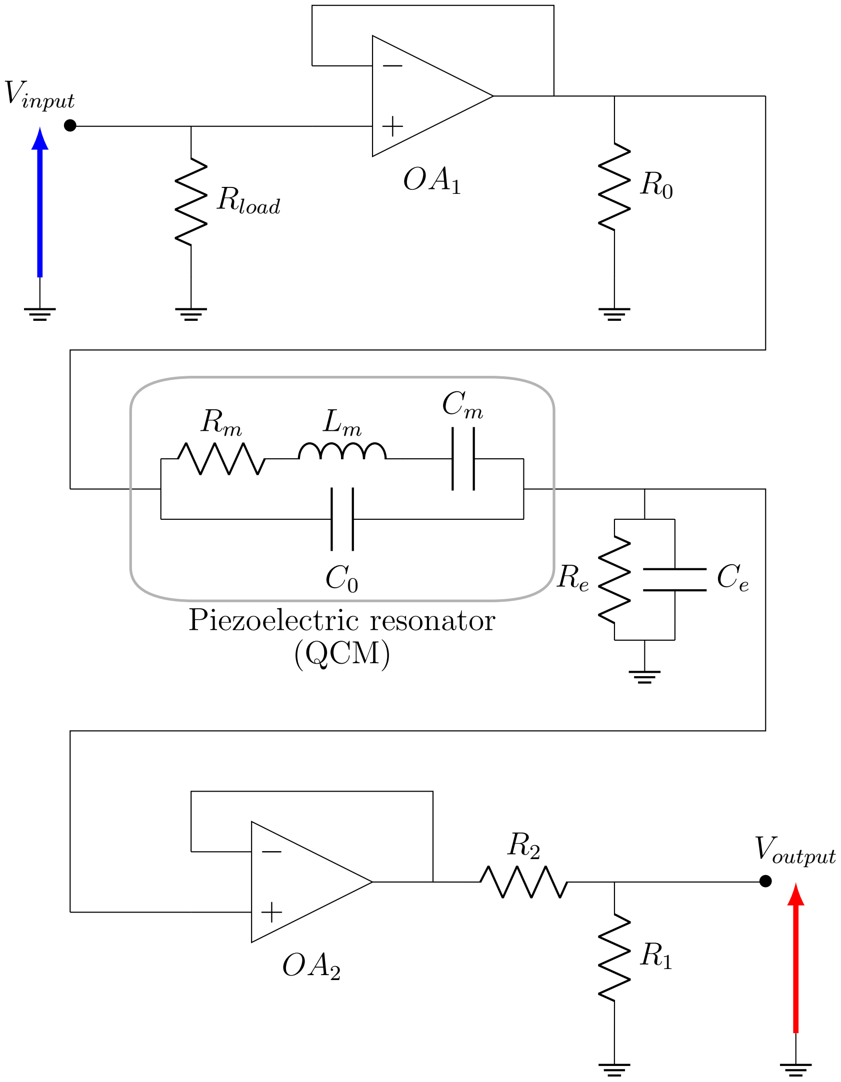

Figure 53: Detailed circuit of the QCM based filter

IV. A. 1. b QCM input

The input signal of the filter is the output of the Red Pitaya DAC. The Red Pitaya being designed to supply circuits of impedance equal to 50 Ω (impedance load given in the specifications of the board, see [276]), there is a need to add a 50 Ω parallel resistor before the QCM (R_{load}). In order to ensure that the impedance of the rest of the circuit is constant and high enough compared with R_{load}, a first voltage follower OA_1 is set up between R_{load} and the QCM. This voltage follower is implemented with *operational amplifiers* (OA) which have, in theory, an infinite input resistance and an output resistance equal to zero. It is indeed necessary to keep away from a short circuit configuration at the terminals of the DAC, especially at a frequency close to the RtF where the impedance of both the QCM and R_e / C_e are low (since $g_3 \ll 1$). Such an undesired condition occurs experimentally when OA_1 is removed.

IV. A. 1. c QCM output

As mentioned in the previous chapter, the output impedance given by R_e and C_e must have a cutoff frequency lower than the RtF of the filter (condition $g_3 \ll 1$) in order to get an output impedance close to a single capacitance near the resonance (impedance of R_e and C_e given in Eq. 110).

$$\begin{cases} Z_e = \dfrac{R_e}{1 + j \cdot \frac{\omega}{\omega_e}} \\ \omega_e = \dfrac{1}{R_e \cdot C_e} \end{cases} \tag{110}$$

This condition can be written as

$$R_e \cdot C_e \gg \frac{1}{2\pi \cdot f_0} \tag{111}$$

In order to have the same setup for different QCMs of RtF starting from 1 MHz, the previous condition can be rewritten as

$$R_e \cdot C_e \gg 2 \times 10^{-7}\,\mathrm{s/rad} \tag{112}$$

The input impedance of the Red Pitaya ADC is a resistance of 1 MΩ in parallel with a capacitance of 10 pF [276], and their product is equal to 1×10^{-5} s/rad. If we consider the case where they play the role of R_e and C_e (QCM output directly connected to the Red Pitaya ADC), Eq. 112 is satisfied and the resulting filter works experimentally. However in this case, there is no control on the output amplitude which may not exceed 1 V because of the ADC voltage range : it is thus necessary to add a voltage divider stage between the QCM output and the ADC. As a consequence, the ADC impedance can no longer correspond to C_e and R_e : an additional capacitor and resistor must be introduced before the voltage divider.

The voltage divider consists of two resistors R_1 (tunable) and R_2 (fixed). If these two resistors are connected just after the QCM output, their impedance must be sufficiently high with respect to C_e and R_e so as not to disturb the behavior of the output (especially the Q-factor and the phase at the RtF). However, this impedance must also be low enough compared with the ADC impedance. This need for an impedance gradient leads to the choice of adding a second voltage follower AO_2 between the QCM output and the voltage divider. Therefore, the only condition that remains for R_1 and R_2 is that they must be low enough compared with 1 MΩ. Thus, the values of $R_1 \in [0..2\,\mathrm{k\Omega}]$ and $R_2 = 1\,\mathrm{k\Omega}$ were chosen.

This output division must of course be compensated within the FPGA (multiplication with a tunable value). The NCO and ADC/DAC are 14-bits coded for a maximum signal amplitude of 1 V. Since the gain of the resonant filter at the RtF is close to 10 (Fig. 52), 6 additional bits allowing to code numbers 64 times greater is sufficient. For this reason, the digital filter output is coded on 20 bits $(14 + 6)$. Since the input of the filter is a linear combination of the NCO and the filter outputs, the input is also coded on 20 bits.

IV. A. 1. d Choice of the operational amplifier

The two main characteristics to consider when selecting an OA for a specific application are the *gain-bandwidth* and the *slew rate*. With the chosen physical parameters of the filter, the maximum gain G at the resonance do not exceed 10 which, at a frequency of 2 MHz, requires a gain-bandwidth of 20 MHz.

The output signal at the RtF is defined by (without considering any phase)

$$x(t) = G \cdot \sin(\omega_r \cdot t) \tag{113}$$

The maximum output voltage variation is defined by the derivative of the signal with respect to time, therefore the slew rate sr must obey

$$sr > G \cdot \omega_r \tag{114}$$

The minimum slew rate can be roughly rounded to $sr_{min} = 200\,\mathrm{V}/\mu\mathrm{s}$.

The OA LT1358 from Linear Technology has been chosen because it has a slew rate of 600 V/μs and a gain-bandwidth of 25 MHz [286].

The setup depicted on Fig. 53 without R_0 experimentally generates an unstable output signal. Indeed, the high input impedance of OA_2 reflects a part of the incoming electrical waves which travel back to OA_1. Since its output is connected to the inverting input, the high gain of the OA makes OA_1 react to this wave, and send a new one forwards, and so on : an unwanted oscillator is created between both OAs. This is only possible because of the high slew rate, otherwise this wave would be filtered by OA_1. Therefore, an additional tunable resistor R_0, close to 50 Ω, is added after OA_1 to absorb the wave returning from OA_2. This arrangement has been experimentally validated.

IV. A. 1. e Selection of the QCMs

The selected QCM for the experiments [287] has a RtF of 1.8 MHz. It is packaged in order to be in vacuum, and will be called S_1. S_1 can be opened by simple dicing for mass deposition, and this second configuration is called S_2. A picture of the QCMs is given on Fig. 54.

The BVD of S_1 and S_2 are given in Table 8 and their admittance module and phase are plotted on Fig. 55 for illustrating purpose. Each of this information was measured using an impedance analyzer which main characteristics are given in annex 7.

Table 8: Electrical characteristics of S_1 and S_2 (BVD) and values of the resulting parameters.

	R_m	L_m	C_m	C_0	f_0	Q	g_1
S_1	102 Ω	1.06 H	7.05 fF	3.19 pF	1.84 MHz	120 000	0.00220
S_2	135 Ω	1.15 H	6.48 fF	2.83 pF	1.84 MHz	98 600	0.00230

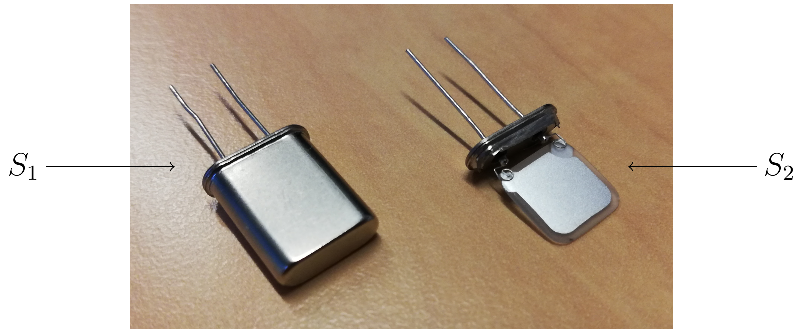

Figure 54: Photography of two QCMs. The one on the left, called S_1, has a RtF of 1.8 MHz, and the one on the right, called S_2, is S_1 without its packaging. S_2 has slightly lower Q-factor and RtF because soaked into gas.

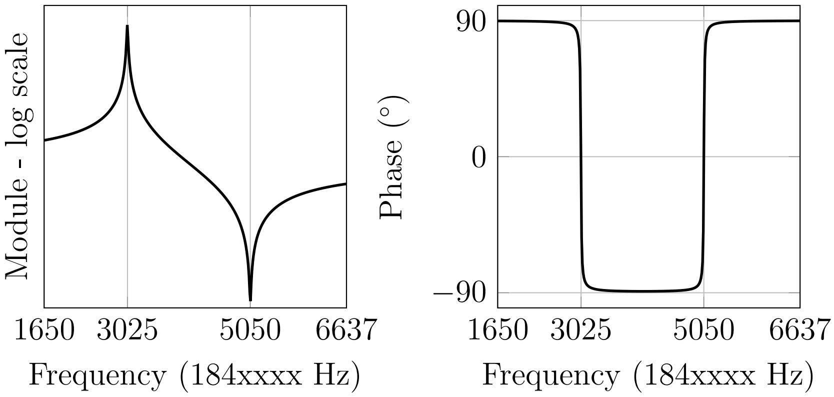

Figure 55: Experimental module and phase of S_1 admittance.

Comment : The impedance analyzer can also be used to plot the simulated impedance gain and phase out of the parameters given in Table 8. The measured impedance and the simulation are superimposed on the analyzer screen.

IV. A. 1. f Choice of the components

The last issue to tackle before the fabrication of the QCM based filter is the choice of the values of C_e and R_e and thus, the determination of g_2 and g_3 for a given QCM. Equation 112 gives a first theoretical limit. Different values for both of the components were tested experimentally on a test board, which revealed additional constraints. Table 9 gives a few observations on the filter output.

The mentioned theoretical limit is visible in red and orange in this table. The indication ”Low Q-factor” points out that the electrical current partly flows though the resistance, which means that Equation 112 is still not satisfied.

Since the comments in blue and green in Table 9 correspond to a domain where Equation 112 is satisfied ($\omega_e \ll \omega_0$), the modulus of the output impedance Z_e is in inversely proportional with C_e (Eq. 110). Therefore, high values of C_e lead to very low output amplitudes, and low values of C_e trigger high output amplitudes and thus voltage saturation of the Red Pitaya ADC.

Table 9: Qualitative experimental observations of the output signal of the QCM based filter. The red color indicates a theoretically forbidden zone. The orange one is at the limit of the condition required by Eq. 112. The blue ones correspond to configurations that lead to unwanted experimental behaviors of the system and the green one is the chosen configuration.

C_e R_e	10 pF -	100 pF -	1 nF -
1 kΩ	$R_e \cdot C_e <$ $2 \times 10^{-7}\,\mathrm{s/rad}$	$R_e \cdot C_e <$ $2 \times 10^{-7}\,\mathrm{s/rad}$	Low Q-factor + Low amplitude
10 kΩ	$R_e \cdot C_e <$ $2 \times 10^{-7}\,\mathrm{s/rad}$	Low Q-factor	Low amplitude
100 kΩ	Low Q-factor + Saturation	OK, slight negative offset	Low amplitude + Slight negative offset
1 MΩ	Saturation + Strong negative offset	Strong negative offset	Low amplitude + Strong negative offset
∞	Saturation + Strong negative offset	Saturation + Strong negative offset	Saturation + Strong negative offset

The presence of R_e is theoretically not a necessity since we aim at reproducing the behavior of a single capacitance. Its absence ($R_e = \infty$) however leads to experimental signal saturation and the appearance of a strong negative offset. No extensive study has been done here to find out the origin of this phenomenon and quantify it. However, it is most likely due to a non ideal behavior of the OAs, that also have some input and output capacitance. These undesired interactions lead to an unwanted charge of C_e over time. The addition of the R_e prevents this presumed phenomenon to happen (it allows the capacitance to discharge), as long as its impedance is not too high (experimentally 100 kΩ maximum).

Finally, the chosen configuration that enables to integrate the signal (additional phase of $-\frac{\pi}{2}$) while keeping a high value for the Q-factor is given in Eq. 115.

$$\begin{cases} R_e = 100\,\mathrm{k\Omega} \\ C_e = 100\,\mathrm{pF} \end{cases} \tag{115}$$

IV. A. 1. g Fabrication

The different components of the QCM based filter have been hand-soldered on a prototype board which is screwed onto a 3D printed base. SMA connectors are used to connect the device to the rest of the system. A commented picture of the device is given on Fig. 56.

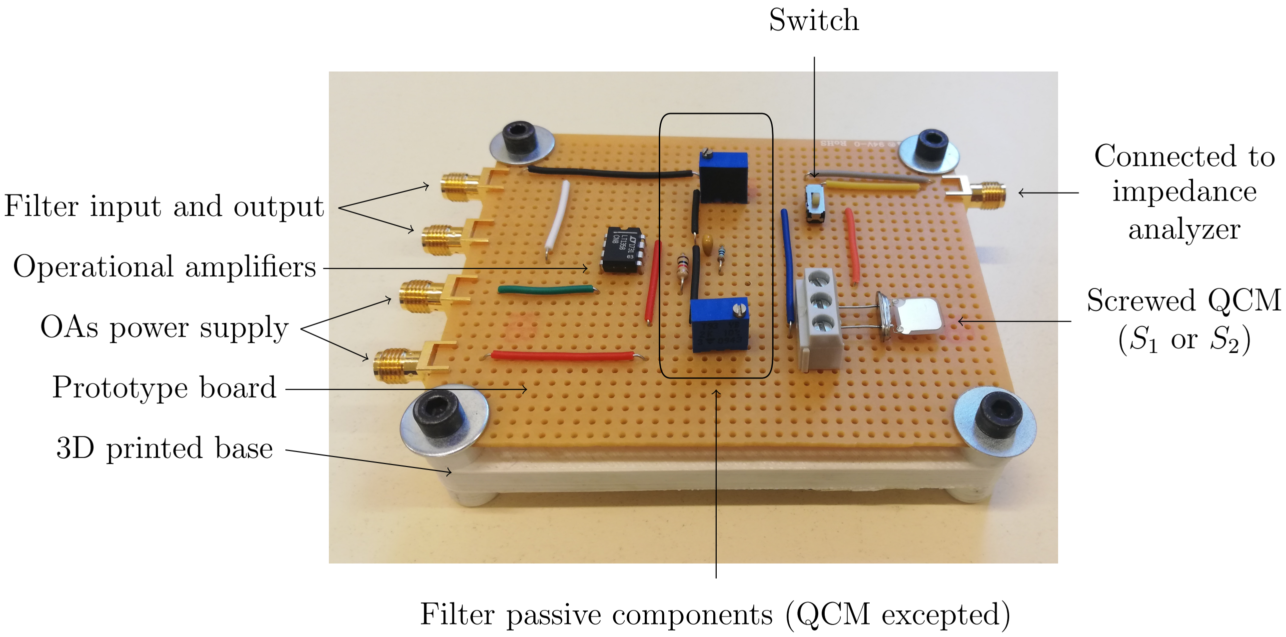

Figure 56: Picture of the fabricated QCM based resonator standing for resonator 2 in the system. The QCM is set horizontally in order to facilitate further mass fixation on its surface through a liquid drop deposition, and a switch has been added to enable the QCM to be connected either to the rest of the filter or to an impedance analyzer. The QCM can be easily changed since it is fixed with simple screws.

IV. A. 1. h Filter frequency response

The response of the QCM based filter indeed corresponds to a resonator which displacement is observed (phase of −90°at the resonance), but contrary to what was done in chapter III, no additional experiments were conducted to characterize this filter in detail (especially the comparison with the Matlab®model). Indeed, many uncertainties may lead to a mismatch between the model and its implementation (quality of the hand-made soldering, non ideal OAs, and so on). The need to implement a filter having the exact response expected is not mandatory here, since the digital resonator, which has been proved to be very versatile and accurate in its frequency response, can be tuned to fit the resonance of this QCM based filter. The actual values of the analogical filter parameters can even be known throughout the tuning of the digital resonator.

IV. A. 2 Design and characterization of the FPGA logical circuit including both analogical and digital filters

IV. A. 2. a Implemented circuit

A sketch of the entire system is depicted on Fig. 57. The NCO generates a sinus or a cosinus signal on 14 bits with tunable frequency. A sinus from the NCO is chosen to be the reference for the phase (and so the delays). Each mathematical operation (addition or multiplication) requires one register that releases data every d samples like in the digital filter presented in chapter III (the same rythm is given to all the operations). The corrector contains both an addition and a multiplication since its role is to multiply resonator 2 output by the inverse gain of the voltage divider R_1 and R_2 from Fig. 53, and it also compensates the negative offset with an addition. The DAC and ADC have a delay of a few dozen of nanoseconds (knowing that a time sample lasts 8 ns) denoted α_1 and α_2, respectively. Resonator 1 introduces a delay of $5.d$ (it corresponds to the delay between the input and output signals that can be counted on Fig. 48) and it is considered that resonator 2 does not add any delay. Two additional tunable registers were added to balance these delays, as explained further.

Comment : An automatically controlled switch is added in the coupling loop to avoid potential signal divergence when the values are updated in the FPGA (same function H_3 from Fig. 48).

The coupling block is implemented again using floating point method (pre-multiplication by $2^{integer}$ and a right bit-shifting in the FPGA). Finally, the total size of the project in the FPGA is slightly below 50 % (block-RAM, LUT and digital signal processors), which lets enough space for a second digital filter for a potential 3 DOF implementation.

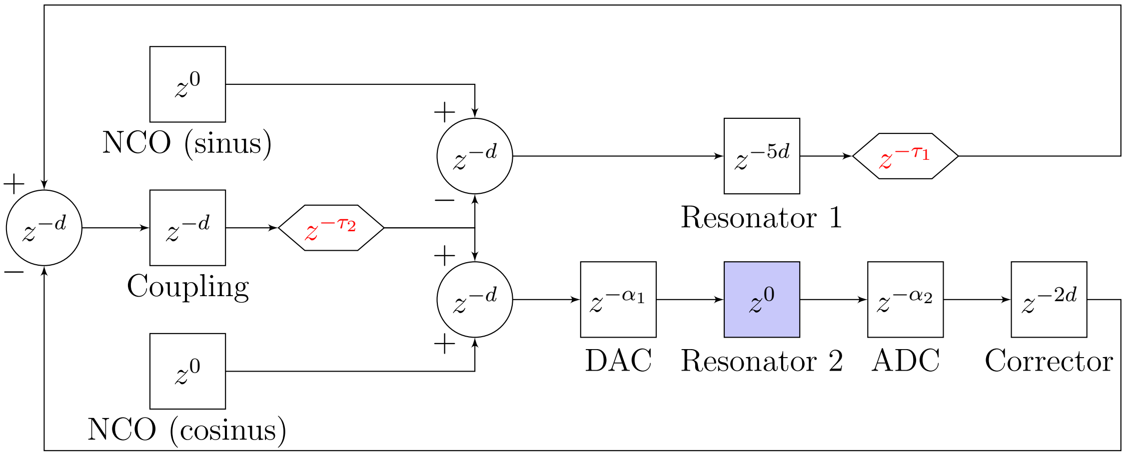

Figure 57: Global sketch of the coupled system, including the delays corresponding to each operation. The only non digital element is resonator 2 (QCM based filter), in blue. Tunable delays were added for timing compensations, in red.

IV. A. 2. b Frequency of the second mode

Because the system is coupling two resonators which model is the BVD and not the classic damped resonator, the frequency of the second mode does not obey the expression given in annex 1 $\left(\sqrt{\frac{k+2k_c}{m}}\right)$. Instead of tending towards infinity when the coupling stiffness does so, it tends to the parallel resonance, as depicted on Fig. 58. This particularity does not represent a problem as long as the series and parallel resonances of the chosen resonator are separated by a frequency gap much larger than its resonance bandwidth (which is the case of our QCM).

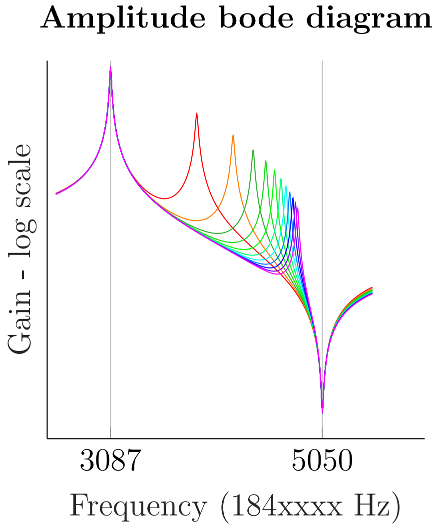

Figure 58: Simulated amplitude Bode diagram of the coupled system with two resonators S_1 excited with a phase of 90 degrees for different coupling values κ which range from 1 (in red) to 100 (in purple), going through the rainbow colors. Only resonator 1 is here represented because the response of the second resonator is very similar for such high coupling values.

Comment : Another consequence of this difference is the notion of ”weak coupling”. Indeed, ML occurs when the resonances are close in terms of frequency, which corresponds to a very low value of κ (until $\frac{1}{Q}$) in the case of the damped resonators system. However here, a given frequency gap between both modes corresponds to a higher value of κ.

IV. A. 2. c Compensation of the filter delays

Since the two filters are implemented differently (one being digital, and the other electromechanical), the signals flowing through them are not delayed equally. Indeed, the number of time samples taken by a signal to flow through the digital filter is $5.d$, whereas that of the analogical filter is $\alpha_1 + \alpha_2 + 2d$. Therefore, it is necessary to compensate this imbalance by the addition of a register with a tunable delay τ_1. When $d = 2$, τ_1 experimentally reaches a value of $\tau_1 = 13$.

Comment : The OAs also come along with slight additional delays that are also compensated with τ_1.

IV. A. 2. d Compensation of the coupling delay

Because of the different delays, the coupling contribution ($\kappa \cdot (u_1 - u_2)$) is not added instantaneously with the NCO signal, as it should be according to the differential equations of the coupled system. However, the existence of this delay generates instability. Since this delay cannot be compensated like in the case of the two filters, the idea is to increase this delay enough to be in phase with the next period, since the system is working in sinusoidal regime. Indeed, an additional phase of $2.\pi$ does not influence the steady state. Therefore, another register with a tunable delay τ_2 is added after the coupling. The value of τ_2 of course depends on the frequency. For a RtF of around 1.8 MHz, $\tau_2 \simeq 40$.

When the coupling contribution is slightly in advance over the NCO signal (τ_2 is too low), the second mode has a lower amplitude than it should have ($\tau_2 = 38$ on Fig. 59). In contrast, when τ_2 is too high, the coupling feedback is added with a certain delay to the NCO signal, which generates a higher amplitude of the second mode ($\tau_2 = 40$ and $\tau_2 = 42$), and this phenomenon is stronger when κ increases as depicted on Fig. 59. However, the value of τ_2 does not affect the first mode since the coupling feedback is not involved in this case.

The chosen value for τ_2 is 40 since the second resonance for this value is the closest to the theoretical one, even though this configuration triggers amplitudes slightly higher compared to the theoretical predictions.

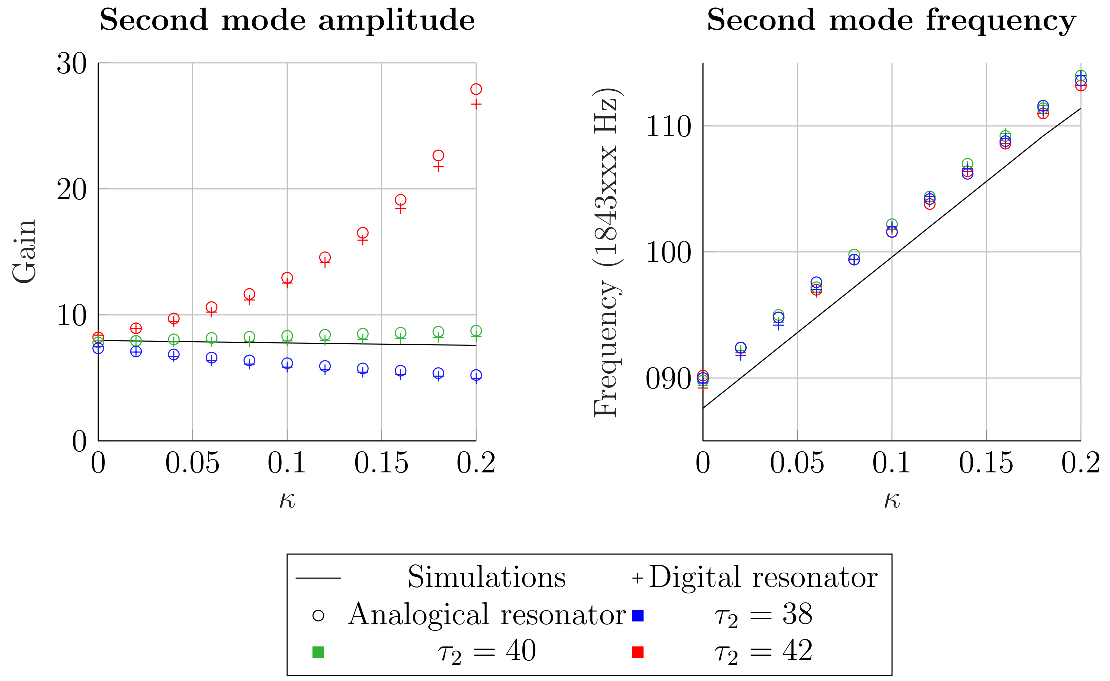

Figure 59: Theoretical and experimental out-of-phase mode amplitude and frequency for different values of coupling κ and delay τ_2. For these simulation and experiments, the resonators inputs are out-of-phase (only the second mode is excited). The values of τ_2 are even because $d = 2$ (odd values yield identical results since the calculations are done one time sample out of two). The amplitude depends on τ_2, which is not the case of the RtF that is slightly higher than the predictions (around 2 Hz, most likely due to an initial slight imbalance between the resonators).

Comment : It could be considered to make a filter which output (here called *out*) represents the electrical current (resistor at the output of the filter instead of a capacitor) or its derivative with respect to time (inductor at the output). Indeed, these physical quantities are in advance over the electrical charge, like velocity and acceleration over displacement in mechanics. Thus, this advance could be used as a compensation of the delays in the coupling loop. In addition with a gain tuning (there is a factor ω between each of these physical quantities), the coupling contribution $\kappa \cdot (out_1 - out_2)$ could indeed represent a linear combination of the output displacements $\kappa \cdot (x_1 - x_2)$ close to the resonance. However, this method has the drawback to diminish the Q-factor when the output of the filter is a simple resistor, but this problem should not exist with an inductor (if assumed to be perfect). This method could be interesting to implement although it has not been the case in the present work.

IV. B Implementation of mode localization in the hybrid system

In this section, we first present the method for manually setting the digital filter parameters to match the frequency response of the analog filter. Mode localization is then implemented successively with a digital perturbation and a mass perturbation[1]. The results are then discussed and the performance of the system is compared with that found in the literature.

IV. B. 1 Initial tuning

As mentioned earlier, the electrical properties of the QCM are first determined using an impedance analyzer (R_m, L_m, C_m and C_0). Then, the different parameters are calculated and entered into the digital filter within the FPGA. Some of them are manually and slightly modified to fit the resonance of resonator 2 (the QCM based filter) and finally, a non-zero coupling value is applied. A detailed protocol aiming at the tuning of the system is given in Table 10.

Comment : Fitting the frequency response of the digital resonator to that of the QCM-based filter is quite difficult to do over a wide range of frequencies since there are many parameters to tune by hand. Nevertheless, the responses should be as identical as possible in the vicinity of the two resonances. Thus, if a parameter is not assigned the value it should have, another one can compensate for this drift close to the resonances. The operator therefore has a certain freedom to adjust the system by hand. For instance, parameters g_1, g_2 and g_3 have fixed values because they influence different characteristic quantities of the response at the same time (RtF, resonance amplitude...), which makes them very difficult to adjust. However, they may not have the exact right value, which can be compensated by a fine tuning over other parameters such as f_0 or Q, still close to the resonances.

IV. B. 2 Digital perturbation

IV. B. 2. a Setup and method

The Red Pitaya communicates both with the QCM based filter (in real time) and with the computer when requested by the operator, as depicted on Fig. 60. The QCM used in this first setup is S_1 (in vacuum).

---

[1] The method and its implementation detailed in chapters III and IV has already been described in one of our works, but applied on low frequency (a few kHz) and low Q-factor (a few dozen) RLC resonators [1]. These results are not presented here because they only provide an intermediate outcome in demonstrating the method. This preliminary implementation was quite similar (it was only a second-order filter and not a third-order filter), except for why correlated noise appears, and how to get rid of it. Indeed, the low Q-factor of the RLC resonator makes the filter less sensitive to the rounding effect of the right bit-shifting from the floating point method (block 36 from Fig. 48). Therefore in this case, there is no need to increase the number of digits of the IIR feedback (blocks 20 and 32 from Fig. 48). However, the low frequency of this type of filter increases the number of samples per period. The difference between the output values of two consecutive time samples is thus much smaller, resulting in a large estimate of its true value, which is called oversampling. Therefore correlated noise occurs, which can be suppressed by increasing the decimation factor d.

Table 10: Tuning protocol of the coupled hybrid system

Step	Parameter(s)	Comments
1	$\kappa = 0$	A zero coupling must be applied before the tuning.
2	R_1 (not digital)	The output resistance of the QCM based filter must be tuned to set the resonance amplitude to less than 1 V (limit imposed by the ADC of the Red Pitaya).
3	Clock	The clock value used in the calculation of the filter parameters must be adjusted according to the filter simulations, as explained in the previous chapter.
4	n_0, n_1, d	These values were selected in the previous chapter.
5	Corrector offset	The mean value of the QCM based resonator, which has a slight negative offset, must experimentally be equal to zero.
6	g_1, g_2, g_3	This set of values is given by the design of the QCM based filter. It is not intended to be strictly identical to that of the QCM-based filter, since other parameters make it possible to compensate for deviations in the vicinity of resonance.
7	Sinus / Sinus	Both excitation signals (NCO) must be in phase for the next tunings.
8	f_0	The resonance frequencies of the two filters must be experimentally identical.
9	Corrector gain	The corrector gain makes it possible to compensate the voltage divider but also to experimentally adjust the resonance amplitude of the QCM-based filter to that of the digital filter.
10	Q	The bandwidth of the two filters must be experimentally identical.
11	-	Repeat alternatively steps 9 and 10 until both resonators have the same frequency bandwidth and resonance amplitude.
12	τ_1	The two uncoupled resonators must be experimentally in phase.
13	τ_2	This value is set according to the study on the coupling delay (to be also adapted with τ_1).
14	Sinus / Cosinus	The two excitation signals are set with a phase of $-\frac{\pi}{2}$ rad in order to observe both modes.
15	$\kappa \neq 0$	The coupling value is eventually tuned to fit the best coupled configuration.

In order to easily illustrate ML and to show that its implementation was successful, the

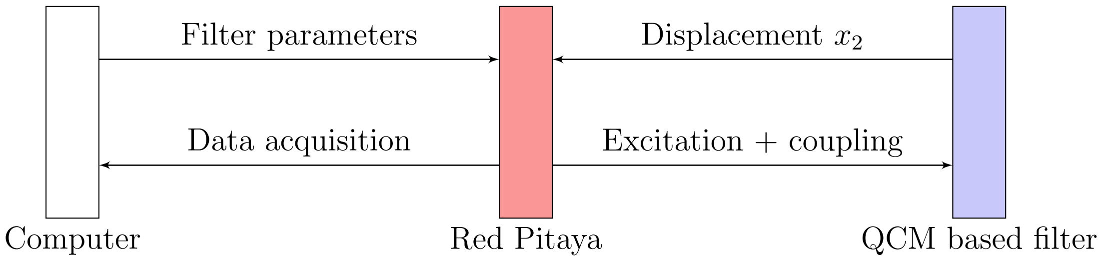

Figure 60: Schematic diagrams of the setup, including acquisition and monitoring systems

perturbations are here applied on the digital resonator.

The simulations allowing comparisons to be made are again carried out in the Laplace domain with Matlab®. Both filters are coupled and subjected to an excitation amplitude A_0 of 0.5 V (not 1 V because the coupling contribution, added with the excitation, may lead to the saturation of the ADC or the DAC) and an excitation phase $\phi_1 - \phi_2 = \frac{\pi}{2}$ with which both in-phase and out-of-phase modes can be observed.

IV. B. 2. b System responses

IV. B. 2. b. i Bode diagrams

As a demonstration of ML, amplitude Bode diagrams are shown on Fig 61, where $\kappa = 0.15$ and $\epsilon \in \{0, 5\,\text{ppm}, 10\,\text{ppm}, 15\,\text{ppm}\}$.

Figure 61 shows that the mode number i is getting localized on the resonator i, $i \in \{1, 2\}$, as the perturbation ϵ on resonator 1 increases, which is very well predicted by the simulations. Besides, it can be observed that the amplitudes of the QCM are lower than those of the digital resonator. This is only due to the sign of the phase $\phi_1 - \phi_2$: the phenomenon is inverted when this sign is changed. Finally, the difference of resonance amplitudes between both modes for a given resonator slightly drifts from the predicted results. This deviation is due to the contribution of coupling in the second mode : the delay $\tau_2 = 40$ makes the second mode amplitude being a little higher, as explained previously (Fig. 59).

IV. B. 2. b. ii Normalized sensitivities

For a better understanding of our results, the normalized sensitivity $NS(i, j)$ is defined in Eq. 116 for resonator i and mode j as the relative shift of resonant amplitude $\delta A(i, j)$ over the relative perturbation shift ϵ. The reference amplitude is the one of a single resonator without perturbation $A_{\epsilon=0,\kappa=0}$.

$$NS(i, j) = \frac{\delta A(i, j)}{A_{\epsilon=0,\kappa=0}} \cdot \frac{1}{\epsilon} \tag{116}$$

This definition allows to draw both theoretical and experimental sensitivity maps as a function of the coupling ratio κ and the perturbation ϵ, as previously done in chapter II.

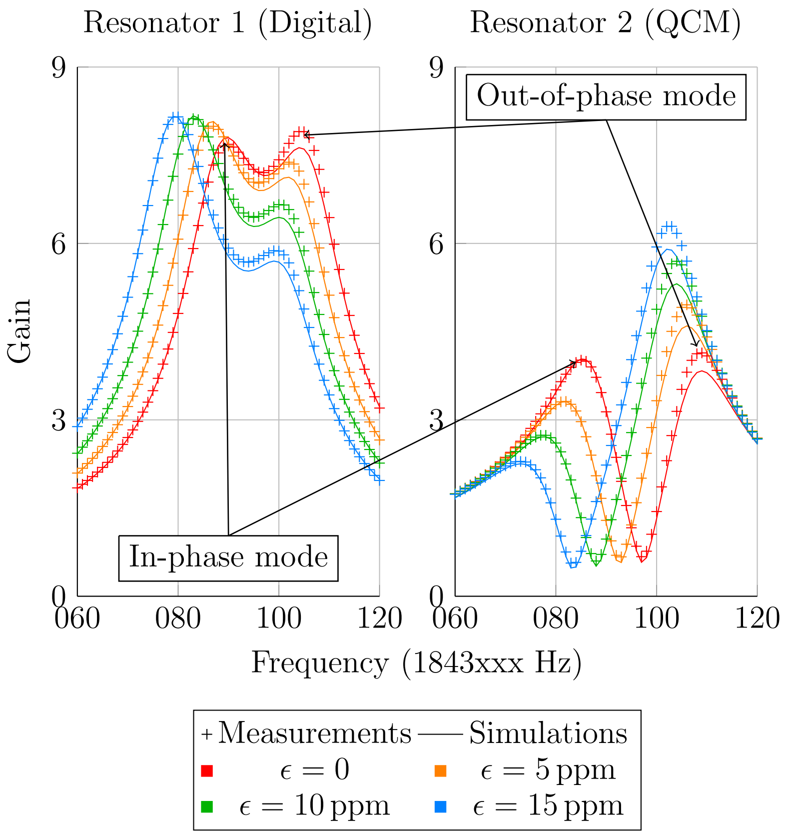

Figure 61: Amplitude of the Bode diagrams of the coupled system digital-QCM for a coupling ratio $\kappa = 15\%$ and different perturbations ϵ applied numerically on resonator 1 : Matlab®simulations versus experimental data. Simulations and experimental results are very close and the frequency gap between both modes is close to the very narrow bandwidth (a few dozen of Hz), which corresponds to favorable conditions for ultra sensitive mode localization.

The results are presented on Fig. 62 and Fig. 63. There is a region where the NS is equal to zero for the second mode of each resonator for low coupling ratio κ. This area corresponds to mode aliasing, where in-phase and out-of-phase modes become undistinguishable. Moreover, in this example, the phase of 90 degrees between both excitations triggers the apparition of an anti-resonance on resonator 2 (Fig. 61), which postpones mode aliasing phenomenon as the coupling κ decreases.

In terms of values, there is a maximal sensitivity (30 000) close to the mode aliasing region and for small perturbations, which is predicted by the theory and our simulations. This value also corresponds to $\frac{Q}{4}$, as explained in chapter II (case of the relative shift of resonance amplitude from a single mode as an output metric).

Since both theoretical and experimental results are very close, the simulations can provide calibration data for our sensor since the NS is not linear with ϵ.

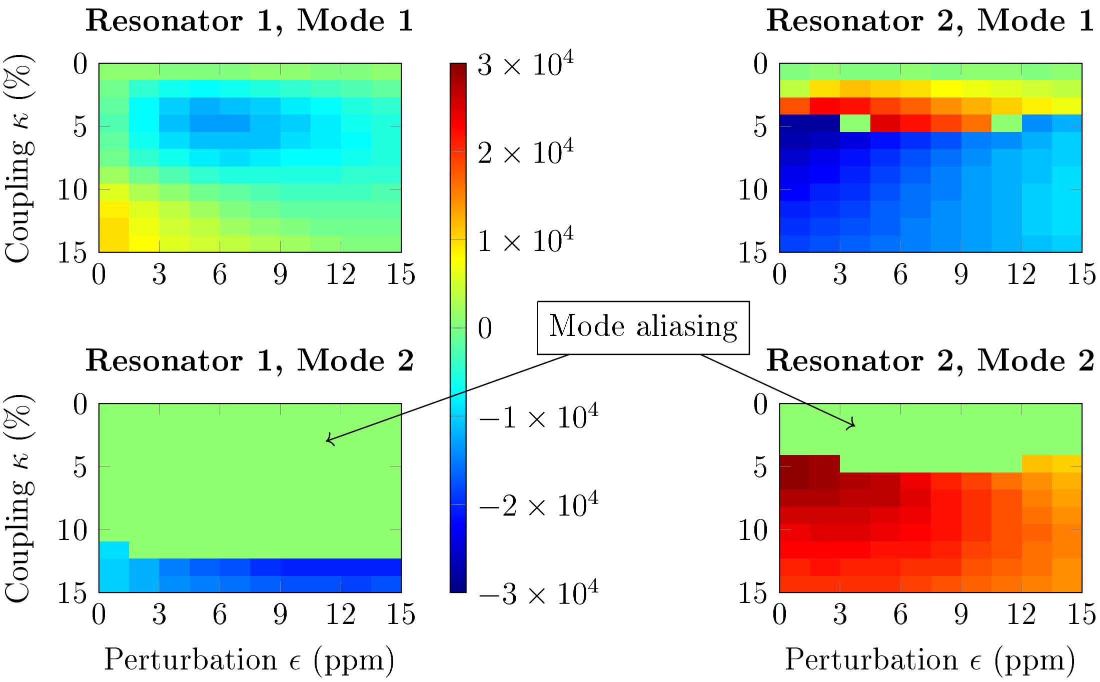

Figure 62: Theoretical normalized sensitivities for both resonators and both modes.

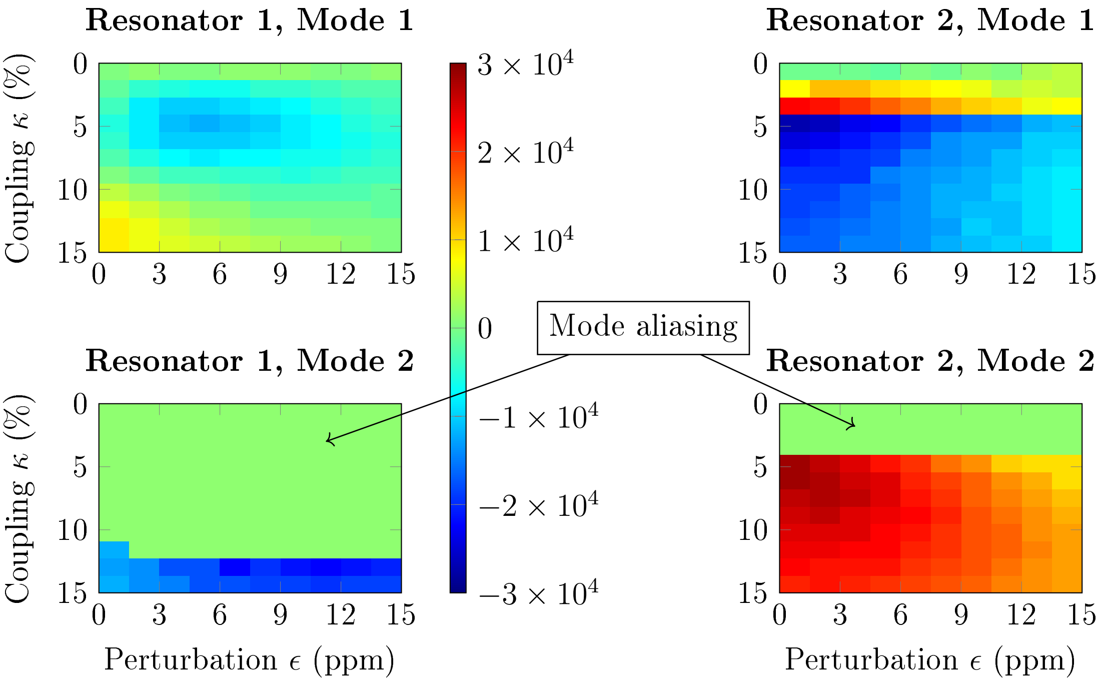

Figure 63: Experimental normalized sensitivities for both resonators and both modes. Extremely high sensitivity (up to 30 000) is reached close to mode aliasing for small perturbations. These results are also very close to the simulations.

IV. B. 3 Mass perturbation

IV. B. 3. a Setup

The second experiment set up to demonstrate ML in our hybrid system uses the QCM S_2 that corresponds to S_1 without its packaging, which enables mass depositions. It has a Q-factor slightly lower because this QCM soaks into air (experimentally $Q = 115\,000$). It can either be integrated into the analog filter or connected to an impedance analyzer, the choice being made through a switch (Fig. 56 and Fig. 64). Therefore, both amplitudes of the coupled system and RtF of the QCM alone can be recorded easily after each mass deposition, without the need to disconnect the QCM from its base. A comparison between both methods is then possible after the experiments.

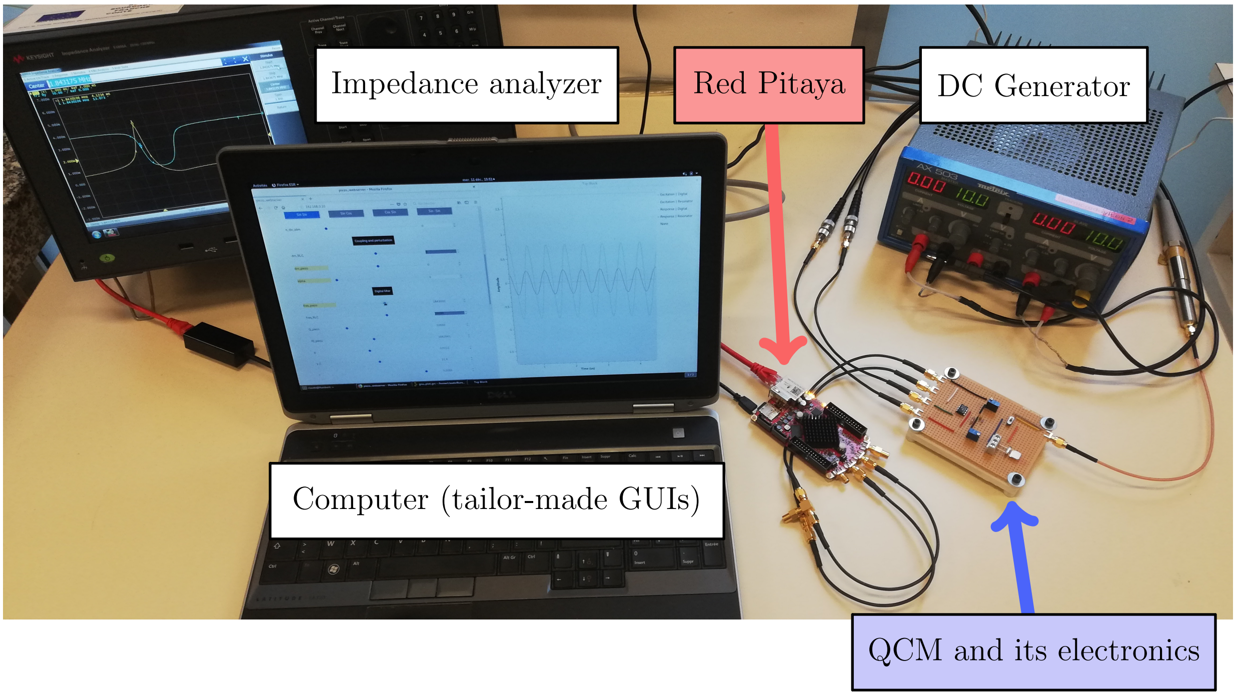

Figure 64: Experimental setup including the piezoelectric resonator, a DC generator, a computer and its GUIs, the Red Pitaya and an impedance analyzer presented in annex 7. The DC generator supplies the OAs.

IV. B. 3. b Mass depositions : method

IV. B. 3. b. i Effective mass

The mass mismatch has so far been expressed as a fraction $\frac{\delta m}{m}$, where the mass m belongs to the equivalent mass-spring model. In a QCM where mass and spring are both represented by the quartz, this mass is not that of the entire quartz but only a part of it : it is called the effective mass, which, in the case of the QCM, can be calculated using the Sauerbrey equation and the RtF sensitivity to mass perturbation, as written in Eq. 117.

$$\begin{cases} \delta m = -\dfrac{A \cdot \sqrt{\rho_q \cdot \mu_q}}{2 f_0^2} \cdot \delta f \\ \dfrac{\delta f_0}{f_0} = -\dfrac{1}{2} \cdot \dfrac{\delta m}{m} \end{cases} \tag{117}$$

where A, ρ_q and μ_q are the electrodes area, density and shear modulus of quartz, respectively.

The combination of these equations leads to Eq. 118, which is the effective mass expression.

$$m = \frac{A \cdot \sqrt{\rho_q \cdot \mu_q}}{4 f_0} \tag{118}$$

In the case of our QCM S_1 and S_2, the electrode is a square of side 7.3 mm, $f_0 = 1.843\,\mathrm{MHz}$, $\rho_q = 2648\,\mathrm{kg\,m^{-3}}$ and $\mu_q = 2.947 \times 10^{10}\,\mathrm{kg\,m^{-1}\,s^{-2}}$, which leads to

$$m = 64.0\,\mathrm{mg} \tag{119}$$

IV. B. 3. b. ii Fluorescent particles

The particles used in these experiments are micro balls of diameter 920 nm in fluorescent resin (the characteristics of these balls are given in annex 7). A colloidal solution of these particles is available, but its concentration (3×10^{11} particles per milliliter) has to be modified to fit some of our requirements. Indeed, the amount of mass to be deposited must be roughly estimated to demonstrate the performances of ML, and the drop size must be chosen to distribute the particles relatively evenly over the surface of the QCM (a required condition to use the Sauerbrey equation).

The sensitive range of our sensor for the output metric of the relative amplitude shift of a single mode is defined to be the perturbation range for which the NS remains high, until half of its maximum value, which roughly corresponds to $\epsilon = \frac{2}{Q}$ (see chapter II). With our Q-factor, this limit can roughly be set around $\epsilon = 20\,\mathrm{ppm}$. In order to stay in the sensitive range, a maximum value of $\epsilon = 15\,\mathrm{ppm}$ is chosen (which is visible on Fig. 62). Given the effective mass of our QCM in Eq. 119, the maximum mass perturbation to be dropped at the surface of the QCM is thus roughly $\epsilon . m = 1\,\mu\mathrm{g}$. For a proper demonstration of ML, five consecutive mass depositions are carried out, requiring $\delta m = 200\,\mathrm{ng}$ to be dropped each time, which corresponds approximately to 3×10^5 particles.

The chosen medium in which the particles should soak is ethanol and not water, both because of its higher wetability with the electrode of the QCM and its higher evaporation speed (experimentally one minute for ethanol and ten minutes for water). The volume of the drop is fixed at $1\,\mu\mathrm{l}$ because such a drop experimentally spreads all over the electrode without overflowing the edge of the QCM.

As a consequence, a dilution of the available solution by a factor 1000 is done (one microliter into one milliliter of ethanol). Thus, a drop of one microlitre of the solution obtained actually contains the 3×10^5 particles required.

IV. B. 3. b. iii Visualization

Since the particles are fluorescent (red light), they can be visualized using a microscope with red lightning, such as the microscope Axio from Zeiss. Different pictures of the surface of S_2 were taken, before and after a drop deposition, and are given on Fig. 65.

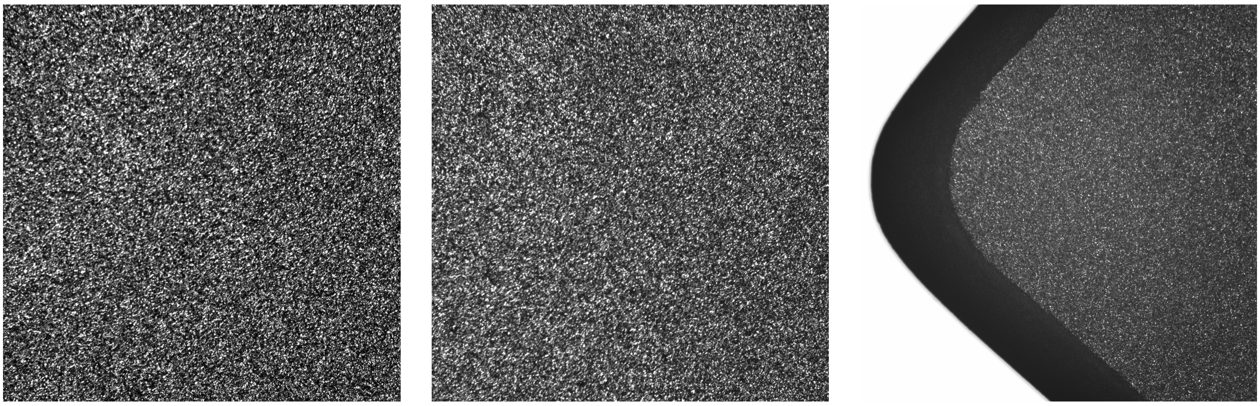

(a) Without balls and fluorescence (magnification of 5)

(b) With balls but without fluorescence (magnification of 5)

(c) With balls but without fluorescence (magnification of 2.5)

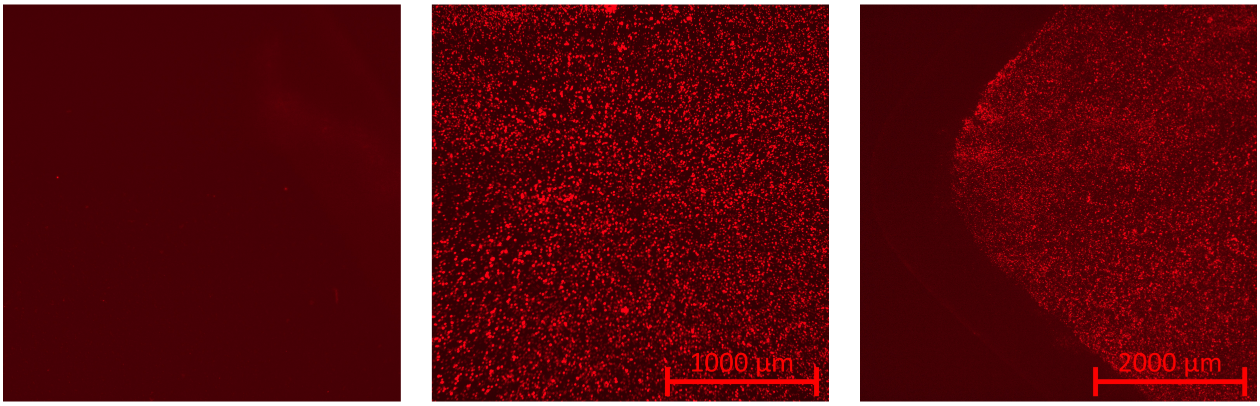

(d) Without balls but with fluorescence (magnification of 5)

(e) With balls and fluorescence (magnification of 5)

(f) With balls and fluorescence (magnification of 2.5)

Figure 65: Visualization of S_2 surface (mainly its electrode) before and after mass deposition (about 300 000 fluorescent balls of diameter 920 nm).

It can be seen on Fig. 65e that the fluorescent balls are homogeneously spread over the metal surface. Furthermore, Fig. 65d confirms that the red dots from Fig. 65e and Fig. 65f indeed corresponds to the particles and are not due to the reflectivity of the metal. The patterns of Fig. 65b and Fig. 65e on the one hand, and Fig. 65c and Fig. 65f on the other hand are very close most probably because the particles are trapped by the roughness of the electrode surface. Finally, Fig. 65f also confirms that the particles are quite homogeneously spread all over the surface, until the edge of the electrode (the dark edge on Fig. 65c being quartz), even though more particles are gathered on the top left corner.

Comment : We're aiming for a deposit of 200 ng per drop. However, only the order of magnitude of the deposited mass is important so as not to exceed around 1 μg after five deposits. Indeed, the exact value of the deposited mass is not of prime importance since a comparison between the ML and RtF shift is performed at each addition of particles.

IV. B. 3. c Responses to mass depositions

IV. B. 3. c. i Description of the experiments

Since the Q-factor is slightly lower for S_2 than for S_1, mode aliasing occurs around $\kappa = 0.15$ on resonator 1, and the NS absolute value for each mode of resonator 2 roughly equals to 2×10^4 in this configuration. This value of coupling is retained for the present experiment, although a slightly higher sensitivity can be achieved for a lower coupling value (let's remind here that the purpose of the present experiment is only to demonstrate ML in our system).

The system is firstly tuned following the protocol described in Table 10. A first frequency sweep is done for $\kappa = 0$ in order to record the resonance amplitude of a single resonator (amplitude reference $A_{r,0}$). Only then a value is given for κ and another sweep is performed to record the two resonances for the balanced configuration ($\delta m = 0$). The switch can be used to disconnect the QCM from the rest of the filter and connect it to the impedance analyzer. This way, the RtF $f_{r,0}$ is recorded for $\delta m = 0$. A drop of 1 μl is then pipetted onto the QCM and left to dry. The RtF is recorded once its value is stabilized, after what the QCM is reconnected to the Red Pitaya (both of the filters being already coupled) and a new frequency sweep is performed around the two RtFs of the coupled system. Fives drops are deposited and the signals are recorded this way, each time using the switch.

This experiment has been successively carried out four times on the same QCM. Between each experiment, the system must be tuned following Table 10, the main modification being a decrease of the eigenfrequency f_0 of the digital resonator.

Comment : Since the perturbation is applied this time on resonator 2, mode 1 localizes on the latter, and mode 2 does so on resonator 1.

IV. B. 3. c. ii Results

Each mass mismatch can be calculated using two different methods throughout Eq. 120 : the RtF shift of the QCM alone or ML in the coupled system.

$$\begin{cases} \dfrac{\delta f_r}{f_{r,0}} = -\dfrac{1}{2} \cdot \dfrac{\delta m}{m} \\ \dfrac{\delta A_{r,i}}{A_{r,0}} = ns_i \cdot \dfrac{\delta m}{m} \end{cases} \tag{120}$$

$\delta A_{r,i}$ is the resonance amplitude shift of mode i, ns_i the NS of ML for mode i, $A_{r,0}$ the reference amplitude, δf_r the RtF shift and $f_{r,0}$ the resonance frequency of the QCM alone.

ns_i corresponds to the NS of the chosen configuration ($\kappa = 0.15$) before mass perturbation, that is $|ns_i| \simeq 2 \times 10^4$. The different δm calculated with both methods are then compared on Fig. 66 for each mass deposition. It can be observed on the left graphic that the results fit relatively well (they follow the function $f(x) = x$), until a perturbation of around 600 ng, over which the mass mismatch evaluated from ML is lower than that from the RtF shift. This phenomenon is due to a drop in the NS value as the perturbation increases. In order to solve this problem, a calibration must be applied. To do so, the calculated mass mismatch from the RtF shift is entered in a Matlab®program that calculates $ns_i(\epsilon)$ for each mass deposition and mode i. These NS values are then used in Eq. 120 to calibrate each data. The corresponding result is plot on the right graphic of Fig. 66. This calibration allows a much better match of the results.

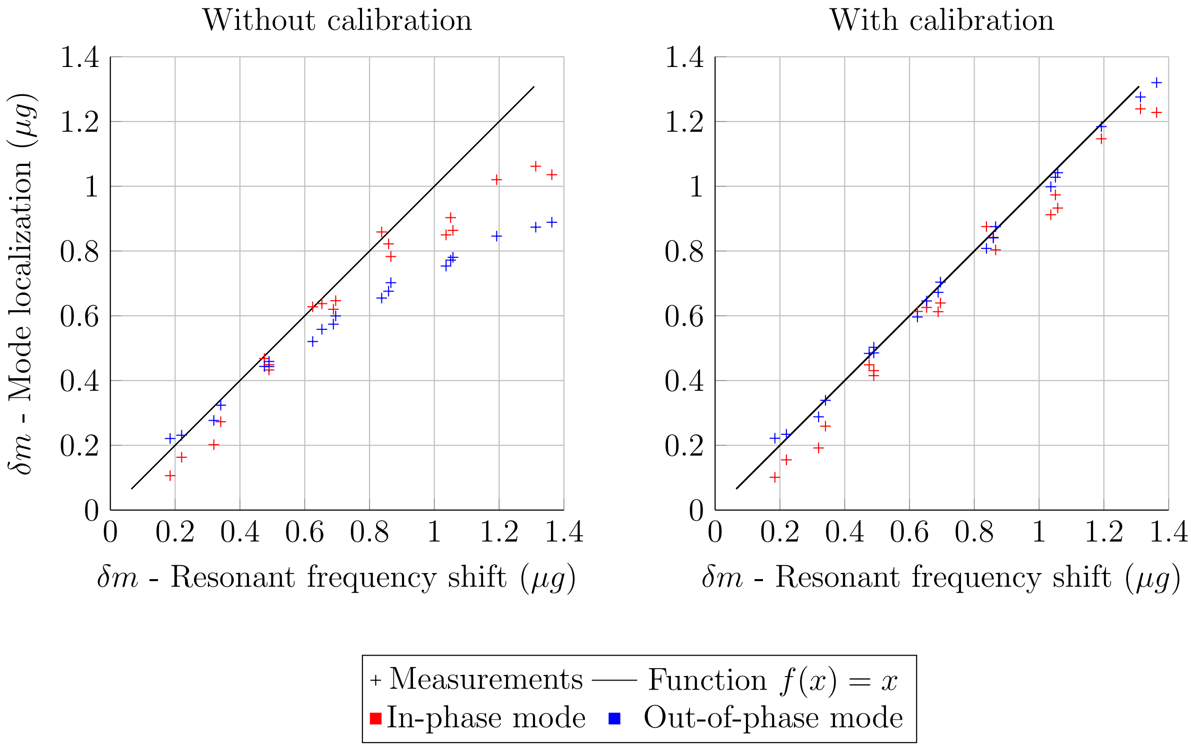

Figure 66: Comparison of the mass mismatch values calculated with two different methods : the RtF shift and ML. The results are shown without calibration using the calculated NS for $\delta m = 0$ (graphic on the left), and with calibration using a variable NS that depends on δm (graphic on the right). All the vibration amplitudes are here measured on the QCM based resonator.

IV. B. 3. c. iii Discussion

Even though the calibration yields satisfying results, a drift between both methods still remains. In order to quantify it, we define D_i for each mode i as the mass mismatch calculated from ML minus that of the RtF shift. Both means values $\overline{D_i}$ and standard deviation σ_i are calculated from the twenty data and given in Eq. 121.

$$\begin{cases} \overline{D_1} = -65.5\,\mathrm{ng} \\ \overline{D_2} = -10.5\,\mathrm{ng} \\ \sigma_1 = 51.9\,\mathrm{ng} \\ \sigma_2 = 21.9\,\mathrm{ng} \end{cases} \tag{121}$$

The average values are both negative most likely because the initial balance in not perfect, which leads to NS values that are actually lower than those predicted by the model.

As for the standard deviations, different causes may explain their relatively high values. First of all, let's remind that the resonance amplitudes are detected throughout an excitation frequency sweep. The accuracy of this measure though strongly depends on the chosen frequency step, which is 0.5 Hz here. Secondly, the SNR is strongly dependent to the averaging factor n_{aq} as shown in chapter III. In this experiment, the number of periods over which the signal is averaged is close to 100. Decreasing the frequency step while increasing n_{aq} should yield lower standard deviations. However, it also drastically increases the time of the frequency sweeps that is already of a few minutes for this acquisition configuration.

The standard deviation also comes from the accuracy of the RtF measurement carried out by the impedance analyzer. The observed frequency variations are around 0.3 Hz, which roughly corresponds to a tenth of the frequency shift for a single mass addition. Once more, this SNR could be decreased by increasing the averaging factor of the impedance analyzer, but this option goes along with longer sweep time which is already around a minute with the averaging factor value chosen in these experiments (16).

These deviations could also been explained by a slow drift of environmental factors such as temperature or humidity, thus leading to a strong mistuning of the system. However, it does not seem to be the case here since no additional deviation of D_i is observed between the first experiment and the fourth one (that is after a coupled of hours).

The fact there are only twenty measurements is the only reason given here to explain that mode 2 yields better results (we think it could have been those of mode 1). Additional experiments should be carried out in the future to clarify this observation.

As a conclusion, ML with real mass depositions has been successfully demonstrated through a comparison with the RtF shift of a single resonator and a calibration of the sensor by the mean of simulation. More accurate results could be obtained (lower standard deviation between the measures) while decreasing the frequency step of the ML frequency sweep and increasing the averaging factor of both ML method and impedance analyzer. However, this solution requires much higher measurement times (so far around ten minutes for each mass deposition).

IV. B. 3. c. iv Limit of detection of the sensor

The last problem to adress is the one of the LOD of our sensor. The standard deviation from Eq. 121 could reasonably stand for an order of magnitude of the LOD. Indeed, when the mass mismatch δm is smaller than the standard deviation, it can be considered that this information is lost below the noise floor whereas above the standard deviation, it can be admitted that the measured signal shift indeed comes from the mass mismatch. As a minimum LOD value, we select the largest standard deviation, that is around 50 ng, which roughly corresponds to $\epsilon_1 = 1\,\text{ppm}$. This standard deviation can also be multiplied by a coefficient representing a level of confidence. For instance the probability that a signal generated by a Gaussian noise (and not the analyte) and which value gets higher than $3 \times \sigma$ above the mean value is 5% [70, 288]. Noise sources should now be clearly identified and analyzed in order to set up a method aiming at increasing the SNR and thus improving the LOD.

One should also take into account that the observed frequency variations over a single RtF measurement was 0.3 Hz, which corresponds to a relative frequency uncertainty of 0.17 ppm. With a NS of $\frac{1}{2}$, the LOD for the frequency shift method is then $\epsilon_0 = 0.33\,\text{ppm}$ with our impedance analyzer settings. ϵ_0 and ϵ_1 being uncertainties of the same order of magnitude, the frequency resolution from this experiment actually corrupts the standard deviations calculated earlier.

Comment : We can also estimate the minimum LOD achievable considering that the ADC and DAC are the only source of noise. Indeed, the peak to peak amplitude is coded on 14 bits, so the minimum relative shift of amplitude reachable is $\frac{1}{2^{13}} = 1.22 \times 10^{-4}$. With a NS of 20 000, the LOD is then $\epsilon_2 = \frac{1}{2^{13} \cdot ns} = 6.11 \times 10^{-3}\,\mathrm{ppm} \ll \epsilon_1$. The ADC and DAC number of bits is thus currently not limiting the resolution during the measurement, but the noise in the ADC and DAC constantly injected in the closed loop might influence the resolution.

IV. B. 4 Short comparison with the literature

This section aims at briefly facing the performances of our hybrid system with those from the literature, based on the main figure of merit used in the mode localization community : the normalized sensitivity. It should be mentioned that in the literature [4], normalized sensitivity is defined for each mode as the relative eigenstate shift modulus. Nevertheless, this definition requires the existence of all the modes on each resonator, which is not the case in configurations where mode aliasing occurs. As a consequence, we have defined in this thesis a sensitivity for each resonator and each existing mode. Still, the two definitions are close enough to compare orders of magnitude.

Firstly, we can see from Table 11 that both resonant frequency and Q-factor of our device are higher than those of other devices using mode localization. Secondly, we can observe that our system is more sensitive than the 2 DoF and 3 DoF systems, which is promising for further improvements of our sensor.

Table 11: Comparison of our hybrid sensor with a few devices using mode localization developed in different teams. Both a previous published work on a QCM of 1 MHz RtF and those from this manuscript are presented here.

Parameter	**Literature**	**This work**
f_0 (Hz)	1.34×10^4 [177] 3.11×10^5 [205] 1.49×10^4 [218]	1.00×10^6 [2] 1.84×10^6 (S_1 and S_2)
Q	[1] 1.34×10^2 [177] [2] 2.12×10^4 [205] [2] 6.22×10^3 [218]	[2] 1.70×10^5 [2] [2] 1.20×10^5 (S_1), 1.15×10^5 (S_2)
Normalized sensitivities		
2 DoF	4.00×10^2 [177] [3] 2.34×10^2 [205]	3.50×10^4 [2] 3.00×10^4 (S_1), 2.00×10^4 (S_2)
3 DoF	[4] 1.36×10^4 [218]	future work

[1] calculated from the bandwidth, [2] in vacuum, [3] calculated, knowing the normalized sensitivity of frequency shift is $\frac{1}{2}$, [4] amplitude ratios as sensor output

Comment : The different measured mass mismatch in this work are relatively high (a few dozen of nanograms) because of the effective mass of the QCM. Indeed, a QCM is a large transducer in comparison with micro-structures such as cantilevers, which can detect masses down to the picogram. The main contribution here, however, is the ratio of this effective mass to the measured perturbation on a structure widely used for mass detection and quantification.

Chapter IV in a nutshell

The last chapter first presents the design of a QCM based filter for mode localization implementation. This filter is designed to be ”plug and play”, in the sense that it can be directly connected to its digital environment, and the QCM can easily be changed. Furthermore, the careful design of the digital circuit enables the successful generation of two vibration modes and the implementation of mode localization between this QCM based resonator and the digital filter. Thus, extremely high normalized sensitivities have been achieved for both digital and mass perturbation, higher than those we found in the literature. Finally, these results are consistent with the simulations for the digital perturbation on the one hand, and with the RtF shift for the mass perturbation on the other hand, which is promising for future developments of hybrid ML. A more detailed discussion of the system’s performance and prospects are given in the general conclusion following this last chapter.

General conclusion

Theoretical results

As planned in the general introduction, chapter II highlights the configurations for which the NS is maximum for a given pair of weakly coupled resonators, in terms of coupling value and Q-factor. Indeed, the optimal NS is proportional to the Q-factor and inversely proportional to the coupling value κ, until mode aliasing occurs. Furthermore, the sensitive range (arbitrary fixed when the NS drops by half) is also inversely proportional to the mass mismatch ϵ.

Chapter II also presents various results on mode localization in identical WCRs through analytical developments and simulations, in particular on the impact of output measurements on normalized sensitivities, LOD and sensitive range : when it comes to consider an output metric based on the amplitude (either amplitude shift or ratio at the resonance for a 2 DOF system, or amplitude shift at fixed frequency for a single resonator), the NS and LOD are in the same order of magnitude for small perturbations ($ns_{max} \in \left[\frac{Q}{4}..Q\right]$). All of them yield a small sensitive range ($\epsilon \in \left\{\frac{1}{Q}, \frac{2}{Q}\right\}$) except for the amplitude ratio ($\epsilon \gg \frac{1}{Q}$), but at the cost of a drastic decrease of the LOD when the perturbation increases because of the drop in SNR. It is also shown analytically that these results seem to be applicable to 3 DOF WCRs, although no extensive study has been conducted in this direction.

Besides, chapter III gives the theoretical basics and a method to design a FIR in series with an IIR of the third order allowing to model high Q-factor resonators. It was shown by the simulation and the experiments that floating point method helps to get rid of correlated noise and yields more accurate filter response.

Experimental achievements

Several milestones from chapter III and chapter IV can be pointed out in the implementation of mode localization on hybrid resonators. There are detailed as follow.

- Digital resonant filter : Successful implementation of a high Q-factor digital resonator using a FPGA. As required in the introduction, it is fully tunable and there is a very good correlation with analytical models (below 0.5% of error on the amplitude). Aside, FPGA data input is monitored throughout tailor made GUIs, as well as data recording and processing.

- QCM based filter : Design and fabrication of a resonant filter including a QCM which output is in proportion with the electrical charge and the mechanical displacement.
- Coupled system : Design and implementation of the hybrid system with tunable coupling and excitation allowing to generate both modes of vibration. The system includes careful compensation of signal propagation delays and is provided with an initial tuning protocol.
- Mode localization on hybrid resonators : Successful generation of tunable mode localization in the hybrid system, both with digital and mass perturbation. There is a very good correlation with the models, especially concerning the superposition of the amplitudes of the Bode diagrams and the maximum reachable NS value of $\frac{Q}{4}$ (relative amplitude shift). The reached LOD is so far estimated to be 50 ng.

Furthermore, the main performances unique to our system can also be listed below. Indeed, our system enables to :

- Generate a second mode of vibration and exploit mode localization on a shear wave resonator widely used in bio-sensing (QCM) with high Q-factor (up to at least 200 000) and high resonance frequency (up to at least 2 MHz).
- Carry out a complete tuning of the digital filter parameters and the coupling value before each experiment. This allows to reach high NS values compared with the literature (until 3×10^4, that is a gain above an order of magnitude) and to get rid of any initial imbalance between the resonators before the measurements.
- Replace the QCM easily and adapt to the geometry of the piezoelectric resonator if needed.

Discussion

The objectives defined at the beginning of the manuscript are completed, and the performances of our system are satisfying in regard to the chosen figure of merit (normalized sensitivity). However, both mode localization in general and our system in its current state have their limits. Indeed, as stated earlier, the decrease in LOD of sensors based on ML over RtF shift has still to be proved for 2 DOF or more despite the high NS of ML, since noise levels are much higher in the case of amplitude than frequency measurements. In this work, the LOD estimated from ML ($\simeq$ 1 ppm) is quite close to the one from the frequency measurements ($\simeq$ 0.3 ppm), and efforts must now be done to improve these performances.

Mass identification is another potential advantage of ML with the design a single input single output sensor [185]. Such a device is composed of N coupled resonators, on which a frequency sweep and a recording of the vibration amplitude of a single DOF is performed. The components of each mode on this particular resonator enables analyte identification, each resonator being functionalized differently. However in our case, all the outputs must be extracted in order to calculate the coupling contribution. Mass identification could thus simply be done with a classic N DOFs uncoupled resonators.

Another advantage of ML is common mode rejection, but the digital nature of one resonator prevents this phenomenon to happen. Indeed, any change in the ambient temperature or pressure affects only the QCM and not the digital filter, thus leading to an imbalance, the localization of energy and a misinterpretation of the measurements. Such an imbalance was however not observed in the time frame of the experiments. Even though our system do not benefit from mode rejection, it is reminded that the system can be balanced before each mass deposition, thus guaranteeing high and known sensitivity by the cancel of any long term drift.

Finally, the main advantage of the presented QCM-based hybrid sensor is what it has been designed for, that is its unprecedented high sensitivity to mass perturbation guaranteed for each mass deposition.

Perspectives

The literature shows that an array of resonators with less stiff external resonators yields higher NS for a given coupling value κ [218]. The resolution of the eigenvalue problem in the case of a 3 DOF system shows indeed that the two first modes gets closer in frequency for a given value of κ (compared with a 2 DOF system), which increases the NS. Nonetheless, one should also keep in mind that mode aliasing might occur for higher values of κ, which could thus prevent from reaching such high NS. As a first perspective of this thesis, extended studies could be carried out to find out the actual gain in sensitivity and decrease in LOD of such systems.

Many improvements are possible on the presented hybrid system. If the decrease in LOD can be proved with a 3 DOF system with stiffer middle resonator, a second digital filter could be implemented in the FPGA, allowing to reproduce and exploit this configuration, especially with bio-entities depositions (there is enough space left in the FPGA for an additional digital filter).

Another possible development concerns the way to calculate the vibration amplitudes. Instead of averaging the maximum minus minimum values over many periods, it could be considered to average the amplitudes of the Fourier transforms at the excitation frequency over the n_{aq} acquisitions, which should be more accurate since the noise from the other frequencies are not taken into account in this calculation. In addition, it could be considered to apply specific windows on the recorded signals such as the Hanning window, in order to limit the spectral leakage around the resonant frequency. More generally, the different noise sources that corrupt the signals should be identified and analyzed in order to find a way to decrease the LOD quite high so far (quantization noise, OA noise, clock jitter and so on).

Furthermore, the calibration of the sensor could be improved as well. Indeed so far, it is done using the mass mismatch calculated from the RtF shift of the QCM alone, which requires an additional impedance analyzer. However, the good correlation between experiments and models shows this calibration could be done using data generated in advance by simulation.

In order to gain time, the tuning protocol could be automatized. It is so far executed by an operator, but the digital aspect of the system could accommodate an additional routine that would automate this delicate part of the process whenever the operator wants to apply it. Moreover, the resonance amplitude tracking could also be done automatically with a PLL directly integrated in the FPGA. Such a modification replaces the long frequency sweep and enables fast resonance tracking resulting in a gain in analysis time.

Still with the goal of gaining time and decreasing the LOD, a closed loop could be set up such as a PLL that tracks the resonances. Let's keep in mind that so far, the measured amplitudes strongly depend on the step size of the frequency sweep.

One last perspective, more general to mode localization, would be to couple an array of resonators in such a way that mode aliasing occurs for all the modes excepted for at least one, which should be at the limit of this condition. In such a hypothetical configuration, this mode slightly apart from the aliasing could strongly localize with the introduction of a perturbation since it would grab the vibration energy from all the other modes that are very close in frequency because of mode aliasing.

Parameters

Below are listed different parameters used in the present manuscript (chapter I excluded), with their meaning and expression when available. Some of them are constants (such as j), others are variables that may be associated with indexes (such as x), and some are generic names that are used in different contexts (such as H). This list is however not exhaustive.

Name	Meaning	Expression
γ	Anti-aliasing coefficient	-
δm	Mass mismatch	-
$\Delta\omega_{-3dB}$	Angular frequency bandwidth	$\frac{\omega_r}{Q}$
Δf_{-3dB}	Frequency bandwidth	$\frac{\Delta\omega_{-3dB}}{2\pi}$
ϵ	Normalized mass/inductance mismatch	$\frac{\delta m}{m}$ or $\frac{\delta L_m}{L_m}$
η	Viscous damping	-
κ	Normalized coupling stiffness	$\frac{k_c}{k}$
λ_n	Normalized eigenvalue	$\frac{\omega_n}{\omega_0}$
τ_1	Number of registers after resonator 1	
τ_2	Number of registers in the coupling loop	
ϕ	Phase	-
ω	Angular excitation frequency	-
ω_0	Angular eigenfrequency	$\frac{1}{\sqrt{L_m \cdot C_m}}$ or $\sqrt{\frac{k}{m}}$
ω_p	Parallel resonant angular frequency	
ω_r	Resonant angular frequency	
ω_s	Series resonant angular frequency	
A	Signal amplitude (excepted in annex 5)	-
a	Input coefficient (Z-transform)	-
b	Output coefficient (Z-transform)	-
C_0	Parallel capacitance (BVD)	-
C_e	Output capacitance	-

C_m	Motion capacitance	-
d	Decimation factor	-
e	Euler's number	-
F	Excitation force	-
f	Excitation frequency	$\frac{\omega}{2\pi}$
f_0	Eigenfrequency	$\frac{\omega_0}{2\pi}$
f_d	Decimated sampling frequency	$\frac{f_s}{d}$
f_r	Resonant frequency	$\frac{\omega_r}{2\pi}$
f_s	Sampling frequency	$\frac{1}{T_s}$
g_1	-	$\frac{C_m}{C_0}$
g_2	-	$\frac{C_e}{C_0}$
g_3	-	$\frac{\sqrt{L_m \cdot C_m}}{R_e \cdot C_e}$
H	Transfer function	-
I	Electrical current	-
I_d	Identity matrix	-
j	Imaginary number	$j^2 = -1$
k	Stiffness	-
k_c	Coupling stiffness	-
L_m	Motion inductance	-
m	Mass	-
n_0, n_1	Digital filter parameters	-
n_{aq}	Number of signal acquisitions for a single amplitude calculation	-
ns	Normalized sensitivity	-
p	Laplace complex variable	
q	Electrical charge	-
Q	Q-factor	$\frac{1}{R_m} \cdot \sqrt{\frac{L_m}{C_m}}$ or $\frac{\sqrt{k \cdot m}}{\eta}$
r	Reduced pulse frequency	$\frac{\omega}{\omega_0}$
R_e	Output resistance	-
R_m	Motion resistance	-
s	-	$j \cdot \frac{\omega}{\omega_0}$
S_1, S_2	QCM names	-
t	Time	-

T_s	Sampling period	$\frac{1}{f_s}$
U	Electrical tension	-
u	Eigenvector	-
V	Electrical potential	-
x	Displacement	-
x_r	Resonance amplitude	-
x_{st}	Static displacement	$\frac{F}{k}$
Y	Admittance	$\frac{I}{U}$
Z	Impedance	$\frac{U}{I}$
z	Complex variable	-

Acronyms

The expressions having an acronym in this thesis are plainly spelled out when used for the first time, starting from chapter I. The acronym follows right after the first occurrence and is indicated between brackets ().

μTAS	**Micro** **T**otal **A**nalysis **S**ystems
ADC	**A**nalog to **D**igital **C**onverter
ASIC	**A**pplication-**S**pecific **I**ntegrated **C**ircuit
BAW	**B**ulk **A**coustic **W**ave
BVD	**B**utterworth-**V**an **D**yke model
CPLD	**C**omplex **P**rogrammable **L**ogic **D**evice
CPU	**C**entral **P**rocessing **U**nit
DAC	**D**igital to **A**nalog **C**onverter
DNA	**D**eoxyribo**n**ucleic **A**cid
DOF	**D**egree **O**f **F**reedom
FBAR	Thin **F**ilm **B**ulk **A**coustic **R**esonator
FET	**F**ield **E**ffect **T**ransistor
FFT	**F**ast **F**ourier **T**ransform
FIR	**F**inite **I**mpulse **R**esponse filter
FPGA	**F**ield **P**rogrammable **G**ate **A**rray
GPU	**G**raphical **P**rocessing **U**nit
GUI	**G**raphical **U**ser **I**nterface
HBAR	**H**igh tone **B**ulk **A**coustic **R**esonator
HDL	**H**ardware **D**escription **L**anguage
IC	**I**ntegrated **C**ircuit
IDT	**I**nter **D**igital **T**ransducer
IIR	**I**nfinite **I**mpulse **R**esponse filter
ISE	**I**on **S**elective **E**lectrode
ISFET	**I**on **S**ensitive **F**ield **E**ffect **T**ransistor
LFE	**L**ateral **F**ield **E**xcitation
LOD	**L**imit **O**f **D**etection
LUT	**L**ook-**U**p **T**able
MEMS	**M**icro **E**lectro **M**echanical **S**ystems
ML	**M**ode **L**ocalization
MOEMS	**M**icro **O**pto **E**lectro **M**echanical **S**ystems
NCO	**N**umerically **C**ontrolled **O**scillator
NEMS	**N**ano **E**lectro **M**echanical **S**ystems
NFS	**N**etwork **F**ile **S**ystem

NS	**N**ormalized **S**ensitivity
OA	**O**perational **A**mplifier
PLL	**P**hase-**L**ocked **L**oop
RAM	**R**andom **A**ccess **M**emory
RF	**R**adio **F**requency
RLC	Inductance/capacitance/resistance circuit (in series)
RtF	**R**esonan**t** **F**requency
SAW	**S**urface **A**coustic **W**ave
SMR	**S**olid **M**ounted **R**esonator
SNR	**S**ignal to **N**oise **R**atio
SPR	**S**urface **P**lasmon **R**esonance
TFE	**T**hickness **F**ield **E**xcitation
WCR	**W**eakly **C**oupled **R**esonators

Glossary

The terms defined in the present glossary are indicated *between stars* when written for the first time in the document, starting from chapter I.

- Actuator : An actuator is a device which converts an instruction into a desired physical behavior.
- Adsorbtion : Adsorbtion is a physical phenomenon that consists of the adhesion of chemical entities (ions, atoms, molecules...) from a phase (gas, liquid or solid) to the surface of a solid, as distinct from absorbtion, in which the entities penetrate a liquid or solid phase in volume.
- Analyte : An analyte is a specific substance to be quantified in a given gas, liquid or solid sample.
- Antifuse FPGA : An antifuse FPGA is a FPGA that is configurable only once. Each gate is configured by fuses, that are either burnt or not during the implementation of the logical circuit. This technology is namely used for spacial applications, in which external radiation may interfere with the static RAM of classic FPGAs and damage the implemented logical circuit [289, 290].
- Application-specific integrated circuit : An ASIC is a unique and taylored IC able to carry out specific tasks. It has a higher development cost than FPGA or CPLD based solutions (since specific masks and cleanroom fabrication are required), so they are usually reserved for high volume production. However they are also smaller, need lower power consumption and yield better performances (speed, reliability...) because of optimization and integration.
- Batch process : Batch process is a micro fabrication process that consists of manufacturing many devices at the same time on a single *wafer*, allowing the increase of the volume of fabrication and the decrease of costs.
- Bio-MEMS : Bio-MEMS are MEMS having interactions with biological entities, usually for medical, environment or agri-food applications.
- Bioreceptor : A bioreceptor is an biological entity (such as DNA, enzyme, cells, virus, antibodies) that is able to fix to another specific biological entity. The signal generated by this fixation is called bio-recognition (pH, mass, heat, light, charge...).
- Bipolar transistor : A bipolar transistor is a type of transistor that is basically composed of two diodes placed back to back. Its electrodes are named emitter, base and collector. A small current going through the base can control the ones passing by the emitter and the collector.
- Bit-shifting : Bit shifting consists of moving each digit of a number's binary representation left or right.

- Bragg reflector : A Bragg reflector is a stack of different layers aiming at reflecting an incoming wave by the generation of a constructive interference from the multiple reflections at each interface. The quality of the interference depends on the relation between the wavelength and the distance between two consecutive layers. A Bragg reflector can be designed for optical, electronical or mechanical applications.

- Bulk acoustic wave : A BAW is a mechanical wave propagating in volume through a material, usually piezoelectric.

- Bulk silicon etching : Bulk silicon etching is a micro fabrication process that consists of carving the silicon in three dimensions until the desired shape is obtained in the substrate.

- Cantilever : A cantilever is a micro beam with a first free end and a second end fixed to the substrate.

- Carbon black : Carbon black is a powder made of pure carbon particles. In practice, it is used as colloidal particles (homogeneously spread in another material), such as in tires.

- Carbon fiber : A carbon fiber is a fiber about 5 to 10 microns large made of carbon.

- Carbon nanotube : A carbon nanotube is a rolled graphene sheet forming a hollow cylinder.

- Ceramic : A ceramic is an inorganic and non-metal material.

- Chip : Chip is a common name for an integrated circuit.

- Clock : A clock is usually a quartz resonator that provides a square signal oscillating between 0 and 1. Every hardware that processes sequential logic does so at a specific rhythm given by a clock. Indeed, such a signal ensures data synchronization between the different logic operations. Without it, unwanted results would occur in a cascade of operations, because each signal delay is different (due to the connection lengths for instance).

- Combinational logic : Combinational logic describes a type of digital circuit which output is a function of the present input (time-independent).

- Correlated noise : Correlated noise, in contrast with uncorrelated noise, is a time dependent noise, meaning its amplitude at a certain time (or time sample) depends on its former values over a certain time range (or number of time samples).

- Data flip-flop : A data flip flop has two single-bit inputs (data and clock) and a single-bit data output. At each rising edge of the clock, the current data input is stored until the next rising edge of the clock, and the previous one is released (becoming the output). In short, a data flip flop delays a one-bit signal from one time sample, but also enables data synchronization. The association of several data flip flops (for signal processing on n-bits signals) is called a register.

- Decimation : Decimation is a way to modify the sampling frequency f_s of a signal. Decimation is also called down-sampling when f_s is diminished (the most easy down-sampling method is to keep one sample every n samples, with $n > 1$) or up-sampling when f_s is to be increased (based on interpolation methods).

- Dielectric : A dielectric is an electrical insulator that polarizes in an electric field. Electric charges, instead of flowing through the material as a they would in a conductor, slightly shift from their average equilibrium positions.

- Diode : A diode is a two-electrode semiconductor that allows the electrical current to flow only from the first electrode to the second.

- Doppler velocimetry : This technique consists of the velocity determination of a transparent fluid from the shift of a laser wavelength triggered by the movement of a fluid.
- Driver : A driver is a program allowing the user to utilize a hardware.
- Dynamic range : The dynamic range of a sensor represents the maximum minus the minimum output signals that it can yield.
- Faradaic current : A faradaic current is an electrical current traveling in a liquid due to oxydo-reduction reactions.
- Feedback : A feedback is the action of a system output on its input. A negative feedback aims at diminishing the output amplitude (and thus tends to stabilize it) whereas a positive feedback aims at increasing the output amplitude (and thus tends to destabilize it).
- Field effect transistor : A FET is a type of transistor which electrodes are named source, gate and drain. The current flowing through the source and the drain is controlled by a voltage applied to the gate. FETs are in competition with the bipolar transistor in the field of electronic communications, and can be used as chemical sensors such as ISFETs.
- Figure of merit : A figure of merit is a parameter allowing the characterization of a device or method and comparing it to similar devices or methods.
- Filter : A filter is a device which output is a selected frequency range of the input.
- Fluorescence : Fluorescence is the emission of light by a substance that has previously absorbed light.
- Gain-bandwidth : The gain-bandwidth of an OA is the product of the maximum output voltage and the working frequency. Thus, a gain-bandwidth of 1 MHz allows to get a gain of one (input amplitude = output amplitude) at a frequency of 1 MHz.
- Graphene : Graphene is a carbon structure in the form of a two dimensional, atomic scale thickness, hexagonal lattice.
- Gyroscope : A gyroscope consists of a spinning wheel that tends to keep its orientation, which makes it a perfect system for angle sensing along one or several axes.
- Hall effect : The Hall effect was discovered in 1879 by Edwin Hall and refers to the production of an electric field in a material through which an electrical current flows perpendicularly to a magnetic field.
- Hardware description language : A HDL aims at the description of the behavior that a circuit must have. In contrast with a programming language, a HDL script is not executed line by line. For instance, a function that shifts an array of n-bits once to the lower order bits can use a ”for” loop which, written with a programming language, results is n successive operations, but not with a HDL since it can be interpreted to generate a block doing the operations in parallel.
- Hardware-in-the-loop : Hardware-in-the-loop is a technique used to characterize embedded systems (controllers). The dynamic system for which the feedback is designed (whether it is electrical or mechanical), is replaced by a mathematical model implemented in a hardware such as a FPGA, and is connected to the controller to be tested. This method enables cheap and safe testing.
- Integrated Circuit : An IC is a set of electronic components ordered on a single piece of semiconductor that performs specific tasks, also commonly called a chip.

- Inter digital transducer : An IDT is a set of two interlocking comb-shaped metallic electrodes deposed at the surface of a piezoelectric material, allowing to generate or sense a SAW.

- Interference : An interference is a phenomenon in which the spatial superposition of two waves a and b results in a wave c which amplitude is different from the algebraic sum of the amplitudes of both waves a and b (the interference is constructive if the amplitude of c is greater, and destructive if lower).

- Ion selective electrode : An ISE is an electrode used in potentimetric mass sensors, able to sense a specific ion : the potential of this electrode varies when the analyte interacts with its surface (made of different kind of glass for instance) or with a bio-receptor fixed to its surface.

- Ion-sensitive field-effect transistor : An ISFET is an ion concentration sensor (such as H_3O^+ in a solution -pH sensor-) in which the current going through the transistor changes accordingly to the ion concentration. An ISFET is a FET whose gate electrode is made of a material sensitive to the ionic analyte (sometimes by the deposition of specific bio-receptors).

- Kalman filter : A Kalman filter is an IIR nowadays broadly used in the estimation of time dependent variables in dynamic systems. It finds its applications in different domains such as defense (radars), finance or navigation. It allows, from the analysis of noisy measurements done over time on a system (position of a target for instance) to obtain a better estimation of the actual values of a variable along with its uncertainties, for a given time sample.

- Label based technologies : Label based technology concerns biosensors that require labels such as fluorescent or radioactive molecules. Attached to the targeted analyte, they help to detect the latter. The sensor signal thus corresponds to the amount of labels. In contrast, label free technology does not require such markers to facilitate the measure, but instead directly uses an intrinsic property of the analyte such as its mass or electrical charge.

- Lab-on-chip : A lab-on-chip is a MEMS that handles very small amount of fluids and performing some tasks for chemical analysis such as the ones carried out by a μTAS.

- Lamb wave : A Lamb wave is a SAW that propagates on both sides of a plate. The particle displacement are out of the plane of the substrate surface.

- Latency : In computing science, latency is the time delay between the instruction and the data transfer.

- Lateral field excitation : Lateral field excitation consists of generating a BAW in a piezoelectric material using two electrodes laid next to each other at the surface of the material.

- Limit of detection : The LOD of a sensor is the smallest sensor input value generating a measurable sensor output signal. Below this value, noise dominates any output signal shift. The LOD should not be confused with the resolution of the sensor output.

- Linear range : The linear range of a sensor represents its output range for which the measured signal (sensor output) is proportional to the measurand value (sensor input).

- Longitudinal bulk acoustic wave : A longitudinal bulk acoustic wave is a BAW whose particle displacement is parallel to the propagation direction of the wave.

- Look-up table : A LUT has an input on n bits and an output on one or more bits. It is an array of 2^n memory cells (one for each input value). Each of these cells has a specific address and stocks information. The value of the input is interpreted as an address and the one of the corresponding cell is then extracted to be the output. In short, all the possible values are stored, which comes to replace a time consuming computation operation by an indexing one.

- Love wave : A Love wave is a shear SAW which particle displacement is the plane of the substrate surface and perpendicular to the wave direction.
- Micro Electro Mechanical Systems : MEMS are devices which size is ranging from one micrometer to a few millimeters. Fabricated using microfabrication processes in cleanroom, they can be classified in different categories such as actuators, sensors, filters or energy harvesting devices. The term of MEMS was proposed during the Micro-Tele-Operated Robotics Workshop held in 1989 in Salt Lake City [291].
- Micro Opto Electro Mechanical Systems : MOEMS are MEMS with additional components having interaction with light. The term MOEMS was introduced in 1993 by Dr. Motamedi at the Critical Reviews of Optical Science and Technology conference [292].
- Micro Total Analysis Systems : μTAS are smart MEMS sensors that perform entire chemical analysis. They can process many tasks alone, such as : fluid flow control, fluid sampling, detection and sensing, electric signal filtering, data processing and sending to a remote entity. μTAS are advanced lab-on-chips.
- Mode aliasing : Mode aliasing is the spectral merge of two resonances whose frequencies are very close to each other.
- Mode localization : Mode localization refers in this thesis to the spatial localization of vibration energy triggered by a slight perturbation in an array of weakly coupled resonators.
- Multiplexer : A multiplexer is a circuit which single output is selected among several inputs.
- Nano Electro Mechanical Systems : NEMS are MEMS at a scale under one micrometer.
- Normalized sensitivity : The normalized sensitivity of a sensor represents the relative change in signal output over signal input.
- Operational amplifier : An operational amplifier is an active electronic component (it needs an external power supply to fulfill its functions). It is a high gain amplifier with a differential input allowing, amongst others, the implementation of analog filters.
- Optical fiber : An optical fiber is a cylindrical wave guide for light whose diameter is usually comprised between 100 μm and a few millimeters. It is composed of one or two transparent materials (glass, plastic...) with different refraction indexes (the highest is the center of the fiber -the core- and the lowest at its periphery -the cladding-), allowing the light to reflect inside the core and thus travel along the fiber.
- Optical path length : The optical path length between two points A and B is the distance traveled by an electromagnetic wave multiplied by the refraction index n of the medium in which it propagates. This length corresponds to the one the wave would travel if it was in the void. The optical path length difference bewteen the two beams of an interferometer determines whether the interference is constructive or destructive.
- Oscillator : An oscillator is a device that is either in open or in close-loop that converts a constant signal into a periodic

one. Oscillators are mainly used for electronic applications (computer clocks, radio transmitter...), but also for sensing purposes.

Open-loop oscillator examples : a mechanical clock, which constant input is the displacement of a weight, generates the periodic movement of a swing by the mean of the escapement. A second example is the violin, which constant input is the straight displacement of the bow generating a stick-and-slip movement on the violin string (the so-called Helmholtz motion [293]). These waves are then changed into an acoustic vibration by the violin. Another type of open-loop oscillator is the relaxation oscillators, which are non-linear systems meant to generate periodic signals that are not sinusoidal. They are usually electrical oscillators (with switches allowing capacitors to charge slowly and discharge suddenly), but some mechanical relaxation oscillators also exist such as the *Tantalus cup*.

Closed-loop oscillator example : the acoustic feedback between a microphone and its speaker. When the former is oriented and connected to the latter, they may together generate an audible acoustic wave with an ever increasing amplitude (until saturation or intervention of the operator). The closed loop gain is determined by the amplifier settings but also the distance d between the microphone and the speaker. When d is small enough, the closed loop gain is higher than 1 for a wide range of frequencies, because the speaker is not a resonator (as it is designed to have a flat spectrum for audible frequencies). The amplified frequencies will then be the ones which wavelengths, in relation with d, satisfy the Barkhausen stability criterion for the phase. In this example, the constant input signal is the power supply of the amplifier and speaker.

- Overflow : A digital signal being coded on n bits, it can only take 2^n possible values, meaning a number whose value is outside this boundary loses its highest-order bit(s). For instance, the numbers 3 and 4 on three bits are (unsigned) 011 and 100 respectively, but are 11 and 00 on two bits, which actually correspond to 3 and 0, respectively.

- Oxidation/reduction reaction : An oxidation/reduction reaction is a chemical reaction involving the exchange of one or several electrons.

- Passive and active sensitivities : In an analog filter, a passive sensitivity is defined as the relative variation of a parameter (such as the RtF or the Q-factor), over the relative variation of the value of one passive component (such as resistors or capacitors). In an active filter, an active sensitivity is also defined as the relative variation of a parameter (such as the RtF or the Q-factor), over the relative variation of the value of an active part of the filter (such as the amplification gain A of an operational amplifier). Since external conditions, such as the temperature, may slightly change the behavior of each electrical component, passive and active sensitivities are interesting to calculate and evaluate from the filter transfer function.

- Photodetector : A photodetector is a sensor that convert a light signal into an electrical signal.

- Photolithography : Photolithography is a micro fabrication process alowing to transfer a geometric pattern on a wafer throughout a photomask. This micro fabrication step allows to protect chosen parts of the wafer for the next microfabrication step.

- Piezoelectricity : Piezoelectricity is the ability of a material to generate charges under stress, and to extend or shrink with voltage (the term ”piezo” comes from the Greek ”to press”).

- Piezoresistivity : Piezoresistivity characterizes the resistivity change of a material subjected to strain. Inspired by the piezoelectric phenomenon, John W. Cookson used the term ”piezoresistivity” for the first time in 1935 [294], which refers to the shift of resistivity with stress, as distinct from the total change of resistance.

- Polymer : A polymer is a large molecule composed of repeated subunits.

- Processor core : A processor core is an essential component of a processing unit, as it is able to read and execute queued up instructions, one by one, at a certain frequency.

- Proof mass : A proof mass is a component of a MEMS whose mass is known.

- Quartz : Quartz is a common piezoelectric crystal.

- Radio frequency : RF are frequencies from around 30 Hz to 300 GHz, suitable for telecommunications. In general, RF refers to frequencies higher than 100 MHz, because the bandwidths of television and mobile phones (so the bigger markets) start around these frequencies. However, extremely lower frequencies are also used (less than 100 Hz for submarine telecommunications).

- Rayleigh wave : A Rayleigh wave is a SAW that is a combination of a planar wave triggering a longitudinal displacement and a shear wave perpendicular to the surface producing a transversal displacement. As a consequence, each particle at the surface has an elliptical movement.

- Register : A register is the association of several data flip flops, allowing to work on n-bits and not single-bit signals.

- Repeatability : The repeatability of a sensor is its ability to yield identical results when the same experiments are carried out several times.

- Resolution : The resolution is the minimum shift of a physical quantity that can be measured above the noise floor.

- Resonator : A resonator is a physical system which vibration amplitude is maximum for one or more frequencies of excitation. It can also be seen as a filter (also called resonant filter in the present manuscript).

- Selectivity : Selectivity is the ability of a mass sensor to sense only one specific entity. Its depends on the affinity between the analyte and the receptor.

- Semiconductor : A semiconductor is a material whose ability to conduct electricity (conductivity) lays between those of a insulator and a conductor. Semiconductors are commonly used in electronic devices as switches or amplifiers, such as silicon.

- Sensitive range : The sensitive range is defined in this thesis for ML based sensors as the range of perturbations ϵ for which the NS is at least equal to half of its maximum value (since the NS decreases when ϵ increases, from $\epsilon = 0$).

- Sensitivity : The sensitivity of a sensor represents the change in signal output over signal input.

- Sensor : A sensor is a device generating a measurable signal (usually electric) from an external stimulus.

- Sequential logic : Sequential logic describes a type of digital circuit whose output is a function of the present and the previous inputs (time dependent).

- SH-SAW : A SH-SAW is similar to a Love wave but with a larger penetration depth.

- Slew rate : The slew rate of an OA is the maximum output voltage variation with respect to time (expressed in Volts per second).

- Static displacement : The static displacement of a damped or undamped resonator is the displacement of the mass when it is subjected to an external constant force.
- Substrate : The substrate is the base material in which a MEMS is fabricated.
- Surface acoustic wave : SAWs are mechanical waves propagating at the surface of a material with a typical penetration depth around their wavelength. Such waves can be Love waves, Lamb waves or Rayleigh waves. Typically on the human scale, an earthquake can generate Rayleigh waves at the surface of the earth crust, source of building damage. In the MEMS field, their amplitudes can go down to a few picometers : generated with IDTs, they propagate on a piezoelectric substrate and are used for filtering or sensing.
- Surface micromachining : Surface micromachining is a micro fabrication process that consists of stacking several layers of different materials before sacrificing one of them at a desired location, thus creating specific shapes such as cantilevers.
- Tantalus cup : The Tantalus cup is a recipient with a u-shaped siphon being continuously filled with water, but that empties out automatically once a certain level of water is reached.
- Time response : For a mass sensor, the time response is the time that elapses between a change in the analyte concentration and its detection by the sensor.
- Thermal bimorph : A thermal bimorph consists of two different materials, one stuck on top of the other. Since the thermal expansion coefficients are different for each material, a movement of the assembly occurs under a temperature change.
- Thermocouple : A thermocouple is a temperature sensor based on the Seebeck effect, which predicts a difference of voltage between both ends of an open loop wire made of two different materials and subjected to a gradient of temperature.
- Thermodynamics : Thermodynamics is a branch of physics dealing with energy and temperature of a system at different thermal equilibrium, as distinct from thermics which deals with time dependent energy transfers happening between two different thermal equilibrium.
- Thermoresistivity : Thermoresistivity describes the dependence of the electrical resistivity of a material to the temperature.
- Thermoscope : A thermoscope is the ancestor of the thermometer : this device is based on the dilatation of air in a chamber with a temperature shift, which triggers the displacement of water in a tube connected to this chamber. It allows to observe a shift in temperature, as distinct from a thermometer that comes along with a scale allowing to measure it.
- Thickness field excitation : Thickness field excitation consists of the generation of a BAW in a piezoelectric material sandwiched between two electrodes.
- Thickness shear wave : A thickness shear wave is a bulk wave whose particle displacement is perpendicular to the propagation of the wave.
- Transducer : A transducer is a device that turns a form of energy or signal into another.
- Transistor : A transistor is a three electrode semiconductor device aiming at either amplifying an electric signal or being used as an electronic switch. The most common transistor types are the bipolar transistor and the field effect transistor.
- Wafer : A wafer is a thin slice of semiconductor in which MEMS are fabricated.

Appendices

Annex 1 : Eigenvalue problem resolution for a 2 DOF undamped resonators system

Let's consider a system composed of two undamped resonators system of stiffness k, mass m and displacement x_i, $i \in \{1, 2\}$, coupled to each other with a spring of stiffness k_c, such as depicted on Fig. 67.

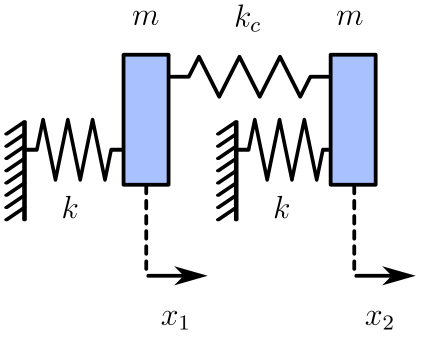

Figure 67: 2 DOF free mass spring system

The application of the second Newton's law to this system yields

$$\begin{cases} m \cdot \ddot{x}_1 + k \cdot x_1 + k_c \cdot (x_1 - x_2) = 0 \\ m \cdot \ddot{x}_2 + k \cdot x_2 + k_c \cdot (x_2 - x_1) = 0 \end{cases} \tag{122}$$

Taking $X = (x_1, x_2)$ as an harmonic solution of angular frequency ω of Eq. 122, the complex notations can be used

$$\begin{cases} X = u \cdot e^{j\omega t} \\ \ddot{X} = -\omega^2 \cdot X \end{cases} \tag{123}$$

Using Eq. 122 and Eq. 123 and dividing by $e^{j\omega t}$ yield a matrix form of the problem

$$\begin{cases} K \cdot u = \lambda \cdot M \cdot u \\ \lambda = \omega^2 \cdot \dfrac{m}{k} \\ M = \begin{bmatrix} 1 & 0 \\ 0 & 1 \end{bmatrix} \\ K = \begin{bmatrix} 1+\kappa & -\kappa \\ -\kappa & 1+\kappa \end{bmatrix} \\ \kappa = \dfrac{k_c}{k} \end{cases} \tag{124}$$

We first aim at determining the two eigenvalues λ_1 and λ_1. Since M is the identity matrix I_d, the aforementioned equation becomes

$$(K - \lambda \cdot I_d) \cdot u = \overrightarrow{0} \tag{125}$$

Which comes to solve

$$det(K - \lambda \cdot I_d) = 0 \tag{126}$$

That is

$$\begin{aligned} \begin{vmatrix} 1+\kappa-\lambda & -\kappa \\ -\kappa & 1+\kappa-\lambda \end{vmatrix} &= 0 \\ (1+\kappa-\lambda)^2 - \kappa^2 &= 0 \\ (1+2\kappa-\lambda) \cdot (1-\lambda) &= 0 \end{aligned} \tag{127}$$

They are then two solutions

$$\begin{cases} \lambda_1 = 1 \\ \lambda_2 = 1 + 2\kappa \end{cases} \tag{128}$$

With $\lambda_i = \omega_i^2 \cdot \frac{m}{k}$ and $\kappa = \frac{k_c}{k}$,

$$\begin{cases} \omega_1 = \sqrt{\dfrac{k}{m}} \\ \omega_2 = \sqrt{\dfrac{k+2k_c}{m}} \end{cases} \tag{129}$$

ω_1 and ω_2 are the two angular eigenfrequencies of the system. We are now looking for their associated mode shape (eigenvectors u_1 and u_2). To do so, the following equation must be solved.

$$\begin{cases} K \cdot u_i = \lambda_i \cdot u_i \\ u_i = \begin{pmatrix} u_{i1} \\ u_{i2} \end{pmatrix} \\ i \in \{1, 2\} \end{cases} \tag{130}$$

Equation 130 gives

$$\begin{cases} (1+\kappa) \cdot u_{i1} - \kappa \cdot u_{i2} = u_{i1} \\ -\kappa \cdot u_{i1} + (1+\kappa) \cdot u_{i2} = u_{i2} \end{cases} \tag{131}$$

For the first mode, subtracting the second equation to the first one in Eq. 131 yields

$$\begin{aligned} (1+2\kappa) \cdot u_{11} - (1+2\kappa) \cdot u_{12} &= u_{11} - u_{12} \\ 2\kappa \cdot (u_{11} - u_{12}) &= 0 \\ u_{11} &= u_{12} \end{aligned} \tag{132}$$

So u_1 could be defined as follow

$$u_1 = \frac{1}{\sqrt{2}} \cdot \begin{pmatrix} 1 \\ 1 \end{pmatrix} \tag{133}$$

For the second mode, adding the second equation to the first one in Eq. 131 yields

$$\begin{aligned} u_{21} + u_{22} &= (1+2\kappa) \cdot u_{21} + u_{22} \\ 2\kappa \cdot (u_{21} + u_{22}) &= 0 \\ u_{21} &= -u_{22} \end{aligned} \tag{134}$$

So u_2 could be defined as follow

$$u_2 = \frac{1}{\sqrt{2}} \cdot \begin{pmatrix} 1 \\ -1 \end{pmatrix} \tag{135}$$

The shape of these two modes are depicted on Fig. 68 and a summary of the different results present in this section is given in Table 13.

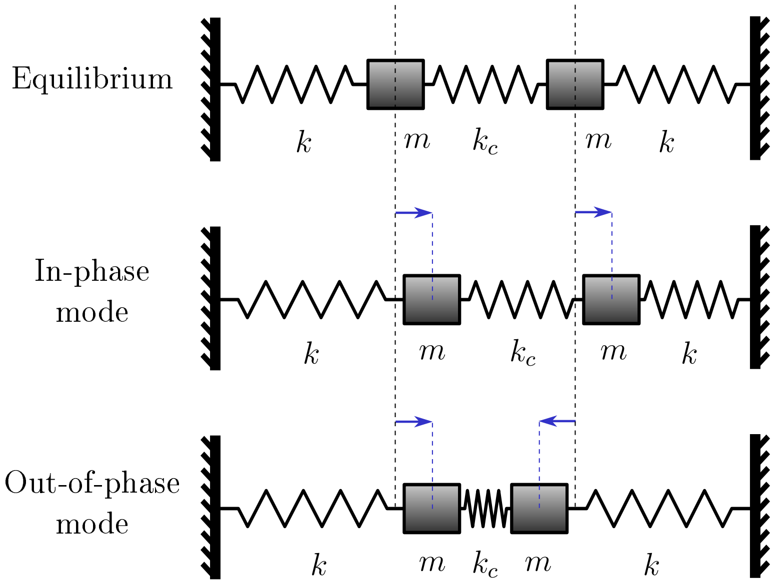

Figure 68: Graphic representation of the modes of a 2 DOF undamped resonators system

Table 13: Eigenvalues and eigenvectors of a 2 DOF undamped resonators system : a summary

Mode name	**Mode number**	**Angular frequency**	**Eigenvector**
In-phase	1	$\omega_1 = \sqrt{\frac{k}{m}}$	$u_1 = \frac{1}{\sqrt{2}} \cdot \begin{pmatrix} 1 \\ 1 \end{pmatrix}$
Out-of-phase	2	$\omega_2 = \sqrt{\frac{k+2k_c}{m}}$	$u_2 = \frac{1}{\sqrt{2}} \cdot \begin{pmatrix} 1 \\ -1 \end{pmatrix}$

Annex 2 : Analytic development of mode localization

The following method has been adapted from [205].

Let's consider a system composed of N undamped resonators of stiffness k, mass m_i and displacement x_i, $i \in \{1..N\}$, coupled to one another with springs of stiffness k_c, such as depicted on Fig. 69.

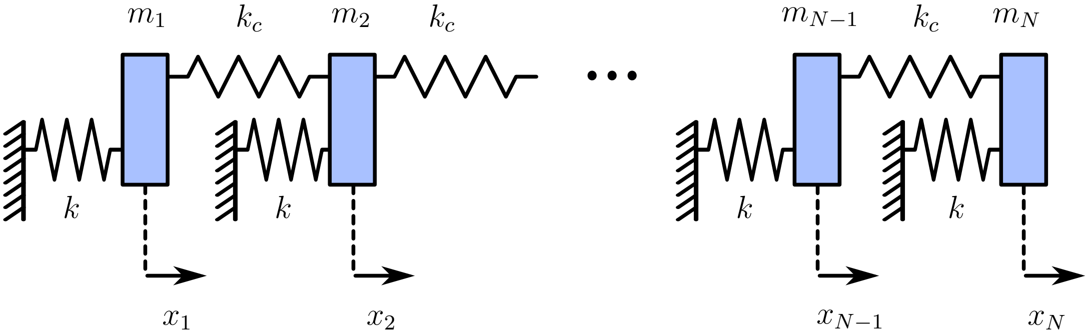

Figure 69: N DOF free mass spring system

Let's first set $m_i = m$ for $i \in \{1..N\}$, with m a fixed value.

The application of the second Newton's law to this system yields

$$\begin{cases} m \cdot \ddot{x}_1 + k \cdot x_1 + k_c \cdot (x_1 - x_2) = 0 \\ m \cdot \ddot{x}_N + k \cdot x_N + k_c \cdot (x_N - x_{N-1}) = 0 \\ m \cdot \ddot{x}_i + k \cdot x_i + k_c \cdot (2x_i - x_{i-1} - x_{i+1}) = 0 \\ \qquad i \in \{2..N-1\} \end{cases} \tag{136}$$

Taking $X = (x_1, .., x_N)$ as an harmonic solution of angular frequency ω of Eq. 136, the complex notations can be used

$$\begin{cases} X = u \cdot e^{j\omega t} \\ \ddot{X} = -\omega^2 \cdot X \end{cases} \tag{137}$$

Using Eq. 137 and Eq. 136 and dividing by $e^{j\omega t}$ yield a matrix form of the problem

$$\begin{cases} K \cdot u = \lambda \cdot M_0 \cdot u \\ \lambda = \omega^2 \cdot \dfrac{m}{k} \\ M_0 = \begin{bmatrix} 1 & 0 & ... & ... & 0 \\ 0 & 1 & & & ... \\ ... & & ... & & ... \\ ... & & & 1 & 0 \\ 0 & ... & ... & 0 & 1 \end{bmatrix} \\ K = \begin{bmatrix} 1+\kappa & -\kappa & 0 & ... & & ... & 0 \\ -\kappa & 1+2\kappa & -\kappa & & & & ... \\ 0 & -\kappa & 1+2\kappa & ... & & & \\ ... & & ... & ... & ... & & ... \\ & & & ... & 1+2\kappa & -\kappa & 0 \\ ... & & & & -\kappa & 1+2\kappa & -\kappa \\ 0 & ... & & ... & 0 & -\kappa & 1+\kappa \end{bmatrix} \\ \kappa = \dfrac{k_c}{k} \end{cases} \tag{138}$$

with K and M_0 being the stiffness and mass square matrices of size N.

Equation 138 is a nondimensional eigenvalue problem having N solutions that corresponds to N modes of vibrations, each one associated to a vibration shape and a specific frequency, described by the eigenvector u_{0n} and eigenvalue λ_{0n}, respectively (with $n \in \{1..N\}$). The problem can be rewritten as

$$\begin{cases} K \cdot u_{0n} = \lambda_{0n} \cdot M_0 \cdot u_{0n} \\ n \in \{1..N\} \end{cases} \tag{139}$$

Since the K and M_0 are symmetric, the N eigenvalues are real and the eigenvectors are orthogonal, such as

$$\begin{cases} u_{0n}^T \cdot M_0 \cdot u_{0m} = \delta_m^n \\ u_{0n}^T \cdot K \cdot u_{0m} = \lambda_{0n} \cdot \delta_m^n \end{cases} \tag{140}$$

where δ_m^n is the Kronecker delta function defined to be equal to 1 when $n = m$ and to 0 otherwise.

We can know rewrite the problem considering that each resonator may be subjected to a small perturbation such as

$$M = M_0 + \delta M \tag{141}$$

where δM is a N by N diagonal matrix that represents the positions and quantities of mass added to the system.

The resulting eigenvectors and eigenvalues can be written as

$$\begin{cases} u_n = u_{0n} + \delta u_n \\ \lambda_n = \lambda_{0n} + \delta \lambda_n \end{cases} \tag{142}$$

Since the N eigenvectors are a base, the perturbation of δu_n can be expressed as

$$\delta u_n = \sum_{i=1}^{N} \alpha_{in} \cdot u_{0i} \tag{143}$$

where α_{in} are small coefficients that need to be determined.

The problem now becomes

$$\begin{cases} K \cdot u_n = \lambda_n \cdot M \cdot u_n \\ \qquad n \in \{1..N\} \end{cases} \tag{144}$$

Substituting Eq. 141 and 142 in Eq. 144 yields

$$K \cdot (u_{0n} + \delta u_n) = (\lambda_{0n} + \delta \lambda_n) \cdot (M_0 + \delta M) \cdot (u_{0n} + \delta u_n) \tag{145}$$

Keeping only the first order leads to

$$\underbrace{K \cdot u_{0n} - \lambda_{0n} \cdot M_0 \cdot u_{0n}}_{=0,\ Eq.\ 139} + K \cdot \delta u_n = \lambda_{0n} \cdot \delta M \cdot u_{0n} + \delta \lambda_n \cdot M_0 \cdot u_{0n} + \lambda_{0n} \cdot M_0 \cdot \delta u_n \tag{146}$$

Premultiplying by u_{0p}^T, $p \in \{1..N\}$ and using Eq. 143 gives

$$\sum_{i=1}^{N} \alpha_{in} \cdot u_{0p}^T \cdot K \cdot u_{0i} = \lambda_{0n} \cdot u_{0p}^T \cdot \delta M \cdot u_{0n} + \delta \lambda_n \cdot u_{0p}^T \cdot M_0 \cdot u_{0n} + \lambda_{0n} \cdot \sum_{i=1}^{N} \alpha_{in} \cdot u_{0p}^T \cdot M_0 \cdot u_{0i} \tag{147}$$

Defining $\delta \mu_{i,n} = u_{0i}^T \cdot \delta M \cdot u_{0n}$ and using Eq. 140 for the case $p = n$, Eq. 147 becomes

$$\alpha_{nn} \cdot \lambda_{0n} = \lambda_{0n} \cdot \delta \mu_{n,n} + \delta \lambda_n + \alpha_{nn} \cdot \lambda_{0n} \tag{148}$$

Which yields

$$\delta\lambda_n = -\lambda_{0n} \cdot \delta\mu_{n,n} \tag{149}$$

With Eq. 142 we can write

$$\lambda_n = \lambda_{0n} \cdot (1 - \delta\mu_{n,n}) \tag{150}$$

Using the definition of λ in Eq. 138, the previous equation yields

$$\omega_n = \omega_{0n} \cdot \sqrt{1 - \delta\mu_{n,n}} \tag{151}$$

Since $\delta\mu_{n,n} \ll 1$, we keep again the first order such as

$$\omega_n = \omega_{0n} \cdot \left(1 - \frac{1}{2} \cdot \delta\mu_{n,n}\right) \tag{152}$$

Finally

$$\delta\omega_n = -\frac{1}{2} \cdot \delta\mu_{n,n} \cdot \omega_{0n} \tag{153}$$

Using Eq. 140 for the case $p \neq n$, Eq. 147 becomes

$$\alpha_{pn} \cdot \lambda_{0p} = \lambda_{0n} \cdot \delta\mu_{p,n} + \alpha_{pn} \cdot \lambda_{0n} \tag{154}$$

Finally,

$$\alpha_{pn} = \frac{\lambda_{0n}}{\lambda_{0p} - \lambda_{0n}} \cdot \delta\mu_{p,n} \tag{155}$$

α_{nn} still needs to be determined. To do so, we use the orthogonal property of u_n as follow

$$u_n^T \cdot M \cdot u_n = 1 \tag{156}$$

Substituting Eq. 141 and 142 in Eq. 156 yields

$$(u_{0n} + \delta u_n)^T \cdot (M_0 + \delta M) \cdot (u_{0n} + \delta u_n) = 1 \tag{157}$$

Keeping only the first order, we obtain

$$u_{0n}^T \cdot M_0 \cdot u_{0n} + u_{0n}^T \cdot M_0 \cdot \delta u_n + u_{0n}^T \cdot \delta M \cdot u_{0n} + \delta u_n^T \cdot M_0 \cdot u_{0n} = 1 \tag{158}$$

Using Eq. 143 gives

$$\underbrace{u_{0n}^T \cdot M_0 \cdot u_{0n}}_{=1,\ Eq.\ 140} + \underbrace{\sum_{i=1}^{N} \alpha_{in} \cdot u_{0n}^T \cdot M_0 \cdot u_{0i}}_{=\alpha_{nn},\ Eq.\ 140} + \delta\mu_{n,n} + \underbrace{\sum_{i=1}^{N} \alpha_{in} \cdot u_{0i}^T \cdot M_0 \cdot u_{0n}}_{=\alpha_{nn},\ Eq.\ 140} = 1 \tag{159}$$

That is

$$\alpha_{nn} = -\frac{1}{2} \cdot \delta\mu_{n,n} \tag{160}$$

In the end, the small variations of eigenvectors and eigenvalues due to a certain mass perturbation distribution can be express as

$$\begin{cases} \delta\omega_n = \underbrace{-\frac{1}{2} \cdot \delta\mu_{n,n} \cdot \omega_{0n}}_{Eq.\ 153} \\ \delta u_n = \underbrace{-\frac{1}{2} \cdot \delta\mu_{n,n}}_{Eq.\ 160} \cdot u_{0n} + \sum_{p=1,\ p\neq n}^{N} \underbrace{\frac{\lambda_{0n}}{\lambda_{0p} - \lambda_{0n}} \cdot \delta\mu_{p,n}}_{Eq.\ 155} \cdot u_{0p} \end{cases} \tag{161}$$

With the definition of λ in Eq. 138, we finally obtain :

Expressions of the shifts of eigenfrequencies and eigenvectors due to a small mass variation in a N DOF coupled undamped resonators system

$$\begin{cases} \delta\omega_n \simeq -\frac{\delta\mu_{n,n}}{2} \cdot \omega_{0n} \\ \delta u_n \simeq -\frac{\delta\mu_{n,n}}{2} \cdot u_{0n} + \sum_{p=1,\ p\neq n}^{N} \frac{\delta\mu_{p,n}}{\left(\frac{\omega_{0p}}{\omega_{0n}}\right)^2 - 1} \cdot u_{0p} \\ \delta\mu_{i,n} = u_{0i}^T \cdot \delta M \cdot u_{0n} \end{cases} \tag{162}$$

With N the number of DOF and for $n \in \{1..N\}$, ω_{0n}, u_{0n}, $\delta\omega_n$ and δu_n are the n^{th} angular eigenfrequency and eigenvector before the addition of mass, small variation of angular eigenfrequency and eigenvector after the introduction of a mass perturbation in the system, respectively. δM is the diagonal N by N matrix containing the normalized small mass shifts $\frac{\delta m}{m}$.

Comment : the same reasoning can be done for a perturbation on the stiffness matrix K, leading to similar results. However, this thesis treats of mass perturbation, so this case was not considered here in order to simplify the calculations and the final result.

Annex 3 : Close loop transfer function of a 2 DOF coupled resonant system

In this annex are presented the expressions of the displacements (or electrical charges for electric circuits) in a 2 DOF coupled resonant system.

Figure 70a depicts a standard coupled mechanical resonant system in forced regime. Each resonator i of mass m_i is described by a set of parameters, including linear stiffness k_i and damping η_i. It can also be seen as a filter characterized by a transfer function with the excitation force F_i as an input and the displacement x_i as an output. Since the system is composed of two coupled resonators, the coupling force comes in addition to the excitation force, as shown on Fig. 70b. This contribution is equal to the coupling ratio $\kappa = \frac{k_c}{k_1}$ multiplied by the displacement difference of the resonators $x_1 - x_2$.

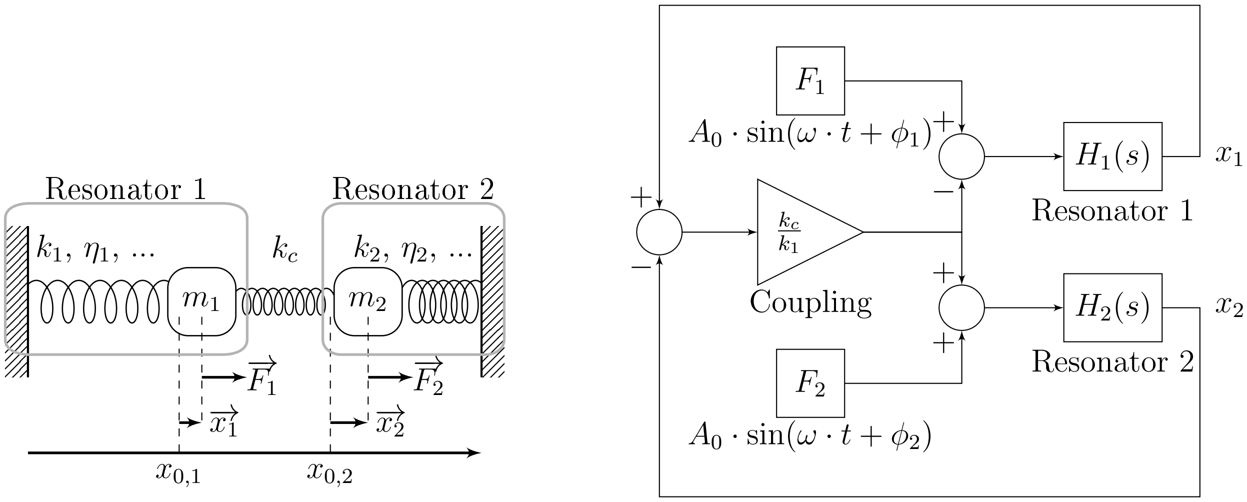

(a) Mass-spring like coupled resonators

(b) Equivalent block diagram of Fig. 70a

Figure 70: 2 DOF coupled resonators

The open loop transfer functions of resonators 1 and 2 are denoted H_1 and H_2 respectively. The following equations can then be written, according to Fig. 70b

$$\begin{aligned} x_1 &= H_1 \cdot (F_1 - \kappa \cdot (x_1 - x_2)) \\ x_1 \cdot (1 + \kappa \cdot H_1) &= H_1 \cdot (F_1 + \kappa \cdot x_2) \\ x_1 &= \frac{H_1}{1 + \kappa \cdot H_1} \cdot F_1 + \frac{\kappa \cdot H_1}{1 + \kappa \cdot H_1} \cdot x_2 \end{aligned} \tag{163}$$

The same way we can write

$$x_2 = \frac{H_2}{1 + \kappa \cdot H_2} \cdot F_2 + \frac{\kappa \cdot H_2}{1 + \kappa \cdot H_2} \cdot x_1 \tag{164}$$

We can now use both Eq. 163 and Eq. 164 to write the transfer functions of the system in close loop

$$\begin{cases} x_1 = \dfrac{H_1 \cdot (1 + \kappa \cdot H_2)}{1 + \kappa \cdot (H_1 + H_2)} \cdot F_1 + \dfrac{\kappa \cdot H_1 \cdot H_2}{1 + \kappa \cdot (H_1 + H_2)} \cdot F_2 \\ x_2 = \dfrac{H_2 \cdot (1 + \kappa \cdot H_1)}{1 + \kappa \cdot (H_1 + H_2)} \cdot F_2 + \dfrac{\kappa \cdot H_1 \cdot H_2}{1 + \kappa \cdot (H_1 + H_2)} \cdot F_1 \end{cases} \tag{165}$$

Let's denote $H_i = \frac{N_i}{D_i}$, $i \in \{1, 2\}$, the following equation can then be written

$$\begin{cases} H_1 \cdot (1 + \kappa \cdot H_2) = \dfrac{N_1 \cdot (D_2 + \kappa \cdot N_2)}{D_1 \cdot D_2} \\ H_2 \cdot (1 + \kappa \cdot H_1) = \dfrac{N_2 \cdot (D_1 + \kappa \cdot N_1)}{D_1 \cdot D_2} \\ 1 + \kappa \cdot (H_1 + H_2) = \dfrac{D_1 \cdot D_2 + \kappa \cdot (N_1 \cdot D_2 + N_2 \cdot D_1)}{D_1 \cdot D_2} \\ \kappa \cdot H_1 \cdot H_2 = \dfrac{\kappa \cdot N_1 \cdot N_2}{D_1 \cdot D_2} \end{cases} \tag{166}$$

We finally obtain

$$\begin{cases} x_1 = \dfrac{N_1 \cdot (D_2 + \kappa \cdot N_2)}{D_1 \cdot D_2 + \kappa \cdot (N_1 \cdot D_2 + N_2 \cdot D_1)} \cdot F_1 + \dfrac{\kappa \cdot N_1 \cdot N_2}{D_1 \cdot D_2 + \kappa \cdot (N_1 \cdot D_2 + N_2 \cdot D_1)} \cdot F_2 \\ x_2 = \dfrac{N_2 \cdot (D_1 + \kappa \cdot N_1)}{D_1 \cdot D_2 + \kappa \cdot (N_1 \cdot D_2 + N_2 \cdot D_1)} \cdot F_2 + \dfrac{\kappa \cdot N_1 \cdot N_2}{D_1 \cdot D_2 + \kappa \cdot (N_1 \cdot D_2 + N_2 \cdot D_1)} \cdot F_1 \end{cases} \tag{167}$$

Annex 4 : Matlab code, Bode diagrams and NS graphs for both damped resonator and piezoelectric filter and different output metrics

```
clear all
close all
clc

%%
% data

resonator_type=1; %0 for RLC, 1 for piezo
SB=1; % 0 for sensitivity plot, 1 for Bode
    diagrams plot

% if SB==0
conf=4; % output metrics : 0 for amplitude
    shift at the restonance, 1 for amplitude
    shift at fixed frequency, 2 for frequency
    shift at the resonance, 3 for phase shift
    at fixed frequency, 4 for amplitude ratio

n_bode=10000; %size of the frequency vector

if or(conf==1,conf==3)
fixed_freq=1
else
fixed_freq=0
end

if resonator_type==0
Q=100;%the axis of the graphs automatically
    adapt to the value of Q
f0=1; %eigenfrequency (set to one for
    normalized frequency)
bode_min=f0*(1-20/Q); %min frequency
bode_max=f0*(1+20/Q); %max frequency
kmmax=100; %max iteration on the mass
    perturbation
dmmax=20/Q; %max perturbation value
kamax=100; %max iteration on the coupling
amax=3/Q; %max coupling value, also used for
    the Bode plot
else
%parameters for the piezoelectric model (
    chapter III)
Q=150000;
f0=999887.5;
bode_min=999910;
bode_max=999960;
g1=2.1E-3;
g2=25.7;
g3=0.0159;
kmmax=10;
dmmax=5/Q;
kamax=10;
amax=30000/Q;
end

if conf==0
valmin=-Q/4;
valmax=Q/4;
elseif conf==1
valmin=-Q/2;
valmax=Q/2;
elseif conf==2
n_bode=300000;
valmin=-0.6;
valmax=0;
elseif conf==3
valmin=-Q;
valmax=Q;
else
valmin=-1.2*Q;
valmax=1.2*Q;
end

ph=-90;%exitation phase on resonator 2

delta=1/2/Q; %normalized frequency offset (
    output metric number 1)

%%
%calculations

opts = bodeoptions('cstprefs');
opts.PhaseVisible = 'off';
opts.Grid = 'off';

astep=amax/(kamax-1);
dmstep=dmmax/(kmmax-1);
bode_step=(bode_max-bode_min)/n_bode;
freq_range=linspace(bode_min,bode_max,n_bode+1)
    ;

Max1=zeros(2,kmmax+1,kamax+1);
Max2=zeros(2,kmmax+1,kamax+1);

w1=zeros(2,kmmax+1,kamax+1);
w2=zeros(2,kmmax+1,kamax+1);

p1=zeros(2,kmmax+1,kamax+1);
p2=zeros(2,kmmax+1,kamax+1);

phi=ph*pi/180;

figure
set(gcf,'Units','Normalized','Position', [0 0
    0.9 0.9]);

for ka=1:kamax+1,
a=(ka-1)*astep;

coupling(ka)=100*a;

(ka-1)/kamax*100 %timing visible in Matlab
    command window

for km=1:kmmax+1
dm=(km-1)*dmstep;

if resonator_type==0

N1=[f0^2];
D1=[1+dm f0/Q f0^2];

N2=[f0^2];
D2=[1 f0/Q f0^2];

else
```

```
N1=[1+dm f0/Q f0^2*(1+g1) 0];
D1=[(1+dm)*(g2+1) f0*(1/Q+(1+dm)*g3*g2+g2/Q) f0^2*(1+g1+g3*g2/Q+g2) f0^3*g2*g3];

N2=[1 f0/Q f0^2*(1+g1) 0];
D2=[g2+1 f0*(1/Q+g3*g2+g2/Q) f0^2*(1+g1+g3*g2/Q+g2) f0^3*g2*g3];

end

n1=sum_poly_coeff(conv(N1,sum_poly_coeff(D2,a*N2)),a*exp(i*phi)*conv(N1,N2));
d1=sum_poly_coeff(sum_poly_coeff(conv(D1,D2),a*conv(N1,D2)),a*conv(N2,D1));

n2=sum_poly_coeff(exp(i*phi)*conv(N2,sum_poly_coeff(D1,a*N1)),a*conv(N1,N2));
d2=d1;

H1=tf(n1,d1);
H2=tf(n2,d2);

[mag1(:),phase1(:)]=bode(H1,bode_min:bode_step:bode_max,opts);
[mag2(:),phase2(:)]=bode(H2,bode_min:bode_step:bode_max,opts); %the phase of the exitation is included in phase2

%%

for k=1:n_bode
Diff1(k)=mag1(k+1)-mag1(k);
Diff2(k)=mag2(k+1)-mag2(k);
end

for k=1:n_bode-1
dDiff1(k)=Diff1(k+1)-Diff1(k);
dDiff2(k)=Diff2(k+1)-Diff2(k);
end

j1=1;
j2=1;

if fixed_freq==0
for k=1:n_bode-1
if j1<3 && Diff1(k)*Diff1(k+1)<=0 && dDiff1(k)<=0 %extremum + concave detection
Max1(j1,km,ka)=mag1(k+1);
w1(j1,km,ka)=freq_range(k+1);
j1=j1+1;
end
if j2<3 && Diff2(k)*Diff2(k+1)<=0 && dDiff2(k)<=0 %extremum + concave detection
Max2(j2,km,ka)=mag2(k+1);
w2(j2,km,ka)=freq_range(k+1);
j2=j2+1;
end
end

else

for k=1:n_bode-1
if km == 1
if j1<3 && Diff1(k)*Diff1(k+1)<=0 && dDiff1(k)<=0 %extremum + concave detection
k1(j1)=k+1;
j1=j1+1;
end
if j2<3 && Diff2(k)*Diff2(k+1)<=0 && dDiff2(k)<=0 %extremum + concave detection
k2(j2)=k+1;
j2=j2+1;
end
end
end

% Amplitudes and phases at fixed frequency

fr1(1)=(bode_min+k1(1)*bode_step);
fr2(1)=(bode_min+k2(1)*bode_step);

f1(1)=fr1(1)*(1-delta);
f2(1)=fr2(1)*(1-delta);

k1b(1)=floor((f1(1)-bode_min)/bode_step);
k2b(1)=floor((f2(1)-bode_min)/bode_step);

Max1(1,km,ka)=mag1(k2b(1));
Max2(1,km,ka)=mag2(k2b(1));

p1(1,km,ka)=phase1(k1(1));
p2(1,km,ka)=phase2(k2(1));

S1=size(k1);
S2=size(k2);

if S1(2)>1 % test existance of mode 2
fr1(2)=(bode_min+k1(2)*bode_step);
f1(2)=fr1(2)*(1-delta);
k1b(2)=floor((f1(2)-bode_min)/bode_step);
Max1(2,km,ka)=mag1(k2b(2));
p1(2,km,ka)=phase1(k1(2));
end

if S2(2)>1
fr2(2)=(bode_min+k2(2)*bode_step);
f2(2)=fr2(2)*(1-delta);
k2b(2)=floor((f2(2)-bode_min)/bode_step);
Max2(2,km,ka)=mag2(k2b(2));
p2(2,km,ka)=phase2(k2(2));
end

end

if km<kmmax
Perturbation(km)=dm*100; %for the plot
end

%amplitude reference
if fixed_freq==1
if km==1
if ka==1
REF=mag1(k1(1));
end
end
else
if km==1
if ka==1
REF=Max1(1,1,1);
end
end
end

if conf==0
%amplitude shift at the resonance

if km>1

NSR1M1(ka,km-1) = (Max1(1,km,ka)-Max1(1,km-1,ka))/REF/dmstep;
NSR1M2(ka,km-1) = (Max1(2,km,ka)-Max1(2,km-1,ka))/REF/dmstep;
NSR2M1(ka,km-1) = (Max2(1,km,ka)-Max2(1,km-1,ka))/REF/dmstep;
NSR2M2(ka,km-1) = (Max2(2,km,ka)-Max2(2,km-1,ka))/REF/dmstep;
```

```
% anti artefact
if abs(NSR1M1(ka,km-1))>valmax
NSR1M1(ka,km-1)=0;
end

if abs(NSR2M1(ka,km-1))>valmax
NSR2M1(ka,km-1)=0;
end

if abs(NSR1M2(ka,km-1))>valmax
NSR1M2(ka,km-1)=0;
end

if abs(NSR2M2(ka,km-1))>valmax
NSR2M2(ka,km-1)=0;
end
end

elseif conf==1
%amplitude shift at fixed frequency

if km>1

NSR1M1(ka,km-1) = (Max1(1,km,ka)-Max1(1,km-1,ka
    ))/REF/dmstep;
NSR2M1(ka,km-1) = (Max2(1,km,ka)-Max2(1,km-1,ka
    ))/REF/dmstep;
NSR1M2(ka,km-1) = (Max1(2,km,ka)-Max1(2,km-1,ka
    ))/REF/dmstep;
NSR2M2(ka,km-1) = (Max2(2,km,ka)-Max2(2,km-1,ka
    ))/REF/dmstep;

end

elseif conf==2
%frequency shift at the resonance

if km>1

NSR1M1(ka,km-1) = (w1(1,km,ka)-w1(1,km-1,ka))/
    f0/dmstep;
NSR1M2(ka,km-1) = (w1(2,km,ka)-w1(2,km-1,ka))/
    f0/dmstep;
NSR2M1(ka,km-1) = (w2(1,km,ka)-w2(1,km-1,ka))/
    f0/dmstep;
NSR2M2(ka,km-1) = (w2(2,km,ka)-w2(2,km-1,ka))/
    f0/dmstep;

end

elseif conf==3
%phase shift at fixed frequency

if km>1

NSR1M1(ka,km-1) = (p1(1,km,ka)-p1(1,km-1,ka))
    /180/dmstep;
NSR1M2(ka,km-1) = (p1(2,km,ka)-p1(2,km-1,ka))
    /180/dmstep;
NSR2M1(ka,km-1) = (p2(1,km,ka)-p2(1,km-1,ka))
    /180/dmstep;
NSR2M2(ka,km-1) = (p2(2,km,ka)-p2(2,km-1,ka))
    /180/dmstep;
end

else

if km>1
NSamplM1(ka,km-1) = ((Max1(1,km,ka)/Max2(1,km,
    ka))-(Max1(1,km-1,ka)/Max2(1,km-1,ka)))/
    dmstep; %mode 1 : resonator 1 over 2
NSamplM2(ka,km-1) = ((Max2(2,km,ka)/Max1(2,km,
    ka))-(Max2(2,km-1,ka)/Max1(2,km-1,ka)))/
    dmstep; %mode 2 : resonator 2 over 1
%       NSamplM1(ka,km-1) = ((Max2(1,km,ka)/Max1
    (1,km,ka))-(Max2(1,km-1,ka)/Max1(1,km-1,ka)
    ))/dmstep; %mode 1 : resonator 2 over 1
%       NSamplM2(ka,km-1) = ((Max1(2,km,ka)/Max2
    (2,km,ka))-(Max1(2,km-1,ka)/Max2(2,km-1,ka)
    ))/dmstep; %mode 2 : resonator 1 over 2

% anti artefact
if abs(NSamplM1(ka,km-1))>valmax
NSamplM1(ka,km-1)=0;
end

if abs(NSamplM2(ka,km-1))>valmax
NSamplM2(ka,km-1)=0;
end
end
end

if SB==1
if ka==kamax
%%
%plot

% Colors
co=abs(km-1)/(kmmax);

if 0<=co && co<0.2
c1=1;
c2=5*co;
c3=0;
elseif  0.2<=co && co<0.4
c1=1-5*(co-0.2);
c2=1;
c3=0;
elseif  0.4<=co && co<0.6
c1=0;
c2=1;
c3=5*(co-0.4);
elseif  0.6<=co && co<0.8
c1=0;
c2=1-5*(co-0.6);
c3=1;
elseif  0.8<=co && co<=1
c1=5*(co-0.8);
c2=0;
c3=1;
end

subplot(2,2,1)
hold on
plot(freq_range,(mag1),'LineWidth',0.5,'color'
    ,[c1 c2 c3]);

subplot(2,2,2)
hold on
plot(freq_range,(mag2),'LineWidth',0.5,'color'
    ,[c1 c2 c3]);

subplot(2,2,3)
hold on
plot(freq_range,(phase1),'LineWidth',0.5,'color
    ',[c1 c2 c3]);

subplot(2,2,4)
hold on
plot(freq_range,(phase2),'LineWidth',0.5,'color
    ',[c1 c2 c3]);


end
end
end
```

```
end

if SB==0
if conf==4

subplot(1,2,1)
imagesc(Perturbation,coupling,NSamplM1);
xlabel('Perturbation␣(%)');
title('NSamplM1');
ylabel('Coupling␣(%)');
colormap('jet');
set(gca, 'fontsize', 20);
colorbar;
caxis([valmin, valmax]);
grid on

subplot(1,2,2)
imagesc(Perturbation,coupling,NSamplM2);
xlabel('Perturbation␣(%)');
title('NSamplM2');
ylabel('Coupling␣(%)');
colormap('jet');
set(gca, 'fontsize', 20);
colorbar;
caxis([valmin, valmax]);
grid on

else

subplot(2,2,1)
imagesc(Perturbation,coupling,NSR1M1);
xlabel('Perturbation␣(%)');
title('NSR1M1');
ylabel('Coupling␣(%)');
colormap('jet');
set(gca, 'fontsize', 20);
colorbar;
caxis([valmin, valmax]);
grid on

subplot(2,2,2)
imagesc(Perturbation,coupling,NSR2M1);
title('NSR2M1');
xlabel('Perturbation␣(%)');
ylabel('Coupling␣(%)');
colormap('jet');
set(gca, 'fontsize', 20);
colorbar;
caxis([valmin, valmax]);
grid on

subplot(2,2,3)
imagesc(Perturbation,coupling,NSR1M2);
title('NSR1M2');
xlabel('Perturbation␣(%)');
ylabel('Coupling␣(%)');
colormap('jet');
set(gca, 'fontsize', 20);
colorbar;
caxis([valmin, valmax]);
grid on

subplot(2,2,4)
imagesc(Perturbation,coupling,NSR2M2);
title('NSR2M2');
xlabel('Perturbation␣(%)');
ylabel('Coupling␣(%)');
colormap('jet');
set(gca, 'fontsize', 20);
colorbar;
caxis([valmin, valmax]);
grid on

end
end

%% Polynoms sum function
function coeff_sum = sum_poly_coeff(x1,x2)

x1_order = length(x1);
x2_order = length(x2);

if x1_order > x2_order
max_order = size(x1);
else
max_order = size(x2);
end

new_x1 = padarray(x1,max_order-size(x1),0,'pre'
    );
new_x2 = padarray(x2,max_order-size(x2),0,'pre'
    );

coeff_sum = new_x1 + new_x2;

return
end
```

Annex 5 : Digital filter coefficients

$$
\left\{
\begin{aligned}
a_0 =& \frac{1}{D}\cdot\Big(A^2\cdot Q + A^2\cdot Q\cdot g_1 + A + Q + Q\cdot\epsilon\Big)\\
a_1 =& \frac{1}{D}\cdot\Big(A^2\cdot Q\cdot g_1 - A + A^2\cdot Q - 3Q - 3Q\cdot\epsilon\Big)\\
a_2 =& \frac{1}{D}\cdot\Big(3Q - A - A^2\cdot Q\cdot g_1 - A^2\cdot Q + 3Q\cdot\epsilon\Big)\\
a_3 =& \frac{1}{D}\cdot\Big(-A^2\cdot Q + A - A^2\cdot Q\cdot g_1 - Q\cdot\epsilon - Q\Big)\\
b_1 =& \frac{1}{D}\cdot\Big(A^2\cdot Q - 3Q - A - 3Q\cdot\epsilon - 3Q\cdot\epsilon\cdot g_2 - A\cdot g_2\cdot g_3\cdot Q + 3g_2\cdot g_3\cdot A^3\cdot Q\\
& -A\cdot g_2\cdot g_3\cdot Q\cdot\epsilon + A^2\cdot Q\cdot g_2 + A^2\cdot g_2\cdot g_3 + A^2\cdot Q\cdot g_1 - A\cdot g_2 - 3Q\cdot g_2\Big)\\
b_2 =& \frac{1}{D}\cdot\Big(-A - A\cdot g_2\cdot g_3\cdot Q - A\cdot g_2\cdot g_3\cdot Q\cdot\epsilon + 3g_2\cdot g_3\cdot A^3\cdot Q - A^2\cdot Q\cdot g_2 - A\cdot g_2\\
& +3Q\cdot\epsilon\cdot g_2 - A^2\cdot Q - A^2\cdot Q\cdot g_1 + 3Q + 3Q\cdot g_2 - A^2\cdot g_2\cdot g_3 + 3Q\cdot\epsilon\Big)\\
b_3 =& \frac{1}{D}\cdot\Big(g_2\cdot g_3\cdot A^3\cdot Q - g_2\cdot Q + A\cdot g_2\cdot g_3\cdot Q\cdot\epsilon - A^2\cdot g_2\cdot g_3 - A^2\cdot Q\cdot g_1 - A^2\cdot Q + A\\
& +A\cdot g_2 + A\cdot g_2\cdot g_3\cdot Q - A^2\cdot g_2\cdot Q - Q\cdot\epsilon - Q\cdot\epsilon\cdot g_2 - Q\Big)\\
D =& Q + A\cdot g_2\cdot g_3\cdot Q\cdot\epsilon + g_2\cdot g_3\cdot A^3\cdot Q + Q\cdot\epsilon + A\cdot g_2\cdot g_3\cdot Q + A^2\cdot Q + Q\cdot\epsilon\cdot g_2 + g_2\cdot Q\\
& + A^2\cdot Q\cdot g_1 + A^2\cdot g_2\cdot g_3 + A + A\cdot g_2 + A^2\cdot g_2\cdot Q\\
A =& \tan\left(\pi\cdot\frac{f_0}{f_s}\right)
\end{aligned}
\right.
\tag{168}
$$

Annex 6 : Verilog sources

Listing IV.1: Decimation

```
‘timescale 1ns / 1ps

module decimation(
data_clk,
decimation_factor,
data_en,
);

parameter counter_size = 16;

input data_clk;
input [counter_size-1:0] decimation_factor;
output data_en;

reg [counter_size-1:0] counter = 0;

always @ (posedge data_clk) begin
if (counter < decimation_factor-1) begin
counter <= counter +1;
end else begin
counter <= 0;
end
end

assign data_en = counter==0;

endmodule
```

Listing IV.2: Left bit shifting

```
‘timescale 1ns / 1ps

module multiply_by_2_pow_n(
n,Din,Dout
);

parameter data_size = 14;
parameter n_size = 4;

input [n_size-1:0] n;
input [data_size-1:0] Din;
output [data_size-1:0] Dout;

reg [data_size-1:0] reg_out=0;
integer i;

always @ *
begin
for(i=0; i<data_size; i=i+1) begin
if (i<n) begin
reg_out[i] <= 1’b0;
end else begin
reg_out[i] <= Din[i-n];
end
end

end
assign Dout = reg_out;

endmodule
```

Listing IV.3: Right bit shifting

```
‘timescale 1ns / 1ps

module divide_by_2_pow_n(
n,Din,Dout
);

parameter data_size = 14;
parameter n_size = 4;

input [n_size-1:0] n;
input [data_size-1:0] Din;
output [data_size-1:0] Dout;

reg [data_size-1:0] reg_out;
integer i;

always @ *
begin
for(i=0; i<data_size; i=i+1) begin
if (i+n<data_size) begin
reg_out[i] <= Din[i+n];
end else begin
reg_out[i] <= Din[data_size-1];
end
end
for(i=0; i<data_size; i=i+1) begin
if (i+n<data_size) begin
reg_out[i] <= Din[i+n];
end else begin
reg_out[i] <= 1’b0;
end
end
end

assign Dout = reg_out;

endmodule
```

Listing IV.4: Switch

```
‘timescale 1ns / 1ps

module onoff(
n,Din,Dout
);

parameter data_size = 24;

input [data_size-1:0] Din;
output [data_size-1:0] Dout;
input [0:0] n;

reg [data_size-1:0] reg_out;

always @ *
begin
case (n)
1’b0 : reg_out <= 0;
1’b1 : reg_out <= Din;
endcase
end

assign Dout = reg_out;

endmodule
```

Listing IV.5: Fixed delay

```
‘timescale 1ns / 1ps

module latency(
clk,
data_i,
data_o
);

parameter data_size = 14;
parameter delay=100; //to be between 0 and 125

input clk;
input [data_size-1:0] data_i;
output [data_size-1:0] data_o;

reg [data_size*126:0] store=0; //(125MHz sampling - 14 is the data_size) -> from 0 to 1us delay
reg [data_size-1:0] reg_out=0;

always @ (posedge clk)
begin
store<=store<<data_size;
store[data_size-1:0]<=data_i;
reg_out<=store[(delay+1)*data_size-1:delay*data_size];
end

assign data_o=reg_out;

endmodule
```

Annex 7 : Characteristics of the impedance analyzer and the fluorescent particles used in this thesis

Table 14: Main characteristics of the impedance analyzer E4990A from Keysight. Datasheet available from [295].

Name	E4990A
Frequency bandwidth	From 20 Hz to 120 MHz
Frequency sweep resolution	1 mHz
Number of samples	From 2 to 1601 points
Input voltage	From 5 mV RMS to 1 V RMS
Averaging factor	From 1 to 999

Table 15: Characteristics of the fluorescent melamine resin particles MF-NB-COOH-S1058 from microparticles GmbH. Additional information is available from [296].

Name	MF-NB-COOH-S1058
Absorbance/Emission wavelength	636 nm/686 nm
Diameter	920 nm
Density	1.510

Bibliography

[1] Claude Humbert, Gwenhael Goavec Merou, Thomas Bertin, Najib Kacem, Vincent Walter, and Therese Leblois. On the Implementation of Mode Localization Between Physical and Digital Resonators. In *2018 IEEE International Ultrasonics Symposium (IUS)*, pages 1–4. IEEE, oct 2018.

[2] Claude Humbert, Gwenhaël Goavec-Merou, Vincent Walter, Najib Kacem, and Therese Leblois. Implementation of a tunable hybrid system with coupled high Q-factor resonators based on mode localization for sensing purposes. *Smart Materials and Structures*, jan 2020.

[3] Robert Bogue. MEMS sensors: past, present and future. *Sensor Review*, 27(1):7–13, jan 2007.

[4] Chun Zhao, Mohammad H. Montaseri, Graham S. Wood, Suan Hui Pu, Ashwin A. Seshia, and Michael Kraft. A review on coupled MEMS resonators for sensing applications utilizing mode localization. *Sensors and Actuators, A: Physical*, 249:93–111, oct 2016.

[5] Jerome Juillard, Pierre Prache, Pietro Maris Ferreira, and Nuria Barniol. Ultimate limits of differential resonant MEMS sensors based on two coupled linear resonators. In *IEEE Transactions on Ultrasonics, Ferroelectrics, and Frequency Control*, volume 65, pages 2440–2448, dec 2018.

[6] A.A. Barlian, W.-T. Park, J.R. Mallon, A.J. Rastegar, and B.L. Pruitt. Review: Semiconductor Piezoresistance for Microsystems. *Proceedings of the IEEE*, 97(3):513–552, mar 2009.

[7] William Thomson. XIX. On the electro-dynamic qualities of metals : Effects of magnetization on the electric conductivity of nickel and of iron. *Proceedings of the Royal Society of London*, (8):546–550, 1857.

[8] P W Bridgman. The effect of tension on the transverse and longitudinal resistance of metals. In *Proceedings of the American Academy of Arts and Sciences*, volume 60, pages 423–449. JSTOR, 1925.

[9] Charles S. Smith. Piezoresistance effect in germanium and silicon. *Physical Review*, 94(1):42–49, apr 1954.

[10] Kensall D. Wise. Integrated sensors, MEMS, and microsystems: Reflections on a fantastic voyage. *Sensors and Actuators A: Physical*, 136(1):39–50, may 2007.

[11] William Paul and G. L. Pearson. Pressure Dependence of the Resistivity of Silicon. *Physical Review*, 98(6):1755–1757, jun 1955.

[12] W. P. Mason and R. N. Thurston. Use of Piezoresistive Materials in the Measurement of Displacement, Force, and Torque. *The Journal of the Acoustical Society of America*, 29(10):1096–1101, oct 1957.

[13] W. G. Pfann and R. N. Thurston. Semiconducting Stress Transducers Utilizing the Transverse and Shear Piezoresistance Effects. *Journal of Applied Physics*, 32(10):2008–2019, oct 1961.

[14] O. N. Tufte, P. W. Chapman, and Donald Long. Silicon Diffused-Element Piezoresistive Diaphragms. *Journal of Applied Physics*, 33(11):3322–3327, nov 1962.

[15] The point-contact transistor. http://ds-wordpress.haverford.edu/bitbybit/bit-by-bit-contents/chapter-eight/8-2-the-point-contact-transistor/.

[16] History of MEMS. *Southwest Center for Microsystems Education (SCME)*, pages 1–20, 2017.

[17] History of MEMS. http://scme-nm.org/files/History of MEMS_Presentation.pdf.

[18] J S Kilby. Miniature semiconductor integrated circuit. may 1959.

[19] Transistors, How do they work ? https://www.youtube.com/watch?v=7ukDKVHnac4.

[20] H. C. Nathanson, W. E. Newell, R. A. Wickstrom, and J. R. Davis. The resonant gate transistor. *IEEE Transactions on Electron Devices*, 14(3):117–133, March 1967.

[21] What is Moore's Law ? https://www.webopedia.com/TERM/M/Moores_Law .html.

[22] Feynman's Talk, 1959. https://www.zyvex.com/nanotech/feynman.html.

[23] K.E. Petersen. Silicon as a mechanical material. *Proceedings of the IEEE*, 70(5):420–457, may 1982.

[24] S. Samaun, K. Wise, E. Nielsen, and J. Angell. An IC piezoresistive pressure sensor for biomedical instrumentation. In *1971 IEEE International Solid-State Circuits Conference. Digest of Technical Papers*, pages 104–105. IEEE, 1971.

[25] Wolf D. Frobenius, A. C. Sanderson, and H. C. Nathanson. A Microminiature Solid-State Capacitive Blood Pressure Transducer with Improved Sensitivity. *IEEE Transactions on Biomedical Engineering*, BME-20(4):312–314, jul 1973.

[26] Susumu Sugiyama, Mitsuharu Takigawa, and Isemi Igarashi. Integrated piezoresistive pressure sensor with both voltage and frequency output. *Sensors and Actuators*, 4:113–120, jan 1983.

[27] Kazuji Yamada, Motohisa Nishihara, Ryosaku Kanzawa, and Ryoichi Kobayashi. A piezoresistive integrated pressure sensor. *Sensors and Actuators*, 4:63–69, jan 1983.

[28] Kyoichi Ikeda, Hideki Kuwayama, Takashi Kobayashi, Tetsuya Watanabe, Tadashi Nishikawa, Takashi Yoshida, and Kinji Harada. Silicon pressure sensor integrates resonant strain gauge on diaphragm. *Sensors and Actuators A: Physical*, 21(1-3):146–150, feb 1990.

[29] K. W. Ragland and R. E. Cullen. Piezoelectric Pressure Transducer with Acoustic Absorbing Rod. *Review of Scientific Instruments*, 38(6):740–742, jun 1967.

[30] A.V. Shirinov and W.K. Schomburg. Pressure sensor from a PVDF film. *Sensors and Actuators A: Physical*, 142(1):48–55, mar 2008.

[31] Robert Bogue. Recent developments in MEMS sensors: a review of applications, markets and technologies. *Sensor Review*, 33(4):300–304, sep 2013.

[32] James Z Liu, James D Cook, and Peter P Dierauer. Disposable and trimmable wireless pressure sensor for medical applications. *US Patent 7059195*, 2006.

[33] David J. Beebe, Arthur S. Hsieh, Denice D. Denton, and Robert G. Radwin. A silicon force sensor for robotics and medicine. *Sensors and Actuators A: Physical*, 50(1-2):55–65, aug 1995.

[34] Yaping Zang, Fengjiao Zhang, Chong-an Di, and Daoben Zhu. Advances of flexible pressure sensors toward artificial intelligence and health care applications. *Materials Horizons*, 2(2):140–156, feb 2015.

[35] L.M. Roylance and J.B. Angell. A batch-fabricated silicon accelerometer. *IEEE Transactions on Electron Devices*, 26(12):1911–1917, dec 1979.

[36] Simon Middelhoek. Celebration of the tenth transducers conference: The past, present and future of transducer research and development. *Sensors and Actuators A: Physical*, 82(1-3):2–23, may 2000.

[37] Leland J Spangler, Christopher J Kemp, and Michael C Graf. Integrated silicon automotive accelerometer and single-point impact sensor. *US Patent 5,495,414*, feb 1996.

[38] Michael William Putty. *A micromachined vibrating ring gyroscope.* PhD thesis, 1995.

[39] J. Bernstein, S. Cho, A.T. King, A. Kourepenis, P. Maciel, and M. Weinberg. A micromachined comb-drive tuning fork rate gyroscope. In *[1993] Proceedings IEEE Micro Electro Mechanical Systems*, pages 143–148. IEEE.

[40] Pierre-Jean Bristeau, François Callou, David Vissière, and Nicolas Petit. The Navigation and Control technology inside the AR.Drone micro UAV. *IFAC Proceedings Volumes*, 44(1):1477–1484, jan 2011.

[41] A. Partridge, J.K. Reynolds, B.W. Chui, E.M. Chow, A.M. Fitzgerald, L. Zhang, N.I. Maluf, and T.W. Kenny. A high-performance planar piezoresistive accelerometer. *Journal of Microelectromechanical Systems*, 9(1):58–66, mar 2000.

[42] D.L. DeVoe and A.P. Pisano. Surface micromachined piezoelectric accelerometers (PiXLs). *Journal of Microelectromechanical Systems*, 10(2):180–186, jun 2001.

[43] K.H.-L Chau, S.R Lewis, Y Zhao, R.T Howe, S.F Bart, and R.G Marcheselli. An integrated force-balanced capacitive accelerometer for low-g applications. *Sensors and Actuators A: Physical*, 54(1-3):472–476, jun 1996.

[44] Gabriel M. Rebeiz. *RF MEMS : theory, design, and technology.* J. Wiley, 2003.

[45] Clark T C Nguyen and Roger T Howe. Quality factor control for micromechanical resonators. In *Tech. Dig. IEEE Int. Electron Devices Meeting*, pages 14–16, 1992.

[46] R. Aigner, J. Ella, H.-J. Timme, L. Elbrecht, W. Nessler, and S. Marksteiner. Advancement of MEMS into RF-filter applications. In *Digest. International Electron Devices Meeting,*, pages 897–900. IEEE.

[47] C.C.W. Ruppel, L. Reindl, and R. Weigel. SAW devices and their wireless communications applications. *IEEE Microwave Magazine*, 3(2):65–71, jun 2002.

[48] H.P. Lobl, M. Klee, C. Metzmacher, W. Brand, R. Milsom, P. Lok, and F. van Straten. Piezoelectric materials for BAW resonators and filters. In *2001 IEEE Ultrasonics Symposium. Proceedings. An International Symposium (Cat. No.01CH37263)*, volume 1, pages 807–811. IEEE.

[49] M. Benetti, D. Cannat, A. D'Amico, F. Di Pietrantonio, V. Foglietti, and E. Verona. Thin film bulk acoustic wave resonator (TFBAR) gas sensor. In *IEEE Ultrasonics Symposium*, volume 3, pages 1581–1584. IEEE.

[50] W. Buff, S. Klett, M. Rusko, J. Ehrenpfordt, and M. Goroli. Passive remote sensing for temperature and pressure using SAW resonator devices. *IEEE Transactions on Ultrasonics, Ferroelectrics and Frequency Control*, 45(5):1388–1392, sep 1998.

[51] G. Watson and E. Staples. In *IEEE Symposium on Ultrasonics*, pages 311–314. IEEE, 1990.

[52] A. G. McNamara. Semiconductor Diodes and Transistors as Electrical Thermometers. *Review of Scientific Instruments*, 33(3):330–333, mar 1962.

[53] Prime Faraday Technology. *An Introduction to MEMS (Micro-electromechanical Systems).* 2002.

[54] Pascal Nicolay. *Les capteurs à ondes élastiques de surface: applications pour la mesure des basses pressions et des hautes températures.* PhD thesis, Université Henri Poincaré-Nancy 1, 2007.

[55] G. L. Pearson. A Magnetic Field Strength Meter Employing the Hall Effect in Germanium. *Review of Scientific Instruments*, 19(4):263–265, apr 1948.

[56] G. Bosch. A Hall device in an integrated circuit. *Solid-State Electronics*, 11(7):712–714, jul 1968.

[57] John N Shive. Photoresistive translating device. *Patent*, apr 1949.

[58] Bell Labs announces the phototransistor, March 30, 1950 — EDN. https://www.edn.com/electronics-blogs/edn-moments/4439062/Bell-Labs-announces-the-phototransistor–March-30–1950.

[59] Charles H. Townes. The first laser. https://www.press.uchicago.edu/Misc/Chicago/284158_townes.html, 2003.

[60] MEMS Journal – The Largest MEMS Publication in the World: MOEMS: history, current status and future trends. https://www.memsjournal.com/2007/04/moems_history_c.html.

[61] Chian Chiu Li. Interferometric MOEMS sensor. *Patent*, feb 2006.

[62] Lukas Willem Snyman. CMOS MOEMS sensor device. *Patent*, jun 2010.

[63] Jacob Y. Wong. NDIR gas sensor. *Patent*, apr 1997.

[64] D. Fourguette, D. Modarress, F. Taugwalder, D. Wilson, M. Koochesfahani, and M. Gharib. Miniature and MOEMS flow sensors. In *15th AIAA Computational Fluid Dynamics Conference*, Reston, Virigina, jun 2001. American Institute of Aeronautics and Astronautics.

[65] Leland C. Clark and Champ Lyons. Electrode Systems for Continuous Monitoring in Cardiovascular Surgery. *Annals of the New York Academy of Sciences*, 102(1):29–45, 1962.

[66] Eun Hyung Yoo and Soo Youn Lee. Glucose biosensors: An overview of use in clinical practice. *Sensors*, 10(5):4558–4576, 2010.

[67] Needle-Free Diabetes: 7 Devices that Painlessly Measure Blood Glucose. https://labiotech.eu/tops/needle-free-glucose-monitoring-for-diabetes-medtech/.

[68] S. Rodriguez-Mozaz, M.-P. Marco, M. J. Lopez de Alda, and D. Barceló. Biosensors for environmental applications: Future development trends. *Pure and Applied Chemistry*, 76(4):723–752, jan 2004.

[69] Alessia Mortari and Leandro Lorenzelli. Recent sensing technologies for pathogen detection in milk: A review. *Biosensors and Bioelectronics*, 60:8–21, oct 2014.

[70] Celine I.L. Justino, Teresa A. Rocha-Santos, and Armando C. Duarte. Review of analytical figures of merit of sensors and biosensors in clinical applications. *TrAC - Trends in Analytical Chemistry*, 29(10):1172–1183, 2010.

[71] Aleksandr Oseev, Benoît Le Roy de Boiseaumarié, Fabien Remy-Martin, Jean-François Manceau, Alain Rouleau, Franck Chollet, Wilfrid Boireau, and Thérèse Leblois. Integration of Microresonant Sensor into a Microfluidic Platform for the Real Time Analysis of Platelets-Collagen Interaction in Flow Condition. *Proceedings*, 2(13):940, dec 2018.

[72] Olivier Lazcka, F. Javier Del Campo, and F. Xavier Muñoz. Pathogen detection: A perspective of traditional methods and biosensors. *Biosensors and Bioelectronics*, 22(7):1205–1217, feb 2007.

[73] Scott P. Nichols, Ahyeon Koh, Wesley L. Storm, Jae Ho Shin, and Mark H. Schoenfisch. Biocompatible Materials for Continuous Glucose Monitoring Devices. *Chemical Reviews*, 113(4):2528–2549, apr 2013.

[74] D Mihov and B Katerska. Some biocompatible materials used in medical practice. *Trakia Journal of Sciences*, 8(2):119–125, 2010.

[75] Kuo-Kang Liu, Ren-Guei Wu, Yun-Ju Chuang, Hwa Seng Khoo, Shih-Hao Huang, and Fan-Gang Tseng. Microfluidic Systems for Biosensing. *Sensors*, 10(7):6623–6661, jul 2010.

[76] Humphry Davy. I. On the fire-damp of coal mines, and on methods of lighting the mines so as to prevent its explosion. *Philosophical Transactions of the Royal Society of London*, (106):1–22, 1816.

[77] J.L. Arlett, E.B. Myers, and M.L. Roukes. Comparative advantages of mechanical biosensors. *Nature Nanotechnology*, 6(4):203–215, apr 2011.

[78] N. Bhalla, P. Jolly, N. Formisano, and P. Estrela. Introduction to biosensors. *Essays In Biochemistry*, 60(1):1–8, jun 2016.

[79] Anh Tuan Mai. *Développement de biocapteurs électrochimiques à base de tyrosinase pour la détection de polluants organiques en phase aqueuse.* PhD thesis, Université Claude Bernard-Lyon I, 2004.

[80] Hans Nilsson, Ann-Charlotte Åkerlund, and Klaus Mosbach. Determination of glucose, urea and penicillin using enzyme-pH-electrodes. *Biochimica et Biophysica Acta (BBA) - General Subjects*, 320(2):529–534, sep 1973.

[81] M Mascini and G G Guilbault. Urease coupled ammonia electrode for urea determination in blood serum. *Analytical chemistry*, 49(6):795–8, may 1977.

[82] P. Bergveld. Development of an Ion-Sensitive Solid-State Device for Neurophysiological Measurements. *IEEE Transactions on Biomedical Engineering*, BME-17(1):70–71, jan 1970.

[83] V. Pachauri and S. Ingebrandt. Biologically sensitive field-effect transistors: from ISFETs to NanoFETs. *Essays In Biochemistry*, 60(1):81–90, 2016.

[84] A. Montrose. *Développement d'un immunocapteur impédimétrique pour la détection et la quantification d'une sous- population cellulaire : Application au diagnostic précoce des infections.* PhD thesis, 2013.

[85] Jack W. Judy. Biomedical applications of MEMS.

[86] Mark C. Lonergan, Erik J. Severin, Brett J. Doleman, Sara A. Beaber, Robert H. Grubbs, and Nathan S. Lewis. Array-Based Vapor Sensing Using Chemically Sensitive, Carbon Black-Polymer Resistors. *Chemistry of Materials*, 1996.

[87] Sadanand Pandey. Highly sensitive and selective chemiresistor gas/vapor sensors based on polyaniline nanocomposite: A comprehensive review. *Journal of Science: Advanced Materials and Devices*, 1(4):431–453, dec 2016.

[88] T.A. Emadi, C. Shafai, D.J. Thomson, M.S. Freund, N.D.G. White, and D.S. Jayas. Polymer-based gas sensor on a thermally stable micro-cantilever. *Procedia Engineering*, 5:21–24, jan 2010.

[89] George F. Fine, Leon M. Cavanagh, Ayo Afonja, and Russell Binions. Metal Oxide Semi-Conductor Gas Sensors in Environmental Monitoring. *Sensors*, 10(6):5469–5502, jun 2010.

[90] Chengxiang Wang, Longwei Yin, Luyuan Zhang, Dong Xiang, and Rui Gao. Metal Oxide Gas Sensors: Sensitivity and Influencing Factors. *Sensors*, 10(3):2088–2106, mar 2010.

[91] Eduard Llobet. Gas sensors using carbon nanomaterials: A review. *Sensors and Actuators B: Chemical*, 179:32–45, mar 2013.

[92] Quan Wang and Behrouz Arash. A review on applications of carbon nanotubes and graphenes as nano-resonator sensors. *Computational Materials Science*, 82:350–360, feb 2014.

[93] Yi-Hua Zheng, Tse-Chao Hua, and Fei Xu. A Thermal Biosensor Based on Enzyme Reaction. In *2005 IEEE Engineering in Medicine and Biology 27th Annual Conference*, pages 1909–1912. IEEE, 2005.

[94] Isolde Simon and Michael Arndt. Thermal and gas-sensing properties of a micromachined thermal conductivity sensor for the detection of hydrogen in automotive applications. *Sensors and Actuators A: Physical*, 97-98:104–108, apr 2002.

[95] Pascal Tardy, Jean-René Coulon, Claude Lucat, and Francis Menil. Dynamic thermal conductivity sensor for gas detection. *Sensors and Actuators B: Chemical*, 98(1):63–68, mar 2004.

[96] Pavel Damborskỳ, Juraj Švitel, and Jaroslav Katrlík. Optical biosensors. *Essays in biochemistry*, 60(1):91–100, 2016.

[97] Shaopeng Li, Mo Yang, Wenfei Zhou, Trevor G. Johnston, Rui Wang, and Jinsong Zhu. Dextran hydrogel coated surface plasmon resonance imaging (SPRi) sensor for sensitive and label-free detection of small molecule drugs. *Applied Surface Science*, 355:570–576, nov 2015.

[98] Claes Nylander, Bo Liedberg, and Tommy Lind. Gas detection by means of surface plasmon resonance. *Sensors and Actuators*, 3(C):79–88, jan 1982.

[99] J Homola. *Present and future of surface plasmon resonance biosensors*, volume 377. Springer-Verlag, oct 2003.

[100] Estevez M.-C., Otte M.A., Sepulveda B., and Lechuga L.M. Trends and challenges of refractometric nanoplasmonic biosensors: A review. *Analytica Chimica Acta*, 806:55–73, 2014.

[101] Clifford K Ho, Michael T Itamura, Michael Kelley, Robert C Hughes, and Others. Review of chemical sensors for in-situ monitoring of volatile contaminants. *Sandia Report*, page 28, 2001.

[102] Reshma Bharadwaj, V.V.R. Sai, Kamini Thakare, Arvind Dhawangale, Tapanendu Kundu, Susan Titus, Pradeep Kumar Verma, and Soumyo Mukherji. Evanescent wave absorbance based fiber optic biosensor for label-free detection of E. coli at 280 nm wavelength. *Biosensors and Bioelectronics*, 26(7):3367–3370, mar 2011.

[103] H. Arwin. Is ellipsometry suitable for sensor applications? *Sensors and Actuators A: Physical*, 92(1-3):43–51, aug 2001.

[104] Marcus J. Swann, Louise L. Peel, Simon Carrington, and Neville J. Freeman. Dual-polarization interferometry: An analytical technique to measure changes in protein structure in real time, to determine the stoichiometry of binding events, and to differentiate between specific and nonspecific interactions. *Analytical Biochemistry*, 329(2):190–198, 2004.

[105] Jane Hodgkinson and Ralph P Tatam. Optical gas sensing: a review. *Measurement Science and Technology*, 24(1):012004, jan 2013.

[106] Bassam Alfeeli, Gary Pickrell, Anbo Wang, Bassam Alfeeli, Gary Pickrell, and Anbo Wang. Sub-Nanoliter Spectroscopic Gas Sensor. *Sensors*, 6(10):1308–1320, oct 2006.

[107] Alejandro Sosa-Peinado and Martn Gonzlez-Andrade. Fluorescent Biosensors for Protein Interactions and Drug Discovery. In *Biosensors for Health, Environment and Biosecurity*. InTech, jul 2011.

[108] Vinalia Tjong, Hua Yu, Angus Hucknall, Srinath Rangarajan, and Ashutosh Chilkoti. Amplified on-chip fluorescence detection of DNA hybridization by surface-initiated enzymatic polymerization. *Analytical chemistry*, 83(13):5153–5159, 2011.

[109] Karolyn M. Hansen and Thomas Thundat. Microcantilever biosensors. *Methods*, 37(1):57–64, sep 2005.

[110] Jürgen Fritz. Cantilever biosensors. *The Analyst*, 133(7):855, jun 2008.

[111] Guanghua Wu, Ram H. Datar, Karolyn M. Hansen, Thomas Thundat, Richard J. Cote, and Arun Majumdar. Bioassay of prostate-specific antigen (PSA) using microcantilevers. *Nature Biotechnology*, 19(9):856–860, sep 2001.

[112] Joan Bausells. Piezoresistive cantilevers for nanomechanical sensing. *Microelectronic Engineering*, 145:9–20, sep 2015.

[113] Roberto Raiteri, Massimo Grattarola, Hans-Jürgen Butt, and Petr Skládal. Micromechanical cantilever-based biosensors. *Sensors and Actuators B: Chemical*, 79(2-3):115–126, oct 2001.

[114] G Y Chen, T Thundat, E A Wachter, and R J Warmack. Adsorption-induced surface stress and its effects on resonance frequency of microcantilevers. *Journal of Applied Physics*, 77(8):3618–3622, 1995.

[115] Kyo Seon Hwang, Sang-Myung Lee, Kilho Eom, Jeong Hoon Lee, Yoon-Sik Lee, Jung Ho Park, Dae Sung Yoon, and Tae Song Kim. Nanomechanical microcantilever operated in vibration modes with use of RNA aptamer as receptor molecules for label-free detection of HCV helicase. *Biosensors and Bioelectronics*, 23(4):459–465, nov 2007.

[116] A. Gupta, D. Akin, and R. Bashir. Single virus particle mass detection using microresonators with nanoscale thickness. *Applied Physics Letters*, 84(11):1976–1978, mar 2004.

[117] Marcio G. von Muhlen, Norman D. Brault, Scott M. Knudsen, Shaoyi Jiang, and Scott R. Manalis. Label-Free Biomarker Sensing in Undiluted Serum with Suspended Microchannel Resonators. *Analytical Chemistry*, 82(5):1905–1910, mar 2010.

[118] T. P. Burg and S. R. Manalis. Suspended microchannel resonators for biomolecular detection. *Applied Physics Letters*, 83(13):2698–2700, sep 2003.

[119] J. L. Arlett and M. L. Roukes. Ultimate and practical limits of fluid-based mass detection with suspended microchannel resonators. *Journal of Applied Physics*, 108(8):084701, oct 2010.

[120] T Ikehara, J Lu, M Konno, R Maeda, and T Mihara. A high quality-factor silicon cantilever for a low detection-limit resonant mass sensor operated in air. *Journal of Micromechanics and Microengineering*, 17(12):2491–2494, dec 2007.

[121] N Kacem, J Arcamone, F Perez-Murano, and S Hentz. Dynamic range enhancement of nonlinear nanomechanical resonant cantilevers for highly sensitive NEMS gas/mass sensor applications. *Journal of Micromechanics and Microengineering*, 20(4):045023, apr 2010.

[122] Dazhong Jin, Xinxin Li, Jian Liu, Guomin Zuo, Yuelin Wang, Min Liu, and Haitao Yu. High-mode resonant piezoresistive cantilever sensors for tens-femtogram resoluble mass sensing in air. *Journal of Micromechanics and Microengineering*, 16(5):1017–1023, may 2006.

[123] Günter Sauerbrey. Verwendung von Schwingquarzen zur Wägung dünner Schichten und zur Mikrowägung. *Zeitschrift für Physik*, 155(2):206–222, apr 1959.

[124] C.K. O'Sullivan and G.G. Guilbault. Commercial quartz crystal microbalances - theory and applications. *Biosensors and Bioelectronics*, 14(8-9):663–670, dec 1999.

[125] Pengchao Si, John Mortensen, Alexei Komolov, Jens Denborg, and Preben Juul Møller. Polymer coated quartz crystal microbalance sensors for detection of volatile organic compounds in gas mixtures. *Analytica Chimica Acta*, 597(2):223–230, aug 2007.

[126] M. Teresa, S. R. Gomes, Karina S. Tavares, and João A. B. P. Oliveira. The quantification of potassium using a quartz crystal microbalance. *The Analyst*, 125(11):1983–1986, jan 2000.

[127] Xiaodi Su, Fook Tim Chew, and Sam F.Y. Li. Self-Assembled Monolayer-Based Piezoelectric Crystal Immunosensor for the Quantification of Total Human Immunoglobulin E. *Analytical Biochemistry*, 273(1):66–72, aug 1999.

[128] Dingzhong Wang, Gengjia Chen, Huaming Wang, Wei Tang, Wei Pan, Na Li, and Feng Liu. A reusable quartz crystal microbalance biosensor for highly specific detection of single-base DNA mutation. *Biosensors and Bioelectronics*, 48:276–280, 2013.

[129] Vo Ke Thanh Ngo, Dang Giang Nguyen, Hoang Phuong Uyen Nguyen, Van Man Tran, Thi Khoa My Nguyen, Trong Phat Huynh, Quang Vinh Lam, Thanh Dat Huynh, and Thi Ngoc Lien Truong. Quartz crystal microbalance (QCM) as biosensor for the detecting of Escherichia coli O157:H7. *Advances in Natural Sciences: Nanoscience and Nanotechnology*, 5(4), 2014.

[130] Guang Jia, Haifang Wang, Lei Yan, Xiang Wang, Rongjuan Pei, Tao Yan, Yuliang Zhao, Xinbiao Guo, Joel M Therrien, and MA Cooper. A living cell quartz crystal microbalance biosensor for continuous monitoring of cytotoxic responses of macrophages to single-walled carbon nanotubes. *Particle and Fibre Toxicology*, 8(4):1–17, 2011.

[131] Re-Ching Lin, Ying-Chung Chen, Wei-Tsai Chang, Chien-Chuan Cheng, and Kuo-Sheng Kao. Highly sensitive mass sensor using film bulk acoustic resonator. *Sensors and Actuators A: Physical*, 147(2):425–429, oct 2008.

[132] Xiaotun Qiu, Rui Tang, Jie Zhu, Jonathon Oiler, Cunjiang Yu, Ziyu Wang, and Hongyu Yu. Experiment and theoretical analysis of relative humidity sensor based on film bulk acoustic-wave resonator. *Sensors and Actuators B: Chemical*, 147(2):381–384, jun 2010.

[133] Martin Nirschl, Anja Blüher, Christiane Erler, Beate Katzschner, Inger Vikholm-Lundin, Sanna Auer, Janos Vörös, Wolfgang Pompe, Matthias Schreiter, and Michael Mertig. Film bulk acoustic resonators for DNA and protein detection and investigation of in vitro bacterial S-layer formation. *Sensors and Actuators A: Physical*, 156(1):180–184, nov 2009.

[134] Da Chen, Shuren Song, Jilong Ma, Zhen Zhang, Peng Wang, Weihui Liu, and Qiuquan Guo. Micro-electromechanical film bulk acoustic sensor for plasma and whole blood coagulation monitoring. *Biosensors and Bioelectronics*, 91:465–471, may 2017.

[135] Da Chen, Jingjing Wang, Yan Xu, Dehua Li, Zhaoxin Li, and Hongwei Song. The pure-shear mode solidly mounted resonator based on c-axis oriented ZnO film. *Applied Surface Science*, 256(24):7638–7642, oct 2010.

[136] R. Boudot, M. D. Li, V. Giordano, N. Rolland, P. A. Rolland, and P. Vincent. A solid-mounted resonator-oscillator-based 4.596 GHz frequency synthesis. *Review of Scientific Instruments*, 82(3):034706, mar 2011.

[137] Jingjing Wang, Da Chen, Yaoguo Gan, Xuejun Sun, and Yingying Jin. High sensitive self-assembled monolayer modified solid mounted resonator for organophosphate vapor detection. *Applied Surface Science*, 257(9):4365–4369, feb 2011.

[138] Wei Wei Pang, Hao Hao Zhang, Jong Jin Jong Jin Kim, Hongyu Hongyu Yu, and Eun Sok Eun Sok Kim. High Q Single-Mode High-Tone Bulk Acoustic Resonator Integrated with Surface-Micromachined FBAR Filter. In *IEEE MTT-S International Microwave Symposium Digest, 2005.*, pages 413–416. IEEE, 2005.

[139] Hao Zhang, Wei Pang, Hongyu Yu, and Eun Sok Kim. High-tone bulk acoustic resonators on sapphire, crystal quartz, fused silica, and silicon substrates. *Journal of Applied Physics*, 99(12):124911, jun 2006.

[140] Hao Zhang, Wei Pang, and Eun Sok Kim. High-frequency bulk acoustic resonant microbalances in liquid. In *Proceedings of the 2005 IEEE International Frequency Control Symposium and Exposition, 2005.*, pages 73–77. IEEE.

[141] R. Fogel, J. Limson, and A. A. Seshia. Acoustic biosensors. *Essays In Biochemistry*, 60(1):101–110, 2016.

[142] Y. Q. Fu, J. K. Luo, N. T. Nguyen, A. J. Walton, A. J. Flewitt, X. T. Zu, Y. Li, G. McHale, A. Matthews, E. Iborra, H. Du, and W. I. Milne. Advances in piezoelectric thin films for acoustic biosensors, acoustofluidics and lab-on-chip applications. *Progress in Materials Science*, 89:31–91, 2017.

[143] G. Kovacs, M.J. Vellekoop, R. Haueis, G.W. Lubking, and A. Venema. A love wave sensor for (bio)chemical sensing in liquids. *Sensors and Actuators A: Physical*, 43(1-3):38–43, may 1994.

[144] Electra Gizeli, Martha Liley, Christopher R. Lowe, and Horst Vogel. Antibody Binding to a Functionalized Supported Lipid Layer: A Direct Acoustic Immunosensor. *Analytical Chemistry*, 69(23):4808–4813, 1997.

[145] María-Isabel Rocha-Gaso, Carmen March-Iborra, Ángel Montoya-Baides, and Antonio Arnau-Vives. Surface Generated Acoustic Wave Biosensors for the Detection of Pathogens: A Review. *Sensors*, 9(7):5740–5769, jul 2009.

[146] Waldemar Soluch. Design of SAW delay lines for sensors. *Sensors and Actuators A: Physical*, 67(1-3):60–64, may 1998.

[147] M. Penza, V.I. Anisimkin, S.A. Maximov, and L. Vasanelli. Selective gas detection using uncoated SAW delay lines. *Sensors and Actuators B: Chemical*, 42(2):103–107, jul 1997.

[148] Wen Wang, Keekeun Lee, Taehyun Kim, Ikmo Park, and Sangsik Yang. A novel wireless, passive CO_2 sensor incorporating a surface acoustic wave reflective delay line. *Smart Materials and Structures*, 16(4):1382–1389, aug 2007.

[149] V.M. Yantchev, V.L. Strashilov, M. Rapp, U. Stahl, and I.D. Avramov. Theoretical and experimental mass-sensitivity analysis of polymer-coated SAW and STW resonators for gas sensing applications. *IEEE Sensors Journal*, 2(4):307–313, aug 2002.

[150] W. D. Bowers, R. L. Chuan, and T. M. Duong. A 200 MHz surface acoustic wave resonator mass microbalance. *Review of Scientific Instruments*, 62(6):1624–1629, jun 1991.

[151] Jeongim Park and Edward T. Zellers. Temperature and humidity compensation in the determination of solvent vapors with a microsensor system. *The Analyst*, 125(10):1775–1782, jan 2000.

[152] Vivien Lacour. *Optimisation d'un microcapteur GaAs à ondes acoustiques et de sa biointerface pour la détection de pathogènes en milieu liquide.* PhD thesis, dec 2016.

[153] Chronos Group. *Frequency Measurement and Control.* 1994.

[154] Grégory Arndt. *System architecture and circuit design for micro and nanoresonators-based mass sensing arrays.* PhD thesis, dec 2011.

[155] Guilherme N.M. Ferreira, Ana Carina Da-Silva, and Brigitte Tomé. Acoustic wave biosensors: physical models and biological applications of quartz crystal microbalance. *Trends in Biotechnology*, 27(12):689–697, 2009.

[156] S. Fanget, S. Hentz, P. Puget, J. Arcamone, M. Matheron, E. Colinet, P. Andreucci, L. Duraffourg, Ed. Myers, and M.L. Roukes. Gas sensors based on gravimetric detection - A review. *Sensors and Actuators B: Chemical*, 160(1):804–821, dec 2011.

[157] P. Ivaldi, J. Abergel, H. Blanc, E. Colinet, E.B. Myers, M.L. Roukes, P. Robert, P. Andreucci, S. Hentz, and E. Defay. DMMP vapor detection with 50NM thick AlN films based microcantilevers. In *2011 16th International Solid-State Sensors, Actuators and Microsystems Conference*, pages 162–165. IEEE, jun 2011.

[158] R.T. Howe and R.S. Muller. Resonant-microbridge vapor sensor. *IEEE Transactions on Electron Devices*, 33(4):499–506, apr 1986.

[159] Hao Zhang and Eun Sok Kim. Micromachined acoustic resonant mass sensor. *Journal of Microelectromechanical Systems*, 14(4):699–706, aug 2005.

[160] Sangjun Park, Inug Yoon, Sungwoo Lee, Hyojung Kim, Ji-Won Seo, Yoonyoung Chung, Alexander Unger, Mario Kupnik, and Hyunjoo J. Lee. CMUT-based resonant gas sensor array for VOC detection with low operating voltage. *Sensors and Actuators B: Chemical*, 273:1556–1563, nov 2018.

[161] Philip S. Waggoner and Harold G. Craighead. Micro- and nanomechanical sensors for environmental, chemical, and biological detection. *Lab on a Chip*, 7(10):1238–1255, 2007.

[162] K. L. Ekinci, X. M. H. Huang, and M. L. Roukes. Ultrasensitive nanoelectromechanical mass detection. *Applied Physics Letters*, 84(22):4469–4471, may 2004.

[163] Nickolay V. Lavrik and Panos G. Datskos. Femtogram mass detection using photothermally actuated nanomechanical resonators. *Applied Physics Letters*, 82(16):2697–2699, apr 2003.

[164] M. Dilena, M. Fedele Dell'Oste, J. Fernández-Sáez, A. Morassi, and R. Zaera. Mass detection in nanobeams from bending resonant frequency shifts. *Mechanical Systems and Signal Processing*, 116:261–276, feb 2019.

[165] B. Ilic, H. G. Craighead, S. Krylov, W. Senaratne, C. Ober, and P. Neuzil. Attogram detection using nanoelectromechanical oscillators. *Journal of Applied Physics*, 95(7):3694–3703, 2004.

[166] P. W. Anderson. Absence of Diffusion in Certain Random Lattices. *Physical Review*, 109(5):1492–1505, mar 1958.

[167] C. O. Orgun and B. H. Tongue. Mode Localization in Coupled Circular Plates. *Journal of Vibration and Acoustics*, 116(3):286, jul 1994.

[168] Michael I. Friswell, Arun Chandrashaker, and Sondipon Adhikari. An Energy Measure for Mode Localization. pages 105–110. Springer, Cham, 2016.

[169] Christophe Pierre, De Man Tang, and Earl H Dowell. Localized vibrations of disordered multispan beams-theory and experiment. *AIAA journal*, 25(9):1249–1257, 1987.

[170] Christophe Pierre. Mode localization and eigenvalue loci veering phenomena in disordered structures. *Journal of Sound and Vibration*, 126(3):485–502, 1988.

[171] Jing Yang, Jie Huang, Jiming Zhong, Hemin Zhang, and Honglong Chang. Self-oscillation for mode localized sensors. In *2017 19th International Conference on Solid-State Sensors, Actuators and Microsystems (TRANSDUCERS)*, pages 810–813. IEEE, jun 2017.

[172] Chun Zhao, Milind Pandit, Boqian Sun, Guillermo Sobreviela, Xudong Zou, and Ashwin Seshia. A Closed-Loop Readout Configuration for Mode-Localized Resonant MEMS Sensors. *Journal of Microelectromechanical Systems*, 26(3):501–503, jun 2017.

[173] Milind Pandit, Chun Zhao, Guillermo Sobreviela, Arif Mustafazade, Sijun Du, Xudong Zou, and Ashwin A. Seshia. Closed-Loop Characterization of Noise and Stability in a Mode-Localized Resonant MEMS Sensor. *IEEE Transactions on Ultrasonics, Ferroelectrics, and Frequency Control*, 66(1):170–180, jan 2019.

[174] Jing Yang, Jiming Zhong, and Honglong Chang. A Closed-Loop Mode-Localized Accelerometer. *Journal of Microelectromechanical Systems*, 27(2):210–217, apr 2018.

[175] Chun Zhao, Milind Pandit, Guillermo Sobreviela, Arif Mustafazade, Sijun Du, Xudong Zou, and Ashwin Seshia. On the noise optimization of resonant MEMS sensors utilizing vibration mode localization. *Applied Physics Letters*, 112(19):194103, may 2018.

[176] Hao Kang, Jing Yang, and Honglong Chang. A Closed-Loop Accelerometer Based on Three Degree-of-Freedom Weakly Coupled Resonator With Self-Elimination of Feedthrough Signal. *IEEE Sensors Journal*, 18(10):3960–3967, may 2018.

[177] Matthew Spletzer, Arvind Raman, Alexander Q. Wu, Xianfan Xu, and Ron Reifenberger. Ultrasensitive mass sensing using mode localization in coupled microcantilevers. *Applied Physics Letters*, 88(25):254102, jun 2006.

[178] V. Walter, G. Bourbon, P. Le Moal, N. Kacem, and J. Lardiès. Electrostatic Actuation to Counterbalance the Manufacturing Defects in a MEMS Mass Detection Sensor Using Mode Localization. In *Procedia Engineering*, volume 168, pages 1488–1491. Elsevier, jan 2016.

[179] Toky Rabenimanana, Vincent Walter, Najib Kacem, Patrice Le Moal, Gilles Bourbon, and Joseph Lardiès. Mass sensor using mode localization in two weakly coupled MEMS cantilevers with different lengths: Design and experimental model validation. *Sensors and Actuators, A: Physical*, 295:643–652, 2019.

[180] Jing Hong, Xiaodong Li, Di Zhou, Shuyi Liu, Xin Liu, and Dong F. Wang. Localization in coupled systems: Part III - vibration characteristics analysis in a mode-localized four cantilever array with and without mass perturbation. In *2018 Symposium on Design, Test, Integration & Packaging of MEMS and MOEMS (DTIP)*, pages 1–5. IEEE, may 2018.

[181] Aaditya R Hambarde and Rajendra M Patrikar. Optimal Design of Coupled Microelectromechanical Resonating Arrays for Mass Sensing. 2015.

[182] Xiaodong Li, Di Zhou, Rui Liu, Shuyi Liu, Xin Liu, and Dong F. Wang. Localization in coupled systems: Part II - Consideration on damping issue in a mode-localized cantilever array. In *2017 Symposium on Design, Test, Integration and Packaging of MEMS/MOEMS (DTIP)*, pages 1–4. IEEE, may 2017.

[183] Xiaodong Li, Di Zhou, Jiajun He, Xin Liu, and Dong F. Wang. Mode-localized cantilever array for picogram order mass sensing. In *2017 IEEE 12th International Conference on Nano/Micro Engineered and Molecular Systems (NEMS)*, pages 587–590. IEEE, apr 2017.

[184] Dong F Wang, Xiaodong Li, Xu Yang, Tsuyoshi Ikehara, and Ryutaro Maeda. Enhancing amplitude changes by mode localization in trio cantilevers with mass perturbation. *Journal of Micromechanics and Microengineering*, 25(9):095017, sep 2015.

[185] Barry E. DeMartini, Jeffrey F. Rhoads, Mark A. Zielke, Kyle G. Owen, Steven W. Shaw, and Kimberly L. Turner. A single input-single output coupled microresonator array for the detection and identification of multiple analytes. *Applied Physics Letters*, 93(5):054102, aug 2008.

[186] Matthew Spletzer, Arvind Raman, Hartono Sumali, and John P. Sullivan. Highly sensitive mass detection and identification using vibration localization in coupled microcantilever arrays. *Applied Physics Letters*, 92(11):114102, mar 2008.

[187] Dong F. Wang, Di Zhou, Shuyi Liu, and Jing Hong. Quantitative Identification Scheme for Multiple Analytes With a Mode-Localized Cantilever Array. *IEEE Sensors Journal*, 19(2):484–491, jan 2019.

[188] Stefano Stassi, Giulia De Laurentis, Debadi Chakraborty, Katarzyna Bejtka, Angelica Chiodoni, John E. Sader, and Carlo Ricciardi. Large-scale parallelization of nanomechanical mass spectrometry with weakly-coupled resonators. *Nature Communications*, 10(1), 2019.

[189] Malar Chellasivalingam, Milind Pandit, Markus Kalberer, and Ashwin A Seshia. Ultra-fine particulate detection using mode-localized mems resonators. In *2019 Joint Conference of the IEEE International Frequency Control Symposium and European Frequency and Time Forum (EFTF/IFC)*, pages 1–5. IEEE, 2019.

[190] Zimu Yan, Yongcun Hao, Wenmu Li, Zhao Zhang, and Honglong Chang. A Mode-Localized Lorentz Force Magnetometer with $1.6\mu\mathrm{T}/\sqrt{Hz}$ Resolution. In *2019 20th International Conference on Solid-State Sensors, Actuators and Microsystems & Eurosensors XXXIII (TRANSDUCERS & EUROSENSORS XXXIII)*, pages 1815–1818. IEEE, jun 2019.

[191] Hao Kang, Jing Yang, Jiming Zhong, Heming Zhang, and Honglong Chang. A mode-localized accelerometer based on three degree-of-freedom weakly coupled resonator. In *2017 IEEE SENSORS*, pages 1–3. IEEE, oct 2017.

[192] Milind Pandit, Chun Zhao, Guillermo Sobreviela, Arif Mustafazade, Xudong Zou, and Ashwin A. Seshia. A mode-localized MEMS accelerometer with 7μg bias stability. In *2018 IEEE Micro Electro Mechanical Systems (MEMS)*, pages 968–971. IEEE, jan 2018.

[193] Hemin Zhang, Boyang Li, Weizheng Yuan, Michael Kraft, and Honglong Chang. An Acceleration Sensing Method Based on the Mode Localization of Weakly Coupled Resonators. *Journal of Microelectromechanical Systems*, 25(2):286–296, apr 2016.

[194] H.M. Zhang, W.Z. Yuan, B.Y. Li, Y.C. Hao, M. Kraft, and H.L. Chang. A novel resonant accelerometer based on mode localization of weakly coupled resonators. In *2015 Transducers - 2015 18th International Conference on Solid-State Sensors, Actuators and Microsystems (TRANSDUCERS)*, pages 1073–1076. IEEE, jun 2015.

[195] Jiaju Liang, Yongcun Hao, Hao Kang, Bing Ruan, and Honglong Chang. A Mode-Localized Voltmeter with Resolution of 46.8 Nanovolts. In *2019 20th International Conference on Solid-State Sensors, Actuators and Microsystems & Eurosensors XXXIII (TRANSDUCERS & EUROSENSORS XXXIII)*, pages 226–229. IEEE, jun 2019.

[196] Jing Yang, Hao Kang, and Honglong Chang. A micro resonant electrometer with 9-electron charge resolution in room temperature. In *2018 IEEE Micro Electro Mechanical Systems (MEMS)*, pages 67–70. IEEE, jan 2018.

[197] Hemin Zhang, Weizheng Yuan, Jie Huang, Boyang Li, and Honglong Chang. A high-sensitive resonant electrometer based on mode localization of the weakly coupled resonators. In *2016 IEEE 29th International Conference on Micro Electro Mechanical Systems (MEMS)*, pages 87–90. IEEE, jan 2016.

[198] Hemin Zhang, Jie Huang, Weizheng Yuan, and Honglong Chang. A High-Sensitivity Micromechanical Electrometer Based on Mode Localization of Two Degree-of-Freedom Weakly Coupled Resonators. *Journal of Microelectromechanical Systems*, 25(5):937–946, oct 2016.

[199] Xin Guo, Bo Yang, and Cheng Li. Design, modeling and theoretical analysis of a novel dual-axis hair flow sensor based on mode localization of weakly coupled resonators. *AIP Advances*, 9(5):055030, may 2019.

[200] P. Thiruvenkata, J. Yan, and A. A. Seshia. Ultrasensitive mode-localized micromechanical electrometer. In *2010 IEEE International Frequency Control Symposium*, pages 91–96. IEEE, jun 2010.

[201] Hemin Zhang, Jing Yang, Weizheng Yuan, and Honglong Chang. Linear sensing for mode-localized sensors. *Sensors and Actuators A: Physical*, 277:35–42, jul 2018.

[202] Hemin Zhang, Honglong Chang, and Weizheng Yuan. Characterization of forced localization of disordered weakly coupled micromechanical resonators. *Microsystems & Nanoengineering*, 3(1):17023, dec 2017.

[203] Bo Peng, Kai-Ming Hu, Lei Shao, Han Yan, Lei Li, Xueyong Wei, and Wen-Ming Zhang. A sensitivity tunable accelerometer based on series-parallel electromechanically coupled resonators using mode localization. *Journal of Microelectromechanical Systems*, 2019.

[204] Siavash Pourkamali and Farrokh Ayazi. Electrically coupled MEMS bandpass filters: Part II. Without coupling element. *Sensors and Actuators A: Physical*, 122(2):317–325, aug 2005.

[205] P. Thiruvenkatanathan, J. Yan, J. E.Y. Lee, and A. A. Seshia. Enhancing parametric sensitivity using mode localization in electrically coupled mems resonators. In *TRANSDUCERS 2009 - 15th International Conference on Solid-State Sensors, Actuators and Microsystems*, pages 2350–2353. IEEE, jun 2009.

[206] Graham S. Wood, Chun Zhao, Suan Hui Pu, Stuart A. Boden, Ibrahim Sari, and Michael Kraft. Mass sensor utilising the mode-localisation effect in an electrostatically-coupled MEMS resonator pair fabricated using an SOI process. *Microelectronic Engineering*, 159:169–173, jun 2016.

[207] Yuan Wang, Chun Zhao, Chen Wang, Delphine Cerica, Mathieu Baijot, Qijun Xiao, Serguei Stoukatch, and Michael Kraft. A mass sensor based on 3-DOF mode localized coupled resonator under atmospheric pressure. *Sensors and Actuators A: Physical*, 279:254–262, aug 2018.

[208] P. Thiruvenkatanathan and A. A. Seshia. Mode-Localized Displacement Sensing. *Journal of Microelectromechanical Systems*, 21(5):1016–1018, oct 2012.

[209] Chun Zhao, Graham S. Wood, Jianbing Xie, Honglong Chang, Suan Hui Pu, and Michael Kraft. A force sensor based on three weakly coupled resonators with ultrahigh sensitivity. *Sensors and Actuators A: Physical*, 232:151–162, aug 2015.

[210] S.H.Pu Zhao, C; G.S. Wood and M.Kraft. Design of an ultra-sensitive MEMS force sensor utilizing mode localization in weakly coupled resonators. *23rd MICROMECHANICS AND MICROSYSTEMS EUROPE WORKSHOP*, (3):1–4, 2012.

[211] M.H. Montaseri, J. Xie, H. Chang, Z. Chao, G. Wood, and M. Kraft. Atmospheric pressure mode localization coupled resonators force sensor. In *2015 Transducers - 2015 18th International Conference on Solid-State Sensors, Actuators and Microsystems (TRANSDUCERS)*, pages 1183–1186. IEEE, jun 2015.

[212] Chun Zhao, Graham S. Wood, Suan Hui Pu, and Michael Kraft. A mode-localized MEMS electrical potential sensor based on three electrically coupled resonators. *Journal of Sensors and Sensor Systems*, 6(1):1–8, jan 2017.

[213] Chun Zhao, Graham S. Wood, Jianbing Xie, Honglong Chang, Suan Hui Pu, Harold M. H. Chong, and Michael Kraft. A sensor for stiffness change sensing based on three weakly coupled resonators with enhanced sensitivity. In *2015 28th IEEE International Conference on Micro Electro Mechanical Systems (MEMS)*, pages 881–884. IEEE, jan 2015.

[214] Chun Zhao. *A Mems sensor for stiffness change sensing application based on three weakly coupled resonators*. PhD thesis, 2016.

[215] Graham S. Wood, Chun Zhao, Ibrahim Sari, Suan Hui Pu, and Michael Kraft. Sensor based on the mode-localization effect in electrostatically-coupled MEMS resonators fabricated using an SOI process. In *2015 IEEE SENSORS - Proceedings*, pages 1–4. IEEE, nov 2015.

[216] Ashwin A. Seshia. Mode-localized sensing in micro- and nano-mechanical resonator arrays. In *2016 IEEE SENSORS*, pages 1–3. IEEE, oct 2016.

[217] M. Manav, G. Reynen, M. Sharma, E. Cretu, and A. S. Phani. Ultrasensitive resonant MEMS transducers with tunable coupling. In *2013 Transducers and Eurosensors XXVII: The 17th International Conference on Solid-State Sensors, Actuators and Microsystems, TRANSDUCERS and EUROSENSORS 2013*, pages 996–999. IEEE, jun 2013.

[218] Chun Zhao, Graham S. Wood, Jianbing Xie, Honglong Chang, Suan Hui Pu, and Michael Kraft. A Three Degree-of-Freedom Weakly Coupled Resonator Sensor with Enhanced Stiffness Sensitivity. *Journal of Microelectromechanical Systems*, 25(1):38–51, feb 2016.

[219] Hao Kang, Jing Yang, and Honglong Chang. A mode-localized accelerometer based on four degree-of-freedom weakly coupled resonators. In *2018 IEEE Micro Electro Mechanical Systems (MEMS)*, pages 960–963. IEEE, jan 2018.

[220] Yuan Wang, Chen Wang, Chun Zhao, Huafeng Liu, Delphine Cerica, Mathieu Baijot, Francois Dupont, Serguei Stoukatch, and Michael Kraft. A Novel Qcm Mass Sensing System Incorporated with A 3-Dof Mode Localized Coupled Resonator Stiffness Sensor. In *2019 20th International Conference on Solid-State Sensors, Actuators and Microsystems & Eurosensors XXXIII (TRANSDUCERS & EUROSENSORS XXXIII)*, pages 1823–1826. IEEE, jun 2019.

[221] C. Zhao, G.S. Wood, J. Xie, H. Chang, S.H. Pu, and M. Kraft. Comparative study of different output metrics for a three weakly coupled resonator sensor. In *2015 Transducers - 2015 18th International Conference on Solid-State Sensors, Actuators and Microsystems (TRANSDUCERS)*, pages 2196–2199. IEEE, jun 2015.

[222] P. Thiruvenkatanathan, J. Woodhouse, J. Yan, and A. A. Seshia. Limits to mode-localized sensing using micro- and nanomechanical resonator arrays. In *Journal of Applied Physics*, volume 109, page 104903. American Institute of Physics, may 2011.

[223] M. Manav, A. Srikantha Phani, and Edmond Cretu. Mode Localization and Sensitivity in Weakly Coupled Resonators. *IEEE Sensors Journal*, 19(8):2999–3007, apr 2019.

[224] Hemin Zhang, Hao Kang, and Honglong Chang. Suppression on Nonlinearity of Mode-Localized Sensors Using Algebraic Summation of Amplitude Ratios as the Output Metric. *IEEE Sensors Journal*, 18(19):7802–7809, oct 2018.

[225] Jiming Zhong, Jing Yang, and Honglong Chang. The temperature drift suppression of mode-localized resonant sensors. In *2018 IEEE Micro Electro Mechanical Systems (MEMS)*, pages 467–470. IEEE, jan 2018.

[226] P. Thiruvenkatanathan, J. Yan, and A. A. Seshia. Common mode rejection in electrically coupled MEMS resonators utilizing mode localization for sensor applications. In *2009 IEEE International Frequency Control Symposium Joint with the 22nd European Frequency and Time forum*, pages 358–363. IEEE, apr 2009.

[227] J. Juillard, P. Prache, P. Maris Ferreira, and N. Barniol. Impact of output metric on the resolution of mode-localized MEMS resonant sensors. In *2017 Joint Conference of the European Frequency and Time Forum and IEEE International Frequency Control Symposium, EFTF/IFC 2017 - Proceedings*, pages 506–509. Institute of Electrical and Electronics Engineers Inc., oct 2017.

[228] Guowei Tao, Hemin Zhang, Honglong Chang, and Bhaskar Choubey. Inverse eigenvalue sensing in coupled micro/-nano system. *Journal of Microelectromechanical Systems*, 27(5):886–895, 2018.

[229] T.H. Hanley, B.J. Gallacher, and H.T.D. Grigg. On the exploitation of mode localization in surface acoustic wave MEMS. *Mechanical Systems and Signal Processing*, 89:27–36, may 2017.

[230] Siamak Hafizi-Moori and Edmond Cretu. Weakly-Coupled Resonators in Capacitive Readout Circuits. *IEEE Transactions on Circuits and Systems I: Regular Papers*, 62(2):337–346, feb 2015.

[231] Guowei Tao and Bhaskar Choubey. A Simple Technique to Readout and Characterize Coupled MEMS Resonators. *Journal of Microelectromechanical Systems*, 25(4):617–625, aug 2016.

[232] Marie Frénéa. Filtres actifs. ENS Cachan, Antenne de Bretagne. http://docplayer.fr/45468754-Filtres-actifs-antenne-de-bretagne.html, 2002.

[233] Stephen M. Steve Trimberger. Three Ages of FPGAs: A Retrospective on the First Thirty Years of FPGA Technology. *IEEE Solid-State Circuits Magazine*, 10(2):16–29, 2018.

[234] A. Ibrahim, W. Simon, D. Doy, E. Pignat, F. Angiolini, M. Arditi, J.-P. Thiran, and G. De Micheli. Single-FPGA complete 3D and 2D medical ultrasound imager. In *2017 Conference on Design and Architectures for Signal and Image Processing (DASIP)*, pages 1–6. IEEE, sep 2017.

[235] Kyung-Chan Jin, Kye-Sung Lee, and Geun-Hee Kim. High-speed FPGA-GPU processing for 3D-OCT imaging. In *2017 3rd IEEE International Conference on Computer and Communications (ICCC)*, pages 2085–2088. IEEE, dec 2017.

[236] A.E. Desjardins, B.J. Vakoc, M.J. Suter, Seok-Hyun Yun, G.J. Tearney, and B.E. Bouma. Real-Time FPGA Processing for High-Speed Optical Frequency Domain Imaging. *IEEE Transactions on Medical Imaging*, 28(9):1468–1472, sep 2009.

[237] Gwenhael Goavec-Merou. *Générateur de coprocesseur pour le traitement de données en flux (vidéo ou similaire) sur FPGA.* PhD thesis, 2014.

[238] Simultaneous oscillation and frequency tracking of multiple resonances via digitally implemented phase-locked loop array. *Patent*, oct 2015.

[239] Shruti Edway and R K Manjunath. Design and simulation of FPGA based all digital phase locked loop (ADPLL). In *2017 3rd International Conference on Applied and Theoretical Computing and Communication Technology (iCATccT)*, pages 259–263. IEEE, dec 2017.

[240] Martin Kumm, Harald Klingbeil, and Peter Zipf. An FPGA-Based Linear All-Digital Phase-Locked Loop. *IEEE Transactions on Circuits and Systems I: Regular Papers*, 57(9):2487–2497, sep 2010.

[241] Alexander Gazman, Colm Browning, Ziyi Zhu, Liam R Barry, and Keren Bergman. Automated Thermal Stabilization of Cascaded Silicon Photonic Ring Resonators for Reconfigurable WDM Applications. In *2017 European Conference on Optical Communication (ECOC)*, pages 1–3. IEEE, sep 2017.

[242] Adriana A. Aguirre, Leonardo D. Muñoz, César A. Martín, María J. Ramírez, and Carlos A. Salazar. Design of Digital PID Controllers Relying on FPGA-based Techniques. *IFAC-PapersOnLine*, 51(4):936–941, jan 2018.

[243] Bas Janssen and Jeedella J.S.Y. Jeedella. Distributed control system : FPGA accelerated PID controller, june 2016.

[244] Ruchi V. Jain, M. V. Aware, and A. S. Junghare. Implementation of a PID control PWM module on altera DE0 kit using FPGA. In *2016 IEEE First International Conference on Control, Measurement and Instrumentation (CMI)*, pages 341–345. IEEE, jan 2016.

[245] Ana L. F. de Barros, Leandro M. Samyn, Jhonatan S. Sobral, Alessandro R. L. Zachi, and Luciana F. Almeida. Frequency Response Characterization of a Sonoluminescence Acoustic Resonator by Using a FPGA-Based Instrumentation. *Journal of Control, Automation and Electrical Systems*, 30(1):104–112, feb 2019.

[246] Ying Xu, Chetan S. Thakur, Ram K. Singh, Tara Julia Hamilton, Runchun M. Wang, and André van Schaik. A FPGA Implementation of the CAR-FAC Cochlear Model. *Frontiers in Neuroscience*, 12:198, apr 2018.

[247] Nariman Roshandel Tavana and Venkata Dinavahi. Real-Time Nonlinear Magnetic Equivalent Circuit Model of Induction Machine on FPGA for Hardware-in-the-Loop Simulation. *IEEE Transactions on Energy Conversion*, 31(2):520–530, jun 2016.

[248] Fernando Alvarez-Gonzalez, Antonio Griffo, Bhaskar Sen, and Jiabin Wang. Real-Time Hardware-in-the-Loop Simulation of Permanent-Magnet Synchronous Motor Drives Under Stator Faults. *IEEE Transactions on Industrial Electronics*, 64(9):6960–6969, sep 2017.

[249] Chen Liu, Xizheng Guo, Rui Ma, Zhongliang Li, Franck Gechter, and Fei Gao. A System-Level FPGA-Based Hardware-in-the-Loop Test of High-Speed Train. *IEEE Transactions on Transportation Electrification*, 4(4):912–921, dec 2018.

[250] J. Mina, Z. Flores, E. Lopez, A. Perez, and J.-H. Calleja. Processor-in-the-loop and hardware-in-the-loop simulation of electric systems based in FPGA. In *2016 13th International Conference on Power Electronics (CIEP)*, pages 172–177. IEEE, jun 2016.

[251] Georg Lauss, M. Omar Faruque, Karl Schoder, Christian Dufour, Alexander Viehweider, and James Langston. Characteristics and Design of Power Hardware-in-the-Loop Simulations for Electrical Power Systems. *IEEE Transactions on Industrial Electronics*, 63(1):406–417, jan 2016.

[252] Xiaoyue Yang, Chunhua Yang, Tao Peng, Zhiwen Chen, Bo Liu, and Weihua Gui. Hardware-in-the-Loop Fault Injection for Traction Control System. *IEEE Journal of Emerging and Selected Topics in Power Electronics*, 6(2):696–706, jun 2018.

[253] Behzad Jandaghi and Venkata Dinavahi. Hardware-in-the-Loop Emulation of Linear Induction Motor Drive for MagLev Application. *IEEE Transactions on Plasma Science*, 44(4):679–686, apr 2016.

[254] Jiantao Qiu, Sen Song, Yu Wang, Huazhong Yang, Jie Wang, Song Yao, Kaiyuan Guo, Boxun Li, Erjin Zhou, Jincheng Yu, Tianqi Tang, and Ningyi Xu. Going Deeper with Embedded FPGA Platform for Convolutional Neural Network. In *Proceedings of the 2016 ACM/SIGDA International Symposium on Field-Programmable Gate Arrays - FPGA '16*, pages 26–35, New York, New York, USA, 2016. ACM Press.

[255] Naveen Suda, Vikas Chandra, Ganesh Dasika, Abinash Mohanty, Yufei Ma, Sarma Vrudhula, Jae-sun Seo, and Yu Cao. Throughput-Optimized OpenCL-based FPGA Accelerator for Large-Scale Convolutional Neural Networks. In *Proceedings of the 2016 ACM/SIGDA International Symposium on Field-Programmable Gate Arrays - FPGA '16*, pages 16–25, New York, USA, 2016. ACM Press.

[256] Rajib Das, Amrita Guha, and Ananya Bhattacharya. FPGA based higher order FIR filter using XILINX system generator. In *2016 International Conference on Signal Processing, Communication, Power and Embedded System (SCOPES)*, pages 111–115. IEEE, oct 2016.

[257] Thanh Chi Pham, Bach Xuan Hoang, Quang Tri Chiem, Linh Duc Tran, and Anh-Vu Ho. Implementation of a short word length ternary FIR filter in both FPGA and ASIC. In *2018 2nd International Conference on Recent Advances in Signal Processing, Telecommunications & Computing (SigTelCom)*, pages 45–50. IEEE, jan 2018.

[258] Albert Ryou and Jonathan Simon. Active cancellation of acoustical resonances with an FPGA FIR filter. *Review of Scientific Instruments*, 88(1):013101, jan 2017.

[259] Cai-hong Liu, Shuang-liang Tian, and Zi-long Liu. Design of FIR Filter Based on FPGA. In *Proceedings of the 2018 International Conference on Sensors, Signal and Image Processing - SSIP 2018*, pages 46–50, New York, USA, 2018. ACM Press.

[260] Koki Arauchi, Shohei Maki, Toshiyuki Inoue, Akira Tsuchiya, and Keiji Kishine. Compact implementation IIR filter in FPGA for noise reduction of sensor signal. In *2017 International SoC Design Conference (ISOCC)*, pages 258–259. IEEE, nov 2017.

[261] Prasad Bharade, Yashwant Joshi, and Ramchandra Manthalkar. Design and implementation of IIR lattice filter using floating point arithmetic in FPGA. In *2016 Conference on Advances in Signal Processing (CASP)*, pages 321–326. IEEE, jun 2016.

[262] D. C. Toledo-Perez, M. A. Martinez-Prado, J Rodriguez-Resendiz, S. Tovar Arriaga, and M. A. Marquez-Gutierrez. IIR digital filter design implemented on FPGA for myoelectric signals. In *2017 XIII International Engineering Congress (CONIIN)*, pages 1–7. IEEE, may 2017.

[263] Arnob Paul, Tanvir Zaman Khan, Prajoy Podder, Md. Mehedi Hasan, and Tanveer Ahmed. Reconfigurable architecture design of FIR and IIR in FPGA. In *2015 2nd International Conference on Signal Processing and Integrated Networks (SPIN)*, pages 958–963. IEEE, feb 2015.

[264] P Priya and S Ashok. IIR Digital Filter Design Using Xilinx System Generator for FPGA Implementation. In *2018 International Conference on Communication and Signal Processing (ICCSP)*, pages 0054–0057. IEEE, apr 2018.

[265] Nagapuri Srinivas, Kankanala Srinivas, Gayadhar Pradhan, and Puli Kishore Kumar. FPGA Implementation for Real-Time Epoch Extraction in Speech Signal. pages 392–400. Springer, Singapore, apr 2018.

[266] L. Gaffuri Pagani, G. Langfelder, P. Minotti, and N. Aresi. A programmable emulator of MEMS inertial sensors. In *2017 IEEE International Symposium on Inertial Sensors and Systems (INERTIAL)*, pages 142–143. IEEE, mar 2017.

[267] Chen Wang, Ethan D. Burnham-Fay, and Jonathan D. Ellis. Real-time FPGA-based Kalman filter for constant and non-constant velocity periodic error correction. *Precision Engineering*, 48:133–143, apr 2017.

[268] Mattia Ricco, Patrizio Manganiello, Eric Monmasson, Giovanni Petrone, and Giovanni Spagnuolo. FPGA-Based Implementation of Dual Kalman Filter for PV MPPT Applications. *IEEE Transactions on Industrial Informatics*, 13(1):176–185, feb 2017.

[269] Yan Ma, Peng Duan, Pengcai He, Fan Zhang, and Hong Chen. FPGA implementation of extended Kalman filter for SOC estimation of lithium-ion battery in electric vehicle. *Asian Journal of Control*, 21(4):2126–2136, jul 2019.

[270] Vulisi Narendra Kumar and Gayadhar Panda. FPGA Implementation of Power Management Algorithm for Wind Energy Storage System with Kalman Filter MPPT Technique. In *2018 31st International Conference on VLSI Design and 2018 17th International Conference on Embedded Systems (VLSID)*, pages 449–450. IEEE, jan 2018.

[271] Jiawei Liao, Michael Jost, Michael Schaffner, Michele Magno, Matthias Korb, Luca Benini, Felix Tebbenjohanns, Rene Reimann, Vijay Jain, Michael Gross, Andrei Militaru, Martin Frimmer, and Lukas Novotny. FPGA Implementation of a Kalman-Based Motion Estimator for Levitated Nanoparticles. *IEEE Transactions on Instrumentation and Measurement*, 68(7):2374–2386, jul 2019.

[272] Jeremy Soh and Xiaofeng Wu. An FPGA-Based Unscented Kalman Filter for System-On-Chip Applications. *IEEE Transactions on Circuits and Systems II: Express Briefs*, 64(4):447–451, apr 2017.

[273] Bibin Johnson, Nimin Thomas, and J. Sheeba Rani. An FPGA Based High throughput Discrete Kalman Filter Architecture for Real-Time Image Denoising. In *2017 30th International Conference on VLSI Design and 2017 16th International Conference on Embedded Systems (VLSID)*, pages 55–60. IEEE, jan 2017.

[274] Fargham Sandhu, Hazlina Selamat, S. E. Alavi, and Vahid Behtaji Siahkal Mahalleh. FPGA-Based Implementation of Kalman Filter for Real-Time Estimation of Tire Velocity and Acceleration. *IEEE Sensors Journal*, 17(17):5749–5758, sep 2017.

[275] Chao Liao, Jinbin Luo, Li Liu, and Chengxiang Liu. Realization of Fiber Optic Gyro Modulation and Demodulation Control System Based on FPGA. In *2017 5th International Conference on Mechanical, Automotive and Materials Engineering (CMAME)*, pages 296–300. IEEE, aug 2017.

[276] Red Pitaya Hardware Specifications V1.1.1. https://www.galagomarket.com/datasheet/redpitaya_hardware specifications.pdf.

[277] FPGA datasheet. https://www.xilinx.com/support/documentation/data_sheets/ds180_7Series_Overview.pdf.

[278] Configurable logic block. https://www.xilinx.com/support/documentation/user_guides/ug474_7Series_CLB.pdf.

[279] Red Pitaya board. https://www.fpga.red/redpitaya-v2/.

[280] Björn Wittenmark, Karl Johan Åström, and Karl-erik Årzén. *Computer Control : An Overview Björn Wittenmark*. 2002.

[281] Vivado Design Suite. https://www.xilinx.com/products/design-tools/vivado.html.

[282] Red Pitaya STEMlab. https://redpitaya.readthedocs.io/en/latest/.

[283] GitHub. https://github.com/oscimp/oscimpDigital.

[284] Buildroot. https://buildroot.org/.

[285] GNU Radio. https://www.gnuradio.org/.

[286] LT1358 specifications. https://www.analog.com/media/en/technical-documentation/data-sheets/135859fb.pdf.

[287] Quartz resonator at 1.8 MHz. https://fr.farnell.com/ael-crystals/x1m843200l010/quartz-1-843200mhz/dp/9509623.

[288] Limits definitions. https://www.ncbi.nlm.nih.gov/pmc/articles/PMC2556583/.

[289] Michael Wirthlin. High-reliability FPGA-based systems: space, high-energy physics, and beyond. *Proceedings of the IEEE*, 103(3):379–389, 2015.

[290] Leonard Rockett, Dinu Patel, Steven Danziger, Brian Cronquist, and J J Wang. Radiation hardened FPGA technology for space applications. In *2007 IEEE Aerospace Conference*, pages 1–7. IEEE, 2007.

[291] Nadim Maluf. An Introduction to Microelectromechanical Systems Engineering. *Measurement Science and Technology*, 13(2):229–229, feb 2002.

[292] M. E. Motamedi. Merging micro-optics with micromechanics: micro-opto-electro-mechanical (MOEM) devices. volume 10271, page 102710G. International Society for Optics and Photonics, dec 1993.

[293] Jim Woodhouse. The acoustics of the violin: a review. *Reports on Progress in Physics*, 77(11):115901, nov 2014.

[294] John W. Cookson. Theory of the Piezo-Resistive Effect. *Physical Review*, 47(2):194–195, jan 1935.

[295] Impedance analyzer E4990A datasheet. https://www.keysight.com/us/en/assets/7018-04256/data-sheets/5991-3890.pdf.

[296] Micro particles. https://microparticles.de/en.

Abstract

There has been an ever growing interest for many years in ultra-accurate mass detection in the health, environment and agri-food fields. In this context, the last decade has seen the emergence of resonant sensors based on Anderson localization in an array of weakly coupled resonators. Known to be highly sensitive to mass perturbations, this phenomenon however requires identical and weakly coupled resonators, which is a challenge due to microfabrication constraints. In order to overcome this limitation, we present in this thesis an alternative solution based on a hybrid system, where a hardware (field programmable gate array, FPGA) plays the role of a resonator as well as the coupling in closed loop with a quartz resonator. The digital aspect of the system allows maximum sensitivity to be achieved with a fine tuning of the different parameters and the implementation of a coupling regardless of the physical resonator geometry. Therefore, mode localization can be generated using shear waves resonant structures such as the quartz cristal microbalance (QCM), widely used in biosensing for its high Q-factor and large binding surface. This solution has been designed, implemented and tested with digital and mass perturbations, and the results are consistent with theoretical models. Finally, the experimental sensitivities achieved in this work are higher than those found in the literature, which is promising for the design of a new generation of ultrasensitive sensors based on Anderson localization. However, these results have yet to be confronted with signal-to-noise ratio problems, as suggested by the theoretical studies carried out in the framework of this thesis.

Keywords : Mass sensing, mode localization, QCM, FPGA, hybrid system

Résumé

Il existe depuis de nombreuses années un intérêt croissant pour la détection de masse ultra-précise dans les domaines de la santé, de l'environnement et de l'agroalimentaire. Dans ce contexte, la dernière décennie a vu l'émergence de capteurs basés sur la localisation d'Anderson dans un réseau de résonateurs couplés. Connu pour être très sensible aux perturbations de masse, ce phénomène nécessite cependant des résonateurs identiques et faiblement couplés, ce qui constitue un défi technique en raison des contraintes de microfabrication. Afin de s'affranchir de ce problème, nous présentons dans cette thèse une solution alternative basée sur un système hybride composé d'une partie numérique (field programmable gate array, FPGA) jouant le rôle d'un résonateur ainsi que du couplage, et d'un résonateur à quartz. L'aspect numérique du système permet d'obtenir une sensibilité maximale grâce à un réglage fin des différents paramètres ainsi que l'implémentation d'un couplage quelle que soit la géométrie du résonateur physique. Par conséquent, la localisation de modes peut être générée sur des structures résonantes à ondes de cisaillement telles que la microbalance à quartz (QCM), qui est largement utilisée dans la biodétection pour son facteur de qualité élevé et sa grande surface de liaison. Cette solution a été conçue, mise en œuvre et testée avec des perturbations numériques et de masse, et les résultats sont conformes aux modèles théoriques. Enfin, les sensibilités expérimentales obtenues dans ce travail sont supérieures à celles trouvées dans la littérature, ce qui est prometteur pour la conception d'une nouvelle génération de capteurs ultrasensibles basés sur la localisation d'Anderson. Cependant, ces résultats doivent encore être confrontés à des problèmes de rapport signal sur bruit, comme le suggèrent les études théoriques réalisées dans le cadre de cette thèse.

Mots-Clefs : Mesure de masse, localisation de modes, QCM, FPGA, système hybride